INTEGRATED GEOPHYSICAL METHODS TO DELINEATE R21 SINKHOLES NEAR OLIFANTSFONTEIN, GAUTENG, SOUTH AFRICA

Nondumiso Mabele

Supervised by

Professor Musa Manzi

A thesis submitted to the Faculty of Science, University of the Witwatersrand, Johannesburg, in fulfilment of the requirements for the degree of

Master of Science

2024

DECLARATION

I Nondumiso Mabele (Student number: 305480) am a student registered for MSc in Geophysics in the year 2024. I hereby declare the following:

- I am aware that plagiarism (the use of someone else's work without their permission and/or without acknowledging the original source) is wrong.
- I confirm that ALL the work submitted for assessment for the above course is my own unaided work except where I have explicitly indicated otherwise.
- I have followed the required conventions in referencing the thoughts and ideas of others.
- I understand that the University of the Witwatersrand may take disciplinary action against me if there is a belief that this is not my own unaided work or that I have failed to acknowledge the source of the ideas or words in my writing.

Signature: 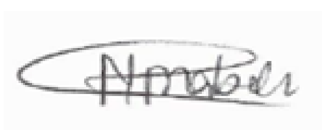 Date: 12-09-2024

ABSTRACT

The Gauteng province in South Africa is known for having a significant portion, at least 25%, of its land is underlain by dolomite rocks. An integrated approach of non-invasive geophysical methods was utilised to map the geometry (shape, size and extent) of the R21 highway sinkhole that formed near Olifantsfontein. These methods include seismic (reflection and refraction), multi-channel analyses of surface waves (MASW), electrical resistivity tomography (ERT), and ground penetrating radar (GPR). The objectives of the investigation were three-fold: (1) to understand the geology and formation of sinkholes in Gauteng; (2) to use geophysical techniques to map and characterize sinkholes in the study area, including determining their geometry, lateral and vertical extents; and (3) to determine the effectiveness of each method in mapping sinkholes.

Despite the high level of noise along the highway, the geophysical surveys were conducted successfully and provided a good basis for the integrated interpretations. This study showcases the importance of utilising multiple geophysical methods to obtain a comprehensive understanding of sinkholes and their subsurface characteristics. It also demonstrates the practical application of these methods in real-world scenarios for improved hazard assessment and risk mitigation. The GPR results suggest that a sinkhole extends by ~2.5 m further into the R21 highway surface with a depth of ~8-10 m (top to bottom). The refraction seismic method suggests that the sinkhole is ~20 m wide, while the ERT results suggest that the sinkhole starts at 10 m and extends to 15 m depth. The results from reflection seismics indicate that the R21 sinkhole is structurally controlled and it is characterised by fracturing and faulting that manifest as diffractions on the seismic sections.

Understanding the extent and characteristics of sinkholes is crucial for infrastructure planning and hazard mitigation, especially in areas prone to subsidence and sinkhole formation like in Gauteng. These findings can inform decision-making processes related to road maintenance, construction, and land use planning in sinkhole-prone regions. The success of the integrated geophysical approach in this study highlights its potential for similar investigations in other areas with karst geology and sinkhole risks.

ACKNOWLEDGMENTS

I would like to sincerely thank my supervisor, Professor Musa Manzi, for all the support, encouragement, and vast expertise during MSc career. I am truly grateful to Musa for seeing the potential in me and encouraging me to pursue my MSc degree. Thank you to my sponsors, Shango Solutions, Jim and Gladys Taylor Trust, and the Council for Geoscience (CGS) for funding me for the past two years. Specifically, I would also like to thank the Council for Geoscience and the South African National Roads Agency Ltd (SANRAL) for allowing me to conduct this research on their site.

I also want to express my gratitude to the Wits School of Geoscience, especially the Head of School (Prof. Gillian Drennan), staff and students from the Geophysics Department who helped to make my time at the university both productive and pleasurable. I have learned a lot from so many of you, and from the bottom of my heart, I just want to thank you all. To the people who dropped everything to help me acquire my data, I just want to say thank you (Dr Sihoyiya, Dr Rapestoa, Jureya, Dr Mutshafa, Sikelela). I will forever be grateful to you all.

I also want to thank my mom, uma-Mlotshwa, for the love and support she gave me throughout my studies. Thank you for your prayers, ma. I truly admire the sacrifices you have made for us as your children. Akwandele bani, ukuthandwa umzali the way osithanda ngakhona. To my brothers, Mlondi and Mzwa, ngiyabonga bo-Mgagule.

To my friends, Mpume, Sphume, Sne, Mini, Themba, Salizwa, Thembi, Skhona, Ntokozo, Nqoh, Mthanti, Ayanda, Ole, Phumza and Thando thank you all for always checking up on me, and giving me words of encouragement, especially when things got tough. Thank you to my extended family, my cousin Thulile, ngibonga uthando lwakho and your support magazi. To my running family, the Dream Chasers, ngiyabonga.

Lastly, to ubaba wami ongasekho, ngisakhula wawuthanda ukungitshela ukuthi “Awufundeli mina, kodwa uzifundela wena”. This kept me going, knowing that you will be very proud of me once I am done. Noma ungasekho, thank you for always encouraging me, your words still echo in my heart and mind.

TABLE OF CONTENTS

DECLARATION ..... **ii**
ABSTRACT ..... **iii**
ACKNOWLEDGMENTS ..... **iv**
LIST OF FIGURES ..... **viii**
LIST OF TABLES ..... **xiv**
LIST OF SOFTWARE PACKAGES USED ..... **xv**
1 INTRODUCTION **16**
1.1 Background 16
1.2 Thesis Structure 19
1.3 Aims of the Research. 20
1.4 Objectives of the Research 20
1.5 Research Questions 20
2 GEOLOGY **21**
2.1 Regional Geology 21
2.2 Local Geology 24
2.2.1 Lyttelton Formation 26
2.2.2 Eccles Formation 26
3 THE NATURE AND DISTRIBUTION OF SINKHOLES **28**
3.1 Sinkhole Formation in the Study Area 28
3.2 Mechanism of Sinkhole and Subsidence Formation 30
3.2.1 Dewatering Scenario Sinkhole 34
3.2.2 Ingress Scenario Sinkhole 35
3.3 Types of Sinkholes 36
3.3.1 Natural Sinkholes 36
3.3.2 Anthropogenic Sinkholes 37
3.4 Impact of Groundwater on Sinkholes 37
4 THEORETICAL BACKGROUND **41**
4.1 The Application of Geophysical Methods in Sinkhole Detection 41
4.1.1 Geophysical Methods 41
4.1.2 Geophysical Investigations in Transvaal Dolomite Formations 42

4.2 Electrical Resistivity Tomography (ERT) 42
4.3 Ground Penetrating Radar (GPR) 47
4.4 Refraction and Reflection Seismic Techniques 49
4.4.1 Seismic Wavefield Propagation 51
4.4.2 Body Waves 52
4.4.3 Surface Waves 53
4.5 Multichannel Analysis of Surface Waves (MASW) 54
5 FORWARD MODELLING 56
5.1 The Importance of Physical Properties in Geophysics 56
5.2 Electrical Resistivity Tomography Forward Modelling 58
5.3 Seismic Forward Modelling 62
6 STUDY AREA AND METHODOLOGY 67
6.1 Location of Study Area 67
6.2 Data Acquisition and Processing 68
6.3 Electrical Resistivity Tomography (ERT) 72
6.3.1 Acquisition 72
6.3.2 Data Processing 74
6.4 Ground-Penetrating Radar (GPR) 78
6.4.1 Data Acquisition 78
6.4.2 Ground Penetrating Radar Processing 80
6.5 Seismic Survey 93
6.6 Multi-Channel Analysis of Surface Waves (MASW) Survey 101
6.6.1 Data Acquisition 101
6.6.2 Processing of Multichannel Analysis of Surface Waves Data 102
7 RESULTS AND INTERPRETATION 106
7.1 Electrical Resistivity Tomography 106
7.2 Ground Penetrating Radar 110
7.3 Refraction and Reflection Seismics 118
7.4 Multichannel Analysis of Surface Waves 120
8 DISCUSSION 124
9 CONCLUSIONS 137
References 139

Appendix A **155**
Appendix B **159**
Appendix C **176**
Appendix D **179**
Appendix E **183**

LIST OF FIGURES

Figure 1.1: Map showing the distribution of sinkholes in South Africa, covering the Northwest, Northern Cape, Mpumalanga, Limpopo, and Gauteng province (Department of Public Works, 2003). 17
Figure 1.2: Image of a sinkhole that had formed on the R21 highway, in South Africa (Mabele, 2022). 19
Figure 2.1: Sketch map showing the distribution of the three preserved basins of the Transvaal Supergroup: the Transvaal Basin, the Griqualand West Basin, and the Kanye Basin in Botswana (Eriksson *et al*., 2012; Izon, 2017). 22
Figure 2.2: Lithostratigraphic units of the Chuniespoort Group (Nex, 2005). 23
Figure 2.3: Lithostratigraphy of the study area shows the Malmani dolomite with subordinate chert layers and rich Malmaini dolomite. Syenite dyke and quartzite rocks and mudrocks are also shown on the map (image provided by CGS, 2024) 25
Figure 2.4: Local lithostratigraphy of the study area, showing the chert-rich dolomite of the Eccles formation and the chert-poor dolomite of the Lyttelton formation (image provided by CGS, 2024). 27
Figure 3.1: Distribution of sinkhole sizes amongst three Gauteng municipalities (Constantinou and van Rooy, 2018). 29
Figure 3.2: The weathering process of dolomite (van Niekerk and van der WALT, 2005). 31
Figure 3.3: Illustration of a typical dolomite profile as it has historically been observed in South Africa, with Karoo material typically made up of shale and mudrock as well as the underlying dolomite of the Malmani Subgroup (Trollip et al., 2008). 32
Figure 3.4: Drawings depicting the mechanism of sinkhole formation in ingress and dewatering scenarios (Oosthuizen and Richardson, 2011). 36
Figure 3.5: Occurrence of sinkholes and subsidence on the Far West Rand, showing the different compartments (Oosthuizen and Richardson, 2011). 39
Figure 4.1: Electrode arrangement for a dipole-dipole array, consisting of two sets of electrodes, the current (source) and potential (receiver) electrodes (Montgomery et al., 2020). 43
Figure 4.2: The resistivity of rocks, soils, and minerals. The image depicts, in broad terms, the relative resistivities of significant rock groups (Loke, 2014). 44
Figure 4.3: A schematic diagram of the Wenner array electrode configuration. 'A' and 'B' = current electrodes (I = current), 'M' and 'N' = potential electrodes (V = potential difference) and 'a' = spacing between electrodes (Tesfaldet and Puttiwongrak, 2019). 45
Figure 4.4: A schematic diagram of the Schlumberger array electrode configuration with two outer electrodes 'A' and 'B' = current electrodes (I = current), 'M' and 'N' = potential electrodes (V = potential difference), 'a' and 'b' = spacing between electrodes (Tesfaldet and Puttiwongrak, 2019). 46

Figure 4.5: A schematic diagram of the dipol-dipole array electrode configuration with two outer electrodes 'A' and 'B' = current electrodes (I = current), 'M' and 'N' = potential electrodes (V = potential difference), 'a' = spacing between electrodes (Tesfaldet and Puttiwongrak, 2019). 46
Figure 4.6: Principles of ground penetrating radar (GPR). Reflected waves from boundaries a recorded by the receiver and displayed as a time-varying signal (Ukaegbu et al., 2019). 48
Figure 4.7: Example of seismic waves generated from a hammer striking a metal plate travelling through the subsurface (Liberty and St. Clair, 2018). 50
Figure 4.8: Different types of seismic waves (Ahmad, 2014). 51
Figure 4.9: Deformation of the propagating medium associated with the passage of a P-wave (uniaxial strain) and an S-wave (shear strain) (Dentith and Mudge, 2014). 52
Figure 4.10: The particle motion for surface waves: (a) Rayleigh waves and (b) Love waves (Slideplayer, 2015). 54
Figure 4.11: Schematic diagram of MASW linear array of geophones data acquisition (masw.com, 2023). 54
Figure 4.12: A general procedure of the investigation of the MASW method (Mi et al., 2017). 55
Figure 5.1: Resistivity ranges of rocks found in South Africa (Van Schoor and Mare, 2015). 59
Figure 5.2: Three electrical resistivity forward models created for the R21 sinkhole, filled with water (a), collapse material mixed with air (b), and collapse material (c). 62
Figure 5.3: Image showing the geological models used for 2D acoustic numerical, viewed in Tesseral Pro software. 65
Figure 5.4: Image showing an example of the synthetic shot gathers from 2D acoustic modeling. 65
Figure 5.5: Stacked seismic section showing strong reflections and diffractions. 66
Figure 6.1: A top view image showing the location of the study area. It shows the location of the R21 sinkhole with some of the brick companies and quarries close to the study area, Google Earth. 67
Figure 6.2: (a) Study area showing older sinkholes, shown in red, next to the site; (b) Zoomed-in location of the R21 highway and the sinkhole, shown by the green dashed lines, Google Earth. 68
Figure 6.3: The progression of the sinkholes along the R21 highway. The older sinkholes, started appearing on surface in 2016 and continued to appear until the one on the R21 highway, Google Earth. 70
Figure 6.4: Image showing one of the older sinkholes with dashed white line, in relation to the R21 sinkhole shown in black dashed lines. 71
Figure 6.5: Relative locations of the ERT surveyed profiles, shown in pink lines. Red lines represent the older sinkholes found in the site, while green represents the R21 sinkhole. 73
Figure 6.6: The profile of line 1 with metal electrodes of a 2.5 m spacing on the R21 tarred surface. 73

Figure 6.7: Sequence of measurements to create a pseudosection in a multi-electrode survey (Geotomo Software, 2003). 74
Figure 6.8: Image of the first step of the RES2DINV processing step, where the data is read and analysed. 75
Figure 6.9: Processing steps to remove all the bad points for the line 5 acquired data. 75
Figure 6.10: An example of line 5 field data set, with all the measured bad data points, shown in red. The apparent resistivity data in profile form. 76
Figure 6.11: Final image of the processed and edited data. 77
Figure 6.12: Processing steps used when applying the damping factor. 78
Figure 6.13: The apparent resistivity of the processed data of line 5 in pseudo-section form. 78
Figure 6.14: Ground penetrating radar profiles, shown in different coloured group as how they were acquired in the field. Group R21SINK001 is shown in blue, group R21SINK002 is shown in orange, and group R21SINK003 is shown in yellow. The green circle represents the R21 sinkhole. 79
Figure 6.15: GSSI Utility scan PRO SIR 4000 GPR system used in the R21 sinkhole survey. 80
Figure 6.16: Raw data of line R21SINK001_001, 2701 trace line from group 1. 82
Figure 6.17: (a) The original unprocessed data of profile R21SINK001_001. Highlighted in blue is the static and irrelevant data that were removed once the static correction was applied. (b) GPR section after the application of the static correction. 83
Figure 6.18: GPR section with static correction (a), highlighted in blue is data that had to be adjusted vertically to align zero depth on the vertical axis and (b) shows the result after applying the move start time filter. 84
Figure 6.19: GPR section with start time filter on (a), and (b) shows the section after the removal of background noise. 84
Figure 6.20: GPR section from the previous processing step showing background removal filter (a) and (b) shows the section after running average filter step is applied. 85
Figure 6.21: Image showing the running average filter, from the previous step (a) and (b) shows the section after the subtract-mean (dewow) filter step is applied. 86
Figure 6.22: GPR section after the application of the subtract-mean (dewow) filter from the previous step (a) and (b) shows the section after the application of the gain function filter. 86
Figure 6.23: GPR section with gain function filter applied, from the previous step (a), and (b) shows the section after the application of the bandpass butterworth filter. 87
Figure 6.24: Final processed image of profile (R21SINK001_001) from group one. 88
Figure 6.25: Final processed image of profile (R21SINK001_003) from group one. 89
Figure 6.26: Final processed image of profile (R21SINK002_001) from group two. 90
Figure 6.27: Final processed image of profile (R21SINK003_0015) from group three. 91
Figure 6.28: Final processed image of profile (R21SINK003_001) from group three. .. 92
Figure 6.29: Relative locations of the seismic profiles, line 1 to line 3. 93

Figure 6.30: Geode seismic data acquisition system. 94
Figure 6.31: (a) Land streamer used for the survey, (b) seismic station, and (c) accelerated weight-drop mounted at the back for the vehicle. 94
Figure 6.32: Relationship between the data acquisition, processing, and interpreting (Zhou, 2014). 95
Figure 6.33: Example of raw shot gather (a) and processed shot gather (statics correction) (b), with the raw shot gather frequency spectrum graph (c) and the processed shot gather frequency spectrum graph (d). 97
Figure 6.34: Example of static corrected shot gather (a) and frequency filtered shot gather (b), with the static corrected shot gather frequency spectrum graph (c) and the frequency filtered shot gather frequency spectrum graph (d). 98
Figure 6.35: Example of frequency filtered shot gather (a) and F-K filtered shot gather (b), with the frequency filtered shot gather frequency spectrum graph (c) and the F-K filtered shot gather frequency spectrum graph (d). The area highlighted in blue represents the surface waves. 99
Figure 6.36: Example of F-K filtered shot gather (a) and first break muted shot gather (b), with the F-K filtered shot gather frequency spectrum graph (c) and the first break muted shot gather frequency spectrum graph (d). 100
Figure 6.37: Relative location of the MASW profile, line 1, with the R21 sinkhole shown in dashed green lines. 101
Figure 6.38: Active Multichannel Analysis of Surface Waves data acquisition. (a) Land streamer used for the survey. (b) 6.3 kg sledgehammer used as a source. (c) Accelerated weight-drop mounted at the back for the bakkie. (d) Seismic station. 102
Figure 6.39: Multichannel Analysis of Surface Waves processing workflow. (a) Collected raw shot gathers of the study area. (b) Phase velocity model and (c) 1D shear wave velocity profile vs 1D depth curve. 103
Figure 6.40: (a) Raw shot gather collected with the source offset of 5 m and receiver spacing of 5 m. (b) Corresponding unmuted dispersion image (also called Overtone Image) with dominant higher-mode contamination, phase velocity (y-axis) versus frequency (x-axis). 104
Figure 6.41: (a) The multichannel shot gather collected with the source offset of 5 m and receiver spacing of 5 m with applied muting. (b) Corresponding muted dispersion image of the shot gather. 104
Figure 6.42: 1D shear wave velocity profile from line 1, R21 profile. 105
Figure 7.1: The interpretation of ERT profile 1, oriented south to north along R21 highway with dipole-dipole arrays configuration. The moist clayey soil, low resistivity, and saturated layer is just under the topsoil layer is shown by the range of blue colours. 107
Figure 7.2: The interpretation of ERT profile 2, oriented south to north along R21 highway with dipole-dipole arrays configuration. The dashed purple lines represent the R21 sinkhole. 107

Figure 7.3: The interpretation of ERT profile 4, oriented south to north along R21 highway with dipole-dipole arrays configuration. The dashed purple lines represent the R21 sinkhole, while the black dashed circle lines represent a possible filled cavity. 108
Figure 7.4: The interpretation of ERT profile 5, oriented south to north along R21 highway with dipole-dipole arrays configuration. The dashed green lines represent a possible sinkhole that has not manifested yet on surface, while the red dashed lines represent a weathered rock. 109
Figure 7.5: Lines 1 to 3 in 3-D, showing the areas with the resistive sinkholes. 109
Figure 7.6: Lines 1 to 3 in 3-D, showing the two sinkholes with high resistive zones. 110
Figure 7.7: Metal pieces found on the R21 highway, which could have caused noise on the data. 111
Figure 7.8: (a) Google Earth image with the location of line R21SINK001_001 from group one, (b) Interpreted GPR data are showing diffractions originating from top of the possible sinkholes. The arrows point to the hyperbolic event that formed because of a subsurface feature, while the brighter reflections (highlighted in yellow) originate from the near-surface stratigraphy. 112
Figure 7.9: (a) Google Earth image showing the location of line R21SINK001_003 from group one, (b) GPR image of R21SINK001_003, with diffractions shown by the red lines. The arrows point to the hyperbolic event that formed because of a subsurface feature, while the brighter reflections are highlighted in yellow because they most likely signal a shift in yellow because they most likely signal a shift in stratigraphy. 113
Figure 7.10: (a) Google Earth image with the location of line R21SINK002_001 from group two, (b) Diffractions shown in by dashed red lines in profile R21SINK002_001. The arrow in blue shows the noise from the metal piece that was observed at the site. 114
Figure 7.11: (a) Google Earth image with the location of line R21SINK003_0015 from group three, (b) Profile R21SINK003_0015 showing diffraction on the road which indicates the extent of the sinkhole on the highway. The end of diffracted events is shown by a red line. 115
Figure 7.12: Interpreted GPR data of R21SINK003_003 are represented by the red dashed lines. 116
Figure 7.13: Schematic model depicting the R21 sinkhole and how it was detected by the GPR. (a)This model provides a basic visual representation of how GPR works to detect the presence of a sinkhole beneath the ground surface. It highlights the process of sending and receiving radar waves (in black arrows) and identifying anomalies that indicate the presence of the sinkhole (shown red dashed lines), (b) the diffractions indicate the possible presence of a sinkhole (Parwatiningtyas, 2021). 117
Figure 7.14: Line 3 processed section with R21 sinkhole represented in pink and possible sinkhole shown in red dotted lines. 119
Figure 7.15: Interpreted south-north P-wave seismic tomogram for line 3, with possible sinkhole represented in pink and R21 sinkhole shown in red dotted line. 119

Figure 7.16: Interpreted south-north P-wave seismic tomogram for line 2, a possible sinkhole is sown by a black dashed line. 120
Figure 7.17: Inversion of the data to obtain 2D shear wave velocity seismic section of line 1. The red dotted line shows the weak zone associated with cavities and highly weathered rocks. The black dotted line represents an interface between the top zone and the zones below. The zone from 22 m depth down represents the bedrock or a partially weathered zone. 121
Figure 7.18: MASW Shear wave velocity profile obtained from the dispersion curve from 1D profile 27, with superposed geological interpretations. Velocity is in m/s. 123
Figure 8.1: Combined images of line 1 from each of the four (4) methods: (a) ERT with the R21 sinkhole on the northern section; (b) GPR with the R21 sinkhole, also on the northern section shown by the diffractions; (c) Seismic section, also with the R21 sinkhole on the northern section and (d) with the R21 sinkhole on the northern section. 132
Figure 8.2: A model showing the mechanism for the formation of the R21 sinkhole. The fractures and joins are shown in white on the top layer. The ingress of water is shown by the blue and black lines, also on the top layer. There are two sinkholes with conductive infills, which are shown in orange (possible sinkholes) and red (R21 sinkhole). 133
Figure 8.3: Stormwater drainage location in relation to the older sinkhole and the newer R21 sinkhole. 134
Figure 8.4: Google Earth image showing the location of the stormwater drainage in relation to the R21 sinkhole and the possible sinkhole on the southern ERT section of the profile. 135
Figure 8.5: Model used to depict the formation of the R21 sinkhole. (modified from www.flooddefenders.org). 135
Figure 8.6: (a) High voltage powerlines next to the site; (b) Trucks and cars, which all act as sources of noise along the highway.(c) Shot gathers with background noise. . 136

LIST OF TABLES

Table 3.1: Reported instability events in Gauteng province (Richardson, 2013)........... 30
Table 3.2: Sinkhole events reported in Tshwane vs. Annual rainfall (Richardson, 2013). 40
Table 5.1: Geophysical methods with appropriate physical properties (Kearey et al., 2002; Van Schoor and Fourie, 2015)... 57
Table 5.2: Assumed survey parameters for forward models (a), (b), and (c)................ 61
Table 5.3: The P-wave velocity values and density values used on the R21 geological model.. 63
Table 5.4: Parameters applied to the seismic acquisition simulation in Tesseral Pro software.. 64
Table 6.1: Resistivity acquisition table, with all the lines from the study area.............. 72
Table 6.2: Ground Penetrating Radar acquisition parameters and processing steps... 81
Table 6.3: Processing steps applied in the R21 sinkhole, profile (R21SINK001_001) from group one. 83
Table 6.4: Processing steps applied in the R21 sinkhole, profile (R21SINK001_003) from group one GPR data... 88
Table 6.5: Processing steps applied in the R21 sinkhole, profile (R21SINK002_001) from group two GPR data. 90
Table 6.6: Processing steps applied in the R21 sinkhole, profile (R21SINK003_0015) from group three GPR data. 91
Table 6.7: Processing flow applied in the R21 sinkhole, profile (R21SINK003_001) from group three. 92
Table 6.8: Seismic acquisition parameters for lines 1, 2, and 3................................... 93
Table 6.9: Seismic data processing workflow applied in line 3. 95
Table 6.10: Summary of Multichannel Analysis of Surface Waves field parameters in this study.. 101
Table 7.1: The common resistivity values of known subsurface materials (Nwokebuihe, 2014). 106
Table 7.2: The values of some shear wave velocities (Vs) for common Earth's materials (NEHRP, 1997).. 121
Table 7.3: Estimated shear wave velocity values of soil/rock at R21 highway............ 122

LIST OF SOFTWARE PACKAGES USED

Name of Software	
GLOBE Claritas	Seismic data processing software.
ReflexW	A near-surface geophysical software program used for processing and interpreting wave data. It is specifically designed for analyzing seismic and Ground Penetrating Radar (GPR) data.
Res2dInv	2D geophysical inversion software specifically designed for processing resistivity and induced polarization (IP) data.
RES2DMOD	Forward modelling program for generating the pseudosection from the apparent resistivity values.
SurfSeis	Software by Kansas Geological Survey (KGS) for processing Multichannel Analysis of Surface Waves (MASW) data.
Tesseral Pro program	Allows users to create 2D and 3D geological models of the subsurface. The software provides tools for visualizing the modeled results, inversion results, and comparing them with observed data. This helps in interpreting and analyzing the subsurface structures and anomalies.

1 INTRODUCTION

1.1 Background

Understanding near-surface geological structures such as sinkholes, faults, joints, fractures, and dykes is critical when identifying several geological hazards and developing mitigation strategies (Marghany and Hashim, 2010). These structures can be mapped and detected using geophysical methods (Marghany and Hashim, 2010). The primary aim of this research is to determine if geophysical methods can be used to characterize sinkholes, i.e., define their lateral and vertical extent, shapes, and sizes. The secondary aim is to determine if the geophysical results, in integration with geology, can be used to establish the geological mechanisms through which the sinkholes are formed in the dolomitic environments. Over the past five decades, thousands of sinkholes and subsidence events have occurred. As a result, dolomite land has become one of the critical areas that require geophysical investigation due to the prevalence of subsidence events and sinkholes in South Africa. Dolomite land is described as underlain by dolomite or limestone residuum or shallow bedrock (SANS1936, 2012), of not more than (1) 60 m (if de-watering has not occurred and the local authority oversees monitoring and controlling the groundwater levels in the areas under consideration) or (2) 100 m (if de-watering has occurred or the local authority is not in charge of monitoring or controlling the groundwater levels in the areas under consideration).

The presence of karst-related subsidence and sinkholes in the Gauteng province of South Africa has been the result of Chuniespoort Group dolomite bedrock, which underlies most of these areas (Heath and Oosthuizen, 2008; Constantinou and van Rooy, 2019). According to Oosthuizen and Richardson (2011), among all the provinces with dolomite bedrock in South Africa (Gauteng, Northwest, Mpumalanga, and Limpopo) (Figure 1.1), Gauteng is reported to experience more sinkhole formations due to hydrogeological factors such as groundwater flow and aquifer characteristics. Human influence includes activities such as over pumping of groundwater, aquifer dewatering, water leakages, and urban development. The heavy urbanization in Gauteng, including the construction of buildings, roads, and other infrastructure, may impose additional stress on the ground. In comparison to other provinces, the extent of these formations and the intensity of human activities such as groundwater extraction and urban development are generally less than in Gauteng.

Globally, karst topography covers at least 15.2% of the Earth's surface. Within the Gauteng province, it represents at least a quarter of the total surface area, with an estimated 4 to 5 million people working or residing on dolomite land (Buttrick *et al*., 2001; Goldscheider *et al*., 2020). The number of people living and working within dolomite land could now be easily higher than what Buttrick *et al.* (2001) estimated back in 2001, as the population of Gauteng grew from 8. 8 million in 2001 to 16.1 million in 2022 (Stats SA, 2022). Buttrick *et al.* (2011) estimated that at least 4 - 5 million South Africans reside on such land.

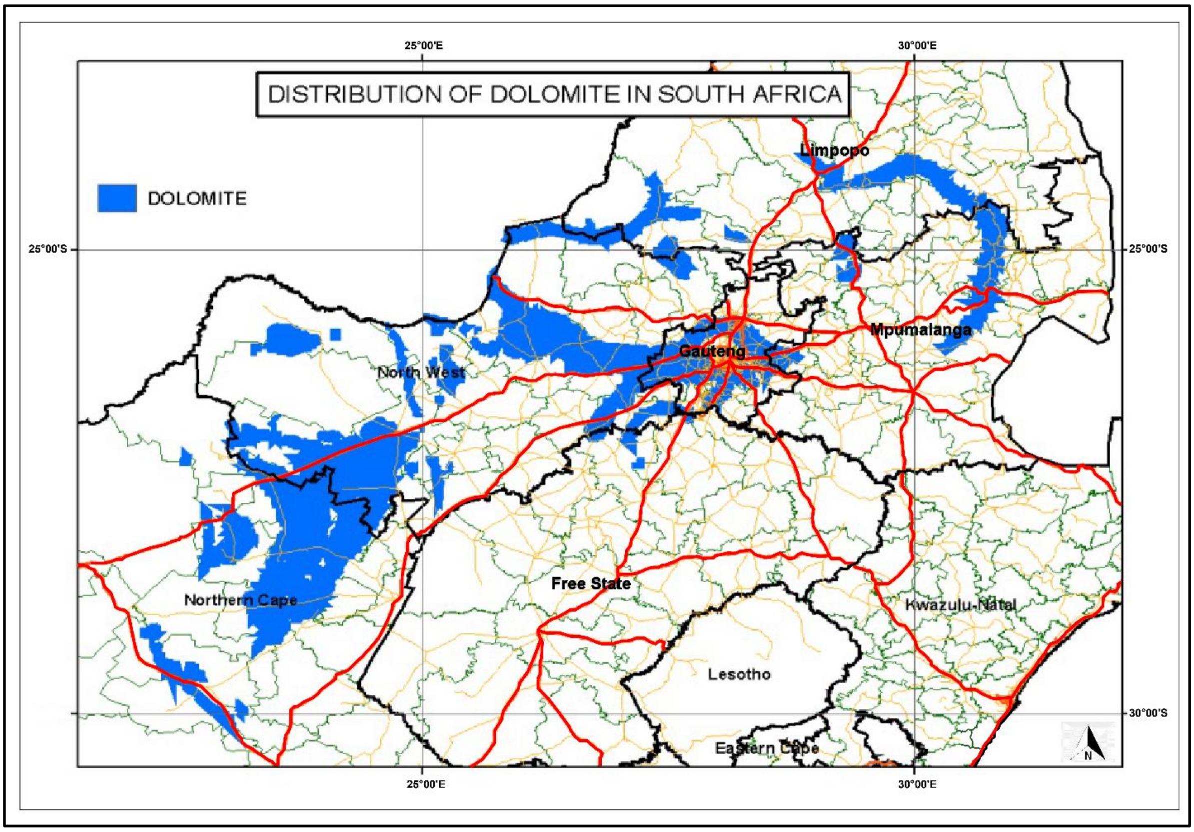

Figure 1.1: Map showing the distribution of sinkholes in South Africa, covering the Northwest, Northern Cape, Mpumalanga, Limpopo, and Gauteng province (Department of Public Works, 2003).

Dolines and sinkholes are frequently used interchangeably in international literature (SANS1936, 2012). The formation of natural sinkholes can be attributed to many factors such as cave roof failure, removal of soluble bedrock (like dolomite) by percolating water, and changes in the water table, primarily lowering. (Oosthuizen and

Richardson, 2011). Several authors have suggested that the underlying geological formations may potentially have an impact on the development of sinkholes and subsidence that are linked to human activity (Closson, 2005; Florea, 2005; Billi *et al*., 2007; Doctor *et al*., 2008). Geological structures (dykes, fractures, faults, and karst features) can create pathways for water infiltration and dissolution of soluble rocks, which can be accelerated or amplified by human activities.

About 96 sinkholes occurred in the greater Ekurhuleni municipality (Richardson, 2013), making it a particularly suitable location for this research. The study area is in Olifantsfontein, also known as Clayville, surrounded by numerous cement and brick quarries such as Clayville Brick and Afrisam. Many of these companies influence the groundwater by dewatering or causing water ingress. The study area is geologically partitioned into the Transvaal Supergroup's Lyttelton and Eccles formations.

The Transvaal Supergroup includes the Chuniespoort Group, which was deposited during the Paleoproterozoic era (approximately 2550 to 2400 million years ago). Within the Chuniespoort Group lies the Malmani Subgroup, which is divided into several formations, including Lyttelton and Eccles formations.

Sinkholes in Gauteng, South Africa, have had significant impacts on the lives of people in the province. In 2022 alone, there were significant road closures because of sinkhole formation, dramatically impacting commuters. Some examples include the R21 highway (Figure 1.2), which is the focus of this study, where two northbound lanes were closed when a sinkhole of about ~15 to ~18 m in diameter formed in February 2022.

Figure 1.2: Image of a sinkhole that had formed on the R21 highway, in South Africa (Mabele, 2022).

It is worth noting that the R21 sinkhole, where the study is conducted, is on one of the busiest national routes and is very important to commuters in South Africa and internationally. O.R. Tambo International Airport serves as a hub for both domestic and international flights. The R21 is a crucial link for passengers and cargo traveling to and from the airport, ensuring efficient connectivity for air travelers.

1.2 Thesis Structure

The dissertation is made up of nine chapters. Chapter 1 summarises the background, introduction and objectives of the study. Chapter 2 provides an overview of the geological setting of the study area. Chapter 3 discusses the nature and distribution of sinkholes. Chapter 4 provides a background of the work that has been done on the four (4) geophysical methods used in the study. Chapter 5 deals with forward modeling and numerical simulations for the surveys. Chapter 6 provides the study's location, geophysical survey designs, and reviews of each geophysical method used in this study. Chapter 7 interprets and discusses the research results, and Chapter 8 discusses the results. Chapter 9 provides the conclusions**.**

1.3 Aims of the Research

The research aims to use geophysical methods in an integrated approach to detect the sinkhole that formed on the R21 highway, which is referred to in this thesis as the "R21 sinkhole".

1.4 Objectives of the Research

The objectives of the study are as follows:

- To investigate the mechanisms and geological processes that drive the formation of sinkholes.
- To use ground geophysics to map sinkholes and define their geometry.
- To assess the advantages and disadvantages of each geophysical method.

1.5 Research Questions

This research seeks to answer the following key questions:

- Can geophysics be used to map the sinkholes?
- What is the smallest size of the sinkhole that can be resolved by geophysical methods?
- What is the most effective geophysical method to delineate sinkholes?
- How are sinkholes formed?

2 GEOLOGY

This chapter provides the literature on the geology of the study area. It mainly looks at the regional and local geology, investigating the formations from which the sinkhole occurred.

2.1 Regional Geology

In South Africa, a significant portion of the urban settlement and industrial development between Johannesburg, Ekurhuleni metropolitan municipalities and Tshwane is built on dolomites from the Malmani Subgroup dolomites (Chuniespoort Group-Transvaal Supergroup). With well-preserved, large stromatolites remaining, it represents one of Earth's earliest carbonate platform successions and was deposited in the tidal, epeiric (i.e., shallow inland) Malmani-Penge Sea within the Transvaal Basin (Eriksson *et al*., 2006). The Transvaal Supergroup, dating from 2.588 to 2.100 billion years ago (Eriksson *et al*., 2006), is located in the Kaapvaal Craton of Southern Africa and is divided into three basins (the Kanye basin in Botswana and Griqualand West and Transvaal basins of South Africa). These basins are significant for their sedimentary deposits, which provide valuable insights into the geological history, economic mineral resources, and scientific research of the region (Figure 2.1). The summary of the stratigraphy is shown in Figure 2.2.

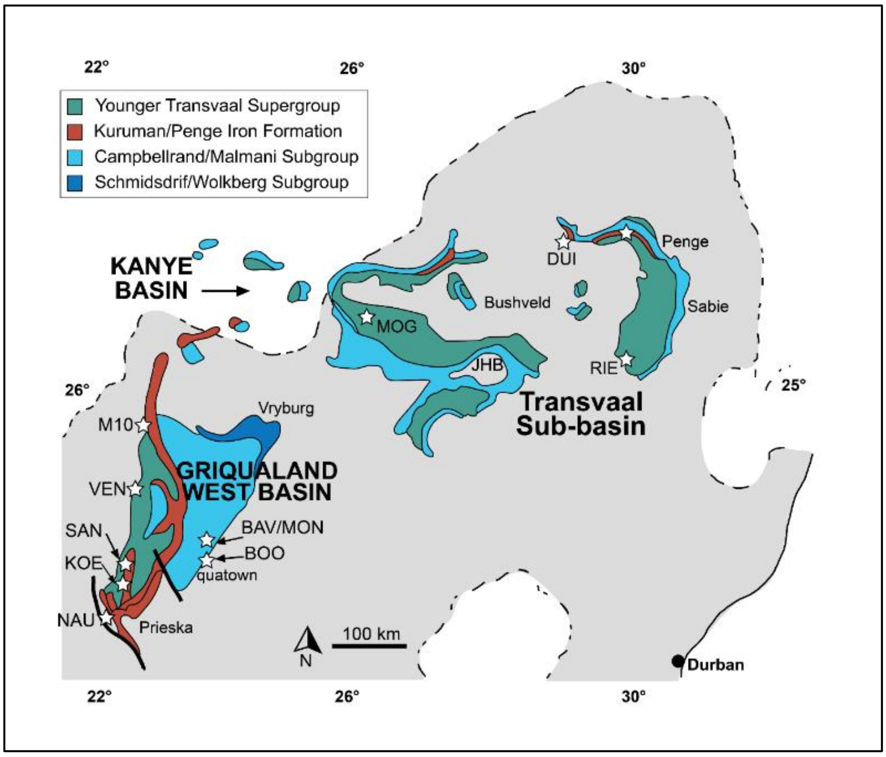

Figure 2.1: Sketch map showing the distribution of the three preserved basins of the Transvaal Supergroup: the Transvaal Basin, the Griqualand West Basin, and the Kanye Basin in Botswana (Eriksson *et al*., 2012; Izon, 2017).

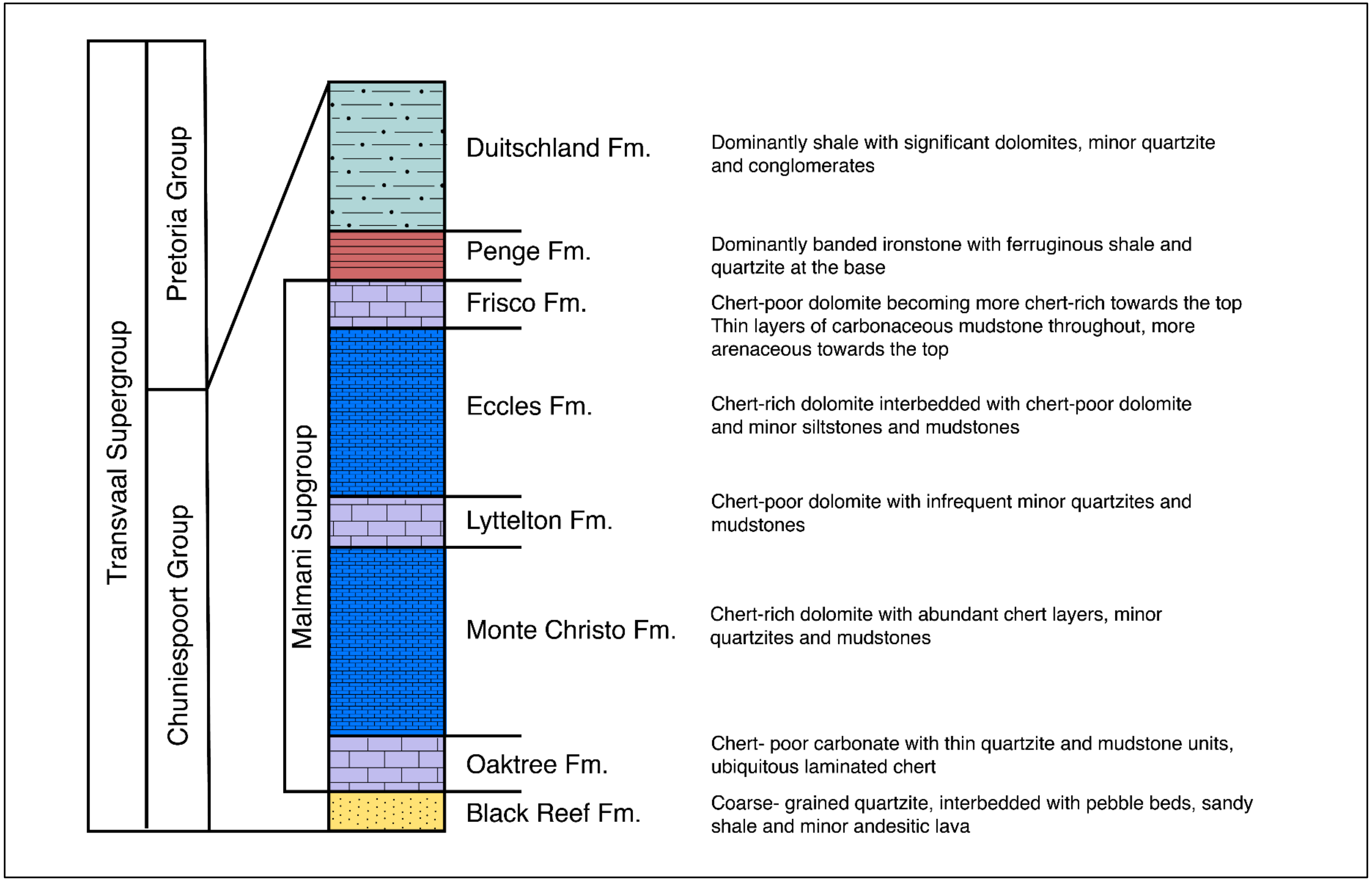

Figure 2.2: Lithostratigraphic units of the Chuniespoort Group (Nex, 2005).

2.2 Local Geology

The study area is located within the Malmani Subgroup of the Chuniespoort Group. The Chuniespoort and Pretoria groups overlie the Black Reef Formation, located at the base of the Transvaal Supergroup. The Chuniespoort Group (~ 2 km thick) consists of lacustrine deposits, dolomites, and Banded Iron Formation (BIF) (Eriksson *et al*., 1995; 2006). It is separated from the Pretoria Group by a regional, angular non-conformity, which represents a period of non-deposition and erosion degradation of approximately 80 million years (Eriksson *et al*., 1995; Eriksson and Reczko, 1995). This unconformity is marked by a chert-shale breccia or insoluble carbonate dissolution residue on the sub-aerial erosion surface (Foster, 1989). The Pretoria Group forms the topmost section of the Transvaal Supergroup. The group is composed primarily of carbonate, interbedded basaltic-andesitic lavas, subordinate meta-conglomerate, meta-diamictite, and intercalated mudstone-sandstone units that have all undergone low-grade metamorphism (Eriksson *et al*., 2006).

About 2300 million years ago, the Malmani dolomites, a component of one of the earliest sedimentary carbonate sequences, were deposited. It is divided into various formations based on the colour and the number of diagenetic chert bands, banded-iron formations, limestone, mudstone, and quartzite interbedded with the carbonates (Button, 1973; Eriksson and Truswell, 1974). Oaktree, Monte Christo, Lyttelton, Eccles, and Frisco are five geological formations that make up the Malmani Subgroup (from oldest to youngest). The study area is located within the Lyttelton and Eccles formations and is shown in Figure 2.3.

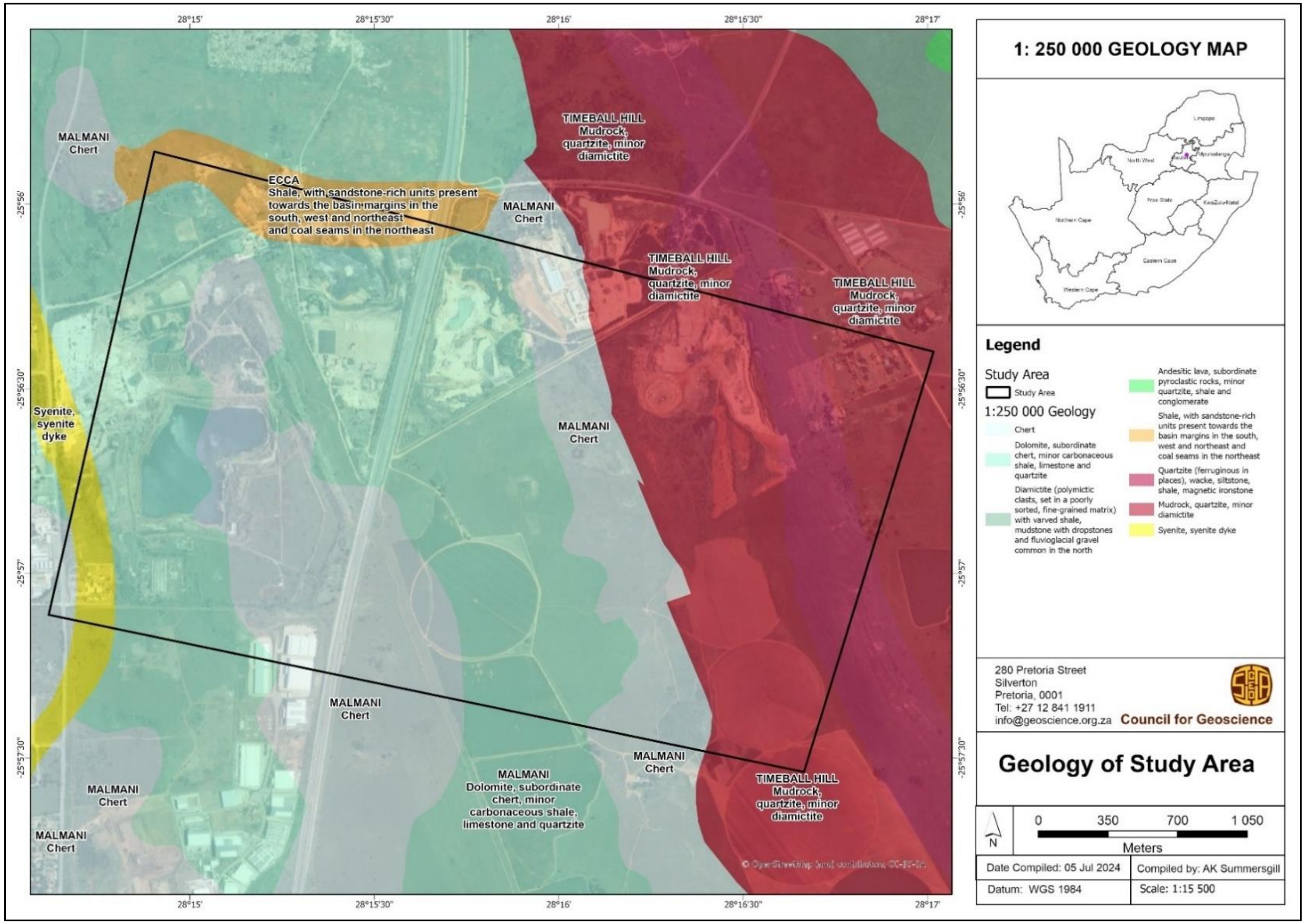

Figure 2.3: Lithostratigraphy of the study area shows the Malmani dolomite with subordinate chert layers and rich Malmaini dolomite. Syenite dyke and quartzite rocks and mudrocks are also shown on the map (image provided by CGS, 2024).

2.2.1 Lyttelton Formation

The Lyttelton Formation overlies the Eccles Formation. The Lyttelton and Eccles Formations highlight significant changes in lithology, particularly in terms of chert concentration and dolomite colour (Obbes, 2000). The increase in chert content and the transition from dark brown to grey dolomite suggest different sedimentary environments and processes during deposition. Stromatolitic dolomites, shales, and quartzites make up the 100–200 m of the Lyttelton Formation (Erikson *et al.*, 2001). It is made up of chert-poor dolomite that becomes more chert-rich towards the bottom of the stratigraphy. The dark-grey dolomites in this formation tend to weather into a dark chocolate brown colour. The high manganese concentration in the dolomite is responsible for the layer's dark chocolate brown weathering. Altered dolomite (WAD) and ferroan soils form from this weathering.

2.2.2 Eccles Formation

The cherty Eccles Formation (Figure 2.4), which ranges in thickness from 100 to 600 m, overlies the Lyttelton Formation (Erikson *et al.,* 2001). It comprises alternating, well-bedded chert layers and light grey dolomites (Obbes, 2000). Button (1973) classifies this formation as the "upper chert and dolomite zone. The distinct "bread and butter" structure of the Eccles Formation serves as a notable stratigraphic marker, aiding in geological interpretations and mapping. This formation shares some similarities with the Monte Christo Formation regarding the presence of chert, which can be found in bands that range in thickness from a few micrometers to 2 m, ripple marks, and oolites (Foster, 1989). These features are diagnostic of an intertidal to supratidal environment comparable to the modern-day example of Shark Bay, Western Australia (Logan *et al*., 1964) and the tidal freshwater marshes of Everglades, Florida (Monty and Hardie, 1976). The formation is further distinguished by the well-known "bread and butter dolomite" formation of the chert. This is made up of chert layers that are 3 cm wide and spaced 15 cm apart. It also contains minor calcite crystals and Stromatolites (Cyanobacterial laminations) (Obbes, 2000). Obbes (1995) identified nine zones within this formation based on specific stromatolites, chert bands, and chert-in shale breccia in the Broederstroom area.

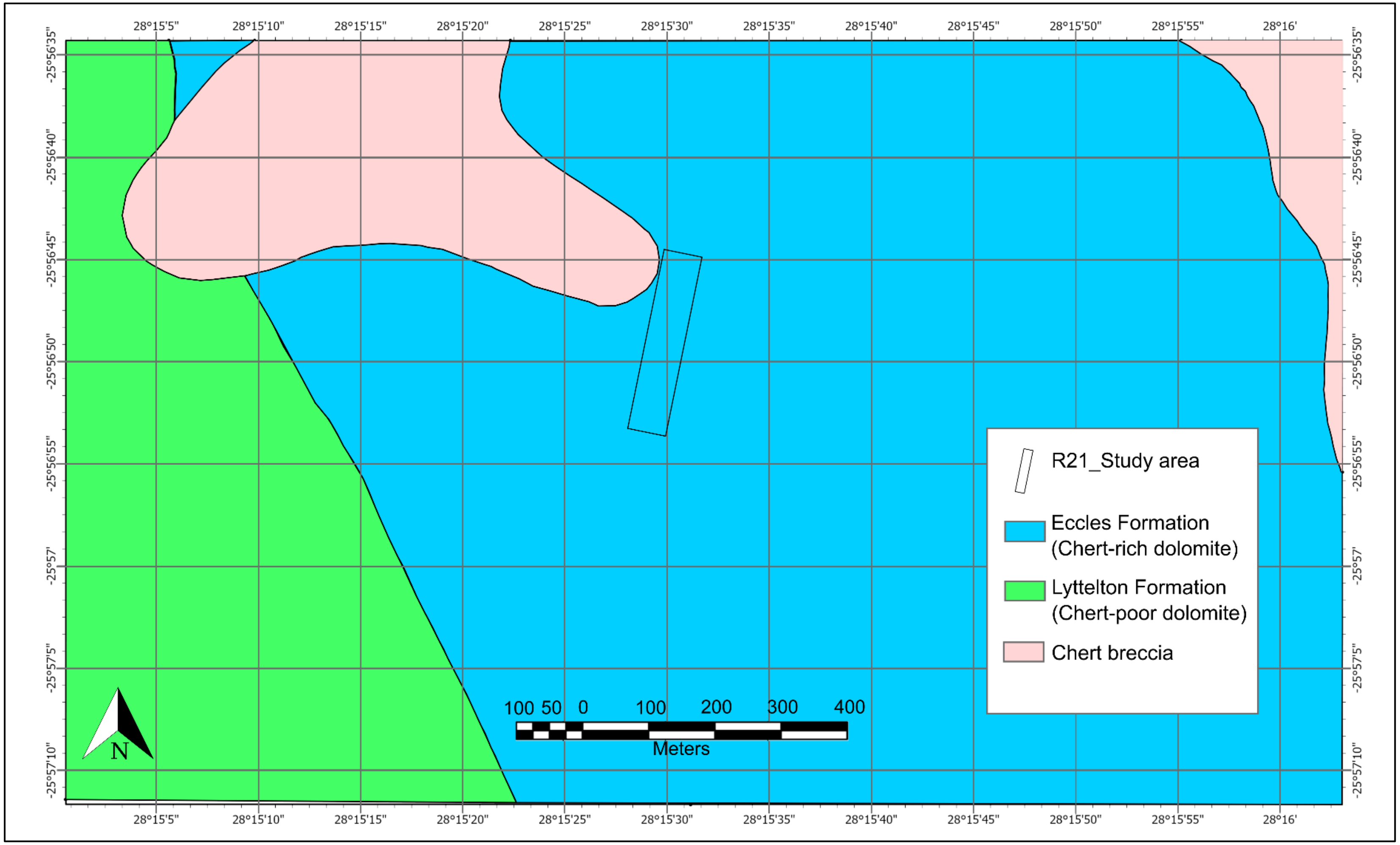

Figure 2.4: Local lithostratigraphy of the study area, showing the chert-rich dolomite of the Eccles formation and the chert-poor dolomite of the Lyttelton formation (image provided by CGS, 2024).

3 THE NATURE AND DISTRIBUTION OF SINKHOLES

3.1 Sinkhole Formation in the Study Area

Amongst all the provinces consisting of dolomite bedrock in South Africa (Gauteng, Northwest, Mpumalanga, and Limpopo), the Gauteng province is known to have the most sinkhole events (Oosthuizen and Richardson, 2011). The formation of sinkholes, especially in densely populated urban areas, has detrimental social and economic consequences. Data on the occurrence of sinkholes and subsidence have been gathered separately by various consultants, businesses, research organizations, and the government for the longest time. While not legally mandated, reporting sinkhole and subsidence events to a central authority in South Africa is crucial for public safety, infrastructure protection, land use planning, environmental impact assessment, insurance considerations, scientific understanding, emergency response, and public awareness. Establishing a system for reporting and sharing such data enables proactive measures to mitigate sinkhole-related risks. This approach ensures the safety and well-being of communities in sinkhole-prone areas and helps in sustainable development practices. The class action lawsuit by the 300 homeowners of Hideaway Hill estate in South Dakota underscores the complexities and risks associated with development in areas with old underground mines and potential geological hazards. It raises important legal and ethical questions about disclosure, transparency, and public safety. The outcome of the lawsuit will likely have implications for future developments in similar areas, emphasizing the need for thorough geotechnical studies and informed decision-making to protect homeowners and ensure responsible development practices (Mining.com, 2021). This was after a sinkhole began to develop on the road in this estate in April 2020.

Since the early 2000s, municipalities such as the Ekurhuleni Metropolitan Municipality have hired several experts to create a dolomite division inside the municipality, produce a database, and manage the dolomite hazards. Council for Geoscience (CGS) has also maintained its sinkhole and subsidence events database.

Though having a central database is an ongoing task that is continuously updated with each event, researchers have been trying to combine all the available data from these separate bodies so that a central database for sinkholes and subsidence can exist. Constantinou and Van Rooy (2018) studied the size and distribution of over 2600 sinkhole and subsidence events (involving the municipalities of the City of Tshwane, West Rand, and Ekurhuleni) across the Gauteng province. According to the study, more than 70% of small- to medium-sized sinkholes (based on their diameter) were reported in the Ekurhuleni municipality (Figure 3.1; Constantinou and Van Rooy, 2018). In the South African engineering geology sector, sinkhole diameter is a crucial consideration since decisions about the use and design of land are made based on the estimated sizes of sinkholes (Figure 3.1).

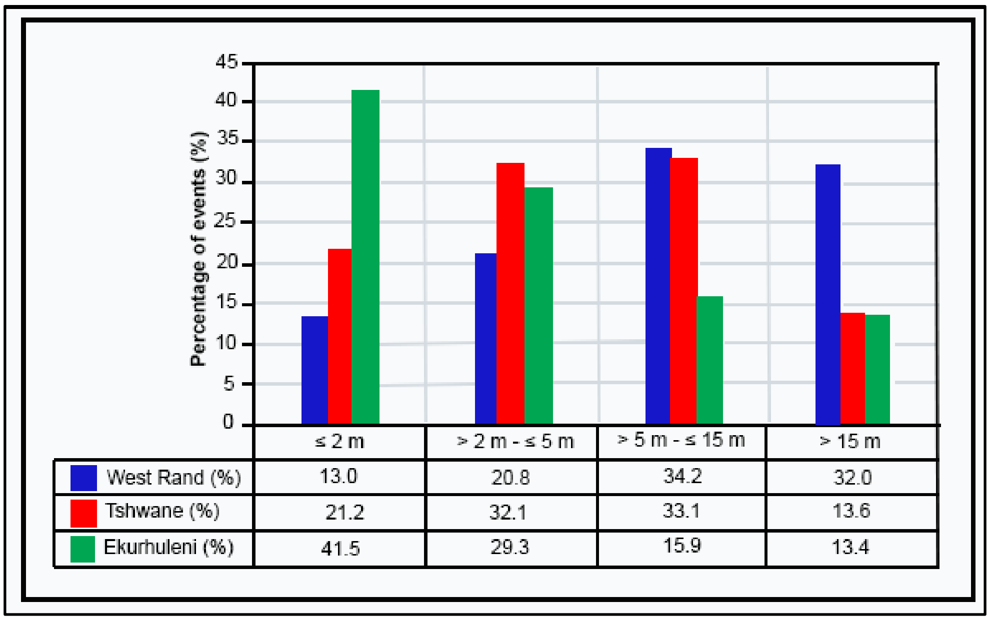

Figure 3.1: Distribution of sinkhole sizes amongst three Gauteng municipalities (Constantinou and van Rooy, 2018).

Richardson (2013) studied 3048 sinkholes, subsidence, cracks, and some undefined events within the Gauteng province. Tshwane recorded the highest number of events, followed by the West Rand, Ekurhuleni, and Johannesburg (Table 3.1; Richardson, 2013).

Table 3.1: Reported instability events in Gauteng province (Richardson, 2013).

	SINKHOLE	SUBSIDENCE	CRACKS	UNDEFINED	TOTAL	(%)
TSHWANE (%)	824 (59.2)	398 (28.6)	46 (3.3)	130 (9.3)	1393	**45.70**
WEST RAND (%)	1195* (81.1)	110 (7.5)	106 (7.2)	62 (4.2)	1473	**48.33**
EKHURHULENI (%)	96 (57.8)	41 (24.7)	7 (4.2)	22 (13.3)	166	**5.45**
JOHANNESBURG (%)	16 (100)	0	0	0	16	**0.52**
TOTAL	**2131**	**544**	**159**	**214**	**3048**	
(%)	**69.9**	**17.9**	**5.2**	**7.0**		**100**

* Events prior to 1983 had to be inferred from historical maps which may have generalised the event as a sinkhole.

Olifantsfontein (known as Clayville) is located on the north-west of the Ekurhuleni Metropolitan Municipality in the Gauteng province. The East Rand has around 50% of its total area covered by dolomite bedrock (Kleinhans and Van Rooy, 2016). Jones and Wegener (2008) recorded 27 incidents in the Ekurhuleni Basfontein area. Jones and Wegener (2005) suggested that instability incidents in the Bapsfontein region had sharply increased due to the lowering of the groundwater table (120 m) caused by pumping for irrigation. Since then, four further occurrences have been documented by the Council for Geoscience (CGS) (Heath and Oosthuizen, 2008). Other incidents had been observed close to Springs (1), Kwa-Themba (1), Daveyton (2), and Olifantsfontein and Thembisa (4) (Heath and Oosthuizen, 2008). These observations underscore the significant and varied impacts of agricultural practices on karst environments, necessitating careful management and monitoring to mitigate adverse effects.

3.2 Mechanism of Sinkhole and Subsidence Formation

Karst landforms are created through two primary processes: a two-stage process involving chemical dissolution followed by mechanical erosion, and a one-stage process where both processes occur simultaneously (Rowberry *et al*., 2018). Dolomite, like other carbonate rocks, is generally considered to have low porosity and permeability. Dolomite typically has a porosity of less than 0.3%, making it relatively impermeable. Despite its low porosity, dolomite often contains a network of discontinuities such as fractures, joints, and faults in the rock (Constantinou and Van Rooy, 2018). These discontinuities serve as preferred pathways for water ingress. As the rainwater flows over the surface of the dolomite bedrock, it encounters these discontinuities. The slightly acidic water can then infiltrate into the rock through the fractures and joints, where it starts the process of carbonation (Brink, 1979).

Carbonation occurs when atmospheric carbon dioxide (CO2) dissolves in rainwater (H2O), forming carbonic acid (H2CO3). This weak carbonic acid is relatively mild but effective over time at dissolving carbonate minerals in rocks like dolomite. Over time, continuous exposure to carbonic acid causes gradual weathering and dissolution of the dolomite rock (Oosthuizen and Richardson, 2011) (see Figure 3.2).

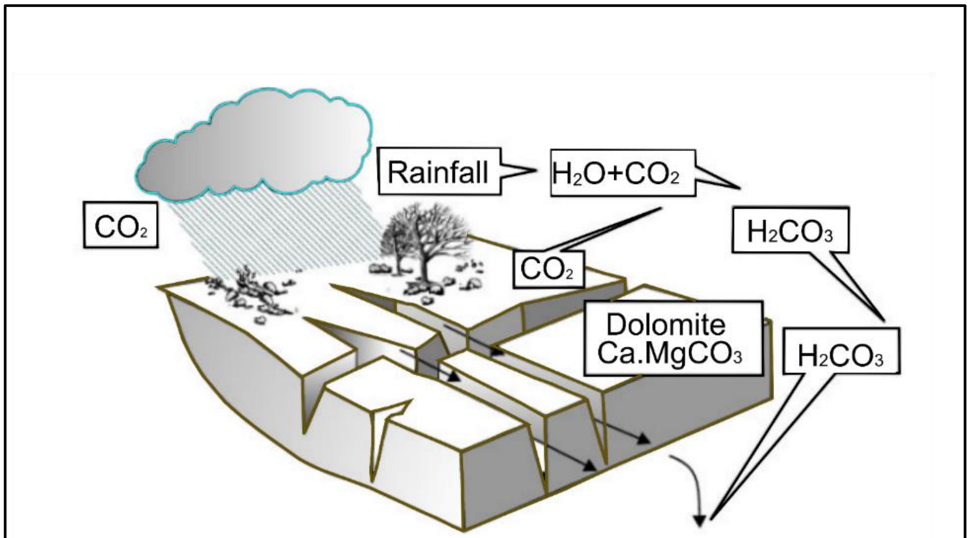

Figure 3.2: The weathering process of dolomite (van Niekerk and van der WALT, 2005).

The vadose zone (above the groundwater table), solution of the bedrock results in the gradual opening of fractures and joints into various shaped grykes or slots between pinnacles of fresh dub-rounded dolomite (Figure 3.3) (Swart, 2019). These openings could extend beneath the groundwater table where the flow of water (CO_2-charged) leads to the slow formation of cavities. Magnetite is dissolved from the rock due to its high solubility, whereas iron and manganese are oxidized to Fe3+ and Mn4+ during weathering (Momubaghan, 2012). In a zone where the rock dissolves preferentially, the cavities will widen. If the widening occurs simultaneously in adjacent cavities, a rock mass may become detached to form a floater, a large dolomite boulder floating in residual products (Figure 3.3) (Jennings *et al*., 1965).

Weathered and altered Dolomite (WAD), also known as residual dolomite, is a material formed through the continued leaching and alteration of dolomite rock. Pedocretes are generally mixtures of parent rock and the cementation of pre-existing soils by the process of leaching. Chert, a practically insoluble mineral that weathers to form chalky material, is found in dolomite strata (Buttrick, 1986). The chert breaks up mechanically over a long period (Swart, 2019).

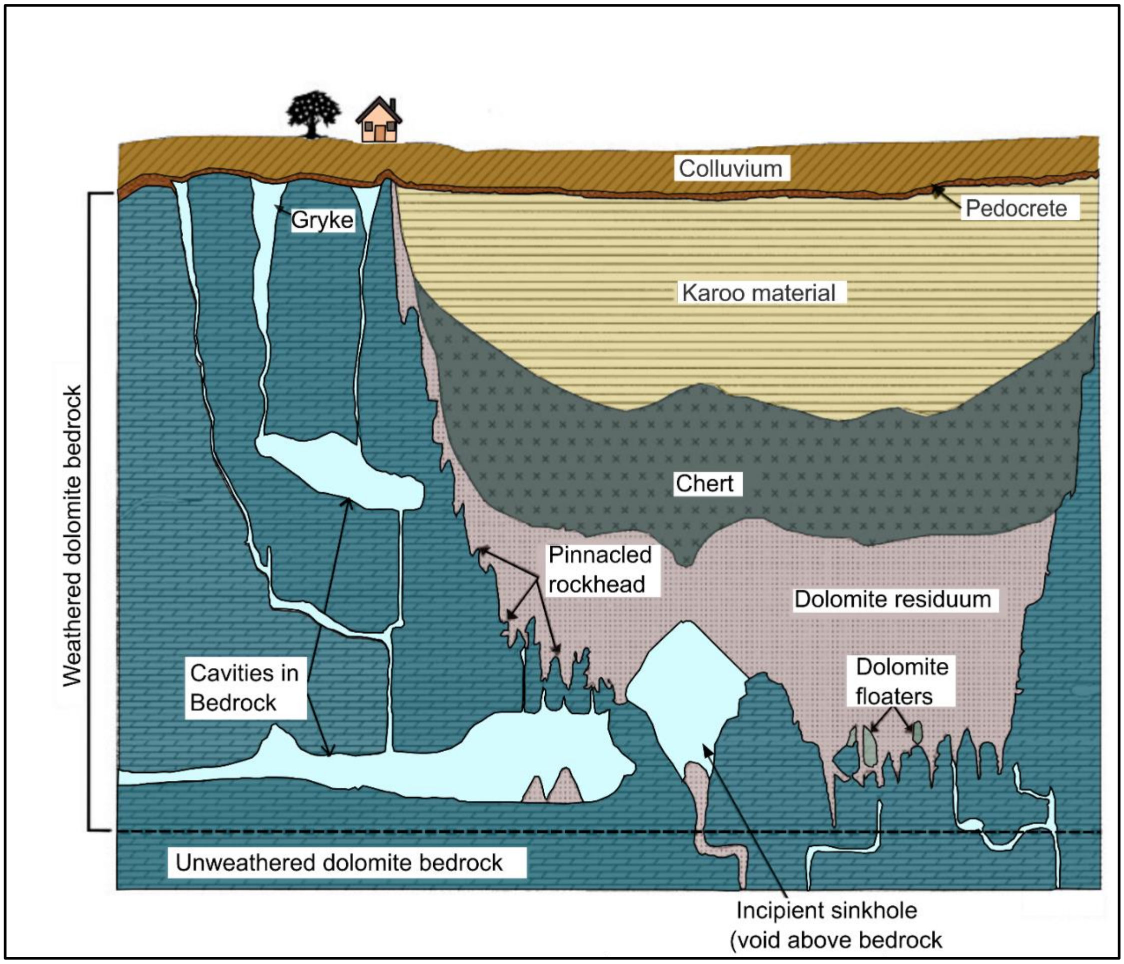

Figure 3.3: Illustration of a typical dolomite profile as it has historically been observed in South Africa, with Karoo material typically made up of shale and mudrock as well as the underlying dolomite of the Malmani Subgroup (Trollip *et al.,* 2008).

In Gauteng, most sinkholes and subsidence formations are caused by either intense ingress of water or dewatering as discussed by Buttrick *et al*. (2001 and 2011). According to Jennings *et al*. (1965), subsidence in dolomitic rocks occurs in one of two ways: (a) gradually, as in the case of caving subsidence, which creates enclosed depressions in the ground surface, and (b) suddenly, as in the case of a sinkhole, which has extremely steep sides and a small lateral extent. Both cases are severe from an economic standpoint, but the second one is precarious due to potential adverse effects on human life.

Several interdependent conditions must occur successively before a sinkhole can form, and it will only form if every one of them is present. Karst formation and the subsequent collapse leading to sinkholes or subsidence are related geological processes, but they occur at different stages and have distinct characteristics. Rainwater, which is slightly acidic due to dissolved carbon dioxide forming carbonic acid, seeps into the ground and gradually dissolves the bedrock. Over time, this process creates voids or cavities in the rock, forming a subterranean network of caves and tunnels. Common karst features include underground rivers, caves, stalactites, and stalagmites. Surface features may include sinkholes, disappearing streams, and springs.

A sinkhole or subsidence occurs when the roof of a cavity or void formed during the karst process collapses, leading to a depression or hole in the surface. As cavities grow larger and closer to the surface, the overlying material becomes unsupported. Triggers for collapse can include heavy rainfall, changes in groundwater levels, added surface weight, or natural erosion. Field observations of sinkholes reveal that they are invariably formed by the collapse of the final arch or dome of the rubble-roofed, air-filled void within the residuum overlying the dolomite (Jennings, 1966). This process occurs when the supporting structure of the rubble arch, which spans the air-filled cavity, fails, causing the overlying material to collapse into the void, creating a sinkhole at the surface. This process underscores the critical role of the residuum in maintaining surface stability. Jennings *et al.* (1965) suggested a series of events that must occur in succession for a sinkhole to form. It's a combination of factors including the presence of rigid material for support, arching of the material, development of a void, a receptacle for eroded material, a disturbing agency for collapse, and the progressive movement of the void towards the surface. Each of these conditions must be present for the formation of a sinkhole, emphasizing the complexity of the process. A sinkhole can only form if any one of these requirements is met in order. But it is important to also not exclude the following factors in sinkhole formation:

- **Depth:** The depth of the void and its proximity to the surface affect the likelihood of sinkhole formation.
- **Transportation of material:** The ability of water or other agents to transport material from the void affects the sinkhole's growth.
- **Nature of underlying strata:** Different types of rocks and soils have varying susceptibilities to dissolution or erosion, affecting sinkhole formation.
- **Structural elements:** geological structures such as faults, fractures, and dykes can influence the movement and flow of water, affecting the development of voids and sinkholes.

3.2.1 Dewatering Scenario Sinkhole

In the late 1960s and early 1980s, the South African national government passed a dewatering policy that allowed mining houses to extract water from these dolomitic aquifers (DWAF, 2006). Kleywegt and Ensulin (1973) conducted a study on the compartmentalised dolomitic rocks (Bank compartment) in the Far East Rand of Gauteng (see Figure 3.5) and they discovered that most sinkholes in this region have developed in low-lying areas where the original water table was up to 30 m beneath the ground surface. Few sinkholes developed in areas where the original water table was between 30 and 60 m below the surface. It was later discovered that several sinkholes (diameter exceeding 5 m) had been formed in the compartments of the Far West Rand, when the water table was lowered by 10 m (Swart *et. al*., 2023). Jones and Wegener (2005) suggested that instability incidents in the Bapsfontein region had sharply increased in the previous ten years as a result of the deliberate lowering of the ground level by 120 m caused by pumping for irrigation.

In areas with dolomite bedrock, there may be cavities and voids within the overburden or bedrock. These cavities are often filled with groundwater, maintaining a natural equilibrium. The groundwater within these cavities provides support to the overlying rock layers. This equilibrium helps to stabilize the surface and prevent the collapse of the cavities.

When the groundwater table is lowered, either naturally or due to human activities such as dewatering for construction or extraction, it disturbs this equilibrium. As the groundwater level drops, the cavities that were previously filled with water are now exposed to air. Without the support of groundwater, the overburden or bedrock above these cavities can become unstable. The exposure of cavities to air accelerates subsurface erosion processes. The accelerated subsurface erosion due to the lowered groundwater table can lead to sinkhole formation (Oosthuizen and Richardson, 2011). The effects of dewatering on the dolomite compartments are well documented; however, the effects of re-watering groundwater levels in the dolomite are poorly understood.

3.2.2 Ingress Scenario Sinkhole

The formation of troughs, pinnacles, and cavities is caused by the concentrated input of water, which encourages the dissolving of the dolomite bedrock into WAD. Sinkholes are created when erodible sediment from the overlying soil is readily accepted by the cavities (Avutia and Kalumba, 2014) (see Figure 3.4).

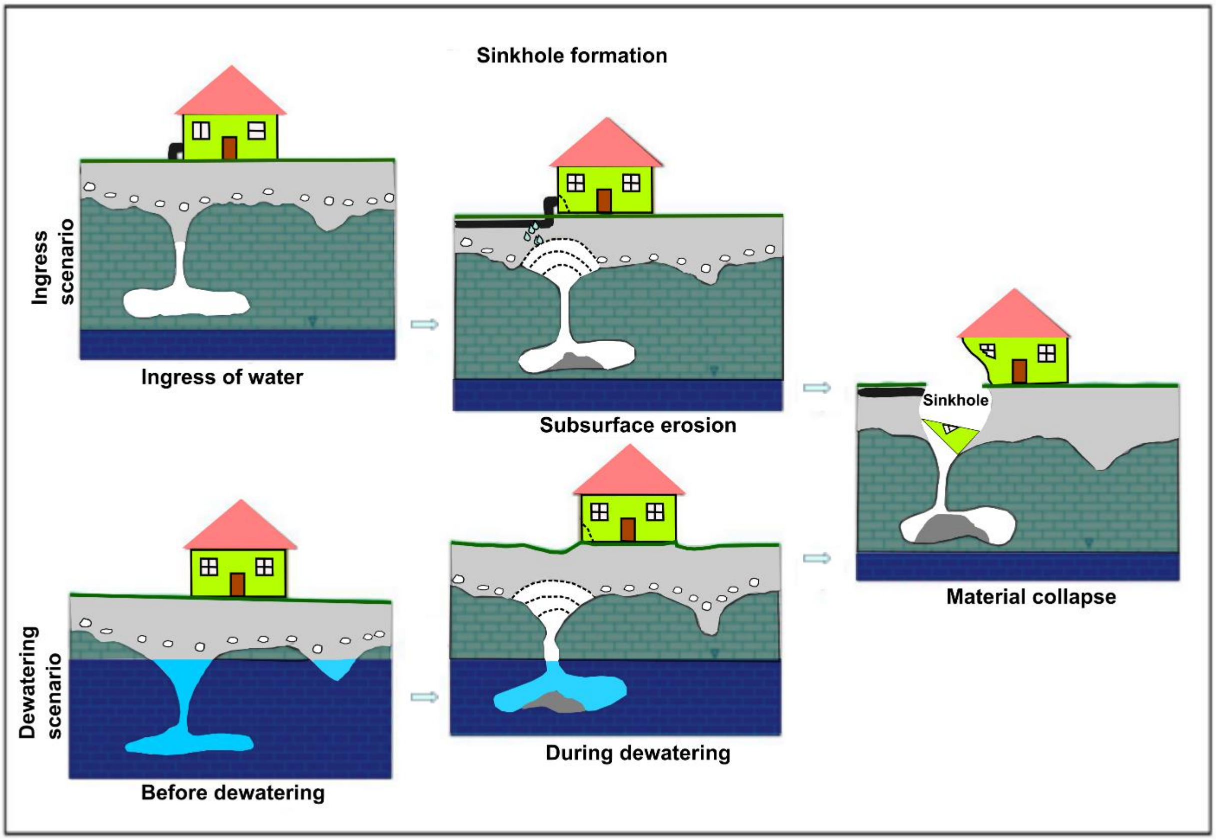

Figure 3.4: Drawings depicting the mechanism of sinkhole formation in ingress and dewatering scenarios (Oosthuizen and Richardson, 2011).

3.3 Types of Sinkholes

Natural processes and human activities, in combination or isolation, can drive the development of sinkholes (Culshaw and Waltham,1987; Delle Rose *et al*., 2004; Parise and Lollino, 2011). Human activities like mining, construction, and groundwater extraction directly generate or exacerbate anthropogenic sinkholes. In many cases, the origin of sinkholes can be a combination of both natural and anthropogenic factors. For example, a naturally occurring cavity in the subsurface may be exacerbated by human activities, leading to a collapse that forms a sinkhole (Culshaw and Waltham 1987).

3.3.1 Natural Sinkholes

Natural sinkhole formation can be greatly influenced by geological features like faults and dykes. These features may open channels for water to seep into the ground below, which could result in the dissolving of soluble rocks and the development of cavities

(Caramanna, 2008). Rainy seasons can lead to the saturation of underlying rocks and the filling of underground voids with water. This increases the load on the roof of these cavities, and if the load exceeds the strength of the rock, the roof can collapse, resulting in sinkhole formation at the surface. Ongoing heavy rainfall and flooding can further contribute to the growth and expansion of the sinkhole (Scheidt *et al*., 2005). Drought conditions can lead to reduced groundwater levels, which in turn reduces the buoyant support for the roof of underground cavities. This can result in the collapse of the roof rock and the sinkhole formation. The continued dissolution of soluble rocks during drought further weakens the roof rock, increasing the likelihood of collapse (Scheidt *et al*., 2005).

3.3.2 Anthropogenic Sinkholes

Human actions have significantly accelerated the rate of sinkhole formation and subsidence over the past 50 to 60 years. When a buried sewage disposal system bursts or leaks, it can release a significant amount of water or wastewater into the surrounding soil. This sudden influx of water can saturate and soften the soil, leading to erosion and the washing away of soil particles. As the soil erodes and gets carried away by the flowing water, it creates voids or empty spaces underground. (Hadjmeliani, 2015; Guarino *et al*., 2018). Mining operations often encounter groundwater, especially in underground mines where water can accumulate in tunnels and shafts. To allow for mining operations to continue, dewatering techniques are employed to pump out the groundwater from the mine workings. If the water table is lowered, this can lead to the collapse of underground voids and the formation of sinkholes (Ali and Choi, 2019).

3.4 Impact of Groundwater on Sinkholes

The importance of groundwater in the formation of sinkholes and surface subsidence cannot be denied. Whether by dewatering or water ingress, the movement of water does have an influence. Ngcobo (2006) stated that the three crucial mechanisms that cause sinkholes to occur are excessive water seepage, water level draw-down, and seismic events. Due to its complicated geology, karstification level, and complex structure, groundwater availability in karst settings varies greatly (Ponta, 2019; Avutia and Kalumba, 2014). Dolomite instability may be influenced by the position of the groundwater table concerning cavities in the strata and erodible residue.

In cases where dykes and faults are highly fractured or weathered, they can increase permeability and act as conduits for groundwater flow. Water can move along these structures, facilitating connectivity between the different aquifers or groundwater reservoirs. On the Far West Rand, dolomite formations are segmented into distinct groundwater compartments by the presence of impermeable syenite dykes, between 6 to 60 m in width (Wagener, 1986; De Bruyn and Bell, 2001). These dykes (Oberholzer dyke, Bank dyke, Venterspost dyke) cut across the Malmani dolomites, which have the effect of forming watertight groundwater units or compartments within the dolomite. The Oberholzer, Bank and Venterspost compartments resulted from dykes cutting across the Malmani dolomites (Figure 3.5). According to Meyer 2014, the dykes are predominantly mafic and are generally considered to be mostly impermeable or have low permeability, thereby acting as barriers to groundwater flow. Consequently, they play a significant role in subdividing groundwater into numerous compartments. These compartments serve as potential channels for groundwater flow in the underlying rocks. Thus, each compartment tends to be entirely waterproof compared to neighbouring compartments and can hold enormous amounts of water (Van Eeden *et al*., 2003). According to residual gravity measurements, dyke contact zones can sometimes be favourable locations for the dissolution of dolomitic strata (Foster, 1989).

The water in these compartments, such as the Oberholzer Compartment, forms a vital water resource for extensive metropolitan areas, especially in semi-arid South Africa (Schrader and Winde, 2014). These compartments also created problems in the mine production and workers' lives in the Carletonville gold mines. For these reasons and uncontrollable water levels in 1964, mines such as Driefontein received authorisation to dewater the dolomite compartments (Van Eeden *et al*., 2003). Strong evidence that transmissive zones can occur at vast depths, as seen in the 1968 inrush of dolomitic groundwater into the Driefontein gold mine at a rate of more than 360 000 m^3/day (Foster, 1989). Groundwater lowering has a detrimental effect on an area's dolomite stability, increasing dolomite-related instabilities. A compartment's equilibrium is therefore disturbed by excessive artificial groundwater level raising or lowering, which leads to fresh subsurface erosion or, in the case of a rising water table, a shift in the soil's cohesive strength that bridges subsurface voids (Van Eeden *at al*., 2003). The formation of additional sinkholes typically continues until a new equilibrium has been attained. Dewatering increased the number of sinkholes that formed on the Far West Rand (Oberholzer, Venterspost, Gemsbok-west, and Bank compartments). It caused around 1200 sinkhole incidents to form (Figure 3.5) (Heath and Oosthuizen, 2008).

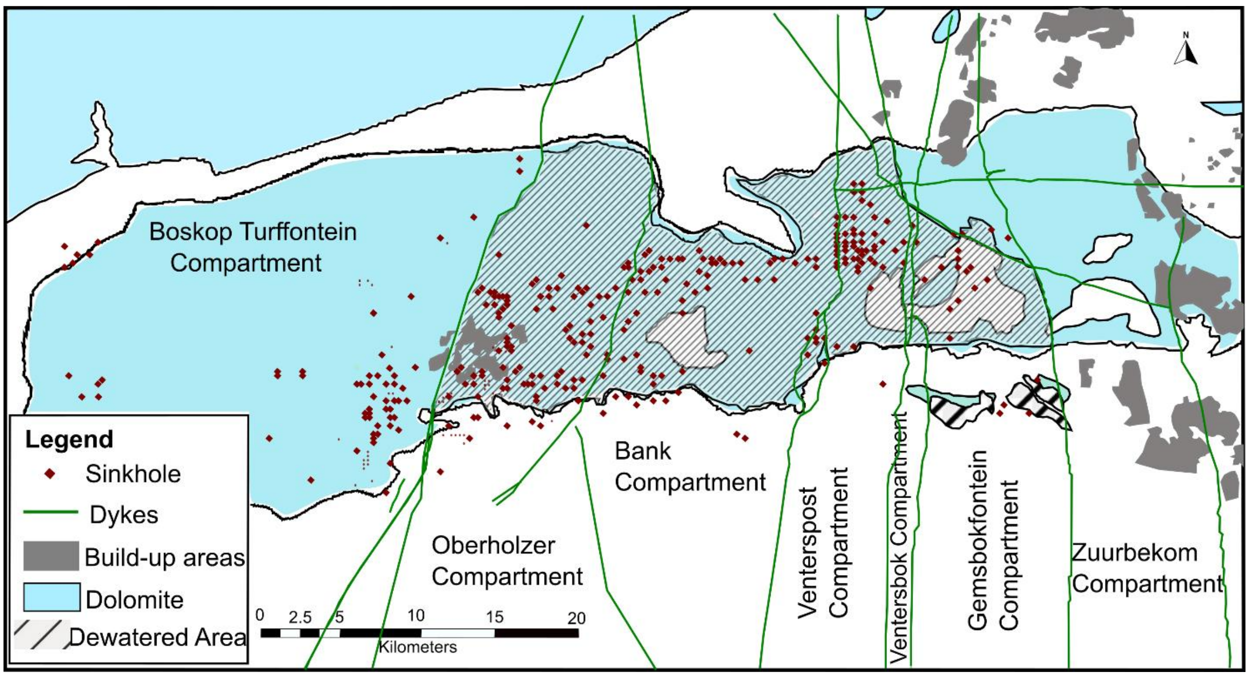

Figure 3.5: Occurrence of sinkholes and subsidence on the Far West Rand, showing the different compartments (Oosthuizen and Richardson, 2011).

Rainfall has a significant influence on the formation of sinkholes. In regions where sinkholes are likely to occur, the likelihood of sinkhole development is directly correlated with the likelihood of heavy rainfall. Therefore, assessing the area's average annual rainfall may also be helpful in correlated variations in groundwater levels. According to Oosthuizen (2013), most sinkholes are developed in the rainy season's latter months in South Africa, primarily in January and February, possibly because the soil profile is entirely saturated at that point (De Bruyn *et al*., 2000; De Bruyn and Trollip, 2000).

Over 430 sinkhole events were recorded in the south of Tshwane before 1997, and over 50 were related to heavy rainfall in 1996. The likelihood of sinkholes forming can increase if the water table can vary (move up and down) outside of its natural range. Richardson (2013) also conducted a similar study, considering 1393 sinkhole events between 1959 and 2011. The results of the study are summarised in Table 3.2.

Table 3.2: Sinkhole events reported in Tshwane vs. Annual rainfall (Richardson, 2013).

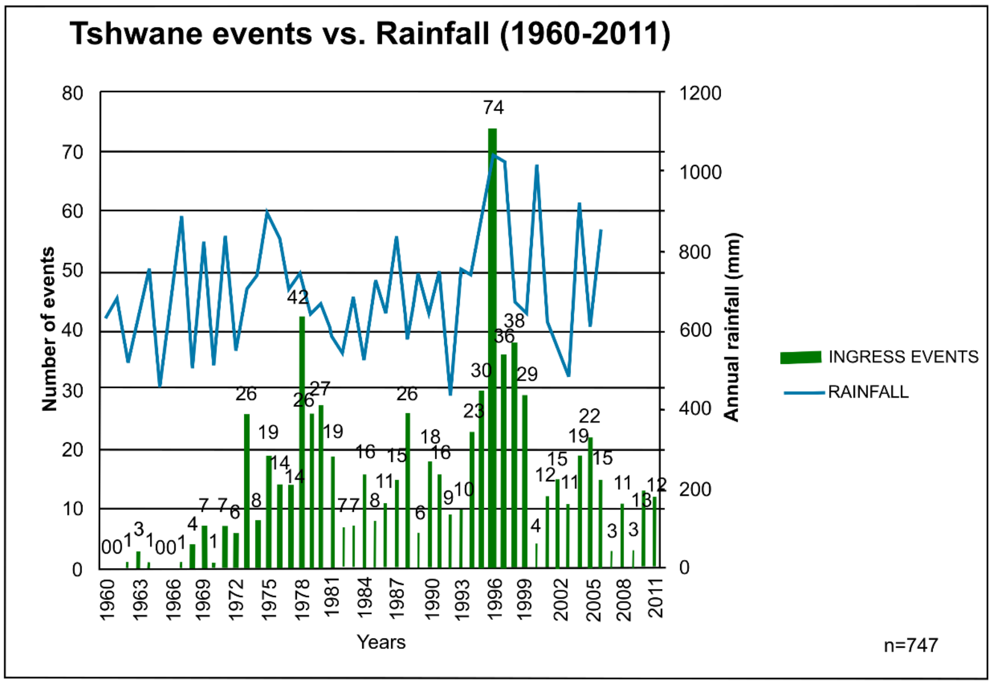

Events reported for Tshwane vs. Annual rainfall (rainfall data suppliied by the SA Weather Service for the Irene Station) (data limited to events with chronological data)

Sinkhole formation is a multi-step process, with each step dependent on the previous one. It requires specific hydrological and geological conditions to align for a sinkhole to form. Understanding these conditions and factors is crucial for assessing and mitigating the risks associated with sinkholes in areas prone to such geological hazards.

4 THEORETICAL BACKGROUND

4.1 The Application of Geophysical Methods in Sinkhole Detection

4.1.1 Geophysical Methods

Geophysical methods are powerful tools for assessing and monitoring sinkholes, providing valuable insights into subsurface conditions and potential hazards. Several geophysical techniques have been suggested for identifying the presence of sinkholes and irregular bedrock profiles (Jennings *et al*., 1965; Montgomery *et al*., 2020). In this study, the following geophysical methods are used: ERT, GPR, and seismic methods such as reflection, refraction, and seismic and MASW methods. Sinkhole fills, generally composed of a mixture of water, air, soil, and sometimes other materials, have different physical properties compared to the surrounding rocks or strata. This physical property contrast is what geophysical methods aim to detect and delineate. It is recommended that all four techniques be incorporated when the site is investigated for sinkhole mapping, particularly when determining the soil-rock interface and physical property (density, seismic velocity, and electrical conductivity) variability of the overburden geology (Avutia and Kalumba, 2014).

Farooq *et al*. (2013) used the electrical resistivity method to assess the extent of karst voids in areas prone to ground subsidence along a road in Yongweol-ri, Muan-gun, South Korea. Nwokebuihe *et al*. (2014) used MASW and ERT to map sinkholes effectively in Missouri, United States of America (USA). Montgomery *et al*. (2020) evaluated the capabilities of GPR, gravity, and seismics to map the position and size of sinkholes along a highway in Alabama, USA. Cueto *et al*. (2018) also describes the integration of geophysical techniques (e.g., GPR, ERT, etc.) applied in the identification of a large sinkhole along the Riyadh metro line 3 in Saudi Arabia. Cardarell *et al*. (2013) present an investigation procedure consisting of the sequential application and integrated interpretation of ERT, P-wave Refraction Tomography) and Self Potential measurements for locating and monitoring piping sinkholes with application to a site in Central Italy. Hussain *et al*. (2020) conducted a study in the environmentally sensitive area of Rio Vermelho, Mambaí, Goiás, Brazil using three geophysical techniques, including ERT, GPR, and Very Low Frequency Electromagnetic (VLFEM) to provide an economical and non-invasive alternative for extracting information about cavities, sinkholes, pathways for water infiltration as well as the degree of karstification of underlying carbonate rocks.

4.1.2 Geophysical Investigations in Transvaal Dolomite Formations

Geophysical investigation techniques are essential for detecting anomalies in dolomite strata, especially in karst environments, where extreme weathering can lead to sinkhole formation. Karst stratum anomalies are a result of carbonate rocks undergoing extreme chemical weathering, leading to the formation of subsurface voids and instability at the surface (Avutia and Kalumba, 2014). A “Special Subcommittee on Research into Water, Underground Cavities and Surface Subsidence in Dolomitic Areas" was established in South Africa in the early 1960s (Roux, 1991) to characterize the subsurface structure of dolomitic areas.

Enslin and Smit (1955) published a paper titled “Geophysical surveys for foundations in South Africa” with special reference to the sinkholes in the dolomitic areas in the south of Pretoria, including the Voortrekkerhoogte-Lyttelton areas.

4.2 Electrical Resistivity Tomography (ERT)

ERT is a well-established exploration technique with a history spanning over a century. Its popularity is due to its effectiveness in providing detailed subsurface information in various fields such as geology, environmental studies, and engineering. The resistivity of the subsurface can be measured using three types of arrays, namely, the Wenner, dipole-dipole, and Schlumberger arrays. Through proper array designs, one can study the fluid saturation, porosity, permeability, and other rock characteristics that exhibit variations in their electrical resistivity (Loke, 2014). A dipole-dipole array, shown in Figure 4.1, is favoured for imaging karst fractures and caves due to its superior vertical and lateral resolution. It can effectively detect the contrasts in resistivity associated with these features, providing detailed images of the subsurface. This array is sensitive to small-scale variations in resistivity, making it well-suited for mapping the complex structures found in karst landscapes (Labuda and Baxter, 2001; Roth *et al.*, 2002).

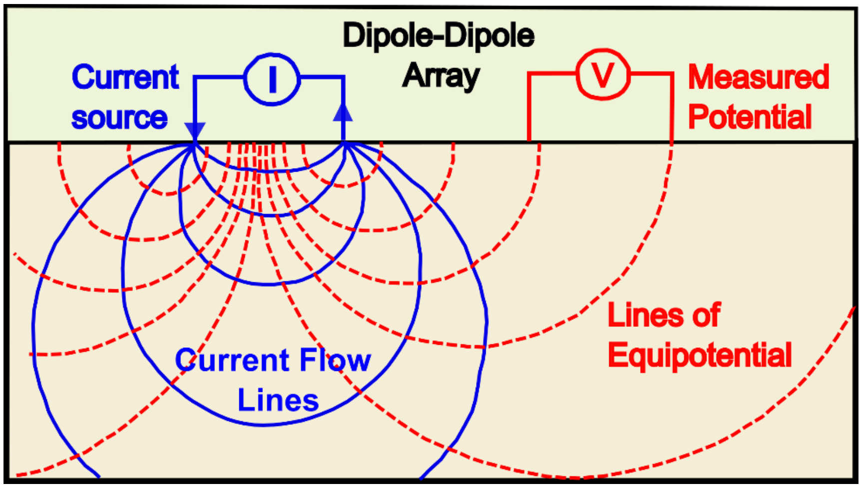

Figure 4.1: Electrode arrangement for a dipole-dipole array, consisting of two sets of electrodes, the current (source) and potential (receiver) electrodes (Montgomery *et al*., 2020).

In geotechnical and environmental investigations, the ERT method has been applied for almost a century (Fehdi *et al*., 2011). It is the most applied method for site investigations in karst regions, mainly when the topsoil is primarily made of clay (Cook and Van Nostrand 1984). Figure 4.2 provides a list of resistivity values for rocks and minerals.

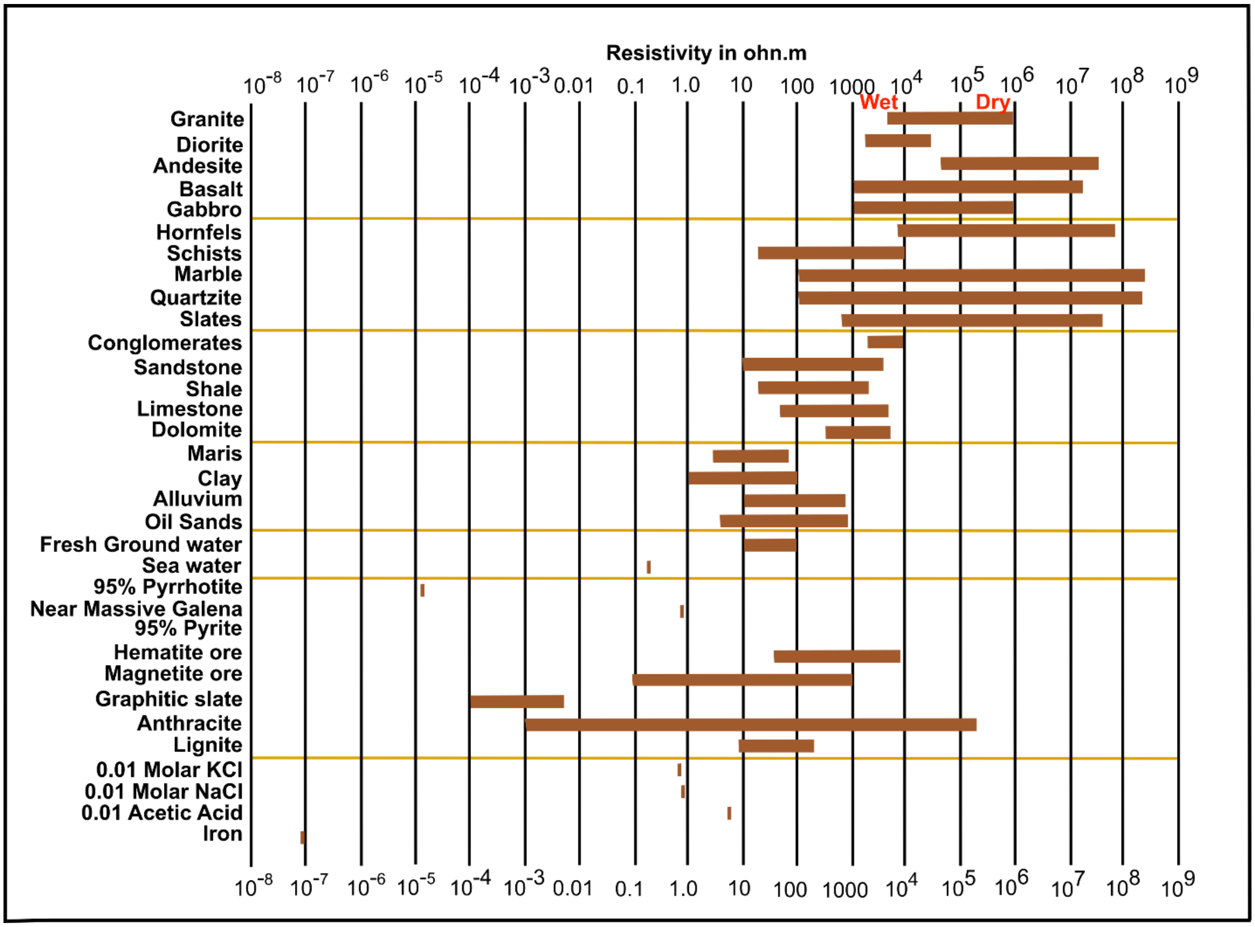

Figure 4.2: The resistivity of rocks, soils, and minerals. The image depicts, in broad terms, the relative resistivities of significant rock groups (Loke, 2014).

2D resistivity surveys can be applied with other geophysical methods to offer more information about the subsurface (Loke, 2014). Because an air-filled sinkhole typically shows good electrical resistivity in contrast with the surrounding rock, the resistivity methods (Loke, 2000a; 2000b) are often preferred when locating sinkholes.

The Physics of Electrical Resistivity Tomography (ERT)

Ohm's Law is the fundamental physical principle employed in resistivity studies, which regulates the flow of current in the ground; resistivity (ρ) is measured by applying a regulated current (I) through electrodes to the surface and then determining the difference (ΔV) between two potential electrodes as shown in Figures 4.3, 4.4 and 4.5 (Niculescu and Andrei, 2021).

The apparent resistivity (ρ_A) is calculated as (Telford *et al*., 1990; Loke, 2020):

$$\rho_A = k\frac{\Delta V}{I} \tag{4.1}$$

$$K = \frac{2\pi}{\left(\frac{1}{r_{C1P1}} - \frac{1}{r_{C2P1}} - \frac{1}{r_{C1P2}} + \frac{1}{r_{C2P2}}\right)} \tag{4.2}$$

Where I the electrical current, which measures the flow of change in a given section of a conductor is measured in Amperes. ΔV is the potential difference between electrodes; r_{C1P1}, r_{C2P1}, r_{C1P2}, and r_{C2P2} are the distances between the respective electrodes and, *k* is a geometric factor dependent on the positions and design of the electrodes. The Wenner array is defined by Equation (4.3) and demonstrated in Figure 4.3.

$$\rho_{Wenner} = 2\pi\alpha\left(\frac{\Delta V}{I}\right) \tag{4.3}$$

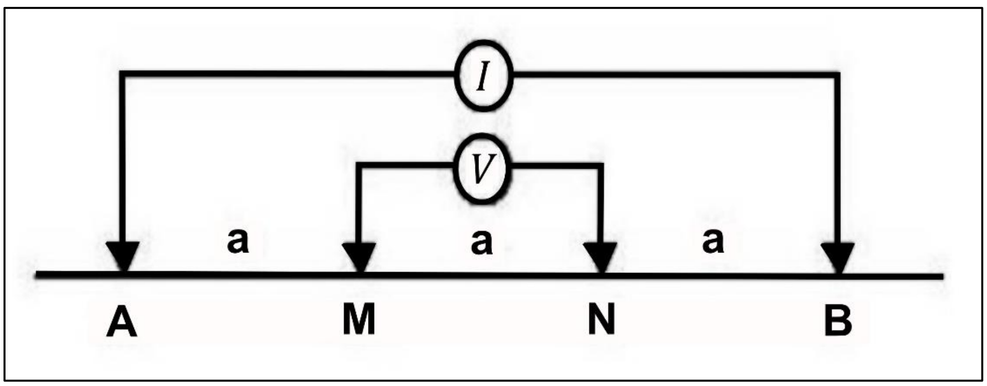

Figure 4.3: A schematic diagram of the Wenner array electrode configuration. 'A' and 'B' = current electrodes (I = current), 'M' and 'N' = potential electrodes (V = potential difference) and 'a' = spacing between electrodes (Tesfaldet and Puttiwongrak, 2019).

The Schlumberger array is defined by Equation (4.4) and demonstrated in Figure 4.4.

$$\rho_{Schlumberger} = \frac{\Delta V}{I}\pi\,\frac{b(b+a)}{\alpha} \tag{4.4}$$

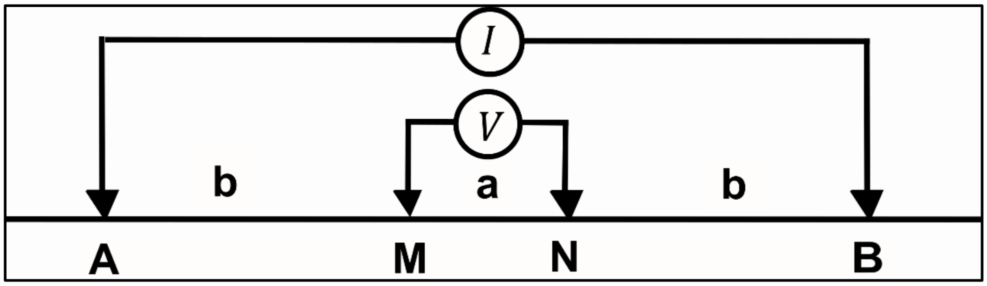

Figure 4.4: A schematic diagram of the Schlumberger array electrode configuration with two outer electrodes 'A' and 'B' = current electrodes (I = current), 'M' and 'N' = potential electrodes (V = potential difference), 'a' and 'b' = spacing between electrodes (Tesfaldet and Puttiwongrak, 2019).

The dipole-dipole array is defined by Equation 4.5 and demonstrated in Figure 4.5.

$$\rho_{dipole-dipole} = \frac{\Delta V}{I}\pi n\alpha(n+1)(n+2) \quad (4.5)$$

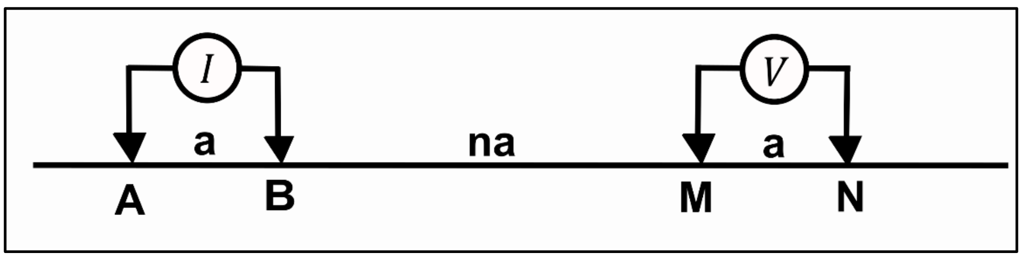

Figure 4.5: A schematic diagram of the dipol-dipole array electrode configuration with two outer electrodes 'A' and 'B' = current electrodes (I = current), 'M' and 'N' = potential electrodes (V = potential difference), 'a' = spacing between electrodes (Tesfaldet and Puttiwongrak, 2019).

The parameters used in the equations above are defined:

ρ = apparent resistivity (Ohm-cm); a = electrode spacing (cm); V = potential difference voltage measured in joule/coulomb; I = current (Ampere); π = *constant* (3.142); and n = an integer.

4.3 Ground Penetrating Radar (GPR)

GPR is a geophysical method that detects changes in the shallow subsurface electromagnetic properties by using propagating electromagnetic (EM) waves (10-1000 MHz) which can be refracted or reflected off subsurface structures before being received and digitally recorded in ways similar to the seismic method. (Fisher *et al.,* 1992; Baker, 2007; Ukaegbu, 2019). A portion of the EM waves are reflected when they encounter a rock layer having a different permittivity to the host rock, while the remaining waves are transmitted through the second layer (Ukaegbu, 2019). Relative permittivity is defined as a material's capacity to store electromagnetic energy before permitting its passage when an electric field is applied to the medium (Baker, 2007). The permittivity of the medium is important in determining the velocity at which electromagnetic waves travel from the antenna into the medium (Ukaegbu *et al.*, 2019). Relative permittivity is a key parameter in electromagnetic wave propagation, especially in GPR and geophysical methods. It can be quantified in the lab or in-situ, and contrasts in relative permittivity between materials influence EM wave reflections. This affects how subsurface features are imaged in GPR surveys, with larger contrasts leading to stronger reflections and better resolution (Bevan, 1998; Baker *et al.,* 2007). The method is site-specific such that the depth of penetration is limited by salt-water intrusion, high conductive pore fluids, and/or clayey soils (Coşkun, 2012; Loke, 2014; Montgomery *et al*., 2020).

Bevan (1998) suggested that the electrical resistivity of the soil and the depth at which a radar antenna would profile are strongly correlated. As shown in Figure 4.6, GPR is typically applied in reflection mode, which involves sending a signal through a transmitter antenna into the soil and structures being studied (Bostanudin, 2013). Since GPR can better map shallow soil and rock conditions, it is frequently applied in sinkhole investigations, but if deeper objects of interest are anticipated, other investigative techniques may need to be paired with it (Coşkun, 2012; Montgomery *et al*., 2020).

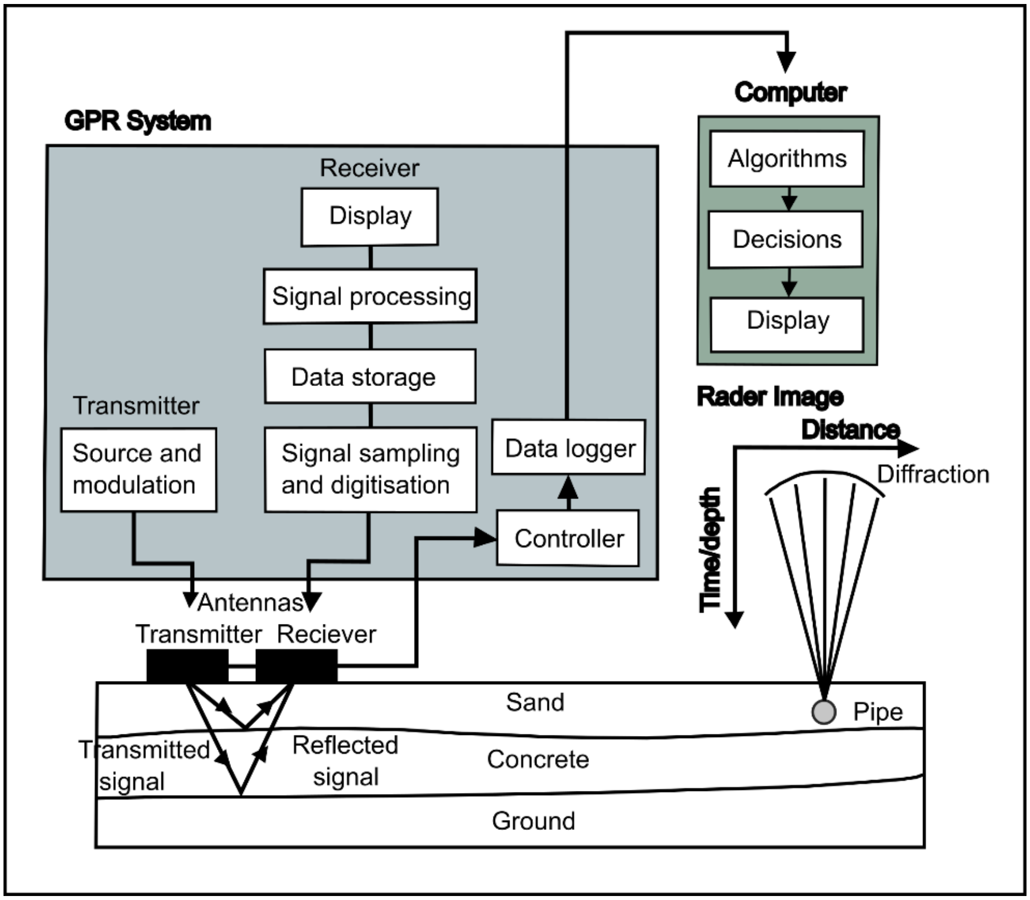

Figure 4.6: Principles of ground penetrating radar (GPR). Reflected waves from boundaries a recorded by the receiver and displayed as a time-varying signal (Ukaegbu *et al*., 2019).

The Physics of Ground Penetrating Radar (GPR)

The physics laws governing EM waves apply to how radar signals move through different types of materials. GPR systems operate with wavelengths on the order of several centimeters (Evans, 2009). Lower end of the frequency range improves penetration depths, while the higher end increases the resolution in structural imaging. Lower microwave GPR is a versatile tool used in various fields, including utility locating, geological surveys, archaeology, and civil engineering. The performance of GPR depends on the surface and subsurface conditions as well as its design and acquisition parameters (Abujarad, 2007). The wavelength of the input signal determines how well the GPR can identify objects on the subsurface.

Relative permittivity (r), magnetic permeability (m), and conductivity (c) are the three principal variables that are of importance in GPR. The dielectric constant is defined by:

$$\varepsilon_r=\frac{\varepsilon_s}{\varepsilon_0} \tag{4.6}$$

where ε_r is the "'relative permittivity" or dielectric constant of the material, ε_s is the permittivity of the material under investigation and ε_0 is the permittivity of vacuum, 8.89 x 10^{-12} F/M (Linde, 2005; Evans, 2009). The dielectric constant's value is significant since it is related to several variables that are crucial for the interpretation of GPR data (Evans, 2009). The link between the dielectric constant and the velocity of the GPR signal passing through the material is defined as:

$$\upsilon=\frac{c}{\sqrt{\mu_r \varepsilon_r}} \tag{4.7}$$

Here, c is the speed of light in free space (≈300 000 km/s), υ is the speed of the GPR signal through the material, μ_r is the relative magnetic permittivity (Henries per meter, H/m), and ε_r is the relative permittivity (Baker *et al.*, 2007; Evans, 2009). Maxwell's equations (Baker *et al.*, 2007) are essential for comprehending the behavior of GPR because they allow for the quantitative description of the relationship between a material's electromagnetic characteristics and electromagnetic wave propagation.

4.4 Refraction and Reflection Seismic Techniques

Seismic methods are concerned with measuring the seismic waves that propagate through Earth's materials. The refraction seismic methods commonly utilise a long array of geophones (cabled or wireless) to record refracted waves. The reflection seismic method, on the other hand, uses geophone arrays and a seismic source to acquire seismic data and record reflected waves. Seismic reflection has been widely used in the petroleum industry for hydrocarbon explorations. The method is also currently used for mineral exploration in hard rock environments and to map the deep crustal structures for tectonic studies. The seismic method can also be used to detect subsurface features such as cavities and tunnels before they lead to sinkholes or subsidence (Onyebueke *et al.*, 2020).

In engineering surveys, seismic refraction and reflection surveys are also frequently utilised for high-resolution characterisation of the subsurface (Loke, 2014). Both approaches can produce precise, in-depth profiles of the subsurface interfaces. For both surveys, the ground is subjected to a source of seismic waves. The seismic signals are then measured with ground motion sensors (geophones) spaced every few meters. The geophones are receivers that record these waves as they are reflected, refracted, or diffracted from the subsurface (Figure 4.7). Geophones are used to record the returning seismic waves, and then the variations in amplitudes and travel times are used to create seismic velocity maps and subsurface images, reflecting boundaries. The stratigraphic and lithological features in the subsurface can be determined by recording and analysing the waves that propagated through them (Loke, 2014).

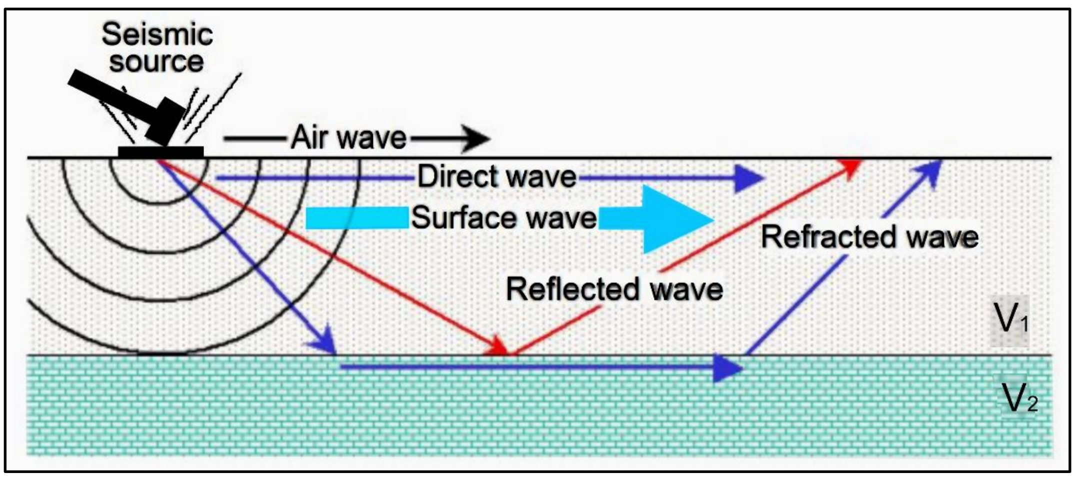

Figure 4.7: Example of seismic waves generated from a hammer striking a metal plate travelling through the subsurface (Liberty and St. Clair, 2018).

A source of energy is applied to the ground for both seismic methods. The shooting requires a more significant energy input to the ground, and the seismic energy sources include a shotgun, accelerated weight-drop, drophammer, and vibroseis trucks. Refracted seismic signals travel laterally through the higher velocity layer (refractor), generating a 'head-wave' that returns to the surface (TerraDat, 2020).

Across the globe, reflection seismic has been utilised to address sinkhole-related issues (Busetti *et al*., 2020). The seismic reflection method employs reflected P-waves in place of refracted P-waves. Interfaces and other heterogeneities in the subsurface will reflect some of the P-wave energy back to the surface, where it will be detected. The subsurface layers can then be determined using these reflections.

4.4.1 Seismic Wavefield Propagation

Geophysicists study seismic waves to determine the layers of the Earth, their thickness, and the physical properties of these layers. Surface and body waves are the two main types of seismic waves and these are shown in Figure 4.8 (Dentith and Mudge, 2014). Body waves propagate in the interior of a volume of material, while surface waves can move through the surface of the medium (Novotny, 1999; Dentith and Mudge, 2014).

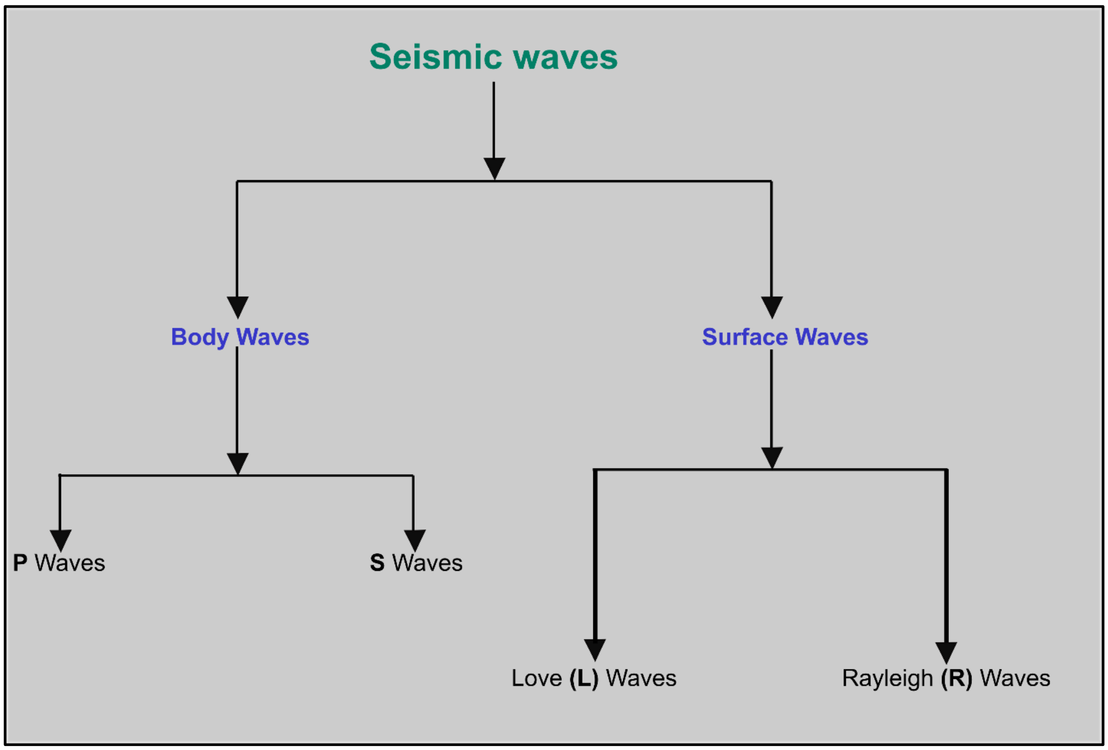

Figure 4.8: Different types of seismic waves (Ahmad, 2014).

The propagation of the waves depends largely on the physical properties of the rocks. Different seismic waves lead to various strains and deformations as they move through the Earth (Dentith and Mudge, 2014). Elastic constants are used to describe how a material reacts to different types of strain. The density (ρ) and appropriate elastic modulus of the material affect how quickly a body wave propagates through it (Dentith and Mudge, 2014).

$$\text{Speed}_{\text{bodywave}} = \sqrt{\frac{\text{elastic modulus}}{\rho}} \tag{4.8}$$

4.4.2 Body Waves

There are two kinds of body waves: primary and secondary waves (Figure 4.19). P-waves (primary waves) are also called dilatational, irrotational, or longitudinal waves. These waves do not rotate; the material is compressed and undergoes rarefaction as the wave travels through it (Novotny, 1999). P-waves can pass through both liquids like pore water and solids like rock. S-waves (secondary waves) are called transverse, shear, equi-voluminal, or rotational waves. As these waves pass through the material, the material is sheared and rotated, but there is no change in volume (Novotny, 1999).

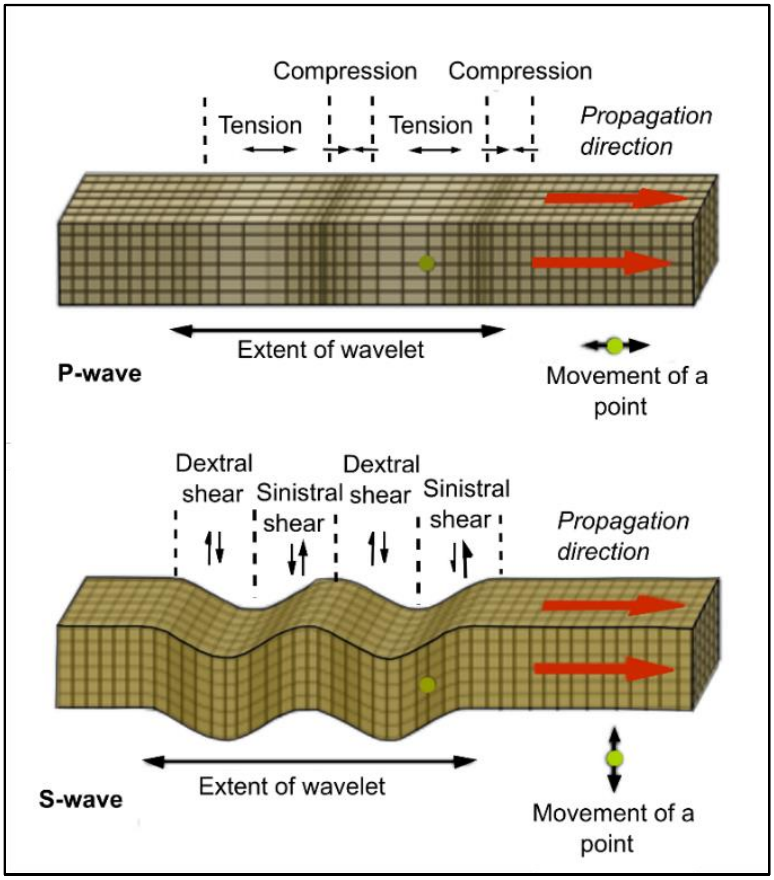

Figure 4.9: Deformation of the propagating medium associated with the passage of a P-wave (uniaxial strain) and an S-wave (shear strain) (Dentith and Mudge, 2014).

From Equation 4.8, P-waves (V_p) and S-waves (V_{s}) are defined as:

$$V_p = \sqrt{\frac{\lambda+2\mu}{\rho}}, V_s = \sqrt{\frac{\mu}{\rho}} \quad (4.9)$$

Where λ and μ are the Lamé coefficients, while ρ represents the density of the material. μ is the shear modulus, but coefficient λ has no direct physical significance (Novotny, 1999). The velocity of P-waves is often greater than that of S-waves (Dentith and Mudge, 2014).

4.4.3 Surface Waves

Over 67% of the seismic energy that is generated is imparted, whereas 26% is imparted to shear waves (S-wave) and 7% to compressional waves (P-waves) (Loke, 2000; Everett, 2013). Love and Rayleigh waves are two types of surface waves. Rayleigh waves are the most used waves in seismic surveys. As the Rayleigh waves pass through the medium, the direction of travel is perpendicular to particle motion along the surface. Rayleigh waves, on the other hand, propagate perpendicular to the travel direction in the horizontal plane (Dentith and Mudge, 2014). Closest to the surface, the wave velocity is retrograde (counterclockwise), but as it descends, it becomes clockwise. Love waves are the fastest between the two and are confined to the crust's surface (Alsulaimani, 2007).

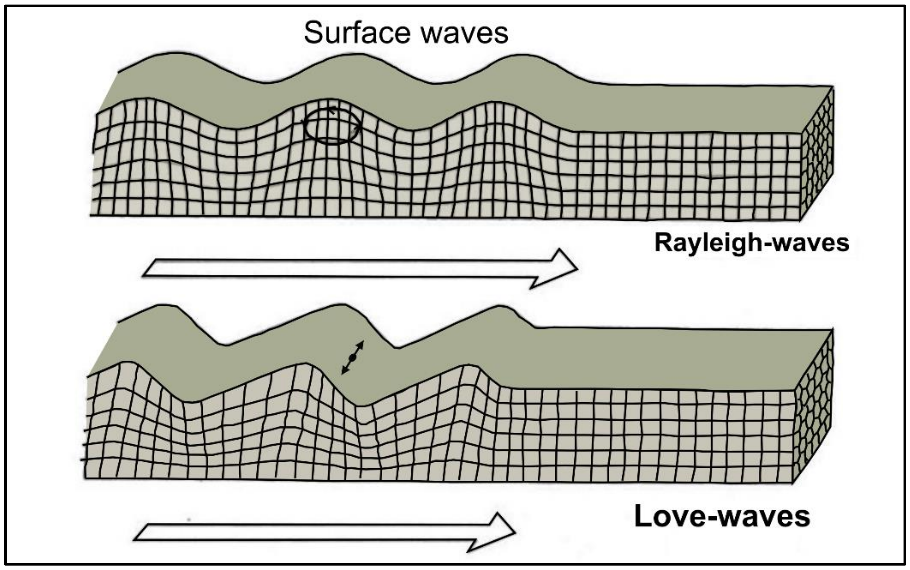

Figure 4.10: The particle motion for surface waves: (a) Rayleigh waves and (b) Love waves (Slideplayer, 2015).

4.5 Multichannel Analysis of Surface Waves (MASW)

MASW is a seismic technique based on the measurement of seismic surface waves produced by active or passive seismic sources to assess the elastic condition of the Earth's subsurface (Figure 4.11) (Alsulaimani, 2017). Due to its efficiency in measuring Shear wave velocities, the MASW approach is now a widely utilised geophysical tool (Park, 2013; Montgomery *et al.*, 2020). Data may be processed quite fast and readily with this method, which is less complicated than some other seismic processing techniques. MASW produces 1D profiles, making it possible to produce pseudo-2D profiles that could record lateral variations of elastic properties.

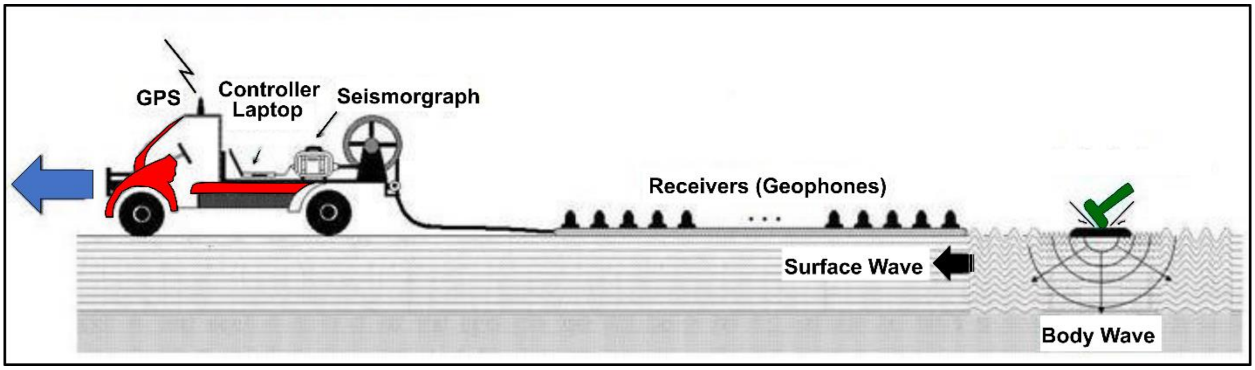

Figure 4.11: Schematic diagram of MASW linear array of geophones data acquisition (masw.com, 2023).

The method has been mainly used in determining the physical characteristics of the near-surface rocks and identifying subsurface weak zones and cavities (Ali *et al*., 2021). Park (2007) suggests that the depth for active MASW methods is usually less than 30 m, but the passive approach allows for an investigation depth of up to a few hundred meters; this depends on the source and array setup. A typical MASW survey includes the following: (a) data acquisition, (b) extraction of the dispersion curves; and (c) inversion analysis for Vs profiles (Xia *et al*., 1999). A typical procedure for the MASW method is shown in Figure 4.12.

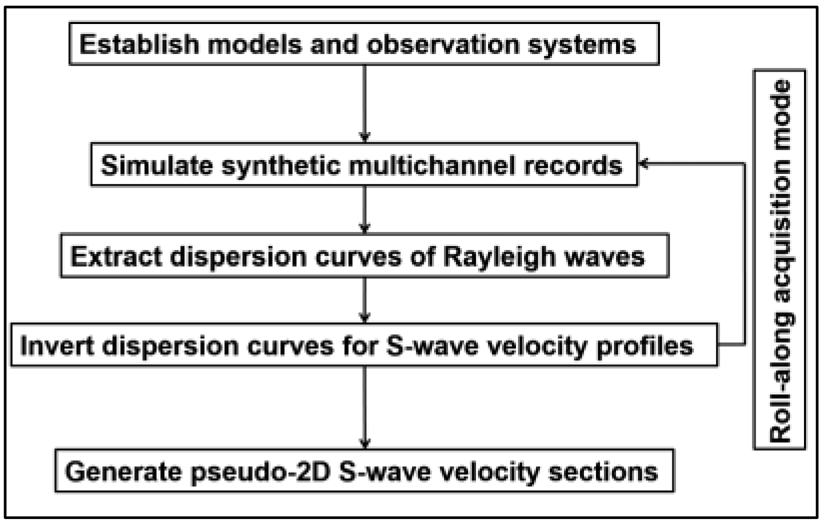

Figure 4.12: A general procedure of the investigation of the MASW method (Mi *et al*., 2017).

5 FORWARD MODELLING

5.1 The Importance of Physical Properties in Geophysics

The Earth is made up of components that have different physical properties. The most common physical properties in geophysics include elastic properties, bulk density, electrical conductivity, dielectric constant, and magnetic susceptibility (Anderson *et al*., 2008). The effectiveness of geophysical methods is determined by the physical characteristics of rocks, including both the geophysical geological target and the host rocks in the area (Van Schoor and Fourie, 2015). The contrast in physical properties between the host and target rock determines the choice of the geophysical method that can be used for a specific purpose (Milsom and Eriksen, 2013).

Several geophysical methods can be applied to measure the different geophysical properties. It is therefore important to ask several questions to narrow down the correct method for each geological problem. Anderson and Cardimona (2000) provided a framework for considering geophysical methods for a study. Researchers can develop a comprehensive geophysical survey plan that considers the physical properties of interest, the methods available, resolution requirements, cost-effectiveness, data complementarity, and integration with non-geophysical data for a robust interpretation of subsurface conditions. Below are key factors and their scientific justifications:

- **Complementarity of methods:** Different geophysical methods are sensitive to different physical properties. For example, combining gravity surveys (sensitive to density variations) with resistivity surveys (sensitive to electrical properties) can provide a more complete picture of subsurface conditions. Gravity surveys can identify density contrasts, while resistivity surveys can delineate the distribution of materials with varying electrical conductivity.
- **Physical properties of interest**: Identify the geophysical properties relevant to the study, such as density, resistivity, magnetic susceptibility, and seismic velocity.
- **Cost:** The cost of geophysical surveys varies, and the choice of method should balance the budget constraints with the need for reliable data. Some methods, like seismic surveys, can be more expensive but offer high-resolution images, while

others, like magnetic surveys, might be more cost-effective for large area coverage.

- **Depth of investigation:** Different methods have varying penetration depths. The choice of method should match the depth range of the geological features of interest.
- **Resolution requirements:** The spatial resolution needed depends on the size and detail of the features being investigated. High-resolution methods provide detailed images but might cover smaller areas or be more costly.
- **Integration with non-Geophysical data**: Plan for the integration of geophysical data with other types of data, such as geological, hydrological, or geochemical information, to enhance the robustness of the interpretation.

Amongst other things, differences in texture, porosity, mineral composition, lithology, and groundwater chemistry may be responsible for the contrast in physical properties (Anderson *et al*., 2008). The target of interest can then be detected, characterised, or mapped using this contrast. Selected geophysical methods and the underlying physical properties are listed in Table 5.1:

Table 5.1: Geophysical methods with appropriate physical properties (Kearey *et al*., 2002; Van Schoor and Fourie, 2015).

Method	**Measured parameter**	**Operative physical property**
Magnetics (including ground and airborne magnetics)	Variations in the strength of the geomagnetic field	Susceptibility and remanence
Gravity	Variations in the strength of the gravitational field of the Earth	Density
Electrical methods including ERT	Earth resistance	Electrical conductivity
Induced polarisation (IP)	Polarization voltages or frequency-dependent ground resistance	Polarisability (often referred to as charge ability)
Ground-penetrating radar (GPR)	Travel times of reflected radar pulses	Dielectric constant and electrical conductivity
Seismic	Travel times of reflected/refracted seismic waves	Density and seismic wave velocities

In this study, the geological structure under investigation is a sinkhole and is ideally expected to be located at shallow depths (within top 50 m). This would be characterised by acoustic velocity, EM velocity, dielectric constant, density, electrical conductivity, and resistivity (Anderson and Cardimona, 2000). Numerous geophysical methods, such as GPR, gravity, resistivity, seismic refraction, seismic reflection, and EM would seem potentially viable based on the information shown in Table 5.1. One other important element to consider in choosing the correct method is the suitability of the site conditions for collecting quality geophysical data (Milsom and Eriksen, 2013; Van Schoor and Fourie, 2015). The site conditions are often overlooked during the survey design. In this case study, it is important to note that the site is on the freeway and therefore “noise” may result from traffic, electric power lines, or even wind.

5.2 Electrical Resistivity Tomography Forward Modelling

To create 2D cross-section models for resistivity, RES2DMOD and Res2Dinv software packages were used. The Res2Dmod may help the user select the best array for various geological surveys (Loke, 2002). The Wenner, Wenner-Schlumberger, strong-gradient, dipole-dipole, and pole-dipole arrays are a few examples of regularly used arrays in ERT surveys (Loke, 2002; Montgomery *et al*., 2020). Depending on the type of array chosen for the survey, all the mentioned arrays have their own sets of advantages and disadvantages. For example, the Wenner array is better at mapping horizontal features than vertical ones. Wenner arrays are often effective at detecting lateral changes, but they are not good at detecting vertical changes (Loke, 1999). The dipole-dipole array, however, is particularly sensitive to resistivity changes that occur laterally and rather insensitive to those that occur vertically. According to Loke (2012) and Montgomery *et al*. (2020), this array is good at mapping cavities and dykes but poor at imaging sills or layered strata. Put differently, the dipole-dipole array exhibits superior lateral resolution but lower vertical resolution. After carefully weighing aspects including cost, depth of study, resolution, and practicality, the Res2Dmod should be able to assist in selecting the "optimal" array for a specific survey. The dipole-dipole array was chosen for the R21 sinkhole survey.

Understanding the state of the underlying geology, including the types of rocks and the thickness of the weathered layer, is crucial. This provides a model that closely resembles the reality of the survey to be conducted. Part of creating a forward model means knowing the subsurface rocks in the study area. Van Schoor and Mare (2015) provided a list of rocks found in South Africa and their resistivity ranges (Figure 5.1). The dolomites exhibit resistivity ranges 1000-10000 Ohm.m, clays 1-100 Ohm.m, sandstones 200-8000 Ohm.m and consolidated shales 20-2000 Ohm.m. To provide a sufficient depth of investigation, a 2 m and 2.5 m electrode spacing was chosen.

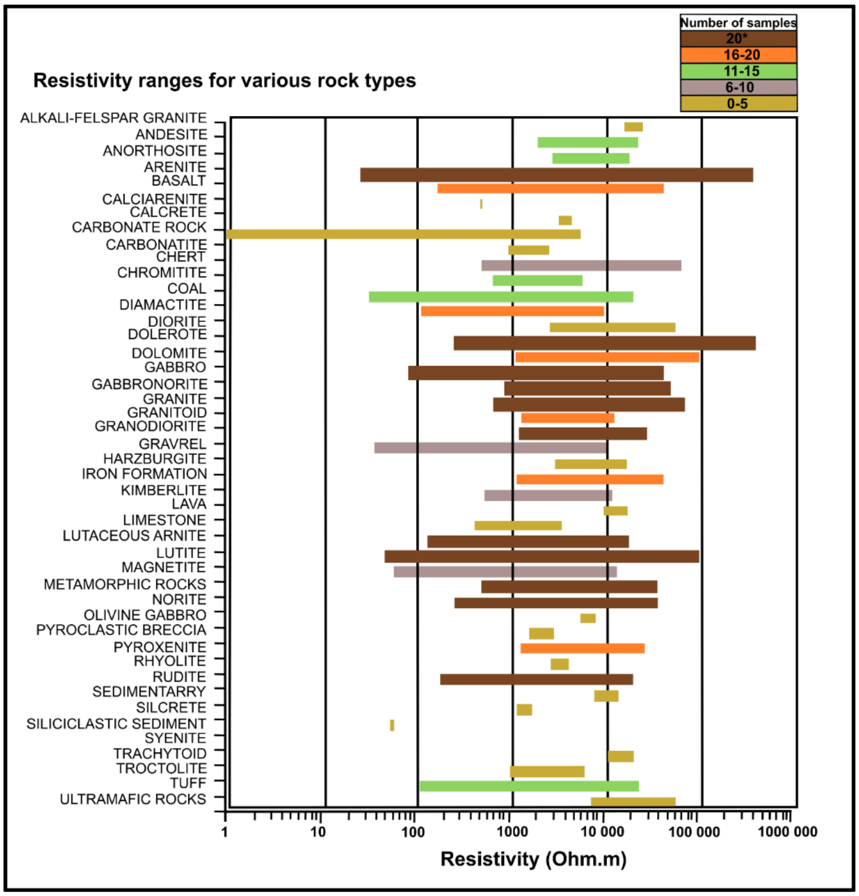

Figure 5.1: Resistivity ranges of rocks found in South Africa (Van Schoor and Mare, 2015).

The finite-difference forward modelling was chosen for this study. To run a model, the parameters were set on the Red2Dmod, the saved data were then extracted using Res2DInv to get the desired model. The subsurface was divided into a sizable number of little rectangular cells. The software requires the resistivity model values to be independently entered in a text file. Three models were created, filled with water (a), collapse material mixed with air (b), and collapse material (c) (Figure 5.2), and Table 5.2 shows the parameters in each model.

The models created could map the sinkholes, with a model (a) showing a possible sinkhole at distances of 64 m to 82 m and depths of 2.18 m and 11.5 m. Model (b) shows a possible sinkhole between 66 m and 85 m distances. The last model (c) shows a possible sinkhole at distances of 66 m and 82 m, at a depth of 3.14 m. In resistivity surveys, water-filled sinkholes often appear as low resistivity anomalies due to the high conductivity of water compared to surrounding materials. Model (a) (water-filled sinkhole) shows lower resistivity values in the area where the sinkhole is located at distances of 64 m to 82 m and depths of 2.18 m and 11.5 m, because water-filled areas generally have lower resistivity compared to surrounding materials, creating a low resistivity anomaly. Model (b), which represents collapse material mixed with air, shows a resistivity signature that reflects this combination. It was expected to have exhibited moderate to high resistivity values compared to the surrounding material. However, this was not the case with the sinkhole in model (b), which shows lower resistivity values.

Model (c), representing collapse material without air, shows resistivity values that reflect the properties of the collapse material. This could range from moderate to high resistivity compared to the surrounding material. The resistivity signature of such sinkholes would depend on the specific properties of the collapse material, such as its composition, porosity, and saturation. This is true in this model as the resistivity values range from 525 to 1343 ohm.m.

Table 5.2: Assumed survey parameters for forward models (a), (b), and (c).

Survey Parameters	**Model**
Line	**Profile (a)**
Number of electrodes	53
Electrode spacing (m)	2.5
Number of nodes	4
Number of apparent resistivity levels	16
Array	dipole-dipole
Model resistivity(ies))	**Values (Ohm.m)**
Weathered layer:	1600
Dolomite layer	1200
Bedrock	2200
Sinkhole fill	80
Survey Parameters	**Model**
Line	**Profile (b)**
Number of electrodes	53
Electrode spacing (m)	2.5
Number of nodes	4
Number of apparent resistivity levels	16
Array	dipole-dipole
Model resistivity(ies))	**Values (Ohm.m)**
Weathered layer:	1000
Dolomite layer	1200
Bedrock	1800
Sinkhole fill	10
Survey Parameters	**Model**
Line	**Profile (c)**
Number of electrodes	53
Electrode spacing (m)	2.5
Number of nodes	4
Number of apparent resistivity levels	16
Array	dipole-dipole
Model resistivity(ies))	**Values (Ohm.m)**
Weathered layer:	1600
Dolomite layer	1200
Bedrock	2200
Sinkhole fill	600

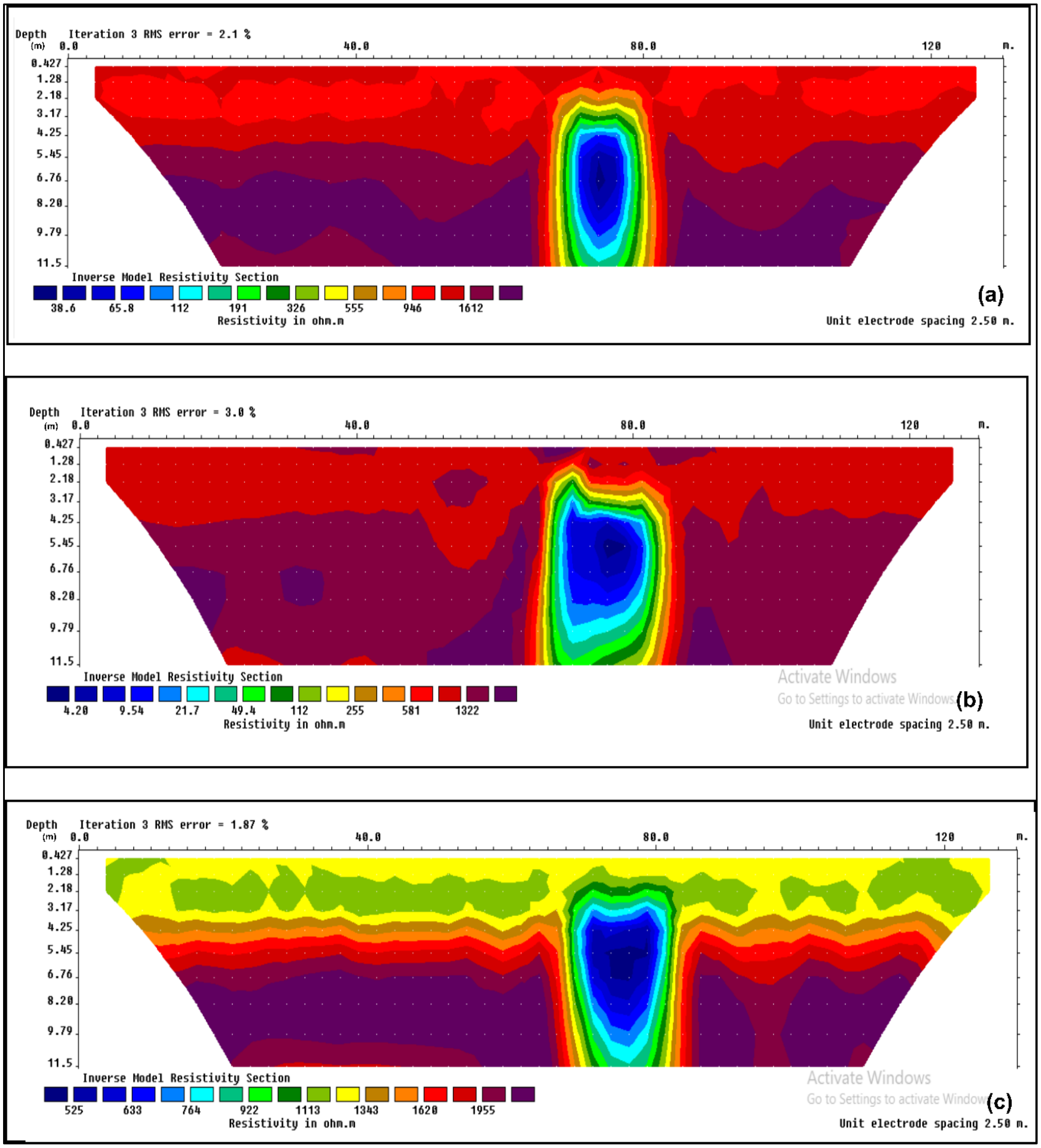

Figure 5.2: Three electrical resistivity forward models created for the R21 sinkhole, filled with water (a), collapse material mixed with air (b), and collapse material (c).

5.3 Seismic Forward Modelling

Different geological models were designed to assist with the design of the seismic survey. Ray-tracing and, in particular, finite-difference numerical modeling enables accurate simulation of the wavefield in different geological conditions. Forward modelling enables the construction of geological cross-section models on the computer that incorporate various rock characteristics and structural complexity levels. Additional data integration options are offered at interactive model building (Tesseral Pro, 2021).

Typically, seismic reflection data are collected from the responses of the seismic wave. It is possible to examine seismic wave propagation through a subsurface body using forward modeling or actual seismic acquisition (Majdi *et al.*, 2021). According to Nanda (2021), reflection events are the most important phenomenon in subsurface imaging. When it comes to seismic processing and imaging, seismic images are related to several attributes such as amplitude, phase, and frequency. These components can be used to deduce some physical attributes, like density and velocity, according to discussions by Bording *et al*. (1987) and Lines and Newrick (2004). Seismic forward modeling is the process of simulating mathematical algorithms using a geological model of the Earth (for example, in the form of density or velocity). With the use of this method, geoscientists may investigate and roughly predict how seismic waves move via a subsurface model.

The Tesseral Pro program, created by Tesseral Technologies ("Tesseral Pro, 2021") is used to design the 2D synthetic model seen in Figure 5.3. The model has a 1200 m overall length and a 1000 m depth. Each layer is configured to have a different velocity value and to reflect a different aspect of the Malmani Subgroup subsurface. The first layer consists of the weathered dolomite with a P-wave velocity of 2000 m/s; the second layer is the bedrock layer with a P-wave velocity of 4500 m/s (Table 5.4). Generally, a wave will move slowly through a medium with low density and quickly through a medium with high density (Majdi *et al*., 2021). As waves move from a less dense to a denser medium, they will also be reflected. Additionally, faster velocity generally suggests that the rock has higher density values.

Table 5.3: The P-wave velocity values and density values used on the R21 geological model.

Rock type	**P-wave velocity (m/s)**	**Density (kg/m^3)**
Weathered dolomite	2000	2000
Bedrock	4500	2600

The densities and velocities of the lithostratigraphy from the geology of the Malmani Subgroup were used to calculate the acoustic impedance of the R21 sinkhole. The acquisition geometry of the R21 sinkhole geological model has 125 shots, with 125 receivers, spaced at 10 m. The 2D acoustic finite-difference modelling was carried out using a 60 Hz Ricker wavelet omnidirectional source, with all receivers active on Tesseral Pro software, the rest of the parameters used to create this model are shown in Table 5.4. A sampling rate of 2 ms and 60 Hz Ricker wavelet were used to compute the 2D-synthetic model. Figure 5.3 shows the 2D synthesis of the R21 sinkhole. The R21 sinkhole geological model is 1.2 km long, trending south-north with a maximum depth of approximately 1 km. The model shows several seismic events detected in the shot gathers, including strong reflections and diffractions associated with sinkhole edges and lithological boundaries (Figure 5.4 and Figure 5.5).

Table 5.4: Parameters applied to the seismic acquisition simulation in Tesseral Pro software.

Acquisition Scheme	**Fixed receiver position**
Source frequency	60 Hz
Wavelet	Ricker
Number of shots	125
Shot interval	10 m
Number of receivers	125
Receiver interval	10 m
Sampling rate	2 ms
Recoding length	500 ms

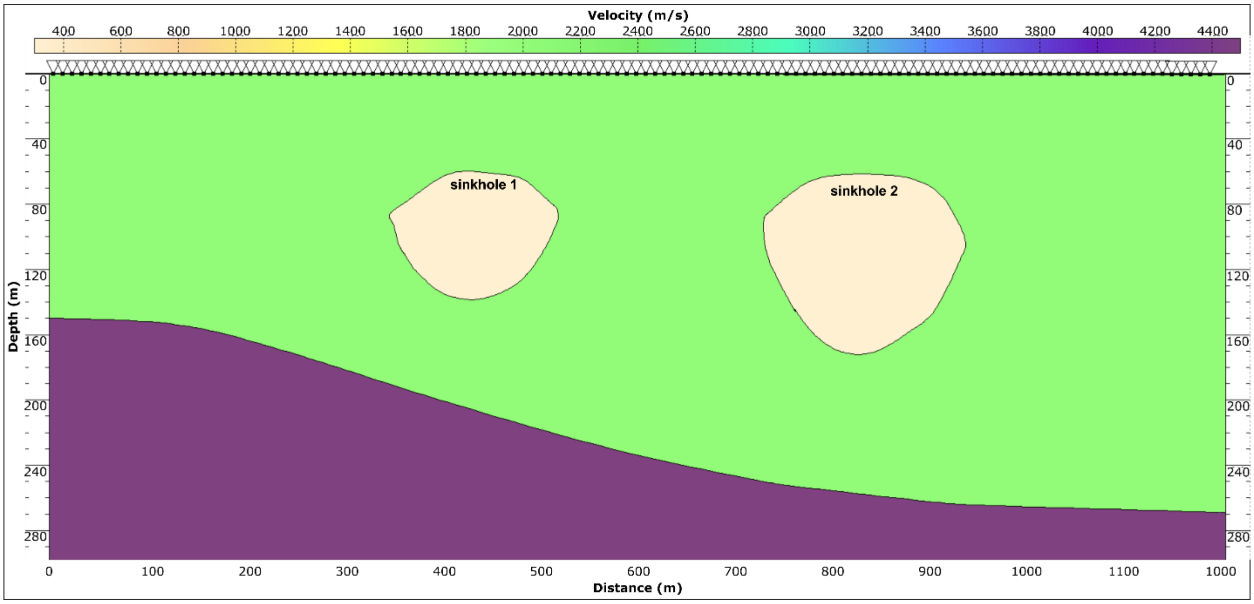

Figure 5.3: Image showing the geological models used for 2D acoustic numerical, viewed in Tesseral Pro software.

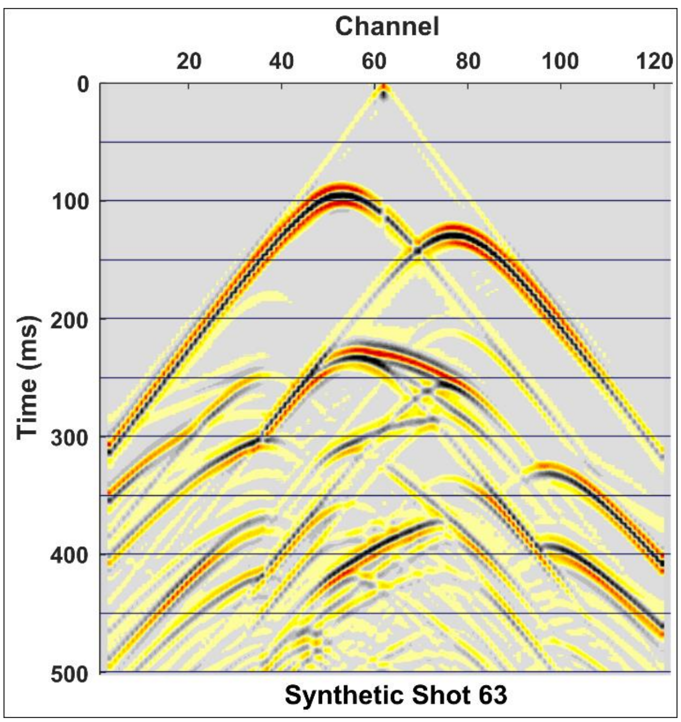

Figure 5.4: Image showing an example of the synthetic shot gathers from 2D acoustic modeling.

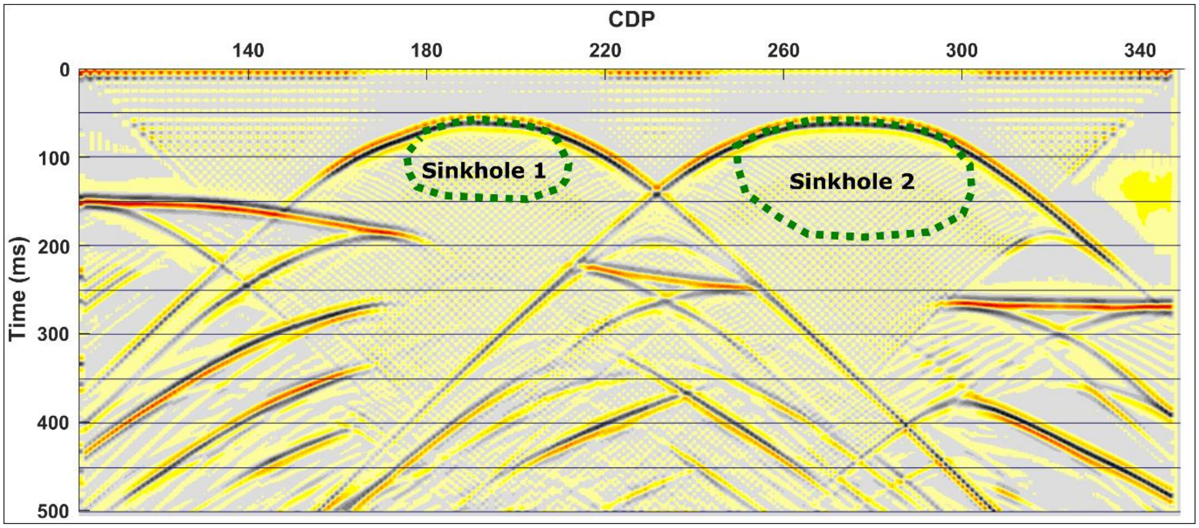

Figure 5.5: Stacked seismic section showing strong reflections and diffractions.

6 STUDY AREA AND METHODOLOGY

6.1 Location of Study Area

The study area is in the small town of Olifantsfontein, also known as Clayville, in Ekurhuleni, Gauteng province. The town gets the name Clayville, because of the underlying bedrock made up of carbonaceous shale, dolomite, and chert from the Chuniespoort Group. It is for this reason that we find numerous mining companies, such as Technicrete, Sterkfontein Bricks, Victoria Bricks, Corobrik, and Afrimat, that all have quarries that extract this clay material for bricks, cement, erosion protection blocks, and pave manufacturers.

The study area is located along the R21 highway and has the following co-ordinates: latitudes 25º 56’ 51.9” S and longitudes 28º15' 27.53” E. The research area is bordered by a Technicrete quarry to the immediate west, a Victoria Bricks quarry to the north-east, and a Sterkfontein Bricks quarry to the north-west (Figure 6.1).

Figure 6.1: A top view image showing the location of the study area. It shows the location of the R21 sinkhole with some of the brick companies and quarries close to the study area, Google Earth.

Between February and April 2022, a sinkhole (here termed R21 sinkhole) with ~ 15 m diameter (as observed on the surface) closed off two northbound lanes of the R21 highway, allowing traffic to flow only on the other two lanes in that stretch of the road. It is worth mentioning that the study area also has much older sinkholes just to the west of the site, near the Technicrete quarry (Figure 6.1). These sinkholes (shown in red) formed as far back as August 2016, proving that this site is prone to formation. The R21 sinkhole formed on one of the busiest national routes or freeways and is very important to commuters in South Africa, especially those traveling from or returning from Africa's busiest airport, O.R. Tambo International. Figure 6.2 (a) shows the study area and the location of the sinkhole along the R21 highway, while Figure 6.2 (b) shows the zoomed-in image of the highway with the sinkhole, shown by the dashed green line.

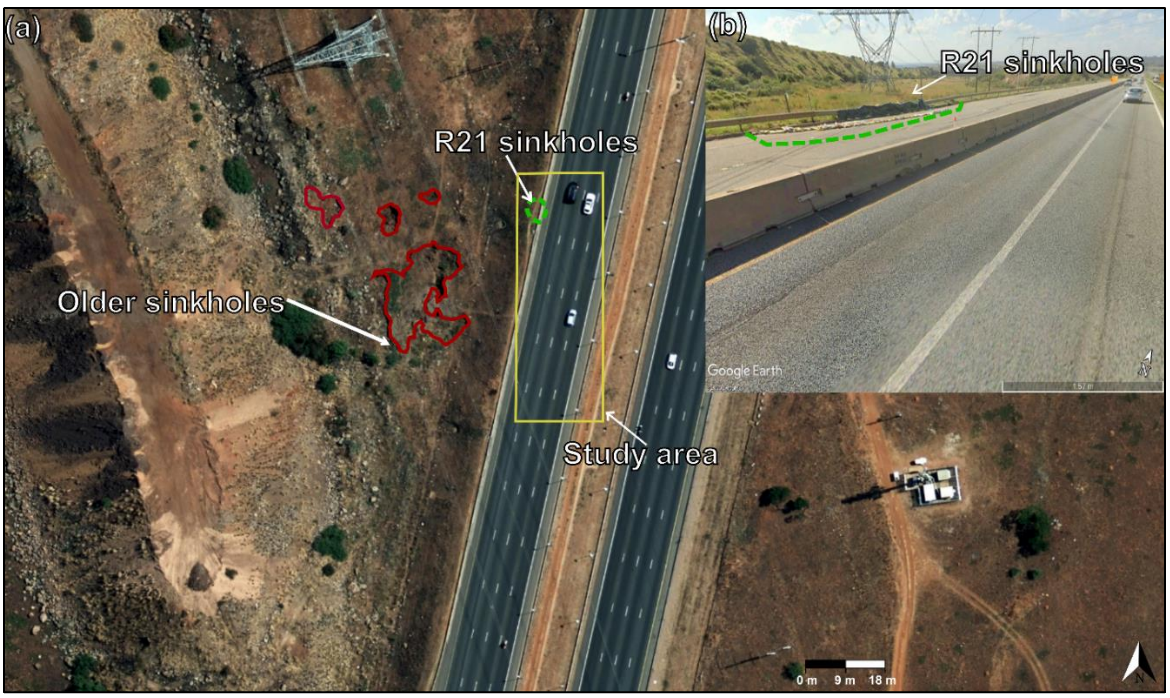

Figure 6.2: (a) Study area showing older sinkholes, shown in red, next to the site; (b) Zoomed-in location of the R21 highway and the sinkhole, shown by the green dashed lines, Google Earth.

6.2 Data Acquisition and Processing

A geophysical investigation was conducted along the R21 Northbound near Olifantsfontein on the 13th of Mach 2022. There are several active quarries near the site, with the nearest one being only a few hundred meters, to the northwest of the site. There have been several sinkholes closer to the site, dating as far back as August 2016, which can be observed by analysing Google Earth images (Figure 6.3). Figure 6.4 shows one of the older sinkholes, about the R21 sinkhole.

The collaboration between geology and geophysics researchers from the School of Geosciences and colleagues from the Council for Geoscience allowed for a comprehensive study of the study area. The integration of ERT, seismic surveys, MASW, and GPR methods likely provided valuable insights into the subsurface conditions, including potential sinkhole or subsidence hazards.

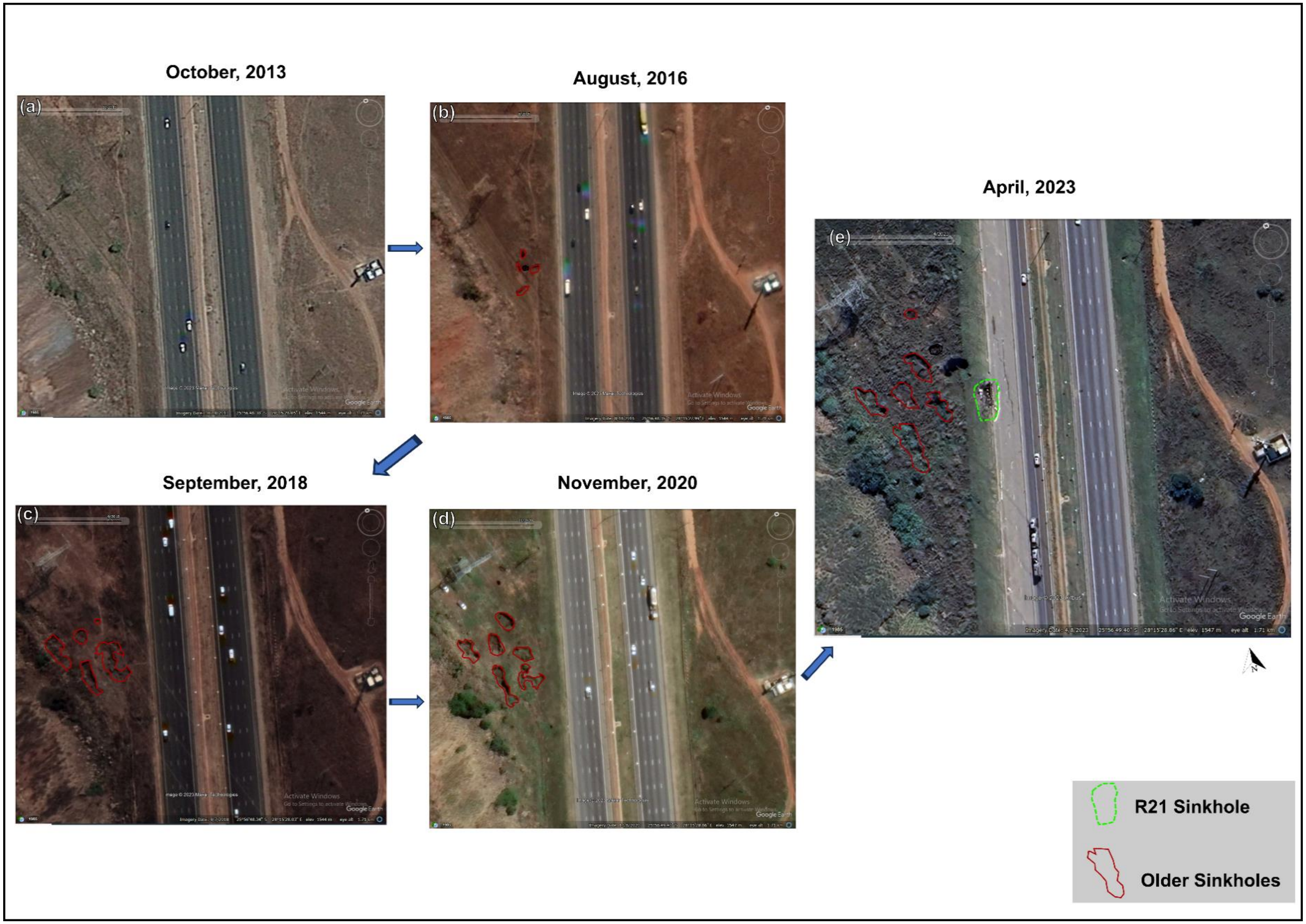

Figure 6.3: The progression of the sinkholes along the R21 highway. The older sinkholes, started appearing on surface in 2016 and continued to appear until the one on the R21 highway, Google Earth.

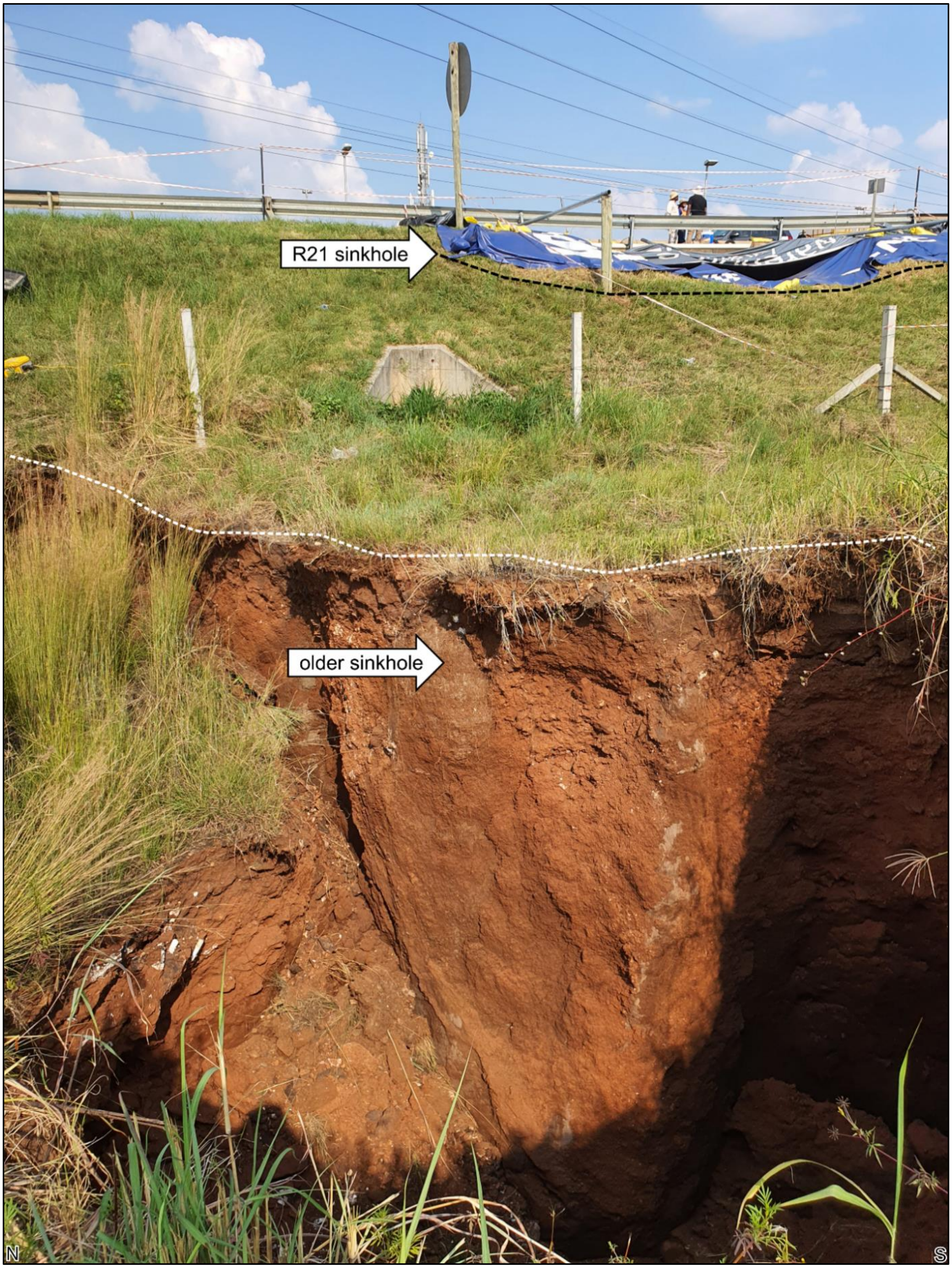

Figure 6.4: Image showing one of the older sinkholes with dashed white line, in relation to the R21 sinkhole shown in black dashed lines.

6.3 Electrical Resistivity Tomography (ERT)

6.3.1 Acquisition

Six (6) dipole-dipole ERT profiles were conducted over the site. The survey was conducted on the 13th of March 2022. Six south-north trending profiles were completed over a day with an electrode spacing of 2.5 m (Figure 6.6) for three profiles and 5 m spacing for the other three. Table 6.1 shows the parameters for all the ERT profiles.

Table 6.1: Resistivity acquisition table, with all the lines from the study area.

	Line 1	**Line 2**	**Line 3**	**Line 4**	**Line 5**	**Line 6**
Profile length (m)	130	130	130	350	260	260
Electrode spacing (m)	2.5			5		
Configuration	Dipole-dipole					

A tape measure is stretched along the planned survey area and the electrodes are inserted into the ground along a length of tape measure. The ERT profiles are shown in Figure 6.5 in relation to the Google Earth imagery. Holes needed to be drilled using a driller before inserting the electrode into the tarred surface. This was to ensure maximum contact with the subsurface as poor soil contact will result in measurement errors. These metal electrodes were pushed into the tar and soil to depths of about 5-10 cm, for example, line 1 with metal electrodes of a 2.5 m spacing on the R21 tarred surface is shown in Figure 6.6.

Furthermore, it's ideal if the electrodes can penetrate deeply enough to touch wet or moist ground (Bevan, 1998). Pouring water around each electrode may increase measurement accuracy in extremely dry soil (Bevan, 1998). Two lines (L5 and L6), out of the six ERT lines were conducted away from the R21 sinkhole, close to the south bound lanes (Figure 6.5). This was done to determine whether the sinkhole does not extend to the south bound lanes.

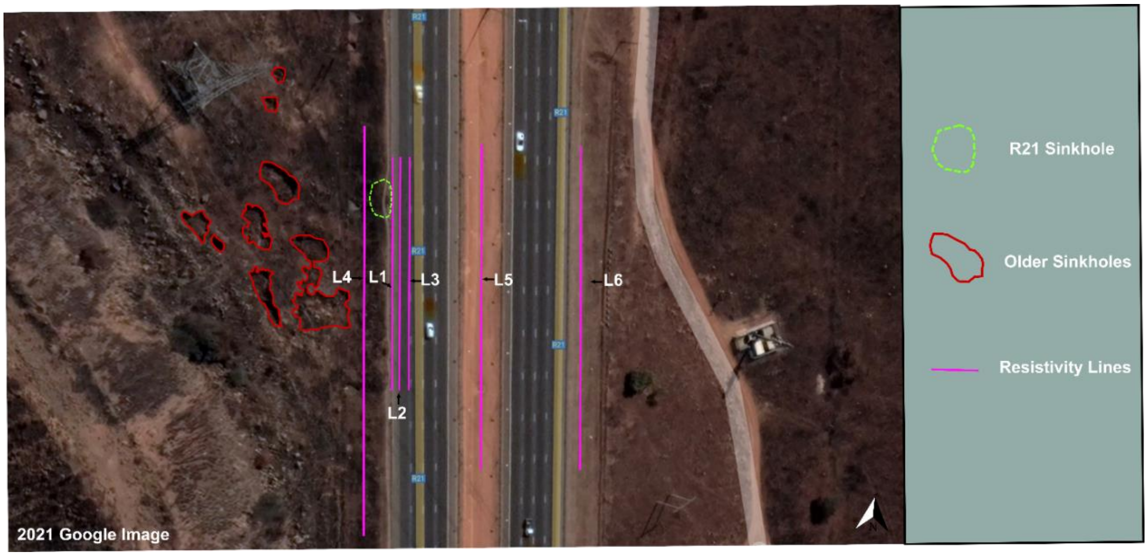

Figure 6.5: Relative locations of the ERT surveyed profiles, shown in pink lines. Red lines represent the older sinkholes found in the site, while green represents the R21 sinkhole.

Figure 6.6: The profile of line 1 with metal electrodes of a 2.5 m spacing on the R21 tarred surface.

6.3.2 Data Processing

A subsurface 2D image can be obtained using the inversion method (Loke and Barker, 1995). This is done by comparing the model response to the measured data (Lindgren, 2014). RES2DINV is a software package that uses information from ERT surveys to create a 2D resistivity model for the subsurface (Geotomo Software, 2003). Figure 6.7 shows a possible electrode layout and measurement flow for a 2D ERT survey.

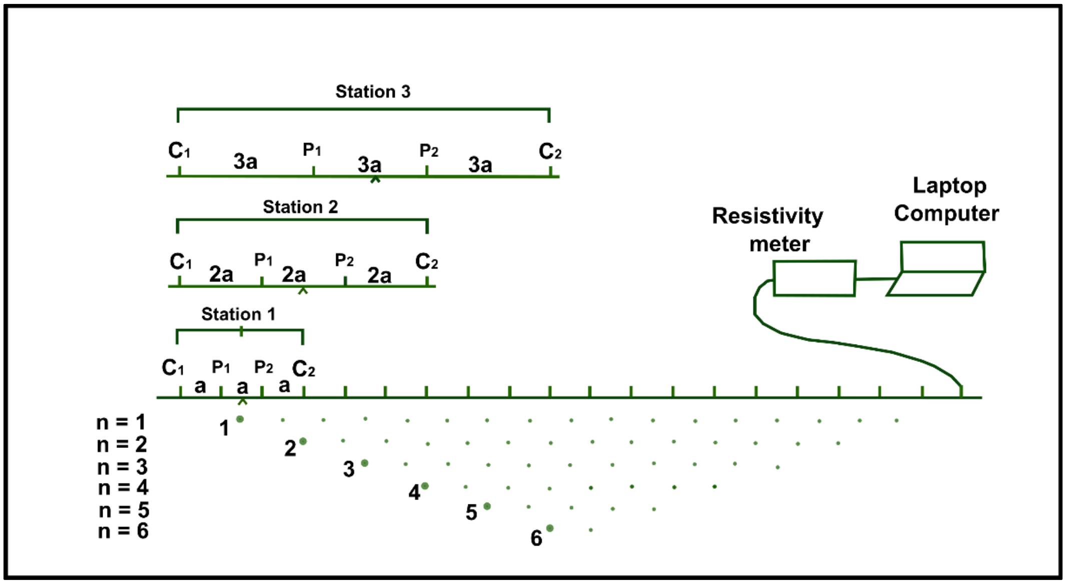

Figure 6.7: Sequence of measurements to create a pseudosection in a multi-electrode survey (Geotomo Software, 2003).

The measured data in this study were modelled using the Res2Dinv (Loke, 2013a) program. Using a grid of rectangular blocks with uniform resistivity, the traditional approach is to utilise an iterative non-linear optimisation method to calculate the blocks' resistivity (de Groot-Hedlin and Constable, 1990; Loke and Barker, 1995; Olayinka and Yaramanci, 2000; Lindgren, 2014).

Data Processing Steps

There are two primary processes in ERT data processing. The first step is to analyse the data sets and remove unrealistic or bad data points (Figures 6.8 and 6.11). The second step includes the running of inversion iterations (Figure 6.12). The inversion creates a 2D resistivity image of the subsurface by several repeated calculations. An image of the subsurface's resistivity in two dimensions that depicts how the resistivity is distributed along a profile is the inversion's ultimate output. Also available is a pseudo section that displays the distribution of apparent resistivity values (Figure 6.13).

The discrepancy between the measured and calculated resistivity values is quantified using the root-mean-squared (RMS) error. The quality of the data improves with decreasing errors (Alsulaimaini, 2017). Loke (1999) suggested that a good model should have an RMS error of 5%. To start the processing of data, RES2DINV is opened, and the file with an extension of .DAT is read.

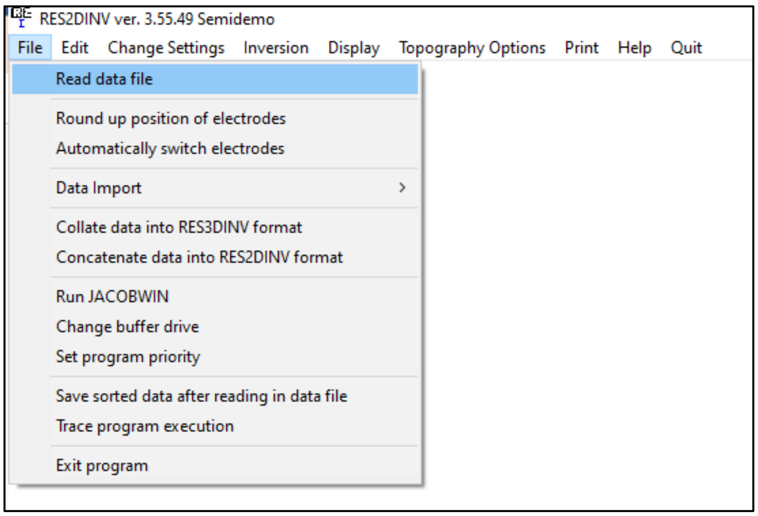

Figure 6.8: Image of the first step of the RES2DINV processing step, where the data is read and analysed.

Similar to other geophysical data methods, bad data points exist in ERT data. Bad data are removed from the database before any processing of the data. Line 5 in Figure 6.10 shows an example where bad data points were removed. To do this option, the following was selected from the submenu.

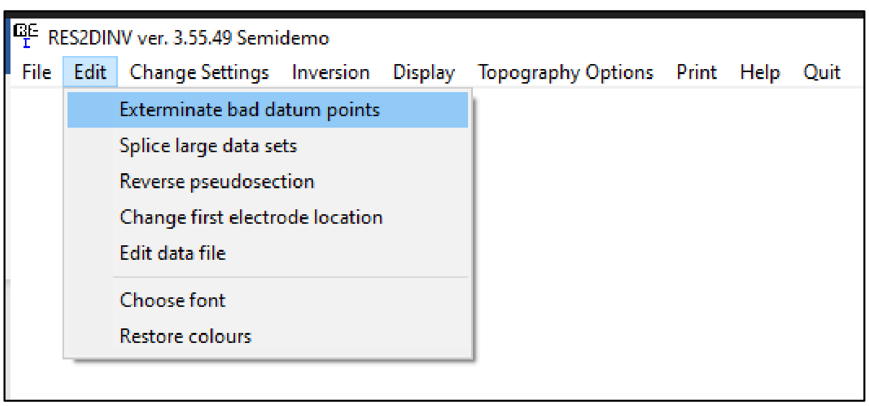

Figure 6.9: Processing steps to remove all the bad points for the line 5 acquired data.

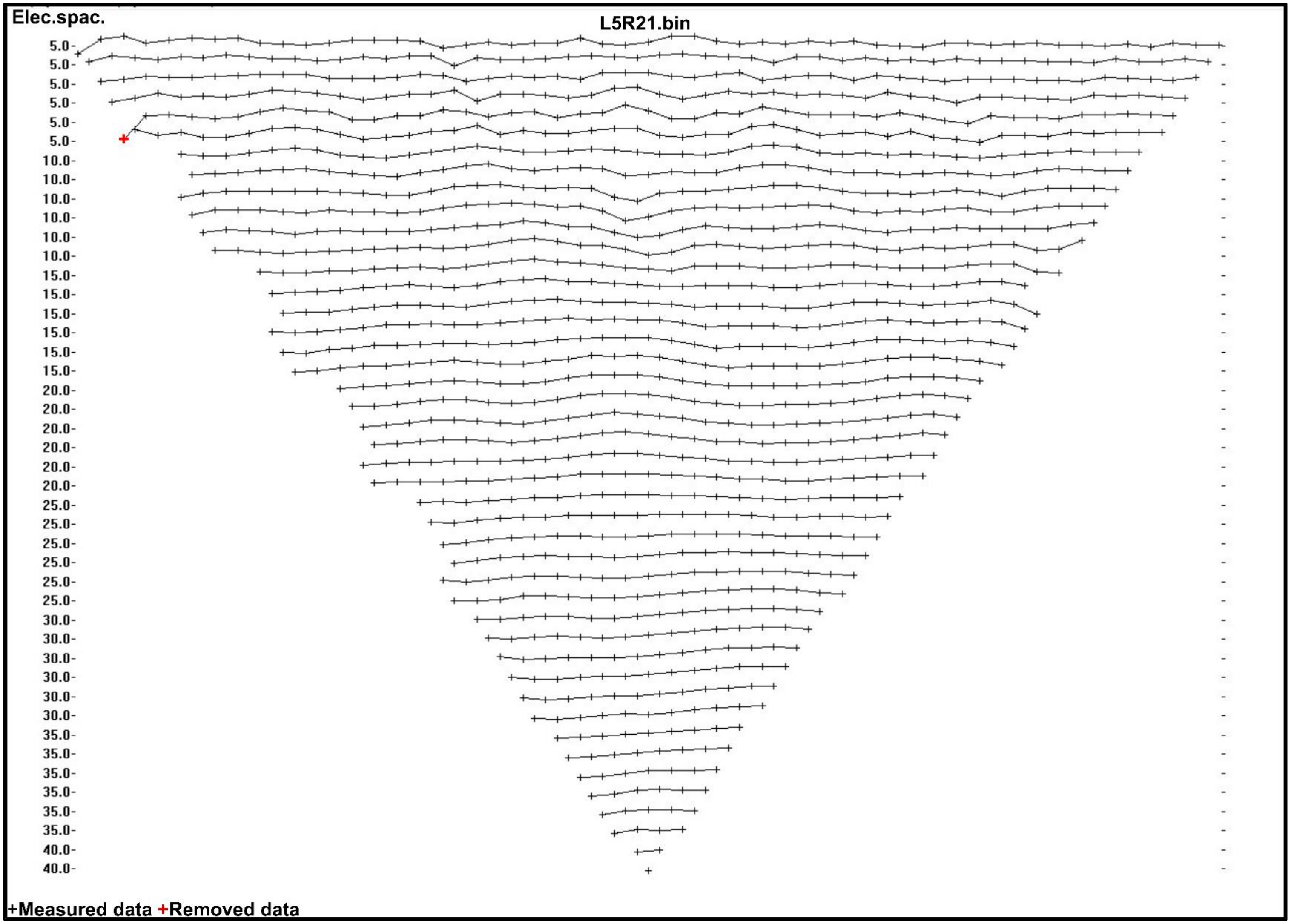

Figure 6.10: An example of line 5 field data set, with all the measured bad data points, shown in red. The apparent resistivity data in profile form.

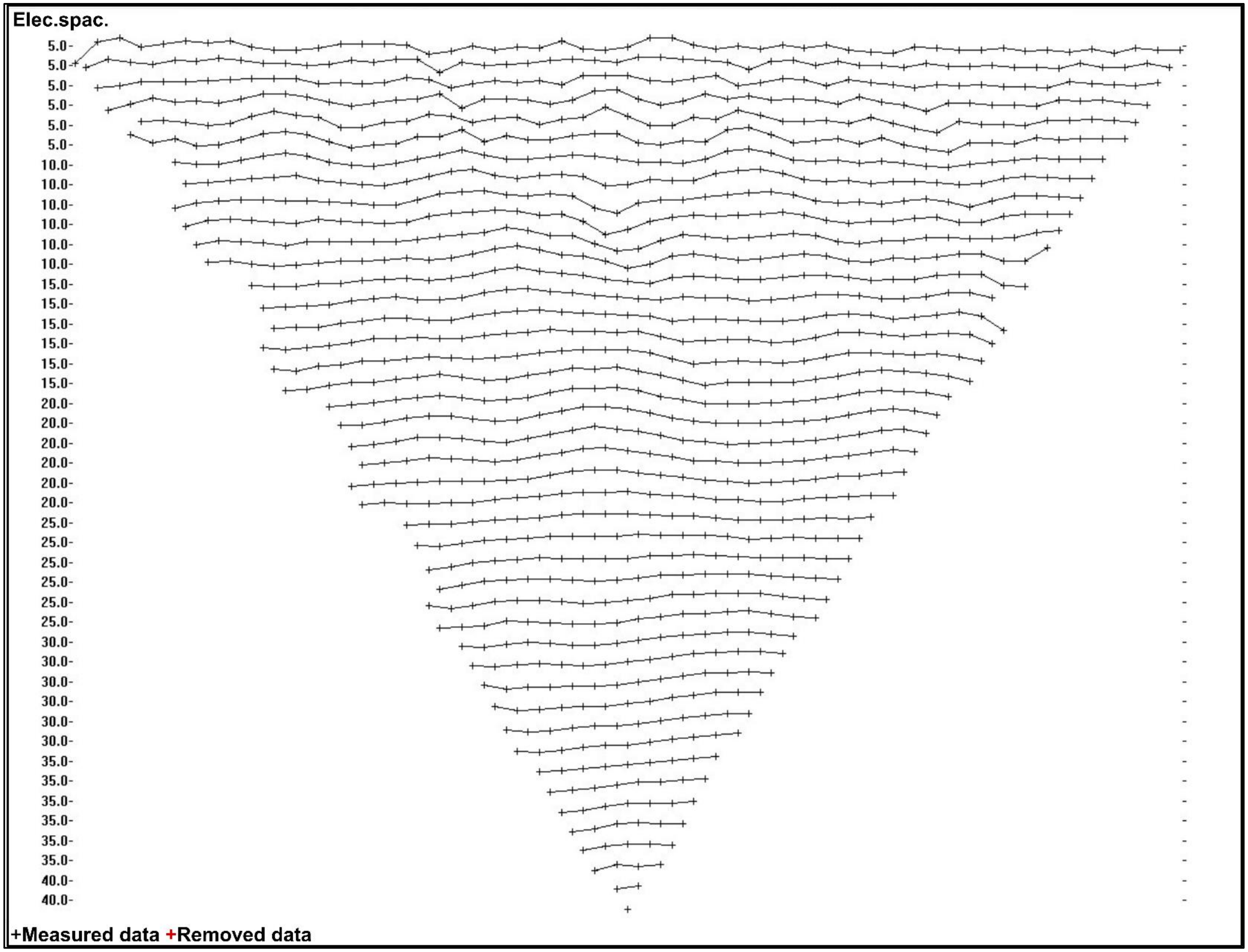

Figure 6.11: Final image of the processed and edited data.

The damping factor in geophysical inversion refers to how much the resistivity is allowed to vary during the inversion process. Below a breakdown of what different damping factor values signify:

- Damping Factor of 1.0: Allows for more variation in resistivity during inversion.
- Typical Range (1.5 to 2.5): Balances data fit and resistivity variation.
- High Damping Factor (e.g., 100): Resists variation, emphasising prior information or initial models.

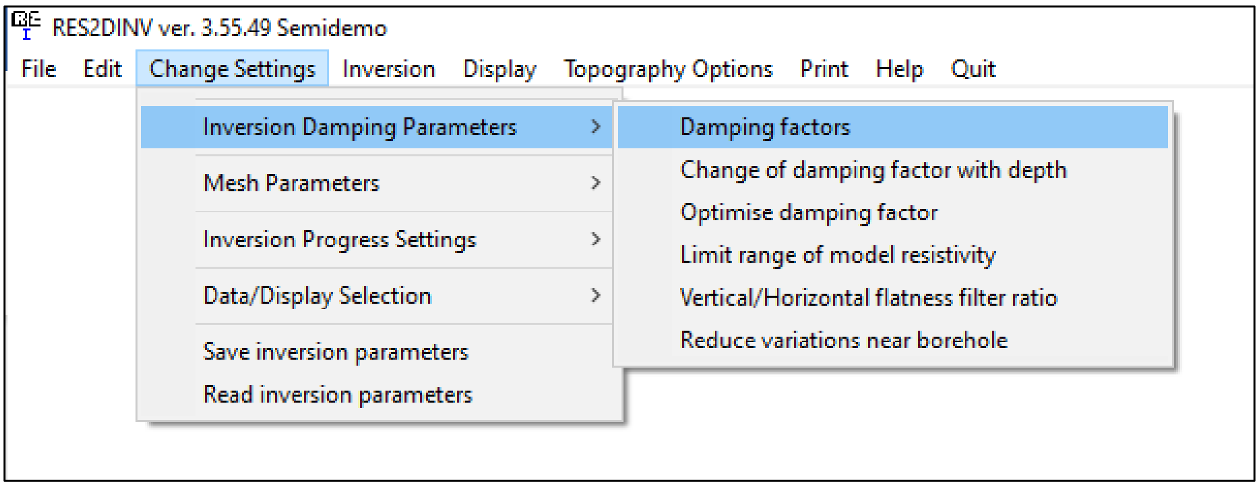

Figure 6.12: Processing steps used when applying the damping factor.

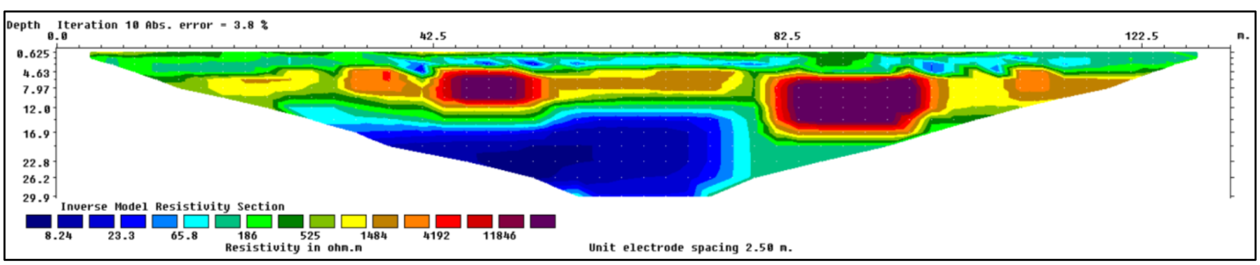

Figure 6.13: The apparent resistivity of the processed data of line 5 in pseudo-section form.

6.4 Ground-Penetrating Radar (GPR)

6.4.1 Data Acquisition

A total of 35 GPR profiles were surveyed along the R21 highway. These profiles were divided into three groups to make working with the data easier. Group R21SINK001 has five 140 m south-north trending lines. Group R21SINK002 has three south-to-north trending lines (90 m long) and two east-to-west trending lines (20 m long) closer to the sinkhole perimeter. The last group, R21SINK003, has 25 east to west trending lines (9 m long) (Figure 6.14).

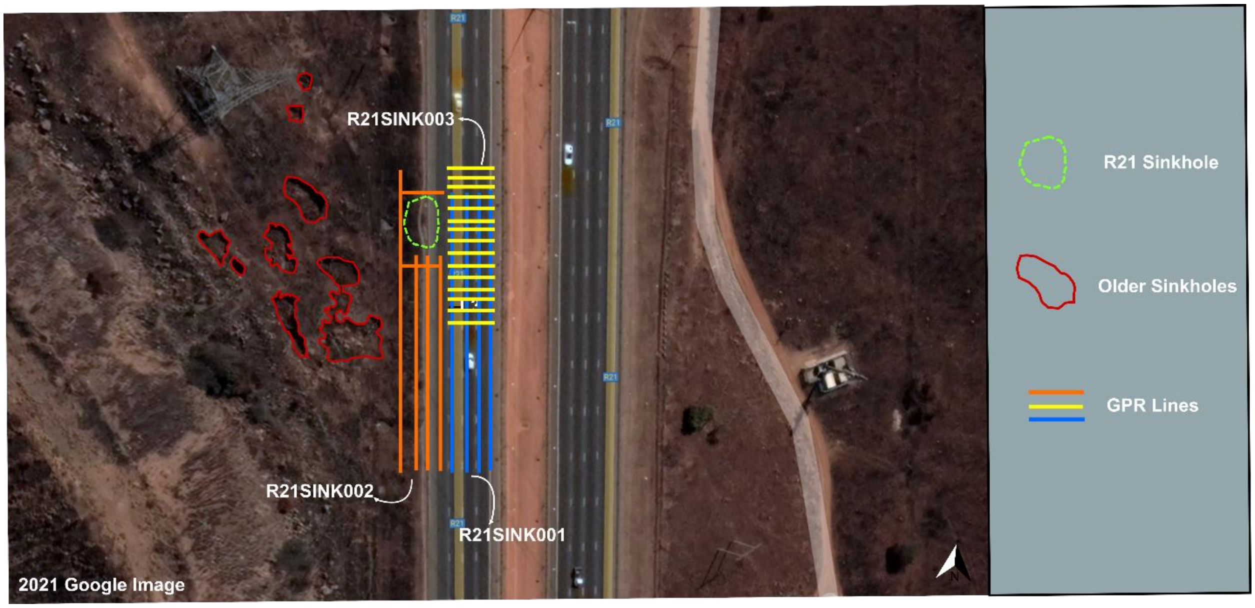

Figure 6.14: Ground penetrating radar profiles, shown in different coloured group as how they were acquired in the field. Group R21SINK001 is shown in blue, group R21SINK002 is shown in orange, and group R21SINK003 is shown in yellow. The green circle represents the R21 sinkhole.

The GSSI System with a 400 MHz antenna was used to acquire data. Typically, a GPR system includes a data-gathering device, transmitting antennas, and receiving antennas (Bostanudin, 2013). As the GPR machine moves along the profile, the detecting signal will change as soon as there are any changes in the subsurface (Liang *et al*., 2022). It is therefore important that the lines be strategically placed to ensure data quality and detection effectiveness. It is important to keep a constant horizontal scale for the radar profiles as it makes it easier to interpret and accurately locate the targets (Bevan, 1998).

The GPR system consists of several key elements, as depicted in Figure 6.15. The control unit manages the timing and recording of these signals, while the display unit allows the user to visualise and interpret the data in real-time. The survey cart or sled facilitates the movement of the antennas across the survey area, and the battery pack provides the necessary power for operation. The antenna housing contains the electronics and antennas essential for transmitting and receiving radar signals.

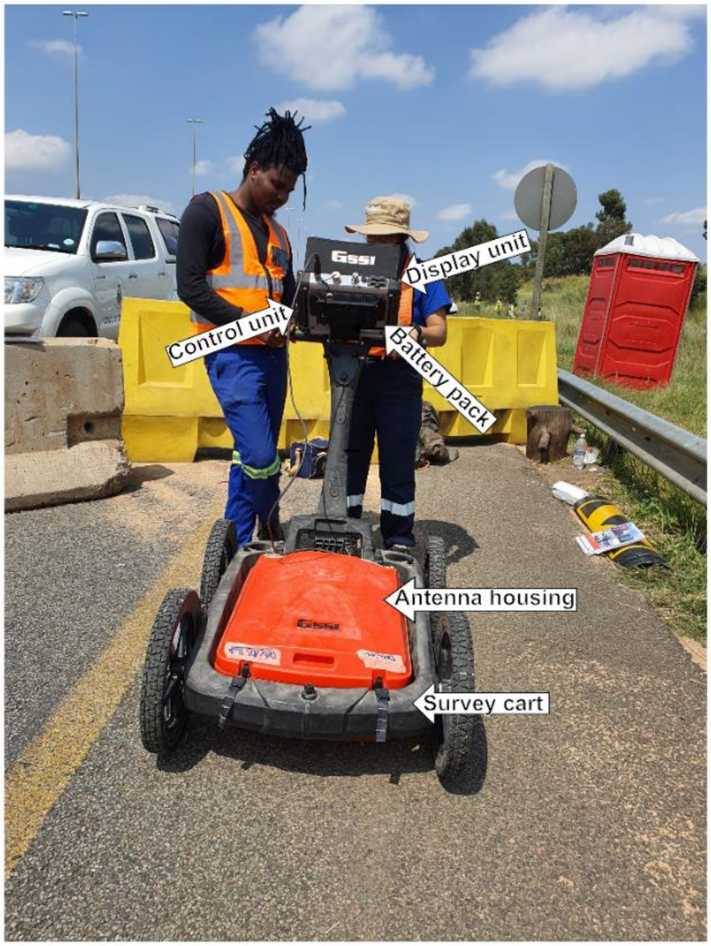

Figure 6.15: GSSI Utility scan PRO SIR 4000 GPR system used in the R21 sinkhole survey.

6.4.2 Ground Penetrating Radar Processing

Once the data has been acquired, data editing is the first stage of processing. The main objective of data processing is to present an image that can be understood as best as possible. Common GPR data exhibit noise and undesired reflections caused by several factors described by Shaaban *et al*. (2009). Editing data includes re-arranging data, creating new data files, updating data headers or background information, relocating the data, and adding elevation data (Annan, 1999).

Table 6.2 shows the steps used to process the data. The Reflexw software was used to import, edit, and process the raw SEG-Y data (Sandmeier, 2008). This is done within the 2D-data analysis module. The data processing steps mainly consisted of static correction, dewow, background removal, and time-depth conversion, which are essential for turning raw geophysical data into interpretable and actionable information. These steps ensure accuracy, reduce noise, and provide a clearer picture of the subsurface, aiding in geological interpretation.

Table 6.2: Ground Penetrating Radar acquisition parameters and processing steps.

Acquisition Item	Parameters		
Line No	R21SINK001	R21SINK002	R21SINK003
Line Length	5 Lines x 140 m	3 Lines x 90 m 2 Lines x 20 m	25 Lines x 9 m
Instrument	GSSI System with 400 MHz antenna		
Trace Spacing	0.02 m		
Survey Direction	W - E	W - E	S - N
Survey Pattern	Zigzag		
Dielectric Permittivity	6 F/m (on the pavement) and 9 F/m (on the grass)		
Some of the Processing Steps			
Energy Decay	0 – 200 ns time window		
Subtract-Mean (Dewow)	1 – 2 ns time window		
Subtracting Average/Background removal	10 – 20 average traces		
Diffraction Stack	Summation width (10 – 20 traces); velocity (0.1 – 0.2 ns)		
Bandpass Butterworth	Lower cut-off (150-220): Lower cut-off (400-600)		
Static Correction	-0.3ns - 0.5ns		

Main Processing Steps:

Background removal: Background removal involves subtracting each trace from the mean of all the traces in a section. It eliminates noise (multiples) and is effective against antenna ringing, linked with surface waves (Joll, 2009; Mendoza *et al*., 2023). This was done by subtracting the mean calculated from a sliding window of between 10-20 traces (Figure 6.16) (Daniels, 2004).

Static correction: Any information gathered while a GPR antenna is stationary is referred to as static data (Cook *et al*., 2022). The horizontal distance travelled is accurately calculated by removing the resulting static and irrelevant data, which also merges the scanned features into a continuous subsurface profile (Figure 6.17 (b)).

Moving start time: Moving the start time refers to the data being adjusted vertically to align time zero (T_0) with zero depth on the vertical axis (Cook *et al*., 2022). During the move start time filtering process, the direct waves are automatically deleted to accurately represent the ground surface (Figure 6.18 (b)). This improves the depth estimates.

Dewow: A low-frequency component can be seen in many GPR data sets, either because of inductive processes or potential limitations by the instruments used (Sandmeier, 2023). Before using any other digital filter techniques, this low-frequency band needs to be eliminated. Dewowing is an important processing step as it brings the data down to a mean zero level (Joll, 2009). This was done by running an average Dewow filter with a length of between 1-2 ns.

Bandpass filtering: Applying a band-pass filter could be an essential step for accurately viewing and interpreting a GPR signal. Fourier transform is used to isolate a specific area of the spectrum using bandpass filtering, which eliminates high- and low-frequency noise (Dojack, 2012).

Examples of the processing workflow and results are shown in Figures 6.16 to 6.24. The processing steps are only for profile R21SINK001_001, group one. For the other groups, only the table with the processing steps is shown (Tables 6.4 to 6.7), as well as the final images (Figures 6.25 to 6.28).

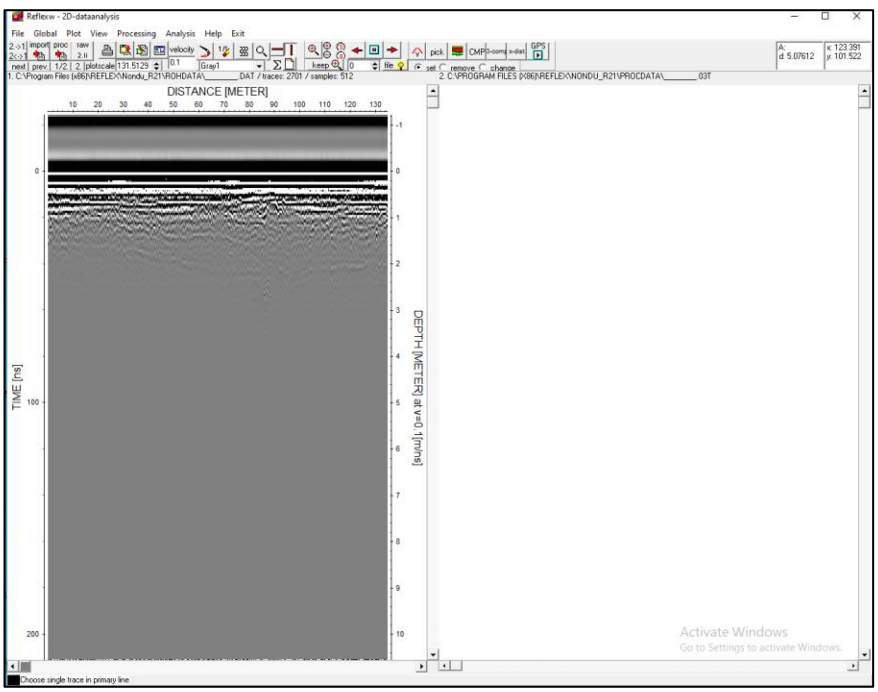

Figure 6.16: Raw data of line R21SINK001_001, 2701 trace line from group 1.

The processing parameters differed from one profile to another and from each group. But most of the processing steps remained the same, like the static correction, bandpass frequency, background removal, gain function and running average. In general, profiles within each group had the same filters applied to them.

Table 6.3: Processing steps applied in the R21 sinkhole, profile (R21SINK001_001) from group one.

Static correction/ Muting	Static correction
Static correction /Muting	Move start time
2D Filter	Background Removal
2D Filter	Running average
1D Filter	Substract-mean (dewow)
Gain	Gain function
1D filter	Bandpass butterworth

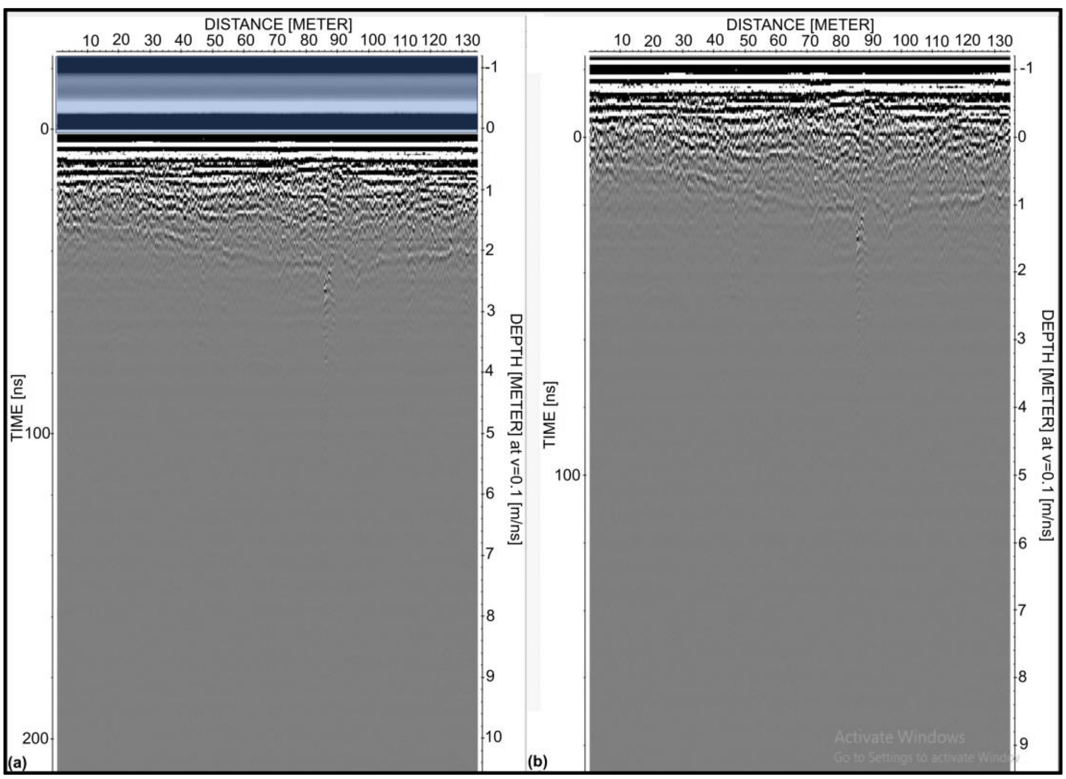

Figure 6.17: (a) The original unprocessed data of profile R21SINK001_001. Highlighted in blue is the static and irrelevant data that were removed once the static correction was applied. (b) GPR section after the application of the static correction.

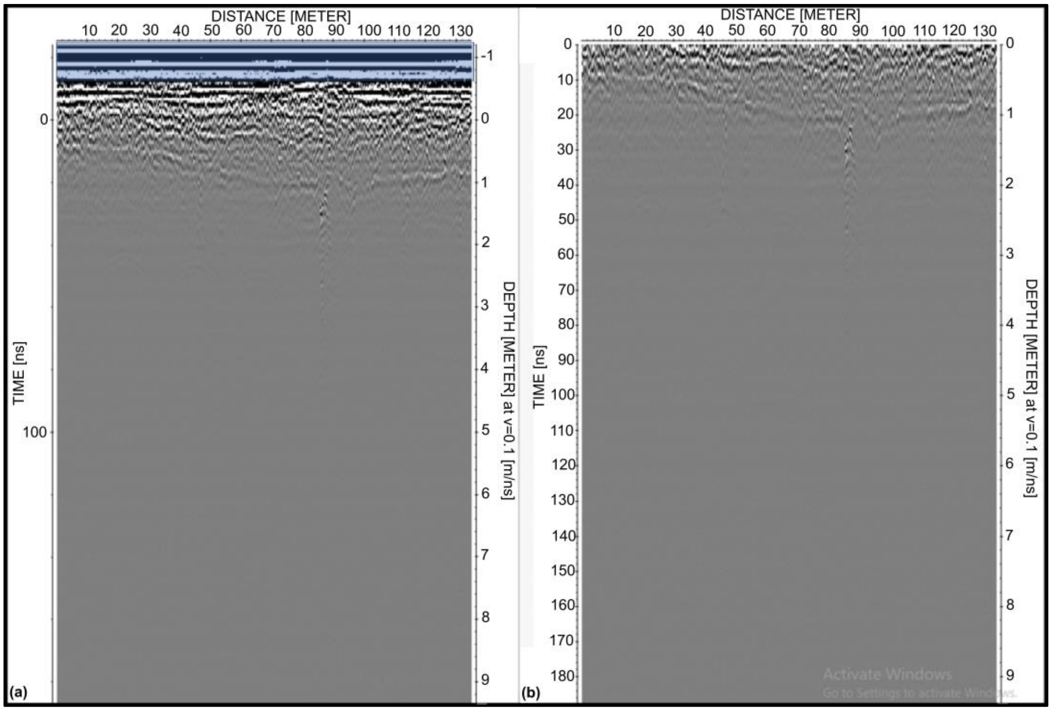

Figure 6.18: GPR section with static correction (a), highlighted in blue is data that had to be adjusted vertically to align zero depth on the vertical axis and (b) shows the result after applying the move start time filter.

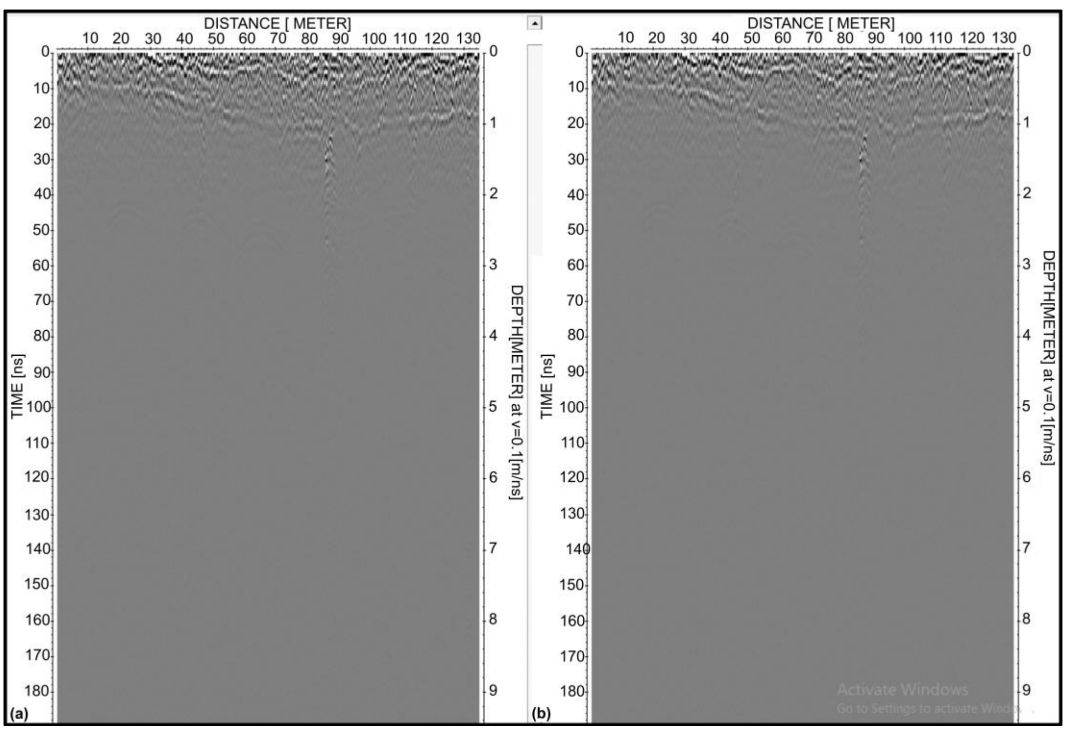

Figure 6.19: GPR section with start time filter on (a), and (b) shows the section after the removal of background noise.

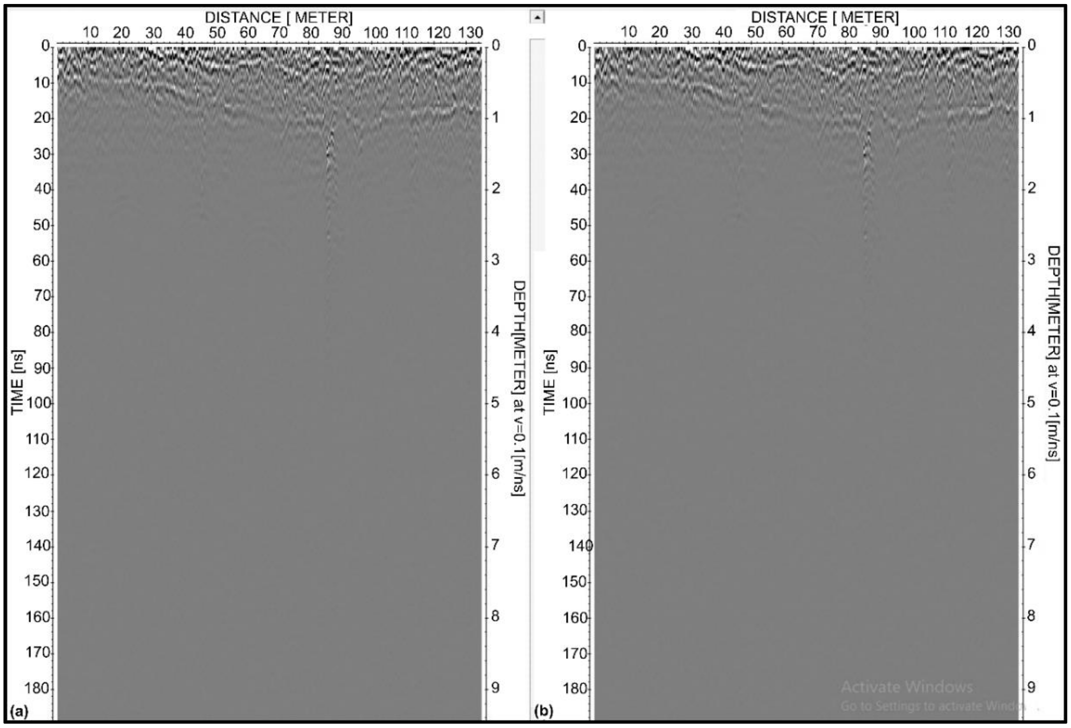

Figure 6.20: GPR section from the previous processing step showing background removal filter (a) and (b) shows the section after running average filter step is applied.

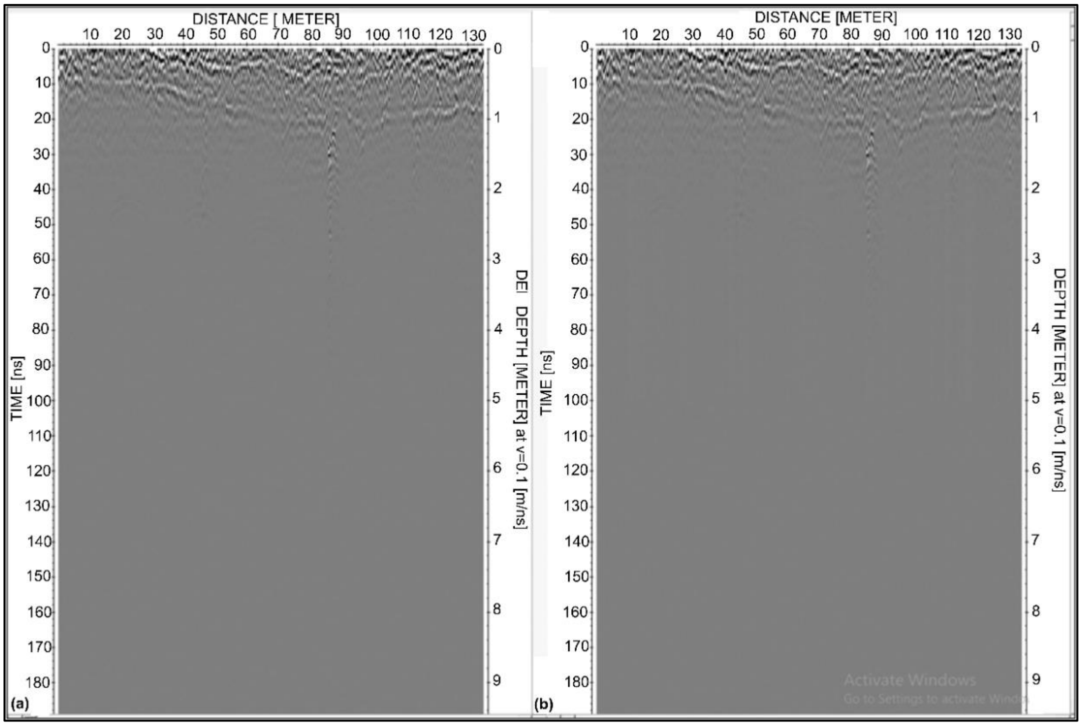

Figure 6.21: Image showing the running average filter, from the previous step (a) and (b) shows the section after the subtract-mean (dewow) filter step is applied.

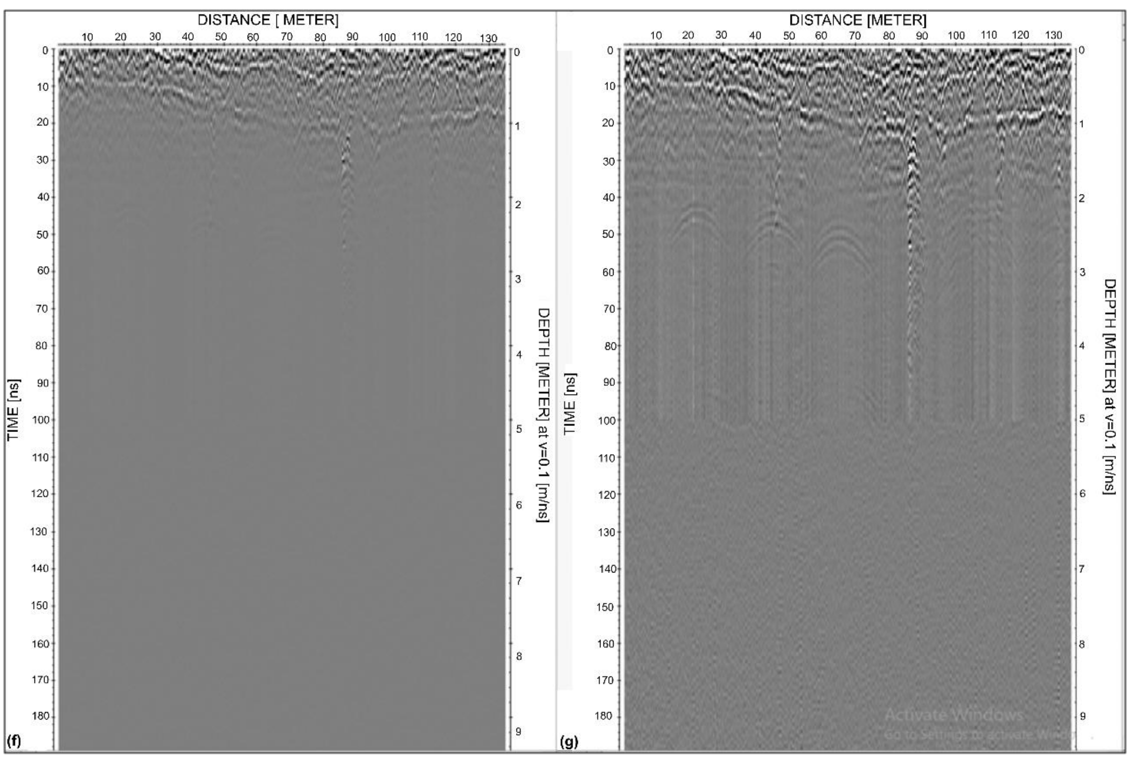

Figure 6.22: GPR section after the application of the subtract-mean (dewow) filter from the previous step (a) and (b) shows the section after the application of the gain function filter.

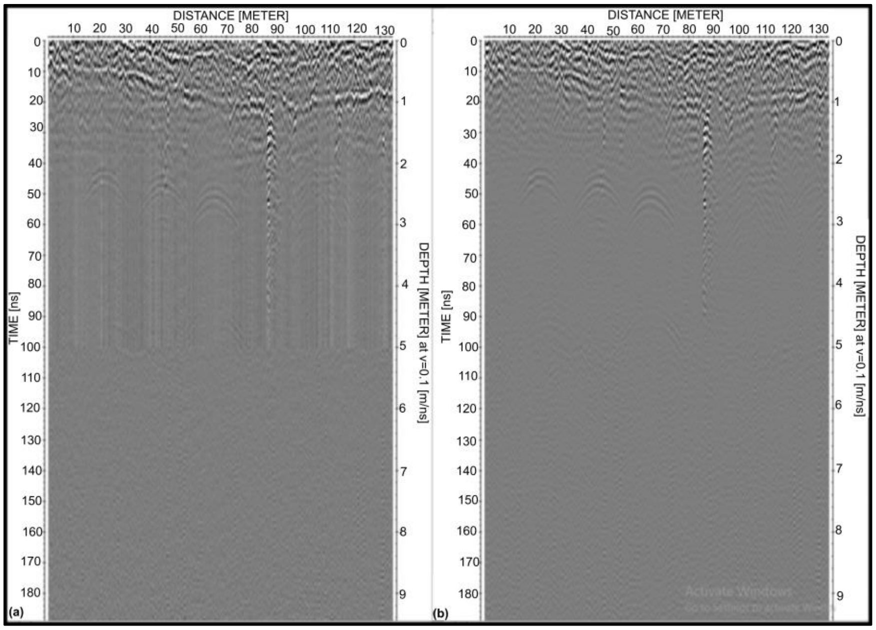

Figure 6.23: GPR section with gain function filter applied, from the previous step (a), and (b) shows the section after the application of the bandpass butterworth filter.

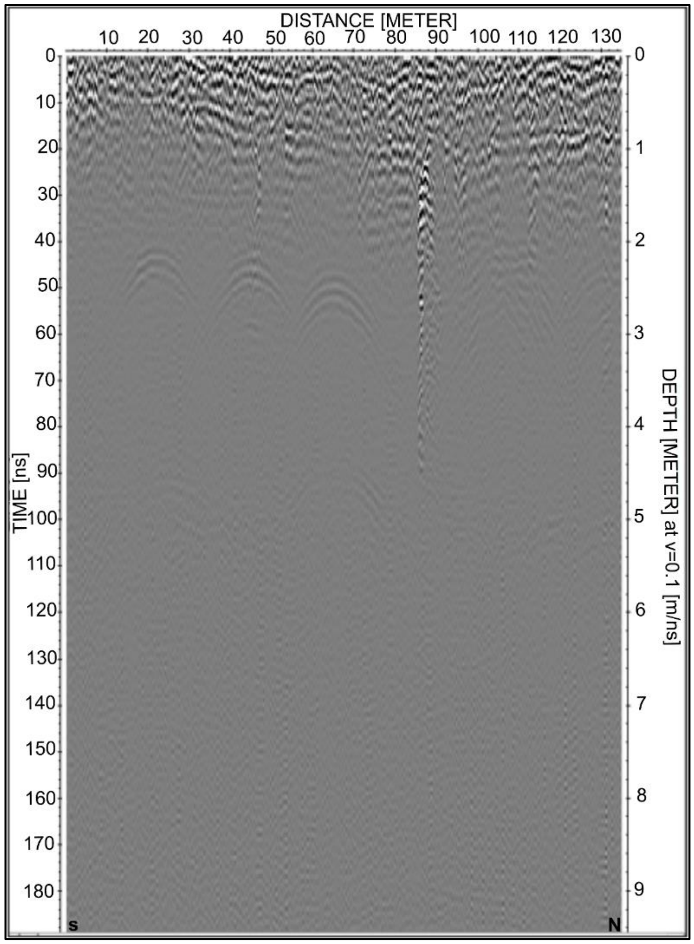

Figure 6.24: Final processed image of profile (R21SINK001_001) from group one.

Table 6.4: Processing steps applied in the R21 sinkhole, profile (R21SINK001_003) from group one GPR data.

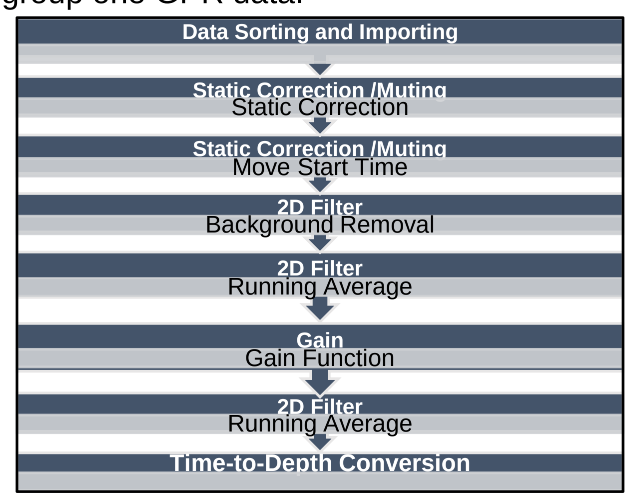

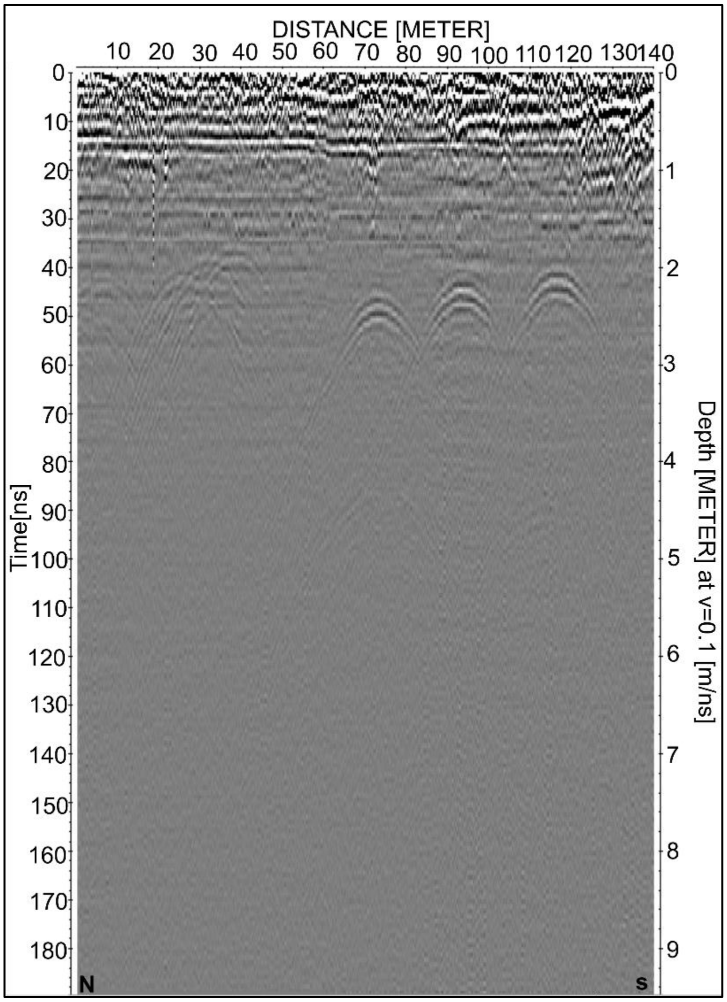

Figure 6.25: Final processed image of profile (R21SINK001_003) from group one.

Table 6.5: Processing steps applied in the R21 sinkhole, profile (R21SINK002_001) from group two GPR data.

Static correction/ Muting	Static correction
Static correction /Muting	Move start time
Gain	Gain functionl
1D Filter	Bandpass frequency
1D Filter	Substract-mean (dewow)
1D Filter	Background removal
2D Filter	Running average
1D Filter	Bandpass frequency

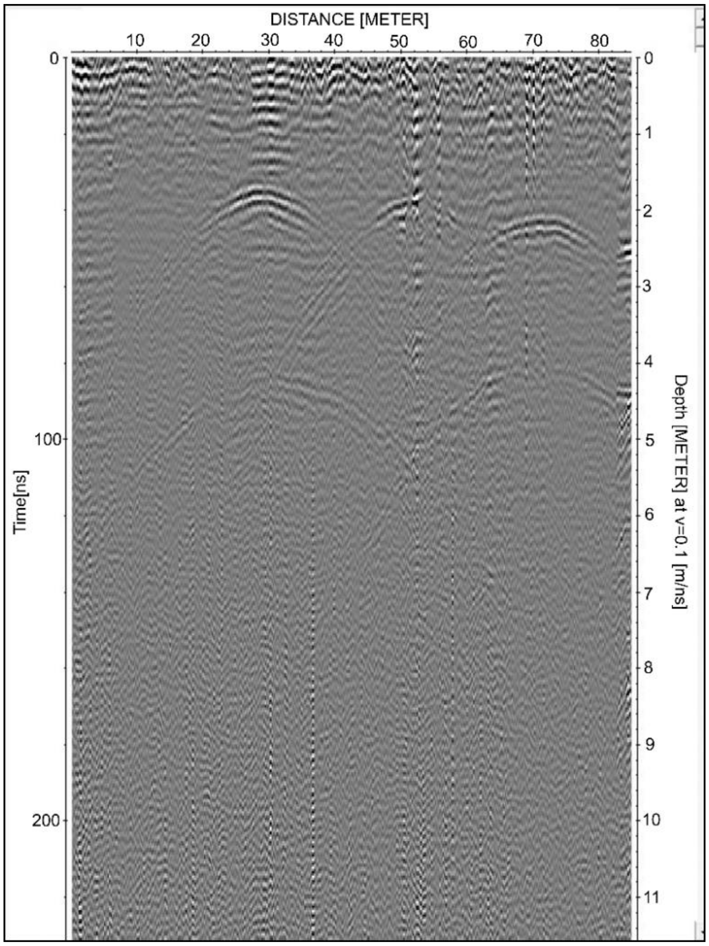

Figure 6.26: Final processed image of profile (R21SINK002_001) from group two.

Table 6.6: Processing steps applied in the R21 sinkhole, profile (R21SINK003_0015) from group three GPR data.

Static correction/ Muting	Static correction
Static correction /Muting	Move start time
1D Filter	Background removal
2D Filter	Running average
1D Filter	Substract-mean (dewow)
Gain	Gain function
1D Filter	Bandpass butterworth

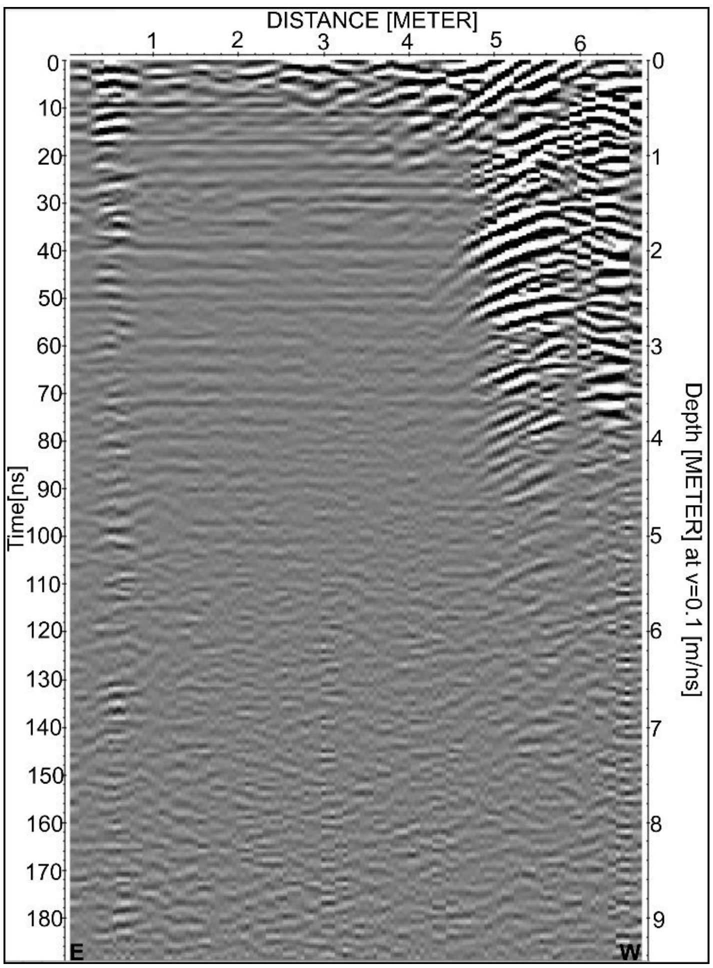

Figure 6.27: Final processed image of profile (R21SINK003_0015) from group three.

Table 6.7: Processing flow applied in the R21 sinkhole, profile (R21SINK003_001) from group three.

Step	Process
Static correction/ Muting	Static correction
Static correction /Muting	Move start time
2D Filter	Background Removal
1D Filter	Substract-mean (dewow)
Gain	Gain function
1D filter	Bandpass butterworth

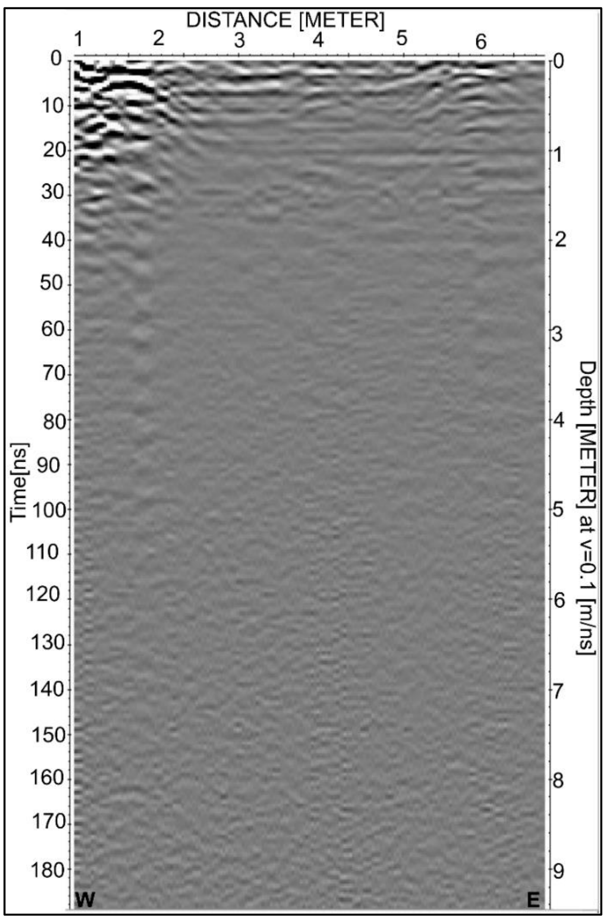

Figure 6.28: Final processed image of profile (R21SINK003_001) from group three.

6.5 Seismic Survey

Refraction Seismic Data Acquisition

Three south-north refraction seismic profiles were conducted on the study area over a day. Table 6.8 shows the seismic acquisition parameters for lines 1, 2, and 3, and the location of the lines is shown in Figure 6.29.

Table 6.8: Seismic acquisition parameters for lines 1, 2, and 3.

Line	Line 1 (96 channel)	Line 2 (48 channel)	Line 3 (24 channel)
Number of receivers	96	48	24
Profile length (m)	250	140	24
Max offset (m)	10 (start only)	10	10
Direction	S-N	S-N	S-N
Recording length (s)	1	1	0.5
Sample interval (ms)	0.5	1	1
Vertical stacks	2	2 (unstacked)	2
Source spacing (m)	5	2.5	1
Source type	6.3 kg Sledgehammer	24 kg Accelerated Weight-Drop	6.3 kg Sledgehammer
Receiver spacing (m)	2.5	2.5	1
Geophone frequency (Hz)	4.5	4.5	4.5
Geophone type	Spike geophone	Spike geophone	Land streamer

Figure 6.29: Relative locations of the seismic profiles, line 1 to line 3.

An accelerated weight drop was used for line 2 (shown in white), while a 6.3 kg sledgehammer was used for line 1 and line 3 (shown in blue) (Figure 6.29). A laptop computer coupled to a Geometrics Geode seismograph, 4.5 Hz geophones, and spread cables make up the seismic data acquisition apparatus. Up to 24 geophones can be recorded on each Geode, and many Geodes can be linked together (Montgomery *et al*., 2020). Figure 6.30 displays the Geode seismic data acquisition system. The geophone spacing is variable (1 to 2.5 meters). Figure 3.31 shows the overall field set-up for the seismic method.

Figure 6.30: Geode seismic data acquisition system.

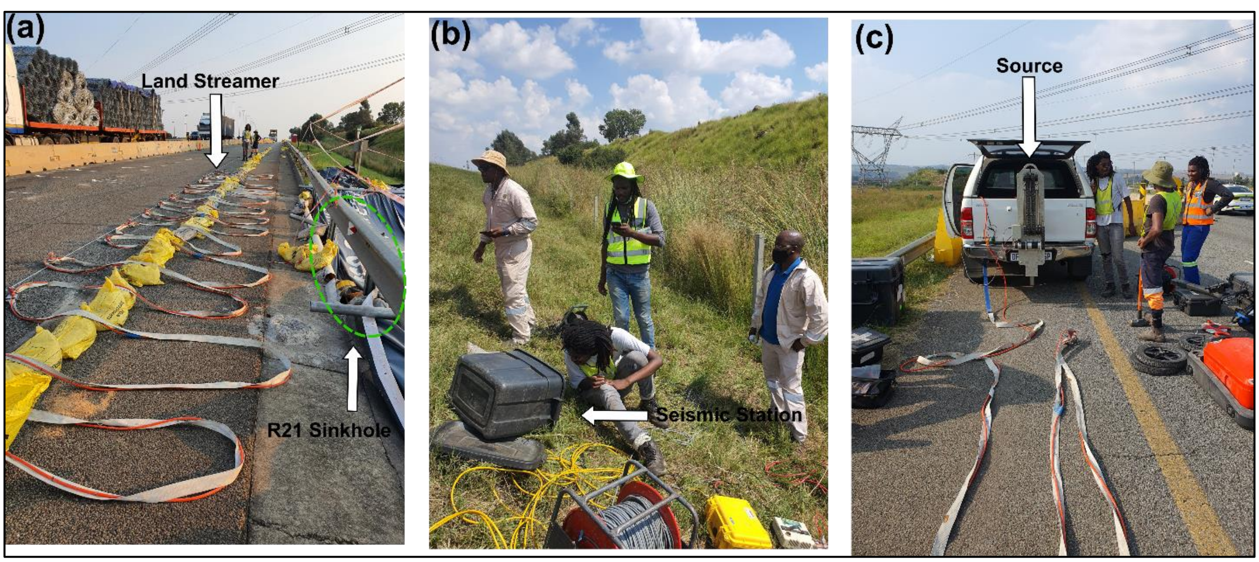

Figure 6.31: (a) Land streamer used for the survey, (b) seismic station, and (c) accelerated weight-drop mounted at the back for the vehicle.

6.5.2 Refraction Seismic Data Processing

Data quality control, or QC, is a process that must be carried out following data acquisition and before data processing (Figure 6.32).

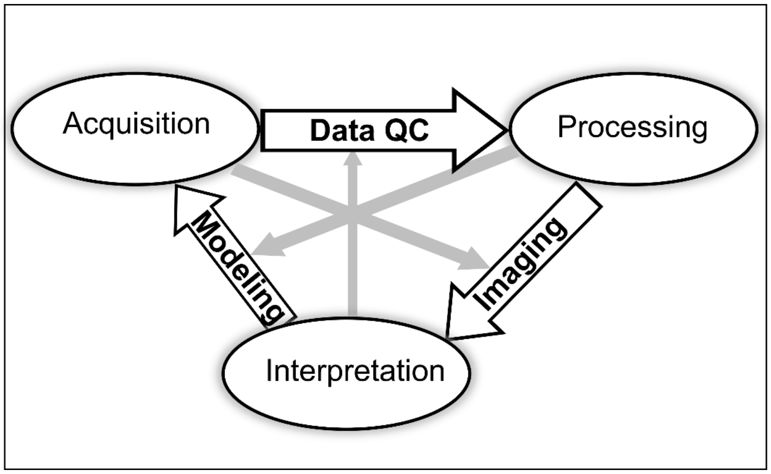

Figure 6.32: Relationship between the data acquisition, processing, and interpreting (Zhou, 2014).

GLOBE Claritas was used to process the acquired seismic refraction tomography data. There are several digital data processing methods available for improving seismic sections. Because different processing workflows apply to different data sets, the processing stages used and their order may vary (Cox *et al*., 2020). Table 6.9 shows some of the processing steps used when dealing with seismic data.

Table 6.9: Seismic data processing workflow applied in line 3.

General Processing Flow
Geometry sorting: 0.5 m CMP bins, spaced at 0.35 m. 1547 m fixed datum, 2000 m/s replacement velocity
First break picking: 912 first arrivals manually picked
Time cut: 100 ms
Statics correction: 1.3 RMS error
Frequency filtering: BS [49.8 49.9 50.1 50.2], BP [70 80 20 290]
FK-filtering
Top mute

The initial step involves sorting the geometry. Sorting the geometry is a fundamental step in seismic data processing. It ensures that the seismic traces are accurately represented in space, based on the acquisition geometry recorded in the seismic record header. (Osinowo, 2020). The second step entailed precisely picking the P-wave first breaks from the seismic signal to create the time-distance curves (Figure 6.33 (a)). The geophone spacing, source location, first arrival time, and distance along the survey line were used to generate the time-distance curves (Al-Saigh and JaddoaAl-Heety, 2014). After that, a static correction was used to take care of the low-velocity layer and elevation (Figure 3.33 (b)).

The next step is applying frequency filtering, which removes unwanted noise, by using a band-stop filter of [49.8 49.9 50.1 50.2]. A bandpass filter was used to eliminate frequencies outside the bandwidth of the input sweep of [70 80 20 290] (Figure 6.34 (a)). The next step was the application of the F-K filter, which is applied to the pre-stacked data to attenuate linear noise (remove multiple reflections, surface waves, and refraction) (Figure 6.35 (a)) (Al-Shakhis, 1987; Collins and Osazuwa, 2010). Theoretically, F-K filters are made to reject noise while allowing the signal to flow through (Al-Shakhis, 1987). A top mute was applied to all raw shots to remove the upper portion of a shot gathers that only contains noise, refractions, and surface waves (Figure 6.36 (c)).

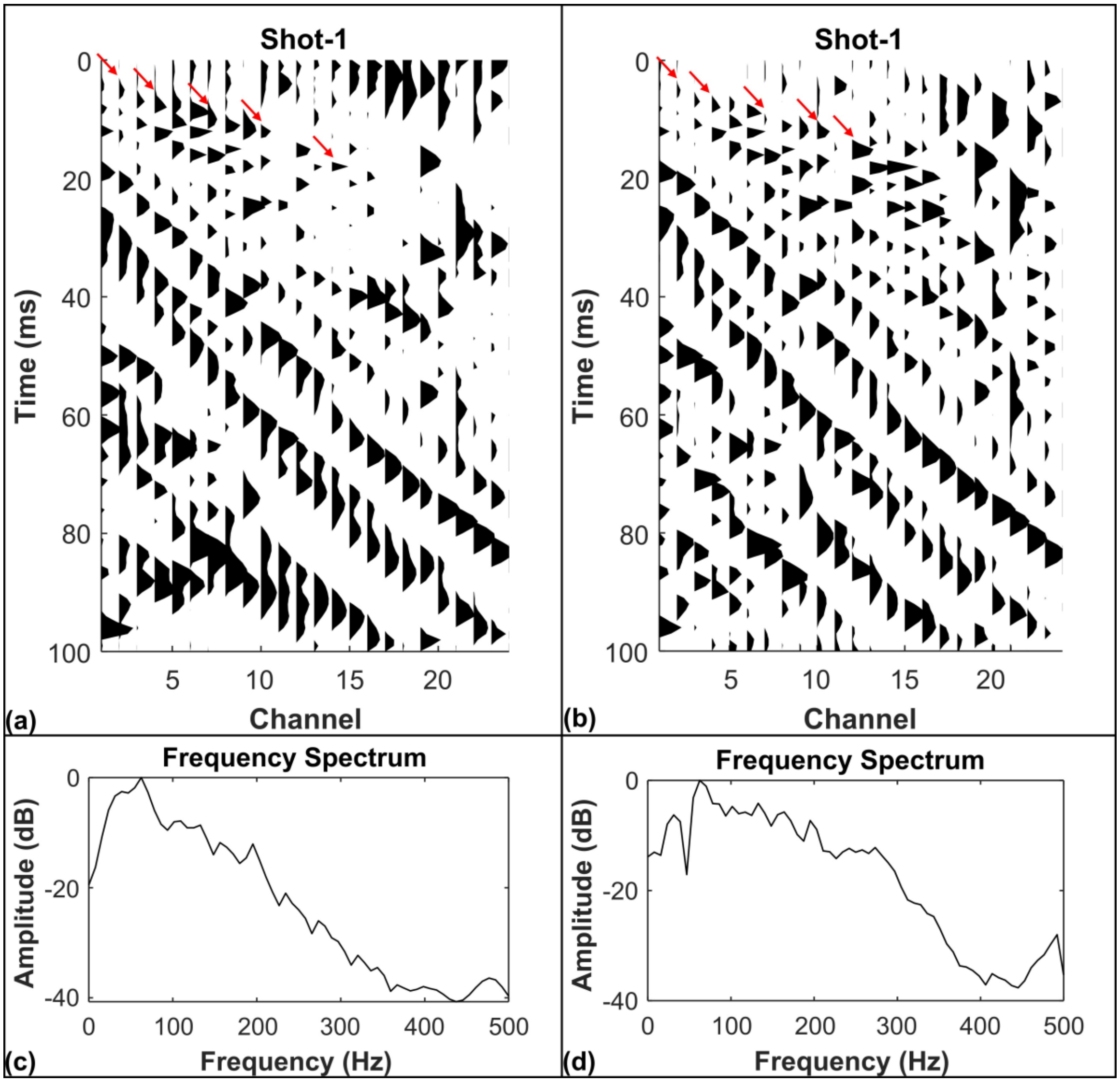

Figure 6.33: Example of raw shot gather (a) and processed shot gather (statics correction) (b), with the raw shot gather frequency spectrum graph (c) and the processed shot gather frequency spectrum graph (d).

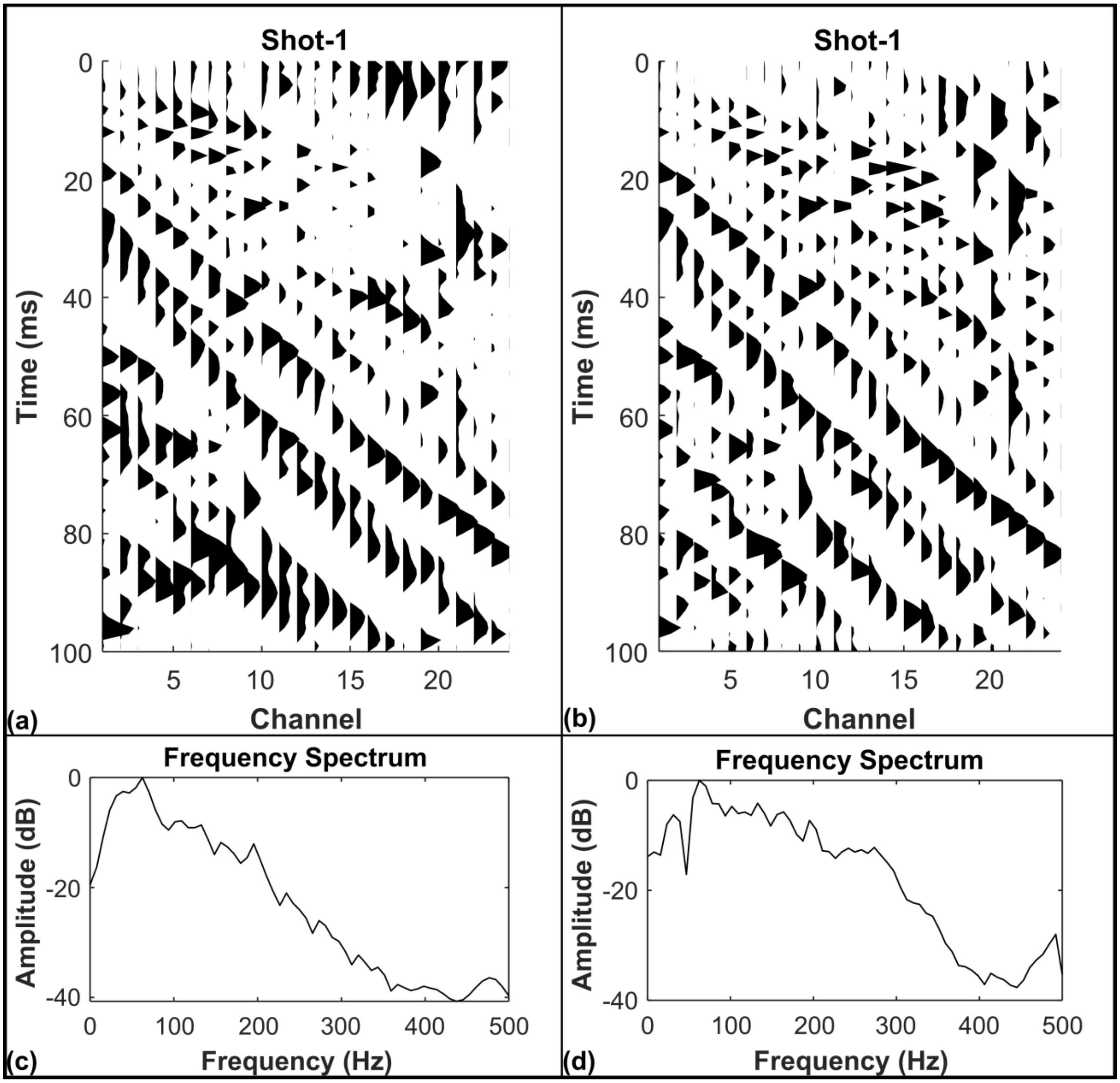

Figure 6.34: Example of static corrected shot gather (a) and frequency filtered shot gather (b), with the static corrected shot gather frequency spectrum graph (c) and the frequency filtered shot gather frequency spectrum graph (d).

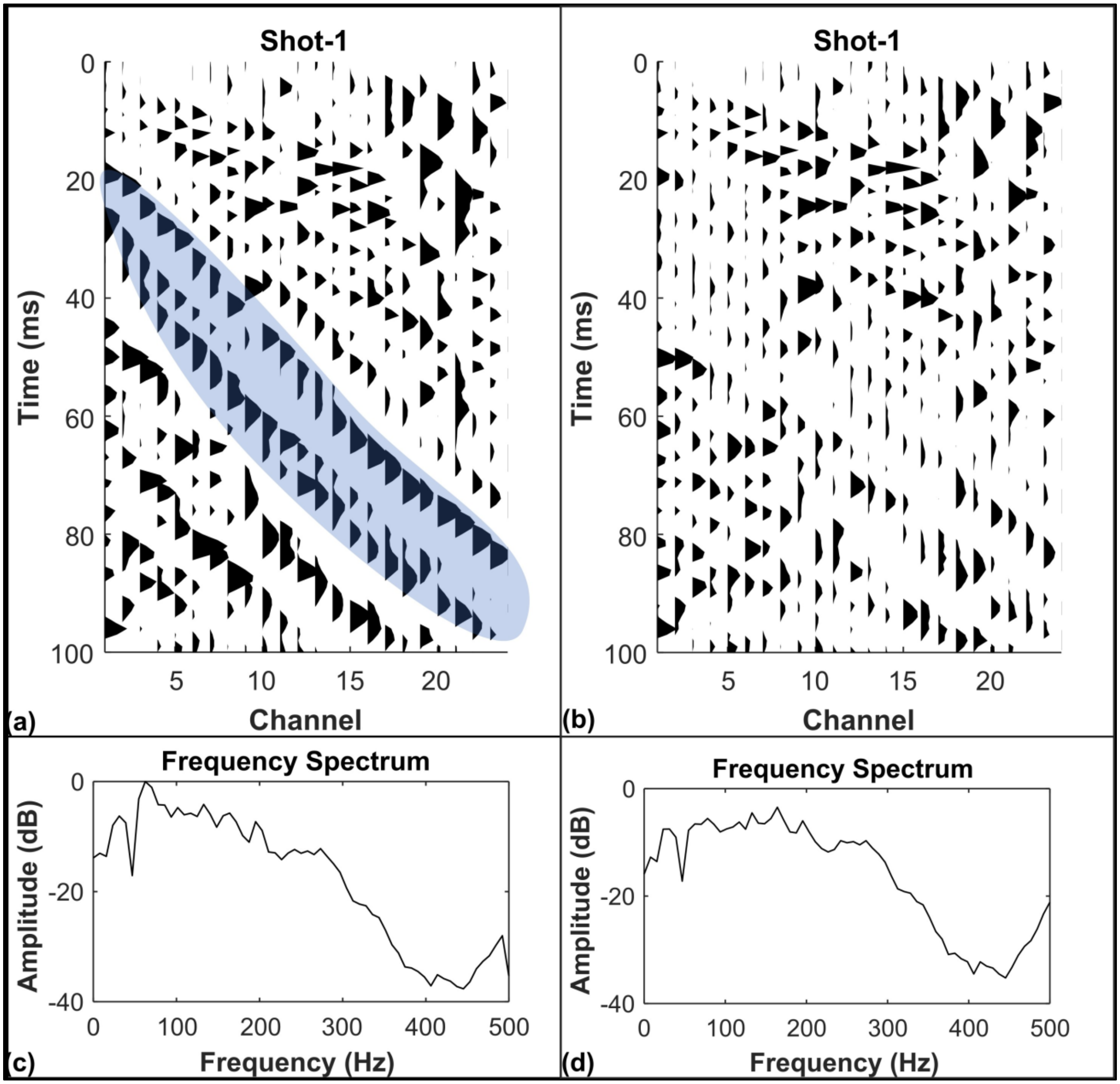

Figure 6.35: Example of frequency filtered shot gather (a) and F-K filtered shot gather (b), with the frequency filtered shot gather frequency spectrum graph (c) and the F-K filtered shot gather frequency spectrum graph (d). The area highlighted in blue represents the surface waves.

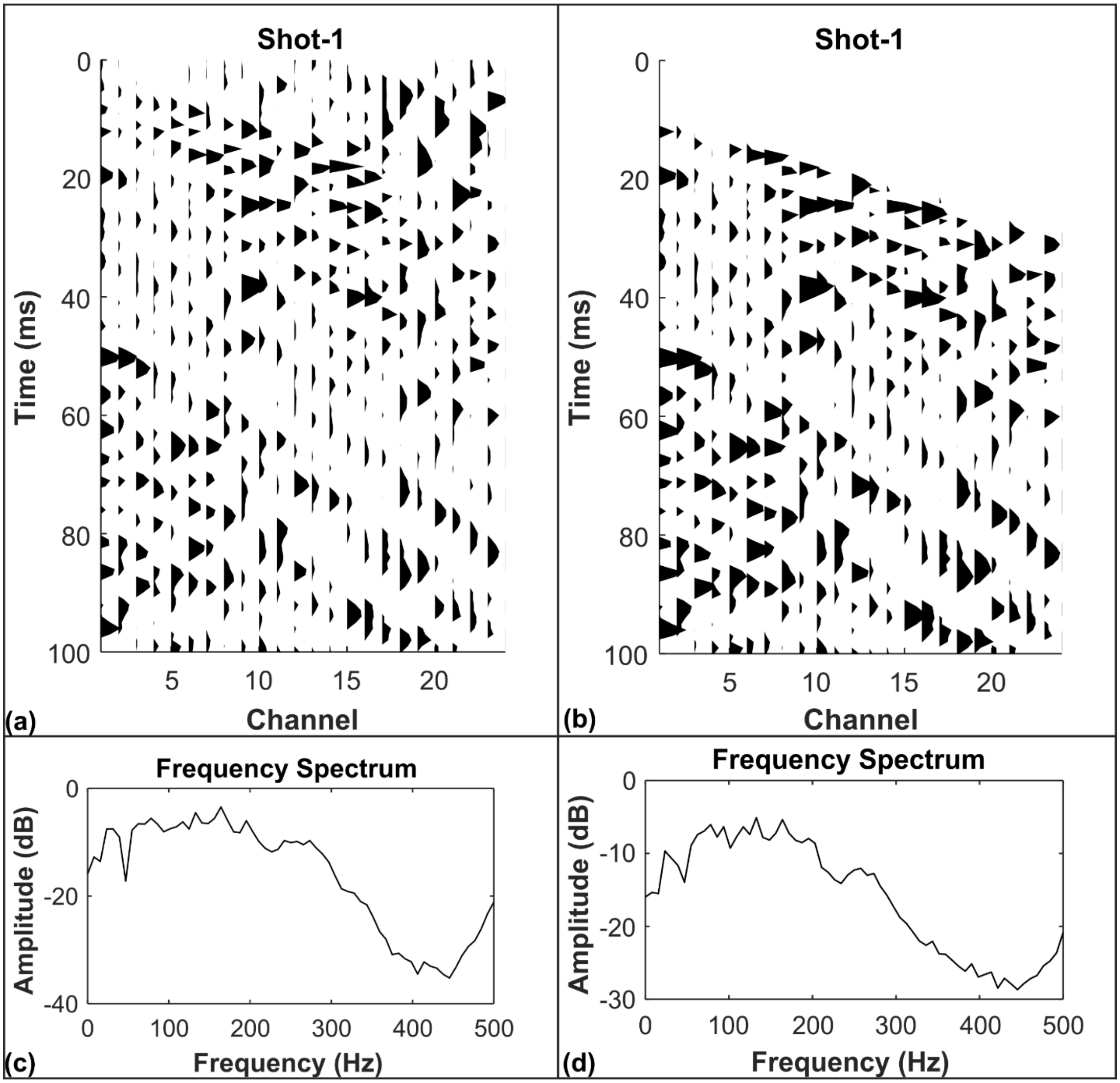

Figure 6.36: Example of F-K filtered shot gather (a) and first break muted shot gather (b), with the F-K filtered shot gather frequency spectrum graph (c) and the first break muted shot gather frequency spectrum graph (d).

6.6 Multi-Channel Analysis of Surface Waves (MASW) Survey

6.6.1 Data Acquisition

MASW data were acquired along the R21 highway, next to a newly formed sinkhole. Figure 6.37 displays the location of the MASW line concerning the current sinkhole.

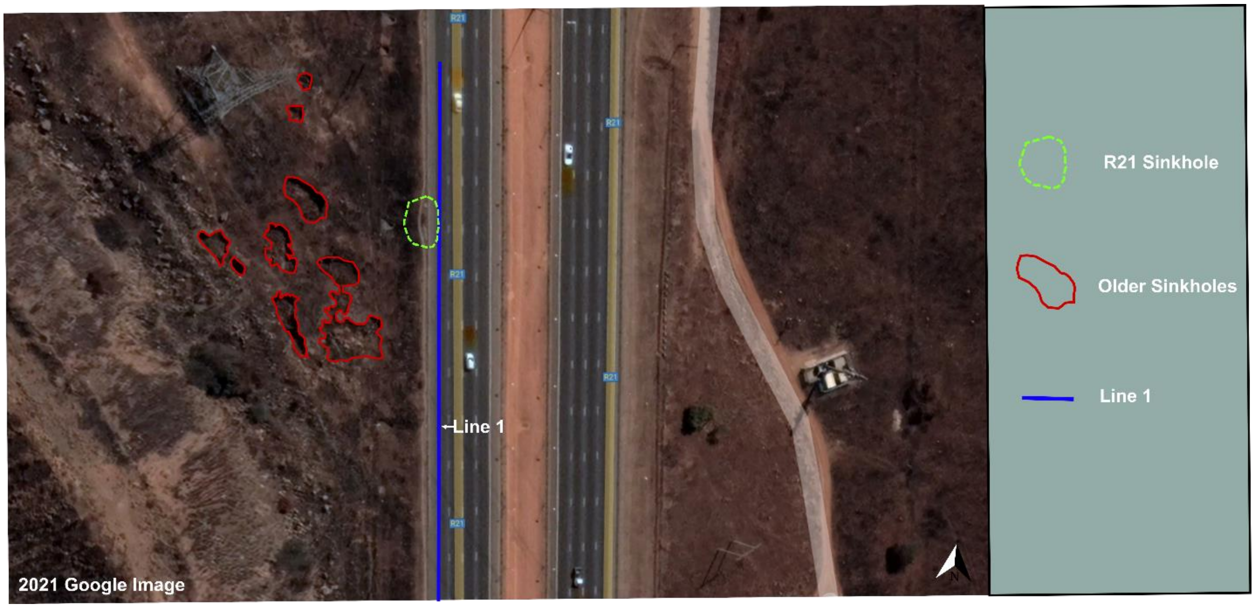

Figure 6.37: Relative location of the MASW profile, line 1, with the R21 sinkhole shown in dashed green lines.

All the survey parameters are shown in Table 6.10. Due to surface conditions, i.e., tarred road, a seismic land streamer was used for the surveys.

Table 6.10: Summary of Multichannel Analysis of Surface Waves field parameters in this study.

Parameters	Line 1 (end-on spread)
Number of receivers	24
Profile length (m)	300
Max offset (m)	10
Direction	S-N
Recording length (s)	1
Sample interval (ms)	0.25
Vertical stacks	2
Source spacing (m)	5
Source type	6.3 kg Sledgehammer and 24 kg Accelerated Weight-Drop

Receiver spacing (m)	5
Geophone frequency (Hz)	4.5
Geophone Type	Land streamer

Two seismic sources were used in this survey, the accelerated weight drop, and the 6.3 kg sledgehammer (Figure 6.38).

Figure 6.38: Active Multichannel Analysis of Surface Waves data acquisition. (a) Land streamer used for the survey. (b) 6.3 kg sledgehammer used as a source. (c) Accelerated weight-drop mounted at the back for the bakkie. (d) Seismic station.

6.6.2 Processing of Multichannel Analysis of Surface Waves Data

The first step was to load the SEG2 field records into SurfSeis software. After that, a flow chart for assessing MASW profiles is produced by converting these records into KGS format. The SurfSeis algorithms analyse every KGS file, and describe the surface wave's characteristics, phase velocity, and frequency (Park and Miller, 2008). A typical MASW survey includes (a) data acquisition; (b) extraction of the dispersion curves; and (c) inversion analysis for Vs profiles (Xia *et al*., 1999) (Figure 6.39). Creating a dispersion image and extracting the dispersion curve in MASW involves computing phase seismic velocities for each frequency component of the data to understand the dispersive nature of surface waves (Alsulaimani, 2007). Inverting the dispersion curve in MASW involves using a least-squares method to fit a mathematical model to the measured curve. Figure 6.39 shows the raw seismic record (Figure 6.39a), the dispersion curve (Figure 6.39a), and the shear wave velocity profile (Figure 6.39a).

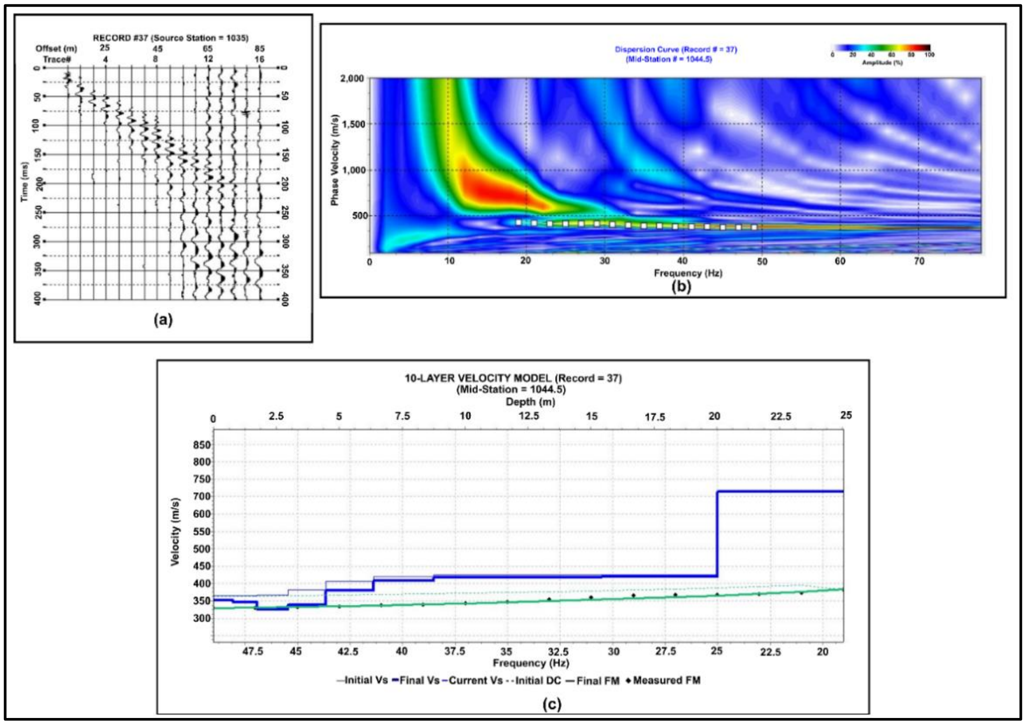

Figure 6.39: Multichannel Analysis of Surface Waves processing workflow. (a) Collected raw shot gathers of the study area. (b) Phase velocity model and (c) 1D shear wave velocity profile vs 1D depth curve.

The dispersion curves (e.g., Figures 6.40-6.41) are used in the inversion process to produce a vertical Shear wave velocity model (Figure 6.42). The data quality greatly influences how these variables will affect the analysis. The following are the variables that have the greatest influence on the dispersion analysis (Miller *et al*., 2001; Alsulaimani, 2007; Liu, 2017; Hu *et al.*, 2018):

- Range of frequency of depth
- Phase velocity ranges
- Higher modes of characterization, and
- Noise reduction

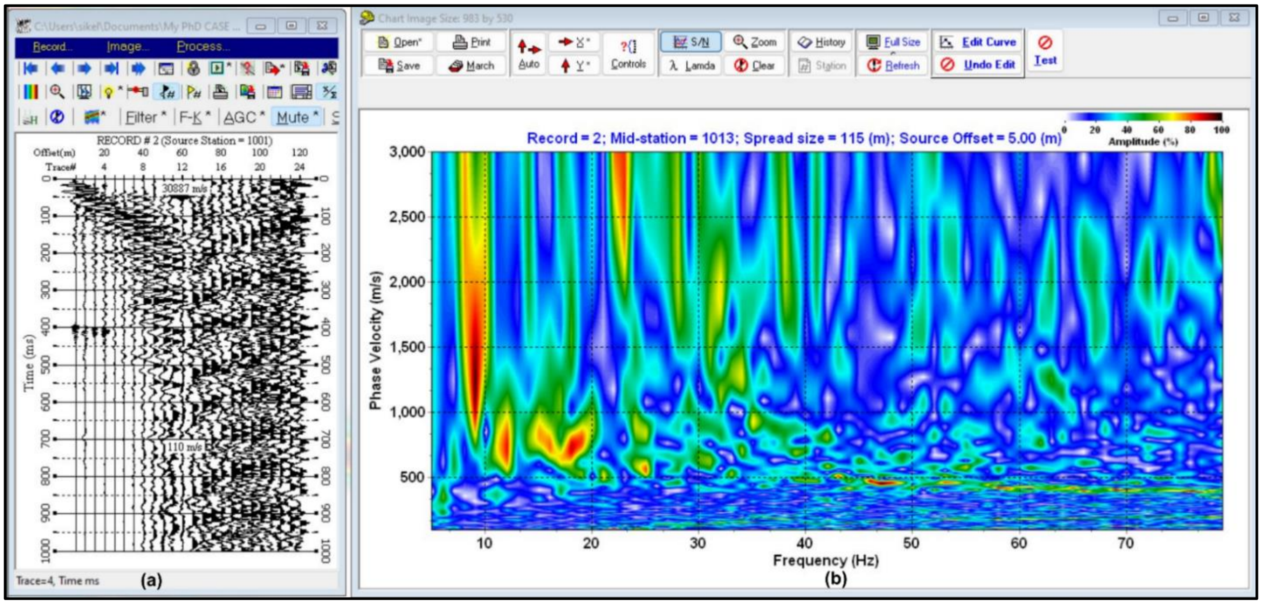

Figure 6.40: (a) Raw shot gather collected with the source offset of 5 m and receiver spacing of 5 m. (b) Corresponding unmuted dispersion image (also called Overtone Image) with dominant higher-mode contamination, phase velocity (y-axis) versus frequency (x-axis).

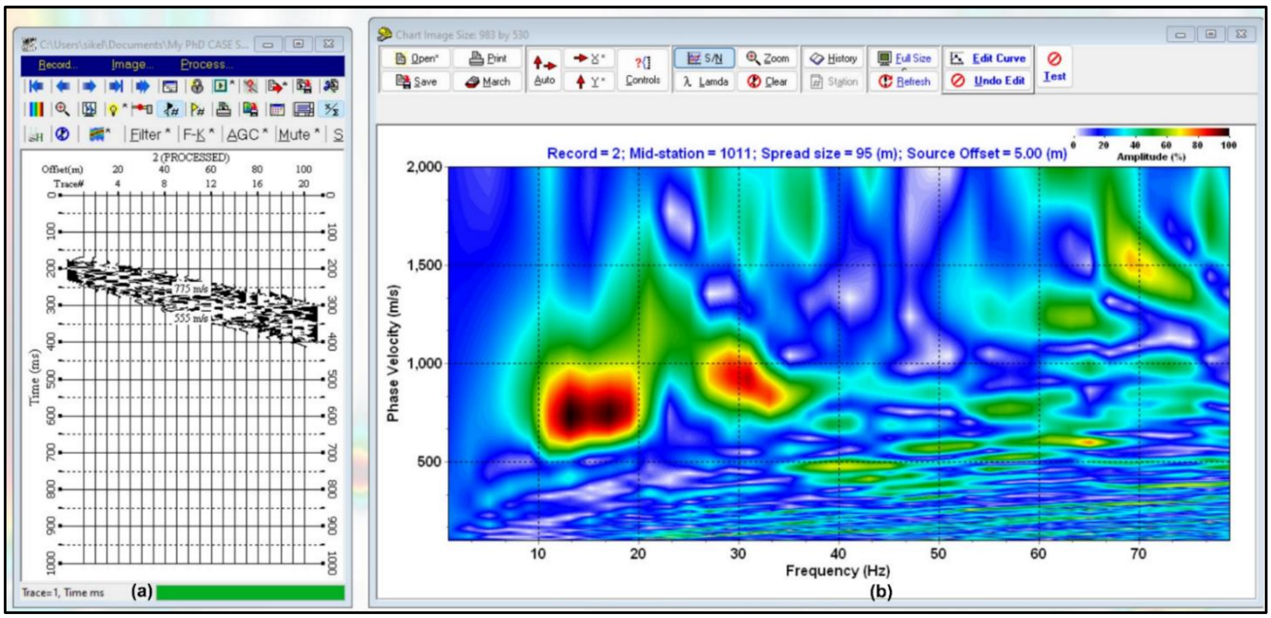

Figure 6.41: (a) The multichannel shot gather collected with the source offset of 5 m and receiver spacing of 5 m with applied muting. (b) Corresponding muted dispersion image of the shot gather.

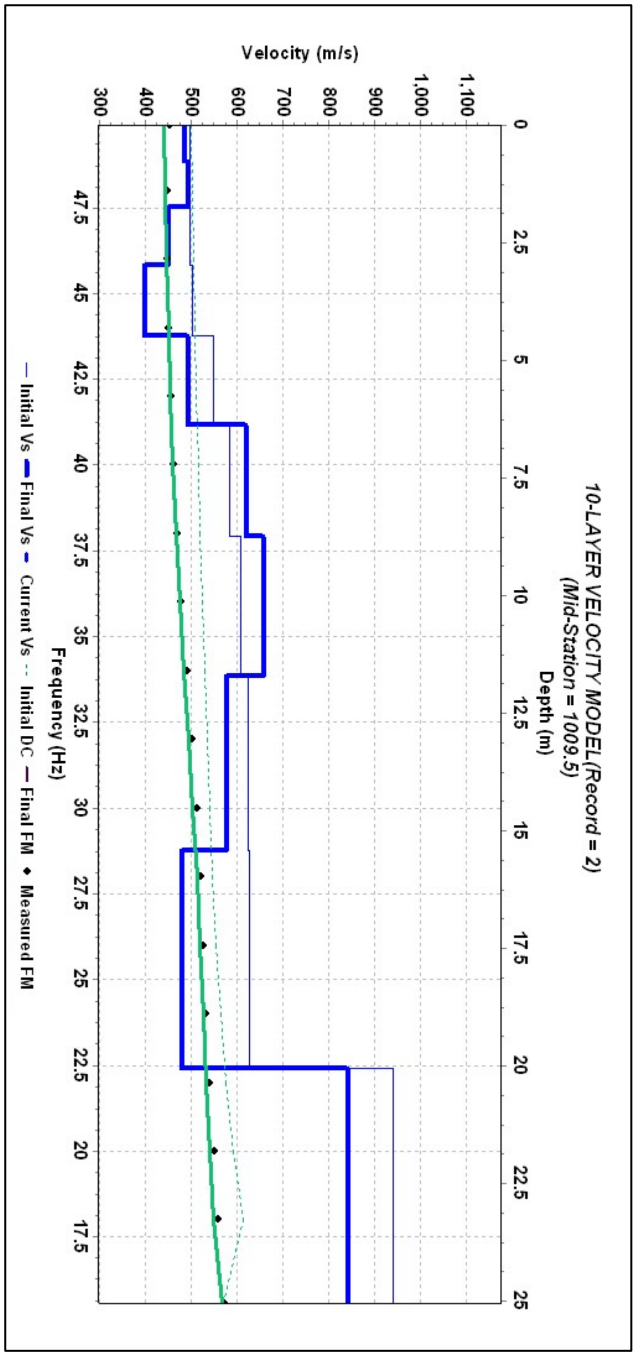

Figure 6.42: 1D shear wave velocity profile from line 1, R21 profile.

7 RESULTS AND INTERPRETATION

The interpretation focuses on five (5) ERT profiles, five (5) GPR profiles, three (3) seismic profiles, and one (1) MASW profile.

7.1 Electrical Resistivity Tomography

The differences in the resistivity of the subsurface mainly indicate different materials within the subsurface. The general resistivity values of some of the materials are shown in Table 7.1. Six (6) ERT profiles were acquired, but only results from four (4) profiles are presented, interpreted, and discussed (Figure 7.1-7.6). Additional information about the results is also included in Appendix A (Figures A1-A6). According to Montgomery *et al*., (2020) and Nwokebuihe, (2014), sinkholes filled with water or saturated material exhibit low resistivity values, while those filled with air exhibit high resistivity values.

Table 7.1: The common resistivity values of known subsurface materials (Nwokebuihe, 2014).

Subsurface material	Description	Resistivity (Ohm.m)
Clay	Low resistivity and is affected by the saturation degree, layer thickness, and layer thickness.	< 100
Fractured rocks and soils	Moderate resistivity	100-400
Relatively compact rock	Slightly higher resistivity values	> 400
Air-filled cavities	High resistivity	>10,000 (usually)

The ERT section (profile 1), shown in Figure 7.1, exhibits two high resistivity zones that are interpreted as possible sinkholes (marked by dashed purple and green circle at starting depths of ~6.72 m). In particular, the high resistivity zone with a dashed purple circle aligns with the position of the sinkhole observed on the surface, thus the detected anomaly is interpreted as a response of the sinkhole (R21 sinkhole). The high resistivity zone marked by a dotted green circle indicates another possible sinkhole (located at distances between ~40 and ~50 m) that has not yet manifested itself on the surface. Above this sinkhole lies a conductive zone, which is interpreted as moist clayey material. A similar anomaly is also present at depths of ~15 m from the ground surface, suggesting areas of high-water saturation (Figure 7.1). The electrical resistivity data also exhibit resistivity values (746 – 1539 ohm.m) that are associated with weathered rocks, while other resistivity values (362 – 746 ohm.m) are related to dry soil.

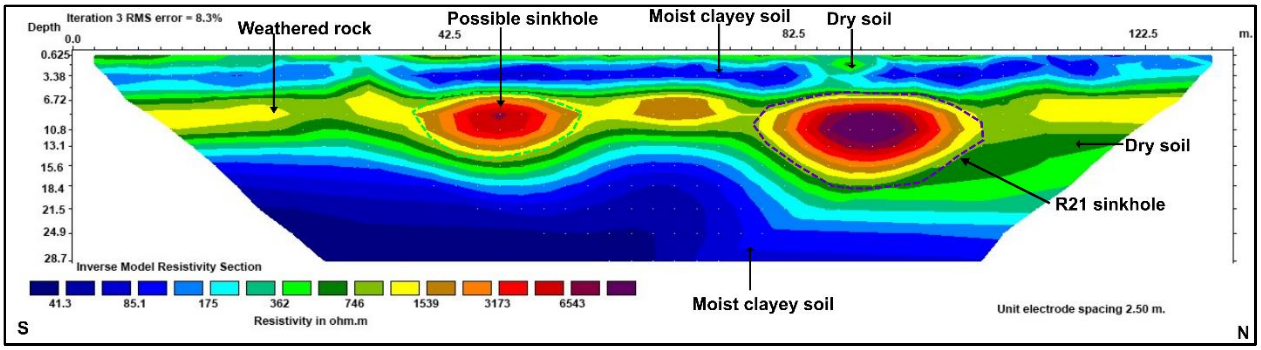

Figure 7.1: The interpretation of ERT profile 1, oriented south to north along R21 highway with dipole-dipole arrays configuration. The moist clayey soil, low resistivity, and saturated layer is just under the topsoil layer is shown by the range of blue colours.

Figure 7.2 (ERT profile 2) shows similar features to Figure 7.1, however, the high resistive anomaly in the south is not delineated. This may indicate that this sinkhole does not extend beyond this ERT section. Furthermore, a high resistivity zone towards the north is well aligned with the position of the R21 sinkhole.

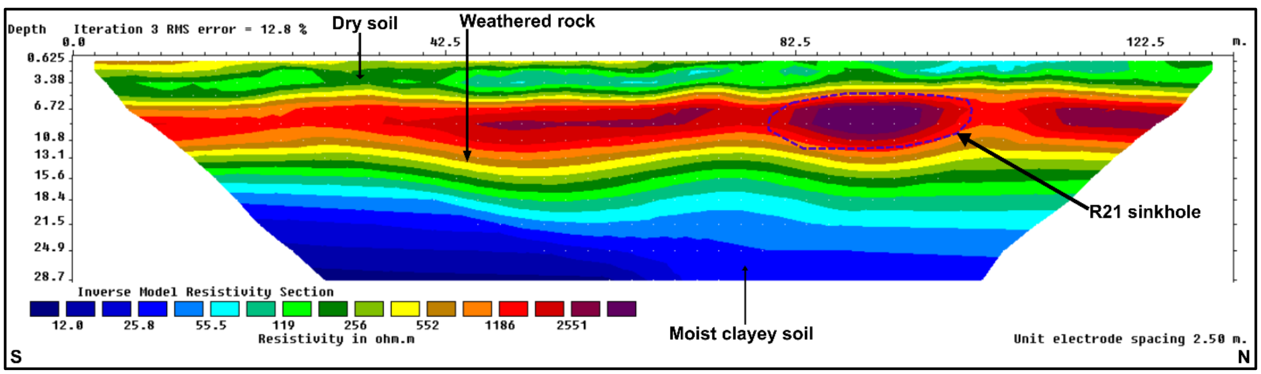

Figure 7.2: The interpretation of ERT profile 2, oriented south to north along R21 highway with dipole-dipole arrays configuration. The dashed purple lines represent the R21 sinkhole.

Profile 4 results are presented in Figure 7.3. This section shows a possible water-filled cavity with low resistivity anomaly at depths between ~14 m to ~49 m on the southern side of the section. This may be true with what was recorded in profile 1, except that there is a change in resistive values as profile 1 was directly above this possible sinkhole and profile 4 is on the side of the highway. There is also a high resistive anomaly on the northern section (between 240 and 360 m distances) of the profile which is associated with the R21 sinkhole. Also delineated by the profile are the areas associated with the dry soil and weathered rocks.

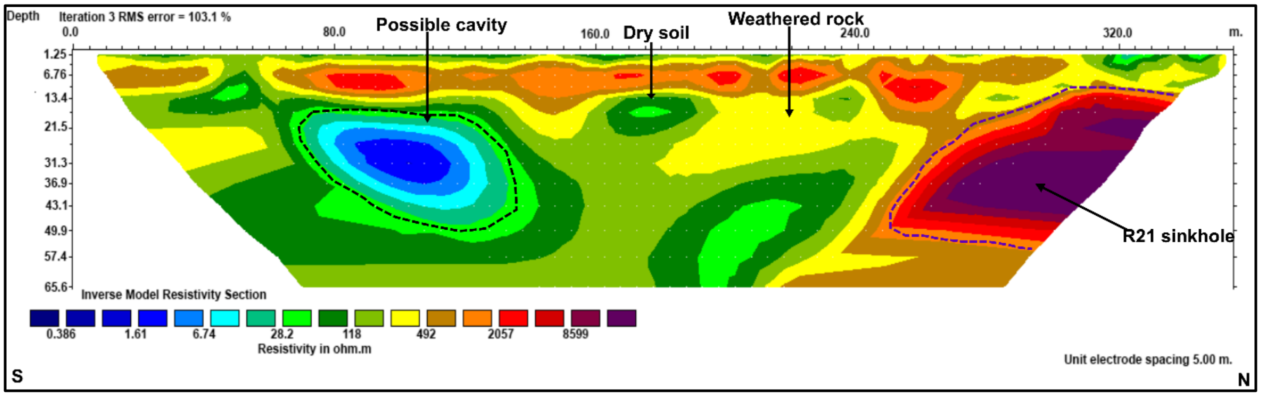

Figure 7.3: The interpretation of ERT profile 4, oriented south to north along R21 highway with dipole-dipole arrays configuration. The dashed purple lines represent the R21 sinkhole, while the black dashed circle lines represent a possible filled cavity.

Figure 7.4 shows the results from profile 5, which is on the south-bound land where the survey was conducted to determine whether the R21 sinkhole extends to the other lanes. Shown in dashed green lines is a high resistive layer, similar to the one observed in profile 1 (Figure 7.1). These high resistive areas on the profiles could suggest that the sinkhole is filled with materials of low electric conductivity such as air or other rock materials. This high resistive zone is also right next to a stormwater drainage system, which could explain that it is developing below the subsurface and has yet to manifest on the surface. Figure 7.4 also shows the delineation of other features that were observed in other profiles such as dry soil and weathered rock (shown by red dotted lines). The weathered rock observed could be clayey-silty materials, which consist of fine-grained particles such as clay and silt, normal common fill materials that can enter karst networks. These materials can be transported by various means, such as surface water runoff, erosion, or sediment deposition.

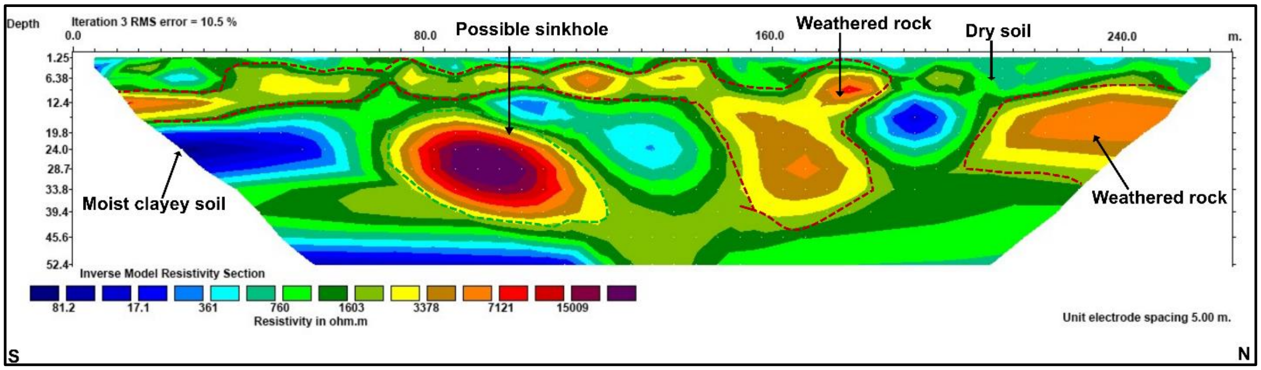

Figure 7.4: The interpretation of ERT profile 5, oriented south to north along R21 highway with dipole-dipole arrays configuration. The dashed green lines represent a possible sinkhole that has not manifested yet on surface, while the red dashed lines represent a weathered rock.

Figures 7.5 and 7.6 show a 3-D model, combining all three profiles. These results clearly outline the two resistive sinkholes, one on the southern side of the profiles as well as the R21 sinkhole on the northern side of the highway. The 3D models provide a clear and detailed visualisation of both the R21 sinkhole on the northern section as well as the possible sinkhole on the southern end of the section, making it easier to understand their locations.

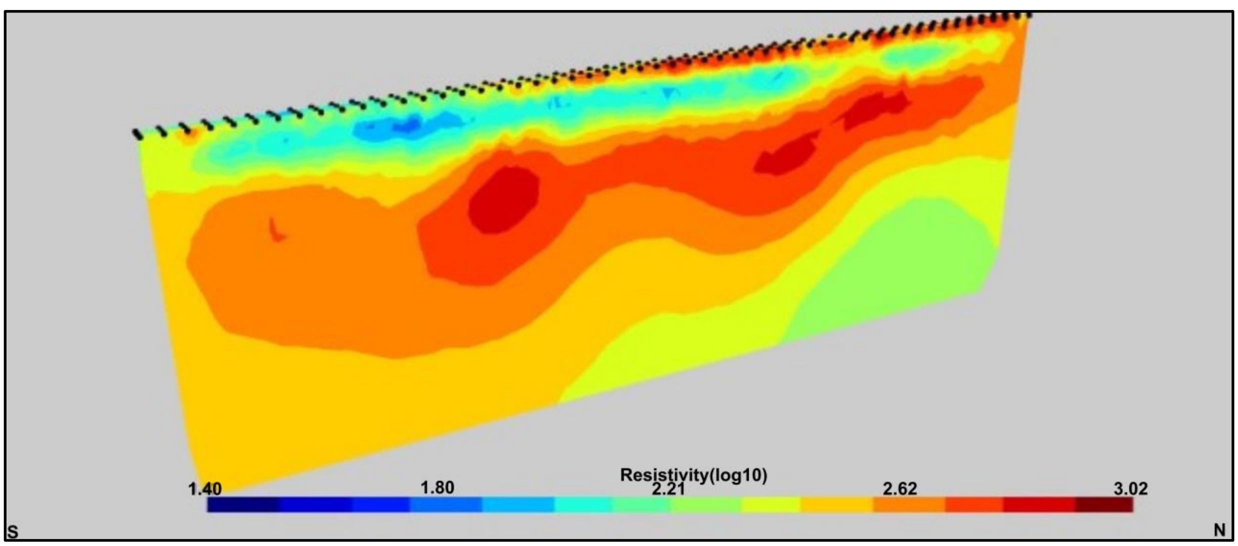

Figure 7.5: Lines 1 to 3 in 3-D, showing the areas with the resistive sinkholes.

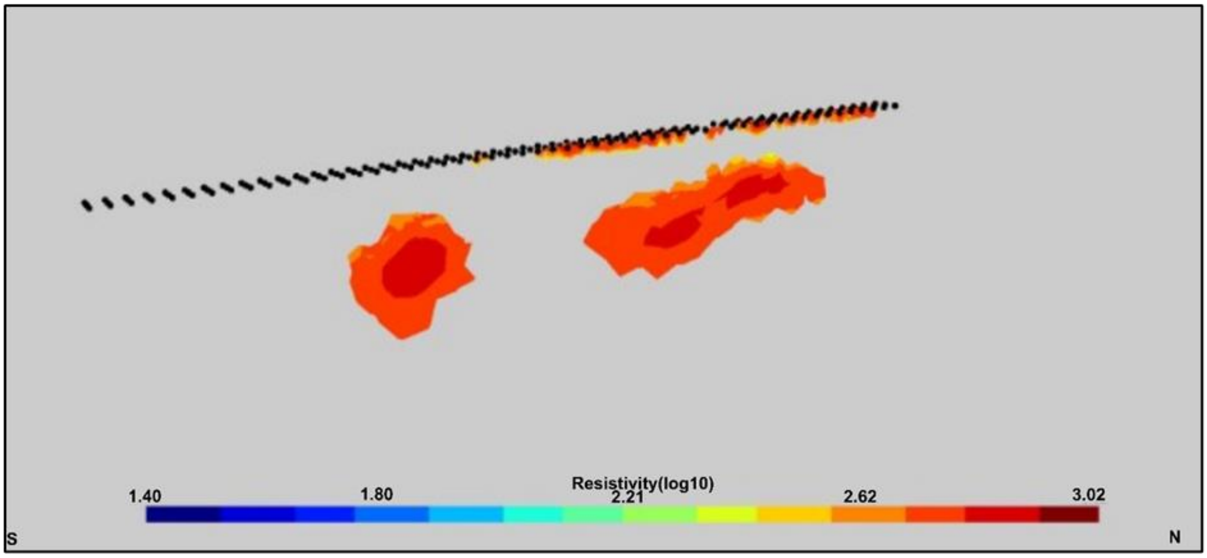

Figure 7.6: Lines 1 to 3 in 3-D, showing the two sinkholes with high resistive zones.

7.2 Ground Penetrating Radar

A total of eight south-north and twenty-seven east-west GPR lines were surveyed as part of the research. Out of these thirty-three (33) profiles, only five (5) have been selected for this interpretation section and discussion. The other profiles are presented under the field result data in Appendix B (Figures B1-B13).

Throughout the site, there were metal pieces (as shown in Figure 7.7) that are used by the road maintenance company when trying to patch the cracks or holes on the highway. These metal pieces caused noise in some of the GPR data (discussed later).

Figure 7.7: Metal pieces found on the R21 highway, which could have caused noise on the data.

Figures 7.8 (a) and (b) (profile R21SINK001_001) display GPR sections that run south-north of the highway. The sand/clay interface is delineated at approximately the same depth, as shown by strong reflection throughout the GPR sections (indicated by the top yellow line in Figures 7.8 (a) and 7.8 (b)). The GPR sections also exhibit a consistent, strong lateral reflection (second yellow line from the top in Figure 7.8 (b)), with varying depths from south to north (i.e., ~2 m in the north and ~3 m in the south). A series of diffractions are also observed between ~2 and ~7 m depths (Figure 7.8 (b), shown by black arrows), and these indicate the position of the sinkhole features such as the collapse features or the edges of the sinkhole. A metal piece observed on the surface is detected as a near-vertical lineament in the R21SINK001_001 section (Figure 7.8 (b), shown by a red arrow).

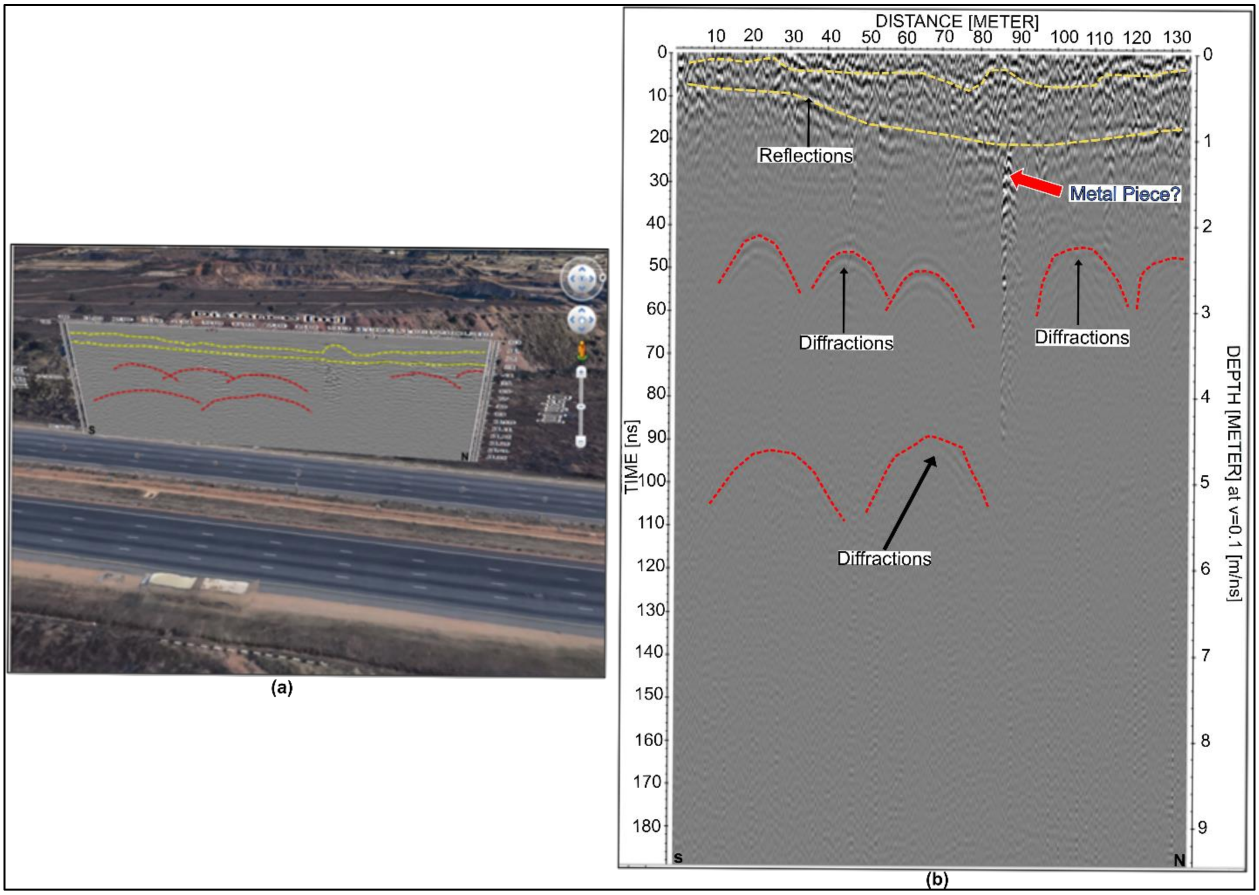

Figure 7.8: (a) Google Earth image with the location of line R21SINK001_001 from group one, (b) Interpreted GPR data are showing diffractions originating from top of the possible sinkholes. The arrows point to the hyperbolic event that formed because of a subsurface feature, while the brighter reflections (highlighted in yellow) originate from the near-surface stratigraphy.

Figures 7.9 (a) and (b) show the results from the south to north trending profile (R21SINK001_003) from group one. The profile also exhibits a series of reflections indicated by the yellow lines, representing an interface between near-surface geological boundaries. A series of diffractions occur between ~2 and ~6 m depths (Figure 7.9 (b), shown by black arrows), which indicate the position of the sinkhole features, the R21 sinkhole being the one on the northern section of the profile. The diffractions observed on the southern section of the profiles could indicate sinkholes that have not yet manifested on the surface.

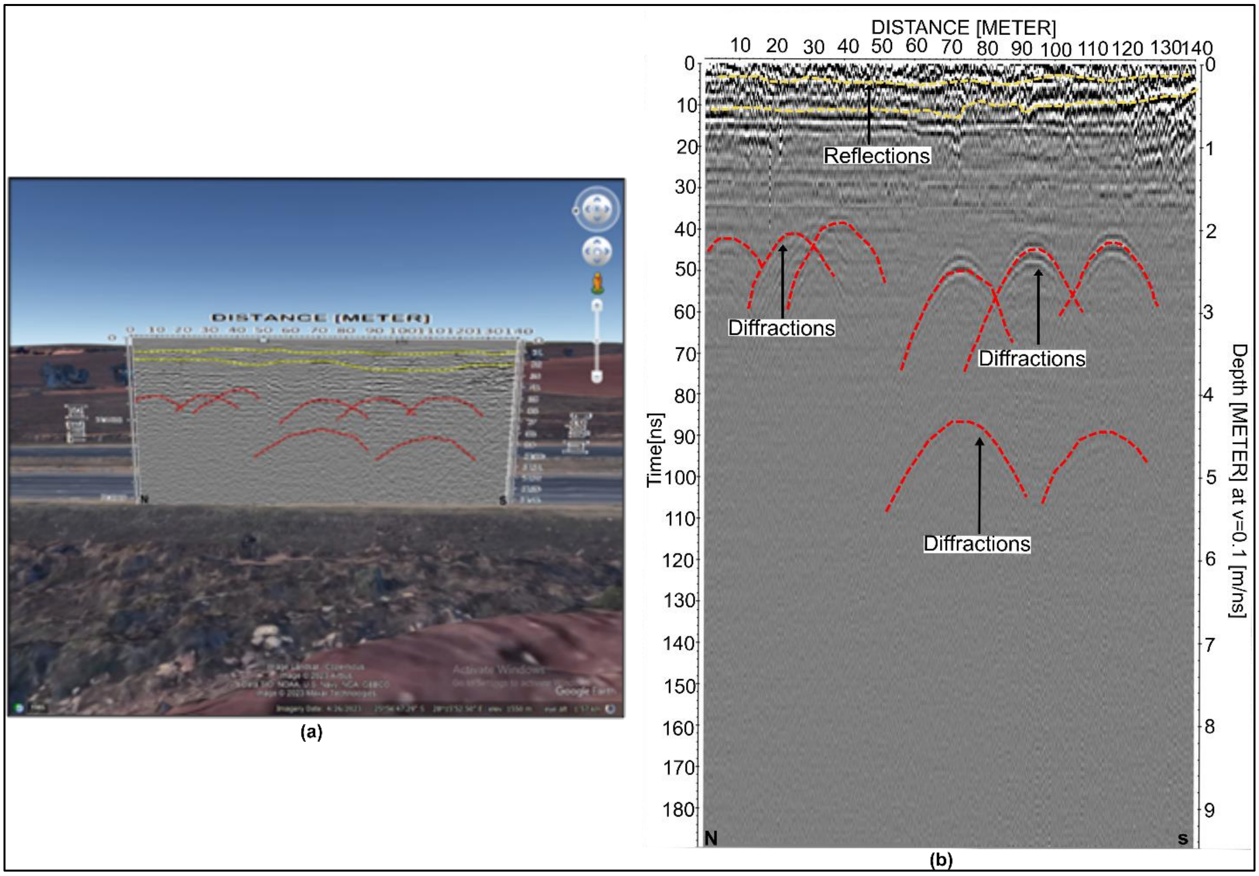

Figure 7.9: (a) Google Earth image showing the location of line R21SINK001_003 from group one, (b) GPR image of R21SINK001_003, with diffractions shown by the red lines. The arrows point to the hyperbolic event that formed because of a subsurface feature, while the brighter reflections are highlighted in yellow because they most likely signal a shift in yellow because they most likely signal a shift in stratigraphy.

Figures 7.10 (a) and (b) show another south to north trending profile from group two, R21SINK002_001, with similar diffractions (shown in red) as R21SINK001_001 and R21SINK001_003. These diffractions occur between ~2 and ~6 m depths and indicate potential sinkhole features that have no expressions surface.

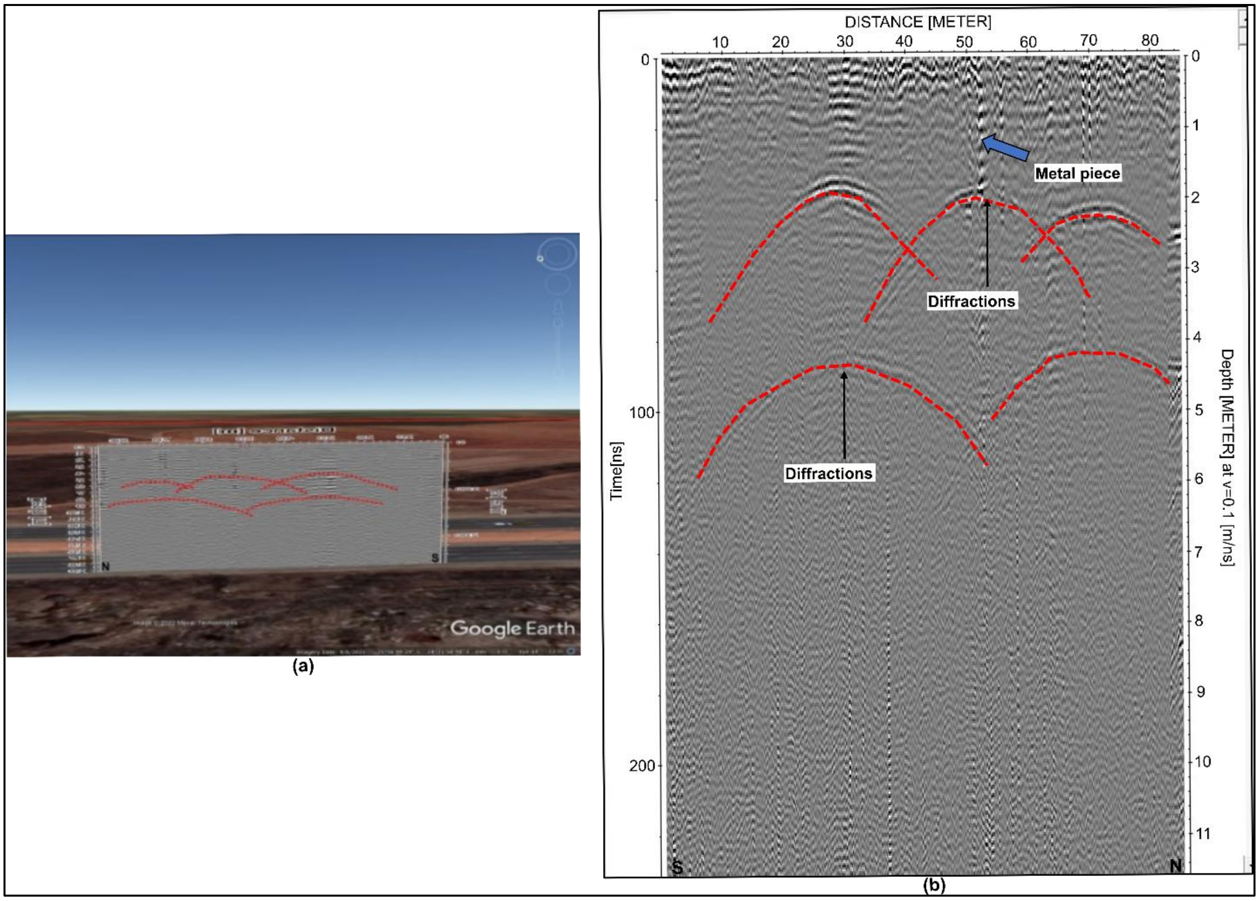

Figure 7.10: (a) Google Earth image with the location of line R21SINK002_001 from group two, (b) Diffractions shown in by dashed red lines in profile R21SINK002_001. The arrow in blue shows the noise from the metal piece that was observed at the site.

An east-west trending profile of R21SINK003_0015 (group three) is shown in Figures 7.11 (a) and (b). The extent of diffractions into the highway is shown by the red dashed line in Figure 7.11 (b). This suggests that the sinkhole extends by ~2.5 m into the highway and has an estimated depth of ~8 m as the diffractions continue to be observed at this depth. Another east-to-west trending profile, also from group three is shown in Figure 7.12. Some diffractions exist closer to the location of the sinkholes. These diffractions are about ~2.5 m into the highway and are at a depth of ~8 m.

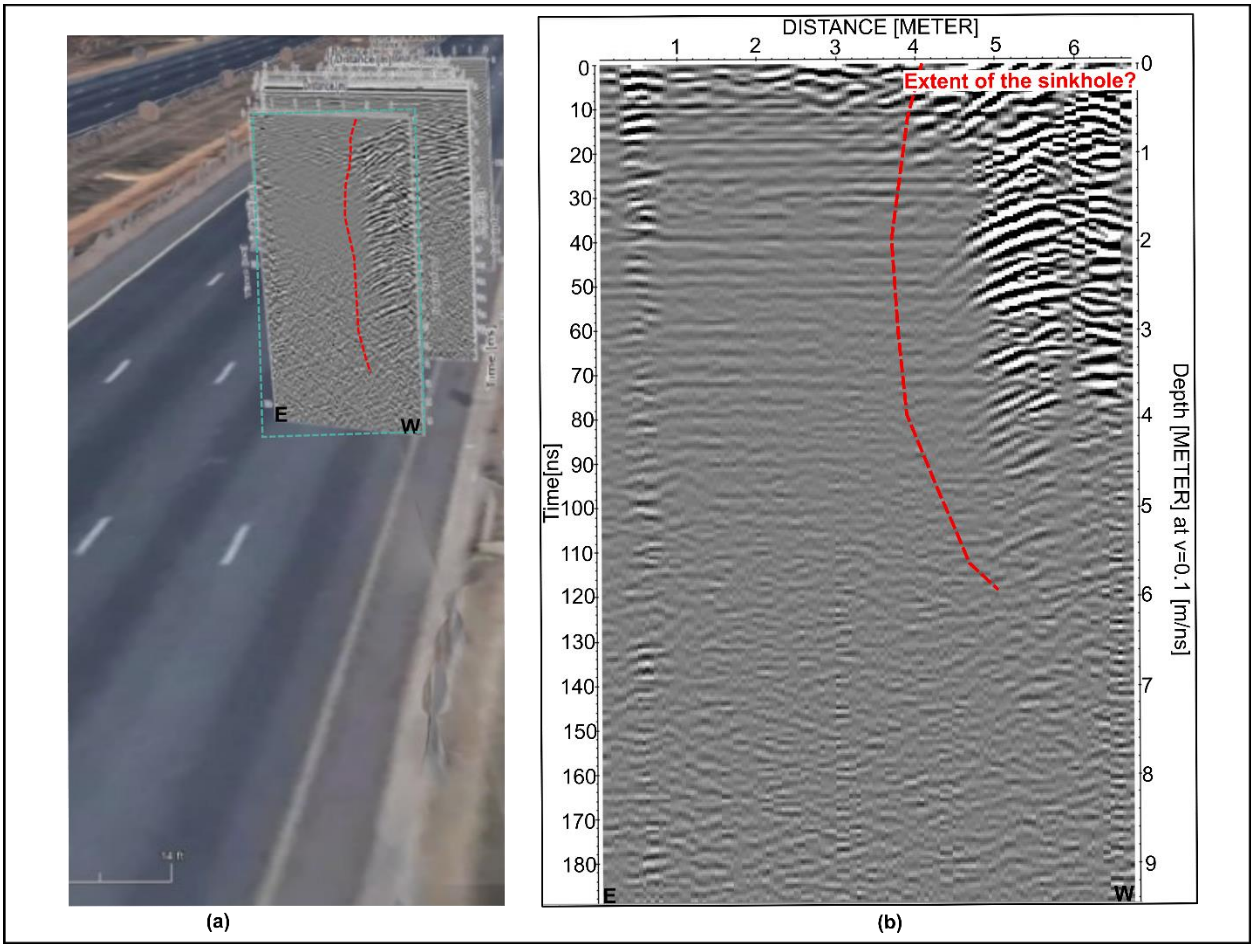

Figure 7.11: (a) Google Earth image with the location of line R21SINK003_0015 from group three, (b) Profile R21SINK003_0015 showing diffraction on the road which indicates the extent of the sinkhole on the highway. The end of diffracted events is shown by a red line.

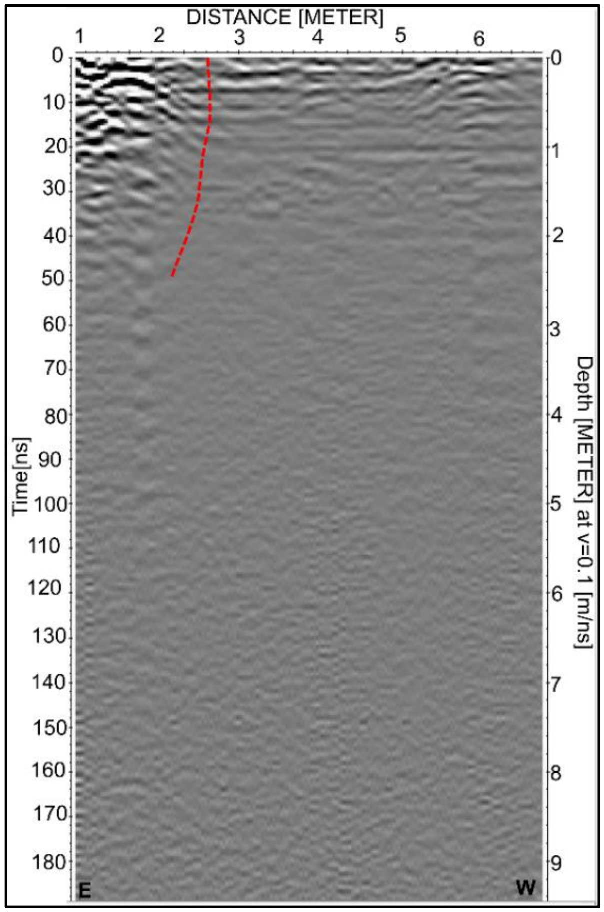

Figure 7.12: Interpreted GPR data of R21SINK003_003 are represented by the red dashed lines.

Figure 7.13 shows the schematic model derived from the GPR section, demonstrating the formation and detection mechanism of the sinkhole. Sinkholes in GPR studies are typically identified by specific characteristics. These features may include hyperbolic responses. When the GPR signal encounters a void or cavity, it can create hyperbolic events. These events can indicate the presence of a potential sinkhole (see Figure 7.13). In GPR sinkhole detection, radar pulses are crucial for creating images of the subsurface and identifying potential sinkholes.

The GPR emits electromagnetic pulses (shown by black arrows in Figure 17.3 (a)) into the ground from an antenna. These radar pulses penetrate the subsurface materials (such as soil, rock, or other geological layers). As the radar pulses encounter different materials with varying electrical properties, they are partially reflected to the surface. The

GPR system's receiver detects the reflections (echoes) of these radar pulses. Sinkholes often create voids or cavities underground. When the radar pulse encounters a void, it generates a distinct hyperbolic reflection, or diffractions shown in Figure 7.13 (b).

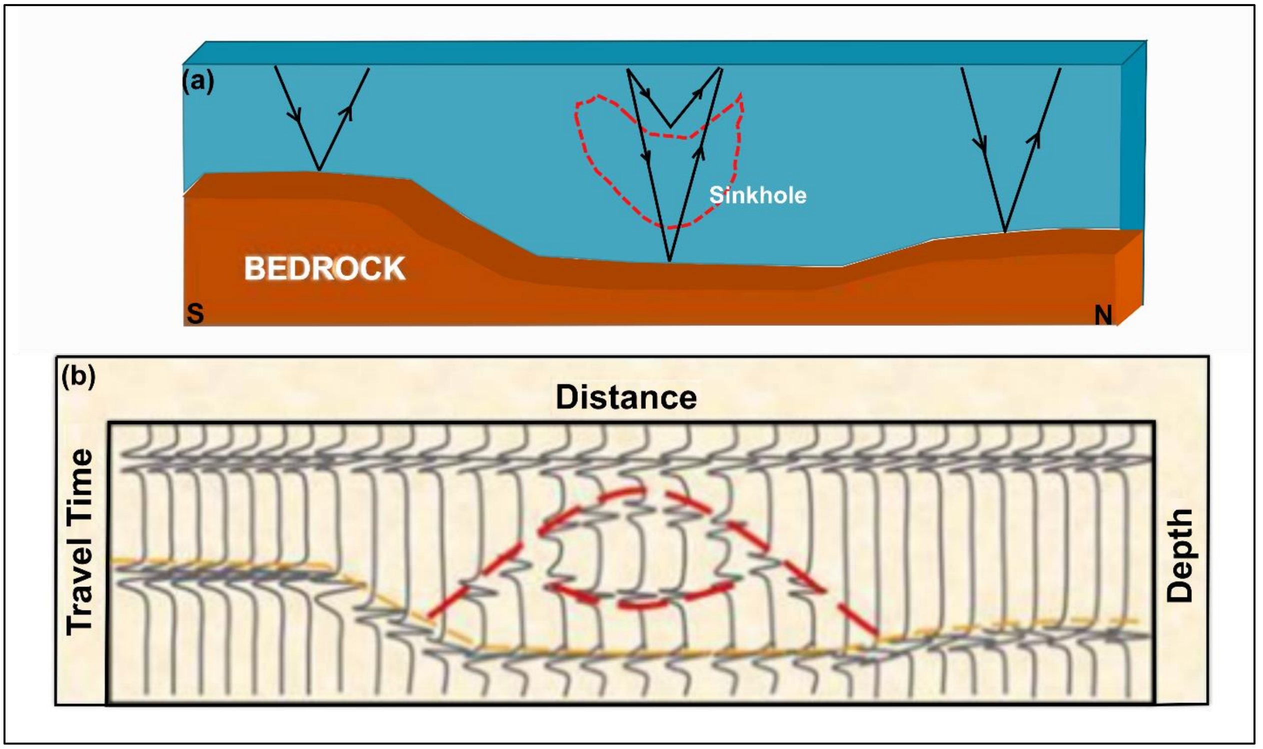

Figure 7.13: Schematic model depicting the R21 sinkhole and how it was detected by the GPR. (a)This model provides a basic visual representation of how GPR works to detect the presence of a sinkhole beneath the ground surface. It highlights the process of sending and receiving radar waves (in black arrows) and identifying anomalies that indicate the presence of the sinkhole (shown red dashed lines), (b) the diffractions indicate the possible presence of a sinkhole (Parwatiningtyas, 2021).

ReflexW was used to create 3D digitised hyperbolas, for all the three groups of GPR data (R21SINK001, R21SINK002, and R21SINK003). This was done by creating time slices of the lines in each group, see appendix B, Figures B14 and B15 under field data results. This was also done for the other two groups (e.g., R21SINK001 and R21SINK003). Time slices were created for each line to create the 3-dimensional hyperbolas, they are shown in appendix B, Figures B16 and B18.

7.3 Refraction and Reflection Seismics

Three seismic refraction and reflection profiles were conducted along the R21 sinkhole. Only the results from profile lines 2 and 3 are presented here. Other profiles are presented under the field result data in Appendix B, Figures C1 to C4. Diffractions, indicated by red and pink dotted lines in Figure 7.14, are well defined by the seismic stacked section. Diffractions occur across the seismic sections between 5 and 15 m depths below ground surface. The diffractions are compartmentalized and dissected by several faults and fractures (black lines) of various orientations and throws. R21 sinkhole is associated with the pink colored diffraction at ~ 70 m offset and at depths between 10 and 18 m below the surface.

Delineation of fractures or faulting around the sinkhole zones may indicate that the sinkholes are structurally controlled. Figures 7.15 and Figure 7.16 show the P-wave refraction tomograms for lines 3 and 2, respectively. The P-wave refraction tomogram in Figure 7.15 shows two low-velocity zones marked by pink and black dotted lines. The low-velocity zone occurs at distances between 0 m and 12 m and between 24 m and 42 m. The dotted black line may represent the R21 sinkhole, at a distance between 24 m and 42 m. This sinkhole is at an elevation between -1536 m and -1544 m corresponding to about 8-10 m depth below the ground surface. A possible sinkhole that has not yet manifested on the surface is shown by the pink dotted lines between 0 m and 12 m distances. This sinkhole is at an elevation of -1538 m and -1547m and is ~12 m wide. The high-velocity zone from an elevation of ~1536 m indicates possible fresh dolomite bedrock. Figure 7.16 shows a low-velocity zone between 19 m and 43 m distances, corresponding to a possible sinkhole collapse structure.

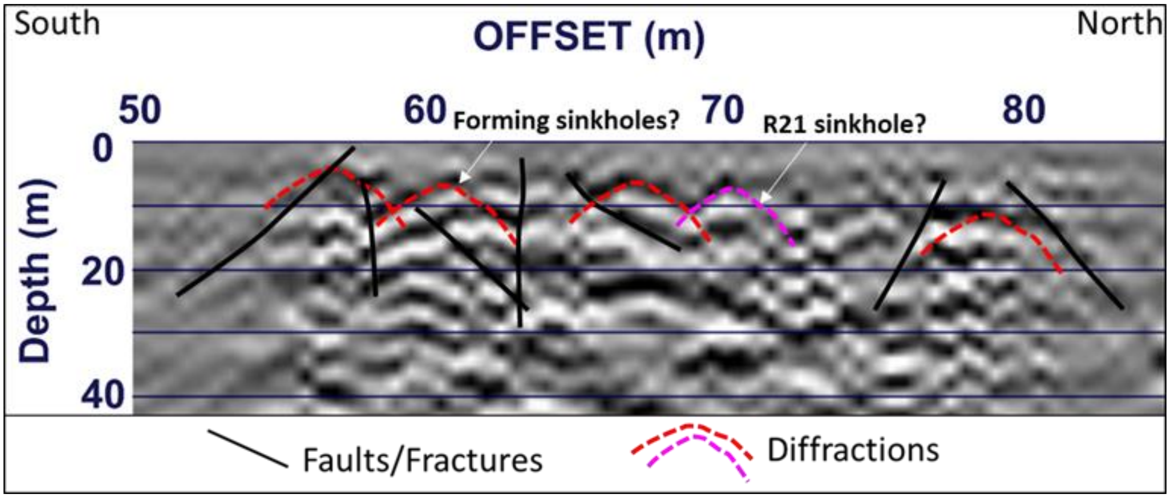

Figure 7.14: Line 3 processed section with R21 sinkhole represented in pink and possible sinkhole shown in red dotted lines.

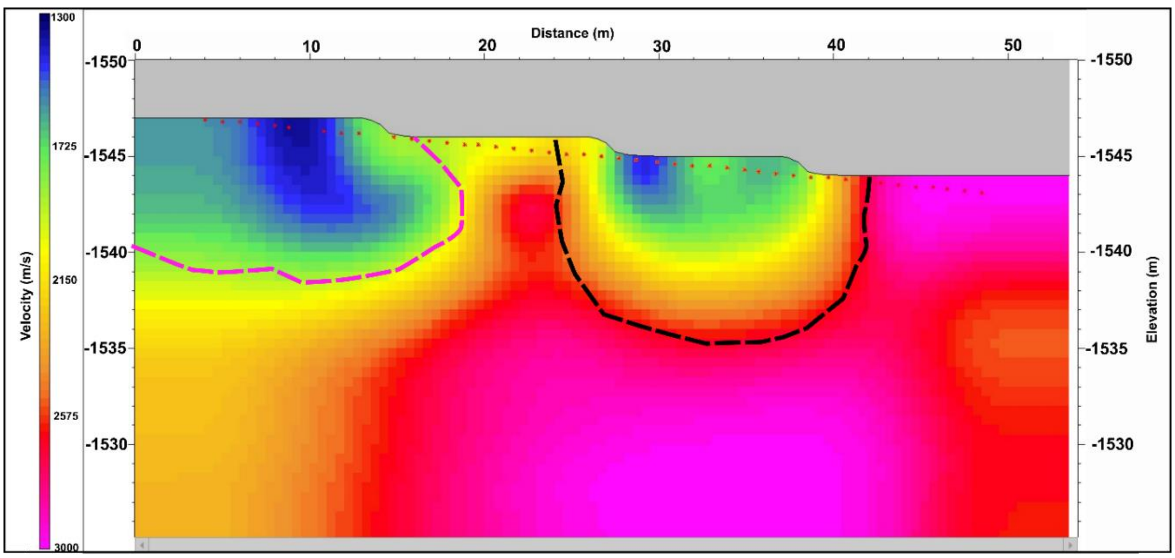

Figure 7.15: Interpreted south-north P-wave seismic tomogram for line 3, with possible sinkhole represented in pink and R21 sinkhole shown in red dotted line.

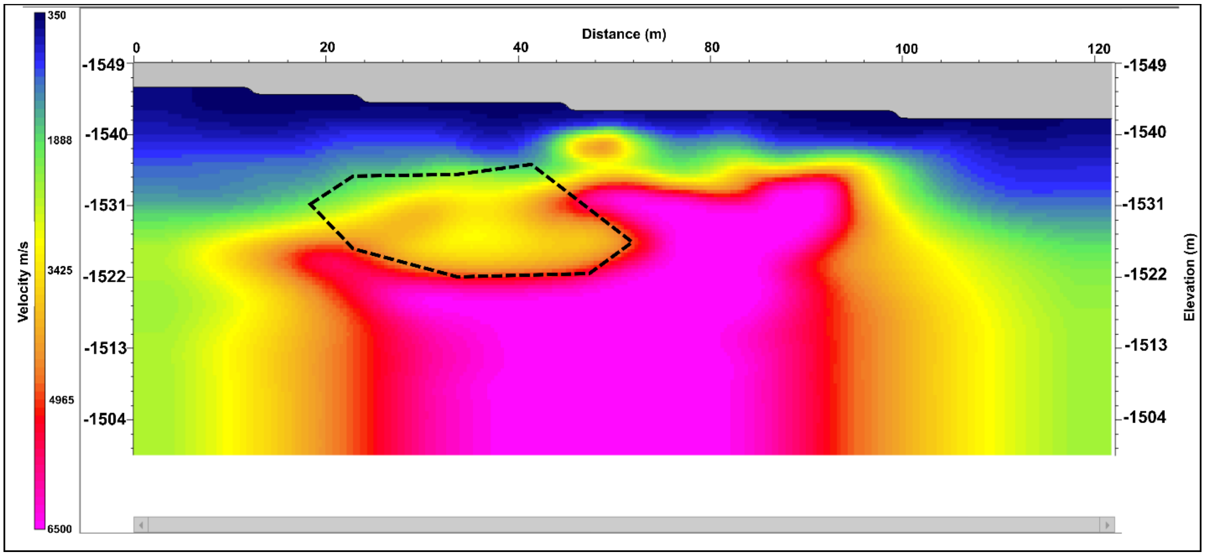

Figure 7.16: Interpreted south-north P-wave seismic tomogram for line 2, a possible sinkhole is sown by a black dashed line.

7.4 Multichannel Analysis of Surface Waves

The Vs (shear wave velocity) values of some common Earth's materials are shown Table 7.2 (NEHRP, 1997) and these were used to constrain the MASW results interpretation. The 2D shear wave velocity model of line 1 is shown in Figure 7.17. The profiles not shown in this section are presented under the field result data in Appendix D, Figures D1 to D4. Multiple 1D Vs profiles were obtained along a seismic line, with each 1D Vs profile associated with its specific location along the seismic line. This spatial information was crucial in creating the 2D cross-section in Figure 7.17. Zone 1 (or layer 1, red dotted line in Figure 7.17) of low shear wave velocities (≤ 500 m/s; bluish-white to deep and sky-blue colour) cover the top 1 to 7 m depth. This layer consists of other anomalies with variable velocities. Generally, based on the velocities, the zone is interpreted to consist of highly fractured dolomite with chert material, clays, silt and gravel.

Layer 2 (below the black dotted line in Figure 7.17) exhibits Vs with intermediate values at the range of 500 m/s≤ Vs≥ 600 m/s (bluish green to green and greenish yellow to yellow colour). The layer lies between 8 and 20 m depth below the ground level with variable thicknesses. Layer 3 has relatively high Vs values (Vs≥600 m/s) (yellow to red and black colour, Figure 7.17), which represent the bedrock and other hard or compacted materials. Shear wave velocity is increasing as a function of depth, which is generally observed where the bedrock is mapped from of 20 m depth down with high Vs values (>

600 m/s). In general, the rocks mapped include dense soil overlain by the stiff soil to depth of 25 m. These results are consistent with those reported in lietrature (Table 7.2).

Table 7.2: The values of some shear wave velocities (Vs) for common Earth's materials (NEHRP, 1997).

Earth Material	Average Vs
Hard rock	>1500 m/s
Very dense soil and soft rock	360-750 m/s
Stiff soil	180-360 m/s
Soft soil	<180 m/s

One possible explanation for the denser surficial soils could be the area's frequent vehicle movements causing compaction. Denser soils exhibit Shear wave velocities ranging from 460 to 580 m/s, while stiff soils have velocities of roughly 260-340 m/s. The estimated Shear wave velocity values of soil/rock at the R21 highway are shown in Table 7.3.

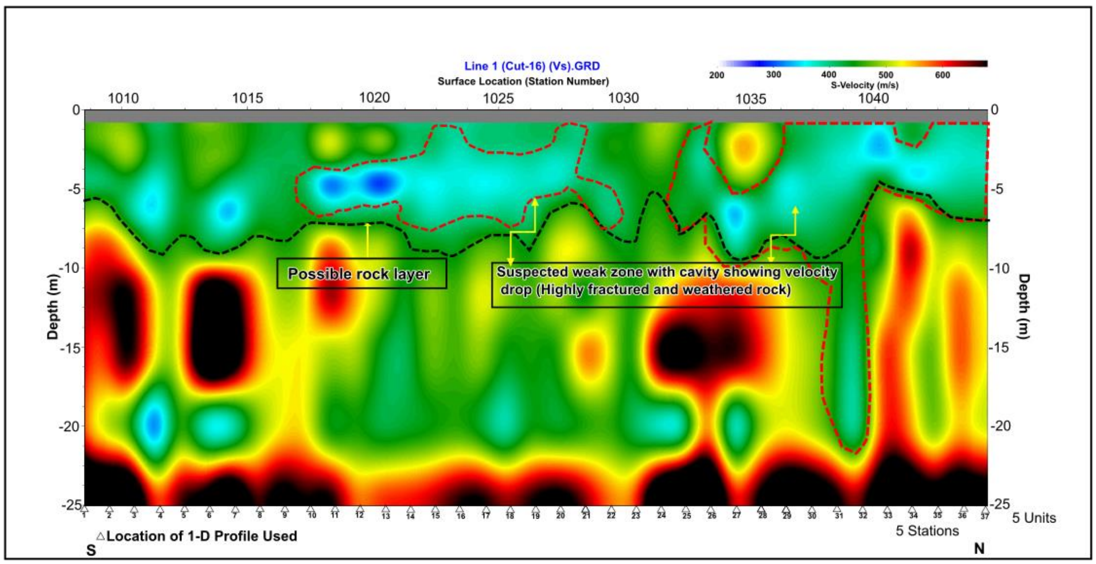

Figure 7.17: Inversion of the data to obtain 2D shear wave velocity seismic section of line 1. The red dotted line shows the weak zone associated with cavities and highly weathered rocks. The black dotted line represents an interface between the top zone and the zones below. The zone from 22 m depth down represents the bedrock or a partially weathered zone.

Table 7.3: Estimated shear wave velocity values of soil/rock at R21 highway.

Depth (m)	Description	Vs (m/s)
0-4.38	Dense soil/soft rock	460-500
4.38-8.75	Stiff soil	280-340
8.75-15.63	Dense soil/soft rock	610-690
15.63-20	Stiff soil	260
20-25	Dense soil/soft rock	580

Shear wave velocity profile from the 1D profile provides Vs values at different depths (Figure 7.18). Seismic velocities generally increase as a function of depth. This is not fully supported by Figure 7.18, indicating different lithologies or material properties along the depth profile. Low Vs values blow high values may indicate layers characterised by subsidences, cavities and fracturing.

The superposed geological interpretation in Figure 7.18 is derived from Table 7.2. There is a notable decrease in Vs from the surface (500 m/s) to 4.5 m depth (250 m/s), indicating a change in subsurface material or compaction. This is a zone of dense soils/soft rock. There is a further decrease in Vs at a depth of 4.5 m (~260 m/s) to 9 m, which could suggest a minor change in material properties or compaction at this depth. The Vs remains relatively constant at 630 m/s, indicating a more uniform material property or lithology, expressing dense soils. There is a sudden drop of velocities at 15.5 to 20 m depths from ~650 to ~260 m/s, respectively. The gradual increase in Vs from the surface to 20 m indicates a change from a softer to a stiffer material, possibly from loose soil to more compacted soil or rock (~500 m/s). The sudden decrease in Vs at 15 m depth suggests the presence of a void or a sinkhole. The lower Vs values below the sinkhole might indicate disturbed or loose material.

While MASW is not the primary tool for sinkhole detection, it provides some indirect indications, especially in terms of anomalous Vs values or irregular layering patterns. For a comprehensive assessment of sinkholes, it's best to combine MASW with other geophysical as done in this study.

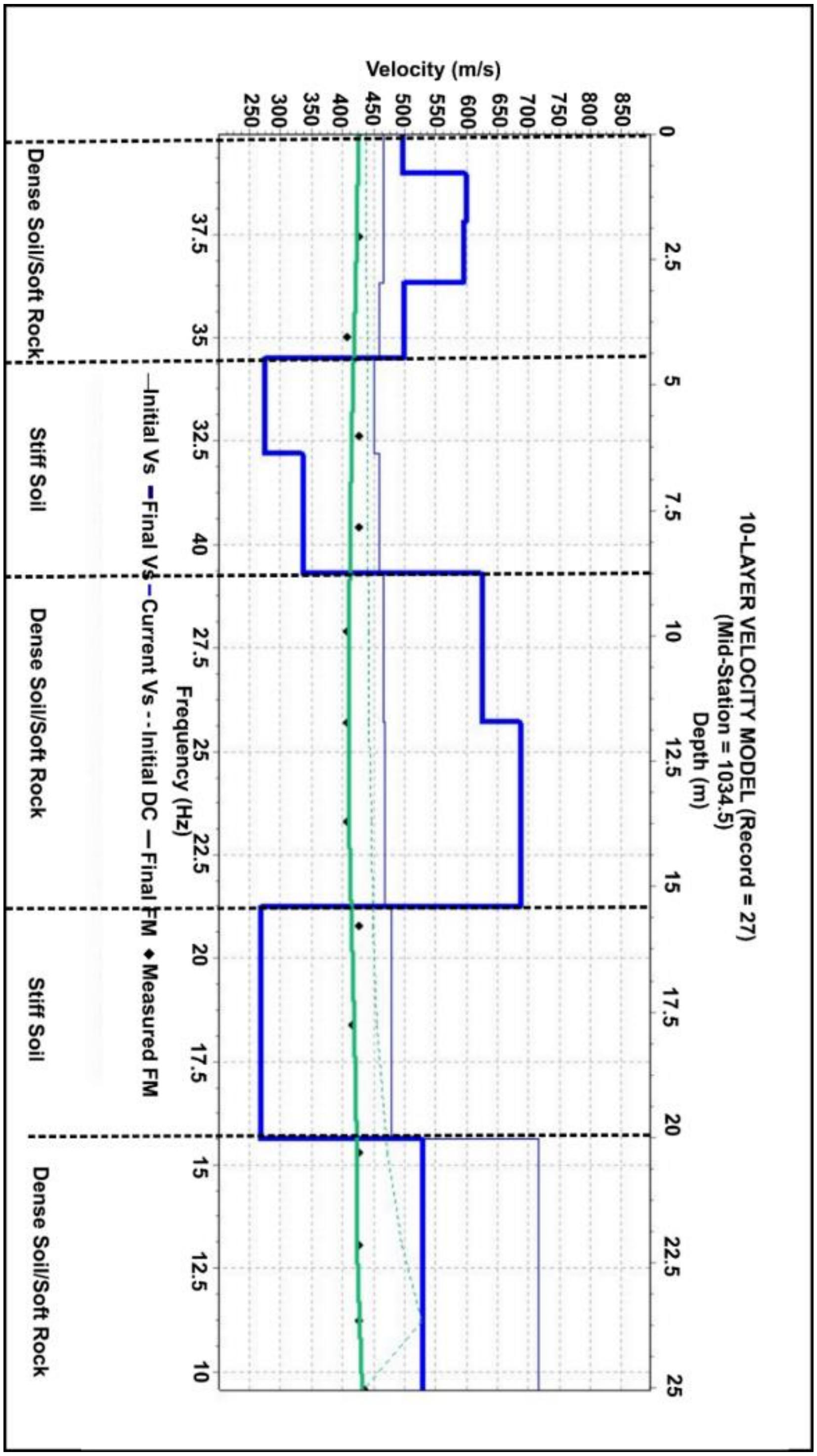

Figure 7.18: MASW Shear wave velocity profile obtained from the dispersion curve from 1D profile 27, with superposed geological interpretations. Velocity is in m/s.

8 DISCUSSION

The Formation of the R21 sinkhole

Sinkhole formation is a complex process influenced by the geology of the area (Beck and Sinclair, 1989). The presence of soluble bedrock, such as dolomite, near the surface is a key prerequisite for sinkhole development. This is the case with the area of Olifantsfontein where the R21 sinkhole is found. Groundwater, as mentioned previously, also plays a critical role in the formation of sinkholes. Groundwater sets the stage for sinkhole collapse or subsidence with its dolomite solution and plays a vital role in sinkhole development. Sinkholes ultimately form due to the natural dissolving of dolomite, which underlies much of Olifantsfontein. This dissolution mechanism is exceedingly slow and occurs over 1000s years. The solution process is most active where numerous vertical cracks (or fractures) in the dolomite facilitate the water flow. The dolomite is generally riddled with channels, conduits, and voids which are the result of countless centuries of natural erosion (Roux, 1991; Van Niekerk and van der Walt., 2005).

Because sinkholes are a response to water circulating the dolomite, they tend to form in areas where the dolomite aquifer is recharged. The area of Olifantsfontein is also referred to as “Clayville”, as the result of the presence of clay in this town. This has resulted in numerous mining companies such as Technicrete, Sterkfontein Bricks, Victoria Bricks, Corobrik, and Afrimat, all having quarries that extract this clay material to make bricks, cement, erosion protection blocks, and pave manufacturers. Rainwater not only infiltrates the groundwater in this area but also contributes to the infiltration of water in these quarries resulting in the fluctuation of the water table. Most, if not all, of these quarries have fluctuations in their water tables.

The mining operations in the mining area around the Far West Rand region played a role in lowering the groundwater level by over 100 meters. This substantial reduction in groundwater levels resulted from dewatering activities associated with mining operations (Buttrick and van Schalkwyk, 1998). The groundwater table lowering in dolomitic aquifers can lead to the destabilization of underground voids and cavities that were previously supported by buoyant groundwater pressure. As the water table recedes, unsupported cavities may collapse, resulting in the formation of sinkholes at the surface. Because sinkholes are localized by underlying geologic factors such as fracture zones, they tend to form in clusters and sometimes in linear patterns. Thus, areas marked by numerous sinkholes, particularly recent ones, are likely to be the areas where new sinkholes form. This is the case with the area where the R21 sinkhole is found. Other sinkholes have formed over the years in this area (see Figure 6.2).

Highways and roads typically have stormwater drainage systems designed to collect runoff from precipitation events. When stormwater runoff is collected by drainage systems and deposited into the surrounding areas, it can saturate the upper layers of the bedrock. Avutia and Kalumba (2014) state that the main mechanisms regarding the mobilization are surface water infiltration and groundwater extraction. Human activities such as the bursting of underground pipelines, buried sewage systems, and stormwater drainage systems can accelerate the formation of sinkholes (Montjane *et al.*, 2020). Guatemala City in Mexico is one of the cities that was affected by sinkholes caused by man-made structures, where sinkholes were formed because of an underground sewage system (Hermosilla, 2012).

The fluctuation in the water table might be due to the extraction of water in the quarry. The location of the R21 sinkhole is about 500 m to 750 m from one of the quarries in Olifantsfontein. This is an acceptable and reasonable distance for hydro-geological processes to begin and cause significant changes such as the equilibrium in the dolomites and changes in the water table, resulting in sinkholes forming. This could be another possibility in explaining the reason why so many sinkholes occur so close to this area since the R21 sinkhole is not an isolated incident. Therefore, the formation of R21 sinkholes and those around it would likely follow the ingress scenario. The infiltrated water may have saturated the upper layers of the dolomite bedrock (Oosthuizen *et al*., 2011). Dolomite dissolution can occur within a wide pH range, between 6 to 8 (Pokrovsky *et al.*, 2001; Oosthuizen *et al*., 2011). Therefore, even under relatively neutral pH conditions, dolomite dissolution can occur, especially over extended periods. It is considered that if a sinkhole is a result of anthropogenic activities, it likely existed for ~50 years while if it's a result of natural occurrences, it might be over 1000 years (Alzahrani, 2020). The presence of fractures and faults (as delineated by the seismic surveys in Figures 7.14-7.16) suggest that these structures might have acted as conduits, allowing the water flow from the surface to the dolomite bedrock. The presence of these structures, together with circulating water eroding the dolomite bedrock, may have accelerated the formation of the sinkhole.

Expansion of structures such as roads and highways that resulted in the water being directed in drainage systems in ways to prevent flooding on these structures has resulted in the infiltration of water on the subsurface, disturbing the state of equilibrium that has prevented sinkholes from forming (see Figure 8.4). The storm water drainage pipes, as shown in Figure 8.4, are diverting rainwater from the highway. It might be this very same water that is slowly eroding the bedrock on the western side of the highway. Water concentration from a single point, in this case this storm water drainage pipes, might be causing the sinkholes to form.

The Use of Geophysical Methods on the R21 Highway Sinkholes

Carbonel *et al.* (2013) conducted a similar study using GPR and ERT to detect a sinkhole in a karst environment, the Zenzano Fault (Iberian Chain, N Spain). Alzahrani (2020) also used two methods, MASW and ERT, to detect a sinkhole in southern Missouri, a region known for its carbonate rocks.

The ERT is the best method out of the four methods used in this research for detecting the R21 sinkhole. This is because of its ability to clearly show the distinct zones showing high resistivity that are normally associated with sinkholes-filled air and unsaturated, conductive material. This zone has resistivity values of between 2551 to 9500 ohm.m. Figure 7.1 shows line 1, which is closest to the R21 sinkhole. This profile has two high resistive zones, at distances of ~37 m to ~57 m and ~78 m to ~104 m. The zone at ~37-~57 m represents a possible sinkhole that has not yet manifested itself on the surface, i.e., it is still forming. The zone between ~78 and ~104 m is the possible location of the R21 sinkhole. The depth range (top to bottom) of the R21 sinkhole is ~6.72 m - ~19 m, while that of the forming sinkhole is at depths between ~6.72 m and ~14 m. The moist clayey soil, low resistivity, and saturated layer exhibit resistivity values of 55.5 to 119 ohm.m (Figure 7.1).

The second profile (line 2) is shown in Figure 7.2 and is 2.5 m parallel to line 1 and has a high resistive zone associated with the R21 sinkhole at 78 m and 103 m distances. On this profile, the sinkhole is found at depths of ~5 m and ~12 m. The next profile is line

4, shown in Figure 7.3, which is also 2.5 m from profile 1, but on the western side of the sinkhole and where most of the older sinkholes are located on the study area, unlike the first two profiles that are on the tarred surface. This profile has a high resistive zone, towards the end of the profile at distances of ~243 m and ~332 m. On this profile, the resistive zone represents the R21 sinkhole and occurs at a depth range between ~12 m and ~57 m.

The last profile, line 5, is shown in Figure 7.4. This profile was designed to determine the extent of the sinkhole into the other south bound lane. This profile sits in between the south bound lane and the north bound lane. The section exhibits a high resistive zone between ~70 m and ~125 m distances along the profile and occurs at ~13 m and ~40 m depths. This could be a sinkhole that has not manifested on the surface. On the northern section of the profile, lies a weathered zone with resistivity values of between 3378 to 7121 ohm.m. The conductive areas in both profiles 4 and 5 suggest a structural linkage between the stormwater drainage system and the potential sinkhole under the R21 highway. This provides some evidence that the formation of sinkholes may be caused by groundwater infiltration (through fractures as defined by the seismic data in Figure 7.14).

To address the question of the ERT method recording the air-filled stormwater drainage systems that are found in the study area, as they are very close to the R21 sinkhole and have similar resistivity values, as shown in Table 7.1. This can easily be explained by the fact that the location of the sinkhole is not exactly on top of stormwater drainage system, but the stormwater drainage system is about ~1- ~2 m further north of the R21 sinkhole (Figure 8.5). The ERT suggests that the sinkhole in this location is ~26 m wide and occurs at ~12.9 m depth, while the diameter of the drainage system is 0.450 m. This clarifies the possibility of the ERT and stormwater drainage system being confused or questioned as the same.

The second method used in this research is the GPR. Figure 7.8 (b), profile R21SINK001_001 (group one), displays a GPR section that runs south to north of the highway. The sand/clay interface is delineated throughout the section. For example, the GPR section exhibits a consistent lateral reflection (shown by the yellow dotted line in Figure 7.8 (b)), with varying depths from south to north (i.e., ~2 m in the north and ~3 m in the south). This reflection is interpreted to represent the interface between near-surface geological boundaries. When electromagnetic (EM) waves encounter a boundary between two different media with contrasting dielectric constants, some of the waves are reflected back into the original medium, while others may be transmitted into the second medium. This occurs at boundaries with distinct lithological units. Understanding how electromagnetic waves interact with these boundaries is crucial for interpreting geophysical data and gaining insights into the subsurface structure and composition (Huggenberger *et al.*, 1994). For example, in a GPR survey of an area with alternating layers of sand and clay, the boundaries between these layers will cause reflections due to their contrasting dielectric constants. If there is a layer of sand that transitions from dry to saturated, this change in water content can also cause a reflection (Huggenberger *et al.*, 1994). The rocks in the study area are primarily weathered, jointed, and fractured dolomites that have frequently solution-widened and been infilled with clay. Figure 7.9 (b) shows a south-to-north trending profile of R21SINK001_003 also from group one. It exhibits a series of reflections indicated by the yellow lines, representing an interface between near-surface geological boundaries. A series of diffractions occur between ~2 and ~6 m depths. Figures 7.11(b) and 7.12 show another south-to-north trending profile from group two, R21SINK002_001 with similar diffractions (shown in red) as in R21SINK001_001 and R21SINK001_003. These diffractions occur between ~2 and 6 m depths. The GPR shows diffractions from the top of sinkholes shown in Figures 7.8 (b), 7.9 (b), and 7.10 (b) (Telford *et al.*, 1990; Fiedler, *et al.*, 2009; Barone, 2012). Typically, the sinkholes are mapped within a depth range of ~2 m to ~6 m.

An east-west trending profile of R21SINK003_003 (group three) is shown in Figure 7.12. Some diffractions exist closer to the location of the sinkholes. These diffractions are about ~2.5 m into the highway and are at a depth of ~8 m. Another east-to-west trending profile (R21SINK003_015 from group three) is shown in Figure 7.11 (b). Shown by the red dashed line in Figure 7.11 (b) are diffractions that indicate the extent of the sinkhole into the highway. This suggests that the sinkhole extends by ~2.5 m into the highway and has an estimated depth of ~8 m. Knowing how far the sinkhole extends into the highway is important as it can help with the planning (e.g., knowing how many to close off and the safety of commuters). This is the reason several (about 25) east-to-west GPR profiles were conducted near the sinkhole. In the area with the R21 sinkhole, the depression of the sand/clay interface into a funnel shape is observed and this is a strong indicator of subsidence at depth. Several reflections mapped at the deeper parts of the section (below the depression of the clay/sand interface) are indicative features of the extent limit of the sinkhole (see Figures 7.8 (b) and 7.10 (b)).

The seismic method is the third method used in this study. The non-continuous, chaotic zone in reflections across the top part of the stacked reflection seismic profile in Figure 7.14 is consistent with the disturbed near-surface rock layers that are caused by sinkholes that probably exist within the dolomitic zone in this region. The absence of comprehensible reflections from the R21 sinkhole as well as the existence of diffractions on the section may indicate that there are structural changes to the overburden, such as faults or fractures. The location of the sinkholes in profile 3 is shown in Figure 7.14 at CDP 100 to 115 and at CDP134 to 155 (R21 sinkhole) indicating these non-continues refection areas that are associated with the sinkholes.

In Figure 7.15, the P-wave tomogram detected two low-velocity zones between distances 0 m and 12 m as well as 24 m and 42 m. The dotted black line in this profile represents the R21 sinkhole between 24 m and 42 m distances. A possible sinkhole that has not yet manifested on the surface is shown by the pink dotted lines between 0 m and 12 m distances (Figure 7.15). Figure 7.16 shows a low-velocity zone between ~19 m and ~43 m distances. This area has a noticeably low velocity and suggests the presence of loose or weakly compacted subsurface material.

The fourth method used in this research is the MASW. Higher shear wave velocities are typically seen in competent rocks and stiff/dry soils as opposed to soft/moist soils and weathered rocks (Alhaj, 2022). The signal-to-noise ratio, however, may be lower in a site with soft and/or widely fractured rocks than in other places where competent rocks and stiff soils dominate. This is due to the variability of the subsurface (in lateral and vertical strata). The complex nature of the site, being a karst environment, may cause a reduction in the imaging resolution of the MASW (Varnavina *et al.*, 2019). The interpretation of the MASW is therefore based on the assumption that detected variations in the subsurface's acoustic characteristics reflect equivalent changes in geology lithology. In this study, the lithologies present were classified and interpreted into two categories as described below.

- Dense soil/soft rock is characterised by Vs less than 750 m/s

- Stiff soils are characterised by Vs less than 350 m/s

The R21 sinkhole is suggested to be on the northern section of the MASW profile, shown in Figure 7.17. A low-velocity zone indicating this sinkhole is shown between station numbers 1032 and 1045, with varying depths of ~1 to ~18 m. On the southern section of the profile is where a possible sinkhole that has not yet manifested itself on the surface is located. This low-velocity zone is between station numbers 1017 and 1028 and at depths between ~1 m and ~7 m (top and bottom). Sinkholes or voids, if air-filled, typically show up as a zone of low shear wave velocity.

According to the MASW results, the low shear velocity zone may have resulted from seepage of rainwater, runoff, and water transported by migration pathways from the water drainage system into the subsurface. This applies to soft or loose soil as well as spaces that are filled with air or water. A closer look into the ERT and MASW results indicates the differences in the two methods for the location of the two sinkholes. This is expected as these two methods measure different parameters.

Integration of ETR, GPR, Seismic and MASW Profiles

Profiles from each of the four methods used in the study are presented in Figure 8.1. All the profiles have similar indicative structures of sinkholes forming towards the northern direction of the site, representing the R21 sinkhole (Figure 8.1(a)-(d)). Similar indicative structures are also observed on the southern side of the profiles, indicating a sinkhole that has not yet occurred on the surface. These sinkholes probably occurred in weaker zones of the rocks and may confirm the possibility of the ingress scenario as a driver for a sinkhole formation. These are also observed on the south-north P-wave refraction tomogram and MASW profiles (Figure 8.1(c), (d)).

All methods used are complementary as they demonstrate different capabilities in mapping the sinkholes and associated geological features. For example, diffractions from the GPR data correspond to the highly resistive zones in the resistivity profiles that are associated with air-filled sinkholes at depths between 4 and 6 m (Figure 8.1(a), (b)). These zones, in turn, correlate well with the low P-wave and S-wave velocity zones in the P-wave tomogram (Figure 8.1(c)) and MASW profile (Figure 8.1(d)), respectively.

The advantage of the resistivity results over other methods is that the resistivity method can differentiate between a water and air-filled sinkhole, while other methods cannot. GPR, on the other hand, is also able to constrain the depth of the sinkhole by mapping the geological interface above the sinkhole. Seismic results can also map the fractures around the sinkhole, which is not easy to do with other methods. Vs model from MASW results is also able to map the sinkhole below the high-velocity zone (road material), which is difficult with the P-wave refraction. Figure 8.2 shows the formation schematic model of the R21 sinkhole as derived from the integrated geophysical results.

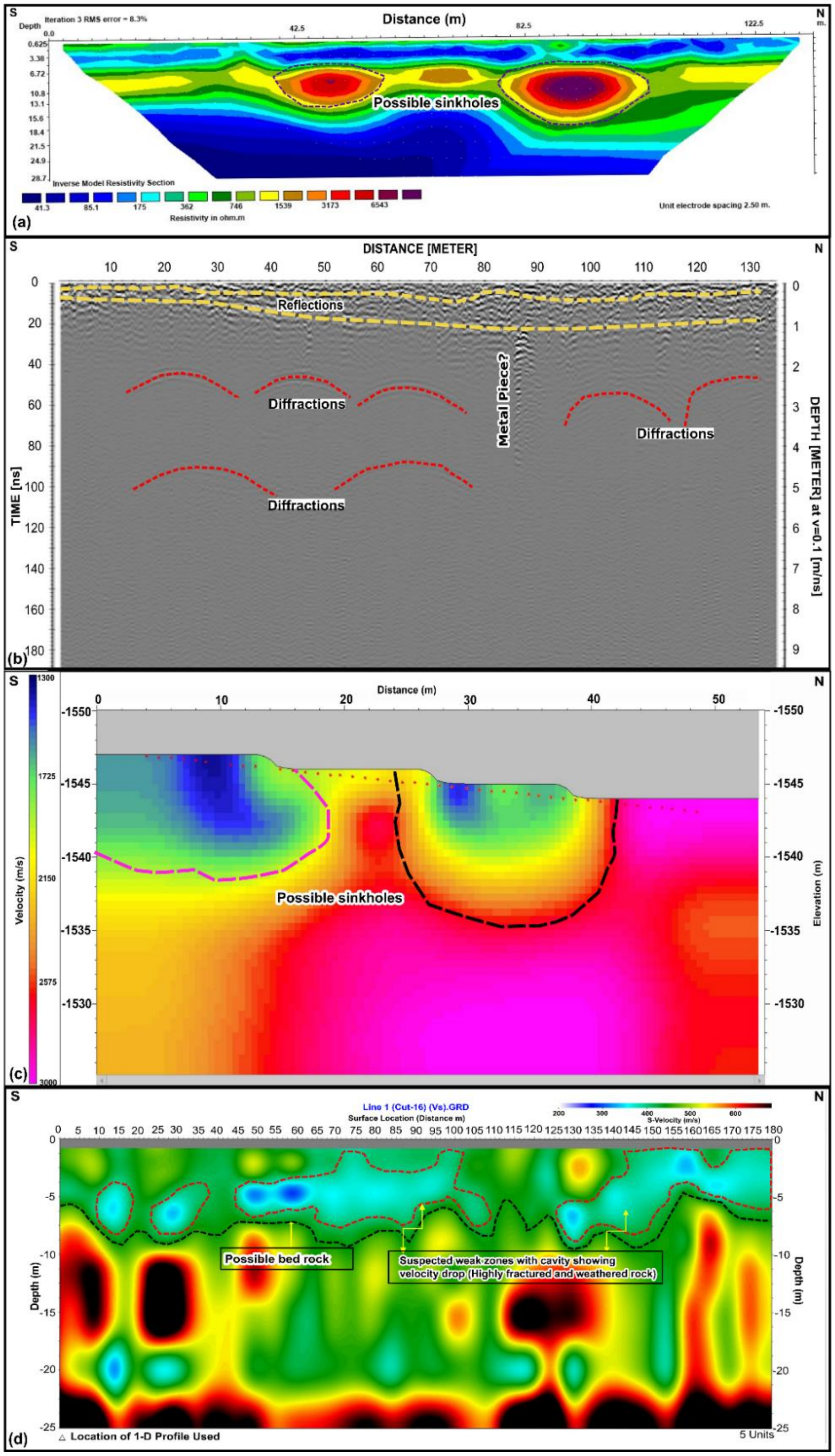

Figure 8.1: Combined images of line 1 from each of the four (4) methods: (a) ERT with the R21 sinkhole on the northern section; (b) GPR with the R21 sinkhole, also on the northern section shown by the diffractions; (c) Seismic section, also with the R21 sinkhole on the northern section and (d) with the R21 sinkhole on the northern section.

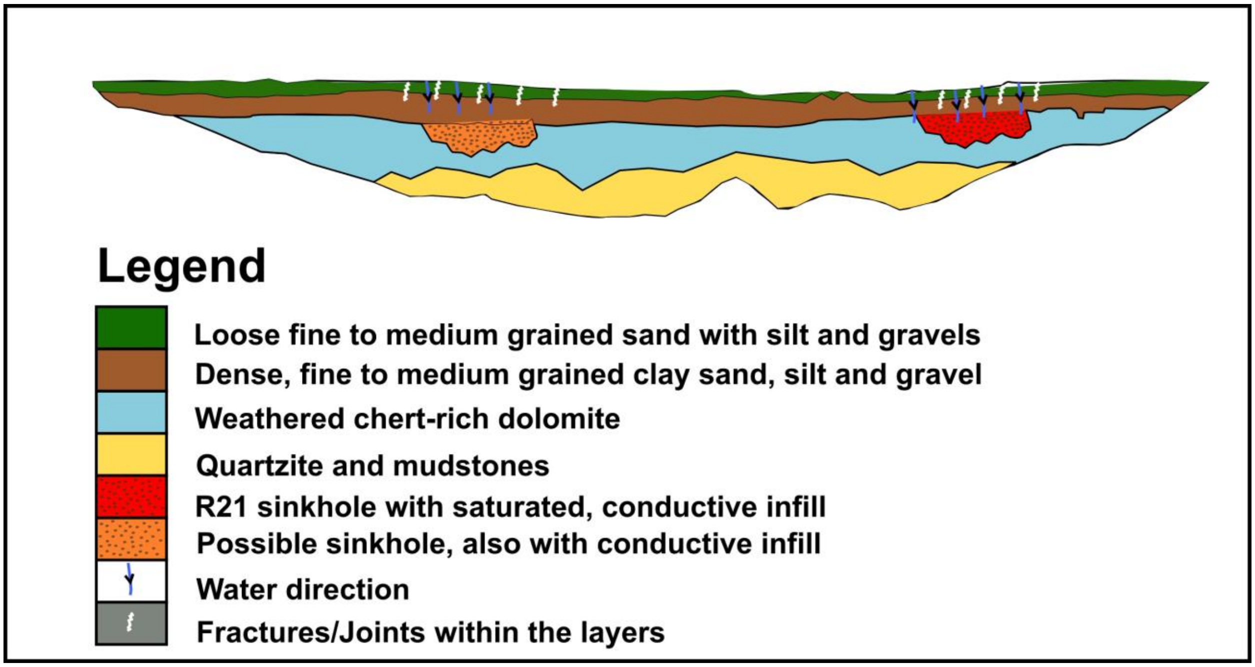

Figure 8.2: A model showing the mechanism for the formation of the R21 sinkhole. The fractures and joins are shown in white on the top layer. The ingress of water is shown by the blue and black lines, also on the top layer. There are two sinkholes with conductive infills, which are shown in orange (possible sinkholes) and red (R21 sinkhole).

Sinkholes are typically not created by simply lowering the water table. Land subsidence often only happens when the support for the material (unconsolidated) above is removed (Foose, 1967) (Figure 8.2). Formation (or triggering) mechanisms may include (summarized in Figure 8.2): (a) change in the water table, (b) shrinkage of the volume, (c) gradient and water velocity increase, (d) loss of buoyant support, and (e) induced recharge.

The stormwater drainage system around the R21 highway is engineered to purposefully direct water from the highway into the subsurface on the sides of the highway. The ERT high resistive sinkhole on the ERT profile 1 may therefore be attributed to seepage of water from the drainage system. Water might have seeped through horizontal and vertical geological features into the subsurface. The subsurface water flow has likely caused the creation of the cover collapse sinkhole, as now observed in R21. The possible version of events is shown in Figure 8.3, the storm drainage system is directly opposite one of the older sinkholes around the study area. It is possible that the R21 sinkhole was also formed in this manner.

In Figure 8.4, the resistivity profile from line 1, the closest profile to the R21 sinkhole, shows the location of the stormwater drainage systems and the location of the 2 sinkholes in very close positions to these drainage systems. In Figure 8.5, the ERT profile 1 shows the positioning of the sinkholes in relation to the storm drainage systems as a model. This, again, emphasises that these sinkholes are structurally controlled and that geological features played a critical role in their formation. These sinkholes were caused by groundwater infiltration and probably got worsened by the dissolution of carbonate minerals due to acidic rainwater inundation and constant irrigation. For future studies, we plan to also use the gravity method to enhance the delineation of the sinkholes.

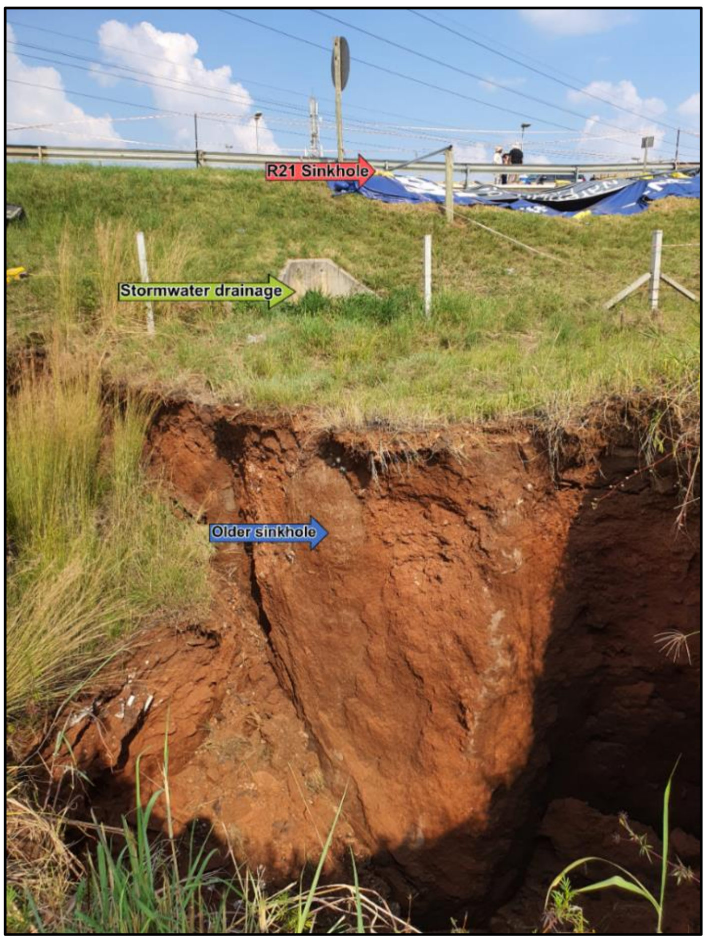

Figure 8.3: Stormwater drainage location in relation to the older sinkhole and the newer R21 sinkhole.

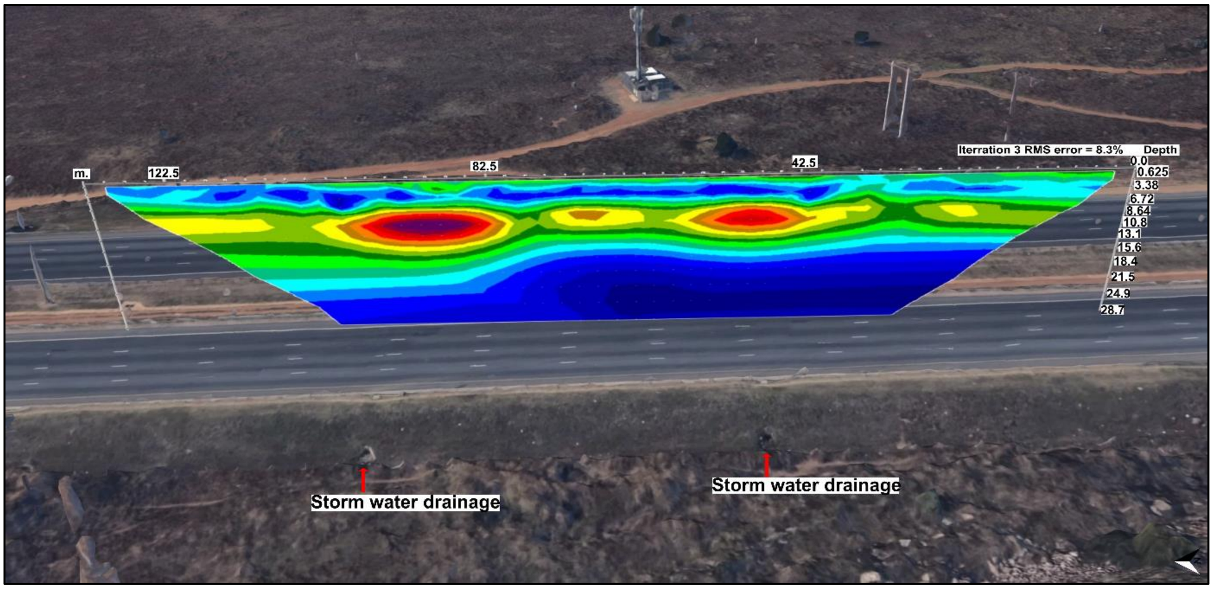

Figure 8.4: Google Earth image showing the location of the stormwater drainage in relation to the R21 sinkhole and the possible sinkhole on the southern ERT section of the profile.

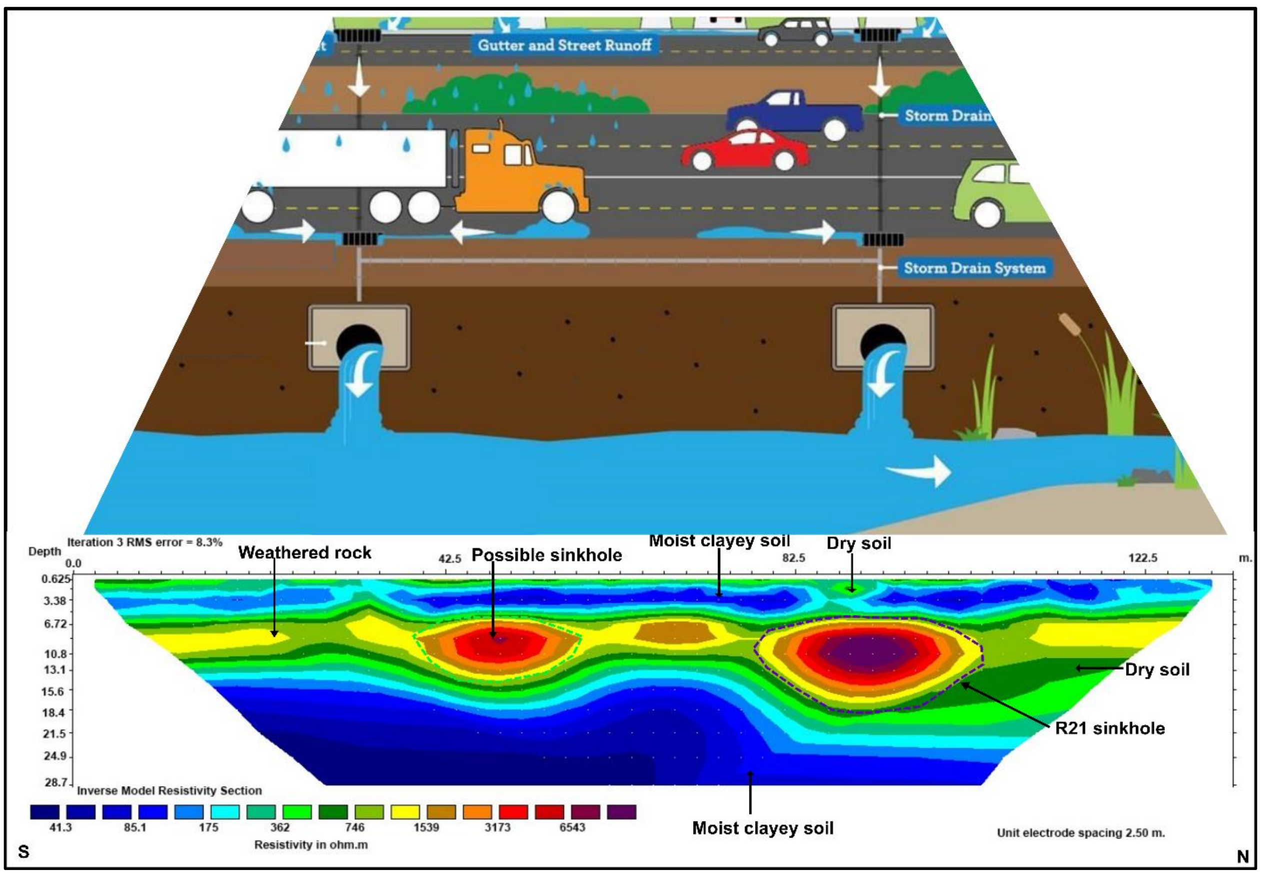

Figure 8.5: Model used to depict the formation of the R21 sinkhole. (modified from www.flooddefenders.org).

Field Challenges

The location of the study area was challenging in terms of noise. Figures 8.6 (a) and (b) show the sources of noise, and high voltage powerlines with trucks and cars along the study area. Figure 8.6 (c) shows the raw shot gathers with background noise. The site has high-voltage power lines that affect some methods such as seismic. Since this is a national freeway, it means that there is always high traffic volume, especially since it's not too far from one of Gauteng's busiest airports (O.R. Tambo International Airport). There were also structures such as metal pieces, shown in Figure 7.10, on the road that were used to restore the road and prevent potholes from forming as part of the maintenance of the freeway by SANRAL (The South African National Roads Agency SOC Ltd). These metal pieces were observed on the GPR data.

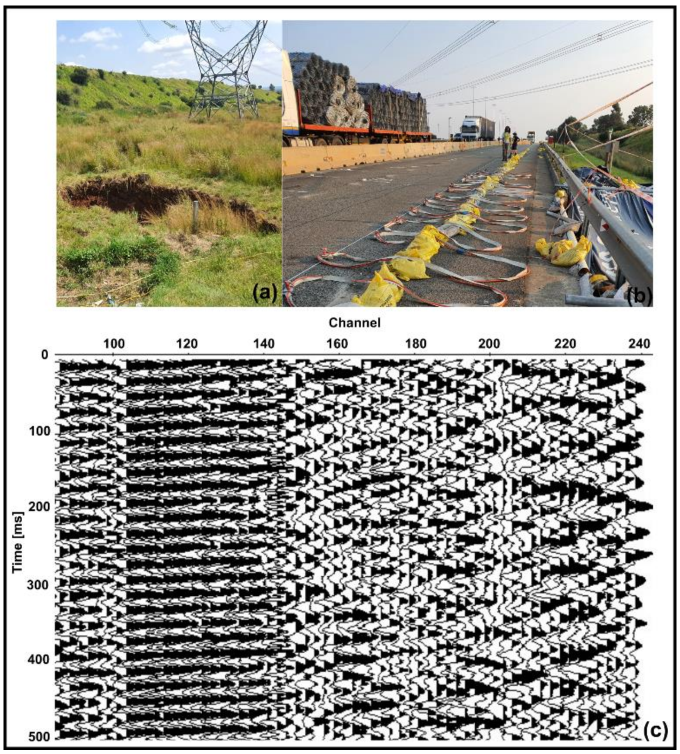

Figure 8.6: (a) High voltage powerlines next to the site; (b) Trucks and cars, which all act as sources of noise along the highway.(c) Shot gathers with background noise.

9 CONCLUSIONS

The central part of the Gauteng province which includes the City of Johannesburg, Tshwane, West Rand, and Ekurhuleni Municipalities (where the R21 sinkhole is located), is represented by the Malmani Subgroup dolomites which belong to the Chuniespoort Group of the Transvaal Supergroup. The R21 highway is a national highway that connects commuters to important sites like the O.R. Tambo International Airport and thus subsurface features (e.g., cavities and sinkholes) diminish the travelling advantages and convenience of using the highway for many people.

Results obtained from integrated electrical resistivity tomography (ERT), seismic, ground-penetrating radar (GPR), and Multichannel Analysis of Surface Waves (MASW) suggest that water ingress from the stormwater drainage system (during times of rain and fluctuation in the water table because of the nearby quarries) might have contributed to the formation of the R21 sinkhole. Water flows into the cavity from below the stormwater drainage system on the side of the highway. The water migrated through joints and fractures into the subsurface. Therefore, it can be concluded that sinkhole development is exacerbated by anthropogenic activities.

The results from this study demonstrate that an integrated approach in geophysical surveys is critical for mapping sinkholes and associated geological structures (fractures and joints) in karst terrain. Surface site observation suggests that the sinkhole is about ~16 m wide, ~8-9 m deep and extends between ~1-2.5 m into the R21 highway. The estimated top of the sinkhole, based on interpretations of the ERT, GPR, seismic, and MASW data, was found to provide an overall depth of between ~8-20 m and about ~30 m wide. GPR results show that it is between ~2 and ~8 m deep and extends ~2.5 m into the highway, while seismic results show that the sinkhole is about ~20 m wide. According to the ERT results, the sinkhole extends to depths of ~12-~20 m, while the MASW results indicate that the R21 sinkhole is ~18 m wide.

This research indicates that sinkholes can be characterised on the subsurface using integrated geophysical methods. The process of rehabilitating the R21 sinkhole should also take into consideration the other sinkhole that has formed on the southern part of the highway. This is important because neglecting this sinkhole could lead to its expansion and potential appearance on the highway itself. Among the four methods used in the study, ERT was found to be the most effective as it was able to clearly define the size and depth of the sinkhole on the R21 highway. This suggests that ERT could be the most preferred method for sinkhole detection and characterization in similar contexts, especially if conducting other surveys is not possible. For future studies, the plan is to incorporate the gravity method to enhance the delineation of sinkholes. Gravity methods can provide valuable information about subsurface density variations, which can be useful for identifying and characterizing sinkholes.

References

Abujarad, F., 2007. *Ground penetrating radar signal processing for landmine detection* (Doctoral dissertation, Otto-von-Guericke-Universität Magdeburg, Universitätsbibliothek).

Ahmad, S.,2014. *Earthquake elastic rebound theory types of waves*. Online available: https://www.slideshare.net/ShakeelAhmad36/earthquacke-elastic-rebound-theory-types-of-waves#8 [accessed: 10 June 2023].

Alhaj, A.H.Z., 2022. *Resistivity Imaging of Prominent Seepage Pathways in Karst Terrain* (Doctoral dissertation, Missouri University of Science and Technology).

Ali, H. and Choi, J.H., 2019. *A review of underground pipeline leakage and sinkhole monitoring methods based on wireless sensor networking*. *Sustainability*, 11(15), pp.4007.

Ali, A., Ullah, M., Barkat, A., Raza, W.A., Qadir, A. and Qamar, Z.U., 2021. *Multi-channel analysis of surface waves (MASW) using dispersion and iterative inversion techniques: Implications for cavity detection and geotechnical site investigation*. *Bulletin of Engineering Geology and the Environment*, 80, pp.9217-9235.

Al-Saigh, N.H. and JaddoaAl-Heety, A., 2014. *Seismic refraction tomography and MASW survey for geotechnical evaluation of soil for the teaching hospital project at Mosul University*. Journal of Zankoy Sulaimani-Part A (JZS-A), 16(1), pp.1.

Al-Shakhis, A.A., 1987. *Relationship between FK filtering and deconvolution in seismic data processing, The. 1980-1989-Mines Theses & Dissertations*.

Alsulaimani, G.S., 2017. *Acquisition of active multichannel analysis of surface waves (MASW) data in karst terrain.* Missouri University of Science and Technology.

Alzahrani, H.A., 2020. *Imaging in Karst Terrain Using the Electrical Resistivity Tomography (ERT) and Multi-Channel Analysis of Surface Waves (MASW) Methods*. Missouri University of Science and Technology.

Anderson, N. and Cardimona, S., 2000. Evaluating the utility of geophysical surveying methods. *Federal Highway Administration and Missouri Department of Transportation special publication, MoDOT web site*.

Anderson, N.L., Croxton, N., Hoover, R. and Sirles, P., 2008. *Geophysical methods commonly employed for geotechnical site characterization. Transportation Research Circular*, (E-C130).

Annan, A.P., 1999. *Practical processing of GPR data. Sensors and software, Ontario*.

Avutia, D. and Kalumba, D., 2014. *Analytical study of dolomite sinkholes in Centurion, South Africa. In Soil Behavior and Geomechanics,* pp. 633-641.

Baker, G.S., Jordan, T.E. and Pardy, J., 2007. *An introduction to ground penetrating radar (GPR)*.

Barone, P.M., 2012. *Archaeology, geophysics and forensic: united we stand, divided we fall. Geophysics*, 1, pp.131-137.

Bevan, B.W., 1998. *Geophysical exploration for archaeology: an introduction to geophysical exploration*.

Beck, B.F., and Sinclair, W.C., 1989. *Sinkholes in Florida: an introduction. Florida sinkhole research institute/ the U.S.G.S*. Orlando, Florida, 1986.

Billi, A., Valle, A., Brilli, M., Faccenna, C. and Funiciello, R., 2007. *Fracture-controlled fluid circulation and dissolutional weathering in sinkhole-prone carbonate rocks from central Italy*. *Journal of Structural Geology*, 29(3), pp.385-395.

Bording, R.P., Gersztenkorn, A., Lines, L.R., Scales, J.A. and Treitel, S., 1987. *Applications of seismic travel-time tomography*. *Geophysical Journal International*, 90(2), pp.285-303.

Bostanudin, N.J.F., 2013. *Computational methods for processing ground penetrating radar data* (Doctoral dissertation, University of Portsmouth).

Brink, A.B.A., 1979. *Engineering Geology of South Africa*, Vol.1, Building Publications, Pretoria.

Busetti, A., Calligaris, C., Forte, E., Areggi, G., Mocnik, A. and Zini, L., 2020. *Non-invasive methodological approach to detect and characterize high-risk sinkholes in urban cover evaporite karst: integrated reflection seismics, PS-InSAR, leveling, 3D-GPR and ancillary data. A NE Italian case study. Remote Sensing*, 12(22), p.3814.

Buttrick, D.B., 1986. *Wad and Ferroan soil developed in the Dolomitic area south of Pretoria*. Msc Thesis, University of Pretoria. pp. 29.

Buttrick, D. and Van Schalkwyk, A., 1998. *Hazard and risk assessment for sinkhole formation on dolomite land in South Africa. Environmental Geology*, 36, pp.170-178.

Buttrick, D.B., Van Schalkwyk, A., Kleywegt, R.J., Watermeyer, R.B. and Trollip, N., 2001. *Proposed method for dolomite land hazard and risk assessment in South Africa. Journal of the South African Institution of Civil Engineering.* 43(2), pp.27-36.

Buttrick, D.B., Trollip, N.Y., Watermeyer, R.B., Pieterse, N.D. and Gerber, A.A., 2011. *A performance based approach to dolomite risk management. Environmental Earth Sciences*, 64(4), p.1127-1138.

Button, A., 1973. *The stratigraphic history of the Malmani dolomite in the eastern and north-eastern Transvaal*. *South African Journal of Geology*, 76(3), pp.229-247.

Carbonel, D., Gutiérrez, F., Linares, R., Roqué, C., Zarroca, M., McCalpin, J., Guerrero, J. and Rodríguez, V., 2013. *Differentiating between gravitational and tectonic faults by means of geomorphological mapping, trenching and geophysical surveys. The case of the Zenzano Fault (Iberian Chain, N Spain). Geomorphology*, *189*, pp.93-108.

Caramanna, G., Ciotoli, G. and Nisio, S., 2008. *A review of natural sinkhole phenomena in Italian plain areas. Natural hazards*, 45(2), pp.145-172.

Cardarelli, E., Cercato, M., De Donno, G. and Di Filippo, G., 2013. *Detection and imaging of piping sinkholes by integrated geophysical methods. Near Surface Geophysics*, 12(3), pp.439-450.

Closson, D., 2005. *Structural control of sinkholes and subsidence hazards along the Jordanian Dead Sea coast. Environmental Geology,* 47(2), pp.290-301.

Collins, C.C. and Osazuwa, I.B., 2010. *The use of FK filter in the elimination of artefacts from a shallow seismic reflection data in Zaria, Nigeria. Global Journal of Pure and Applied Sciences,* 16(3).

Constantinou, S. and Van Rooy, J.L., 2018. *Sinkhole and subsidence size distribution across dolomitic land in Gauteng. Journal of the South African institution of civil engineering*, 60(2), pp.2-8.

Cook, S.N., Torres, M.J., Lamie, N.J., Perren, L.J., Slone, S.M. and Jones, B.J., 2022. *Automated ground-penetrating-radar post-processing software in R programming.*

Cook, K.L. and Van Nostrand, R.G., 1984. *Interpretation of resistivity data* (No. 499). US Govt. Print. Off.

Coşkun, N.A.R.T., 2012. *The effectiveness of electrical resistivity imaging in sinkhole investigations. International Journal of Physical Sciences*, *7*(15), pp.2398-2405.

Cox, D.R., Newton, A.M. and Huuse, M., 2020. *An introduction to seismic reflection data: Acquisition, processing and interpretation. In Regional geology and tectonics*, pp. 571-603.

Comprehensive Long-Term Environmental Action Navy, 2018. *Seismic profiling to map hydrostratigraphy in the Red Hill area, Oahu, Hawaii*.

Cueto, M., Olona, J., Fernández-Viejo, G., Pando, L. and López-Fernández, C., 2018. *Karst-induced sinkhole detection using an integrated geophysical survey: a case study along the Riyadh Metro Line 3 (Saudi Arabia). Near Surface Geophysics*, 16(3), pp.270-281.

Culshaw, M.G. and Waltham, A.C., 1987. *Natural and artificial cavities as ground engineering hazards. Quarterly Journal of Engineering Geology and Hydrogeology*, 20(2), pp.139-150.

Daniels, D.J. ed., 2004. *Ground penetrating radar*, 1.

De Bruyn, I.A., and Trollip, T., 2000. *Ground substance problems associated with dolomatic land Gauteng Province, South Africa. Land subsidence Vol 1, Proceedings of* *the sixth international Symposium on Land substance Revenna/Italy/*24-29 September 2000.

De Bruyn, I.A., Bell, F.G. and Jermy, C.A., 2000. *The problem of sinkhole formation in two dolomite areas of South Africa*. In *ISRM international symposium*. One Petro.

De Bruyn, I.A. and Bell, F.G., 2001. *The occurrence of sinkholes and subsidence depressions in the Far West Rand and Gauteng Province, South Africa, and their engineering implications.Environmental & Engineering Geoscience*, *7*(3), pp.281-295.

De Groot-Hedlin, C. and Constable, S., 2004. I*nversion of magnetotelluric data for 2D structure with sharp resistivity contrasts. Geophysics*, 69(1), pp.78-86.

Delle Rose, M., Federico, A. and Parise, M., 2004. *Sinkhole genesis and evolution in Apulia, and their interrelations with the anthropogenic environment. Natural Hazards and Earth System Sciences,* 4(5/6), pp.747-755.

Dentith, M. and Mudge, S.T., 2014.*Geophysics for the mineral exploration geoscientist*. Cambridge University Press.

Department of Water Affairs and Forestry, South Africa, December 2006. *Vaal River system: large bulk water supply reconciliation strategy: groundwater assessment: dolomite aquifers*. [Online] available: https://www.dws.gov.za/iwrp/Vaal/documents/LargeBulkWater/06_Dolomitic%20Groundwater%20Assessment_Final.pdf [Accessed: 21 March 2024]

Department of Public Works. *Appropriate development of infrastructure on dolomite: Guidelines for consultants. 2003*. [Online] available: https://www.gov.za/sites/default/files/gcis_document/201409/dolomitemanual0.pdf [Accessed: 21 February 2024]

Doctor, D.H., Weary, D.J., Orndorff, R.C., Harlow, Jr, G.E., Kozar, M.D. and Nelms, D.L., 2008. *Bedrock structural controls on the occurrence of sinkholes and springs in the northern Great Valley karst, Virginia and West Virginia.* In *Sinkholes and the engineering and environmental impacts of karst*, pp. 12-22.

Dojack, L., 2012. *Ground penetrating radar theory, data collection, processing, and interpretation: a guide for archaeologists*.

Enslin, JF & Smit, P.J., 1955. *Geophysical surveys for foundations in South Africa with special reference to the sinkholes in the dolomite south of Pretoria. Civil Engineering= Siviele Ingenieurswese,*1955(9), pp.318-322.

Eriksson, K.A. and Truswell, J.F., 1974. *Tidal flat associations from a Lower Proterozoic carbonate sequence in South Africa*. *Sedimentology*, 21(2), pp.293-309.

Eriksson, P.G., Schweitzer, J.K., Bosch, P.J.A., Schereiber, U.M., Van Deventer, J.L. and Hatton, C.J., 1993. The *Transvaal sequence: an overview*. *Journal of African Earth Sciences (and the Middle East)*, 16(1-2), pp.25-51.

Eriksson, P.G., Hattingh, P.J. and Altermann, W., 1995. *An overview of the geology of the Transvaal Sequence and Bushveld Complex, South Africa. Mineralium Deposita*, 30, pp.98-111.

Eriksson, P.G. and Reczko, B.F.F., 1995. *The sedimentary and tectonic setting of the Transvaal Supergroup floor rocks to the Bushveld Complex. Journal of African Earth Sciences*, 21(4), pp.487-504.

Eriksson, P.G., Altermann, W., Catuneanu, O., Van der Merwe, R. and Bumby, A.J., 2001. *Major influences on the evolution of the 2.67–2.1 Ga Transvaal basin, Kaapvaal Craton. Sedimentary Geology*, 141, pp.205-231.

Eriksson, P.G, Altermann, W. and Hartzer F.J, 2006. *The Transvaal Supergroup and its precursors. In Johnson, M.R., Anhaeusser, C.R and Tomas, R.J (Eds). The Geology of South Africa. Geological Society of South Africa, Johannesburg/Council for Geoscience, Pretoria,* pp. 237-260.

Eriksson, P.G., Bartman, R., Catuneanu, O., Mazumder, R. and Lenhardt, N., 2012. *A case study of microbial mat-related features in coastal epeiric sandstones from the Paleoproterozoic Pretoria Group (Transvaal Supergroup, Kaapvaal Craton, South Africa); The effect of preservation (reflecting sequence stratigraphic models) on the relationship* *between mat features and inferred paleoenvironment*. *Sedimentary Geology*, 263, pp.67-75.

Evans, R.D., 2009.*Optimising ground penetrating radar (GPR) to assess pavements* (Doctoral dissertation, Loughborough University).

Everett, M. E., 2013. *Near-Surface Applied Geophysics*.

Farooq, M., Park, S., Song, Y.S., Kim, J.H., Sabir, M.A. and Umar, M., 2013. *Application of electrical resistivity method to evaluate the extent of mortar infiltration in subsurface cavities. Arabian Journal for Science and Engineering,* 38, pp.111-120.

Fehdi, C., Baali, F., Boubaya, D. and Rouabhia, A., 2011. *Detection of sinkholes using 2D electrical resistivity imaging in the Cheria Basin (north–east of Algeria). Arabian Journal of Geosciences*, 4(1), pp.181-187.

Fiedler, S., Illich, B., Berger, J. and Graw, M., 2009. *The effectiveness of ground-penetrating radar surveys in the location of unmarked burial sites in modern cemeteries. Journal of Applied Geophysics*, 68(3), pp.380-385.

Fisher, S.C., Stewart, R.R. and Jol, H.M., 1992. *Processing ground penetrating radar (GPR) data. In CREWES Research Report*, Vol. 4, pp. 11-1.

Flooddefenders.org, 2023. *Why Your Community Needs Better Stormwater Drainage*. [Online] available: https://www.flooddefenders.org/why-your-community-needs-better-stormwater-drainage [Accessed: 26 October 2023]

Florea, L.J., 2005. *Using State-wide GIS data to identify the coincidence betwen sinkholes and geologic structure*. *Geography/Geology Faculty Publications*, pp.14.

Foose, R.M., 1967. *Sinkhole formation by groundwater withdrawal: Far West Rand, South Africa. Science,* 157(3792), pp.1045-1048.

Foster, M.B.J., 1989. *The hydrogeology of dolomitic formations in the southern and western Transvaal. DWAF Technical Report No.* GH, 3643.

Geotomo, S., 2010. *Rapid 2D resistivity & IP inversion using the least-squares method*.

Goldscheider, N., Chen, Z., Auler, A.S., Bakalowicz, M., Broda, S., Drew, D., Hartmann, J., Jiang, G., Moosdorf, N., Stevanovic, Z. and Veni, G., 2020. *Global distribution of carbonate rocks and karst water resources. Hydrogeology Journal*, 28, pp.1661-1677. [Online] available: https://doi.org/10.1007/s10040-020-02139-5 [Accessed: 1 June 2023]

Guarino, P.M., Santo, A., Forte, G., De Falco, M. and Niceforo, D.M.A., 2018. *Analysis of a database for anthropogenic sinkhole triggering and zonation in the Naples hinterland (Southern Italy). Natural Hazards,* 91, pp.173-192.

Hadjmeliani, M., 2015. *August. Degradation of sewage pipe caused Sinkhole: A real case study in a main road*. In *CFM 2015-22ème Congrès Français de Mécanique*. AFM, Maison de la Mécanique, 39/41 rue Louis Blanc-92400 Courbevoie.

Heath, G.J. and Oosthuizen, A.C., 2008. *A preliminary overview of the sinkhole record of South Africa*. In *SAICE Conference on Problem Soils in South Africa,* pp. 3-4

Hermosilla, R.G., 2012. *The Guatemala City sinkhole collapses. Carbonates and evaporites*, 27(2), pp.103-107.

Hu, Y., Xia, J., Mi, B., Cheng, F. and Shen, C., 2018. *A pitfall of muting and removing bad traces in surface-wave analysis. Journal of Applied Geophysics*, 153, pp.136-142.

Huggenberger, P., Meier, E. and Pugin, A., 1994. *Ground-probing radar as a tool for heterogeneity estimation in gravel deposits: advances in data-processing and facies analysis. Journal of Applied Geophysics*, 31(1-4), pp.171-184.

Hussain, Y., Uagoda, R., Borges, W., Nunes, J., Hamza, O., Condori, C., Aslam, K., Dou, J. and Cárdenas-Soto, M., 2020. *The potential use of geophysical methods to identify cavities, sinkholes and pathways for water infiltration*. *Water*, 12(8), p.2289.

Izon, G., Zerkle, A.L., Williford, K.H., Farquhar, J., Poulton, S.W. and Claire, M.W., 2017. *Biological regulation of atmospheric chemistry en route to planetary oxygenation. Proceedings of the National Academy of Sciences*, 114(13), pp.E2571-E2579.

Jennings, J.E., Brink, A.B.A., Louw, A. and Gowan, G.D., 1965. *Sinkholes and subsidences in the Transvaal dolomites of South Africa. Procedures of VI th International Conference on Soil Mechanics & Foundation Engineering, Montreal*, 1(2), pp. 51–54.

Jennings, J.E., 1966. *Building on dolomites in the Transvaal. Civil Engineering= Siviele Ingenieurswese 1966*, 2(1966): 41-62.

Joll, H.M., 2009. *Ground penetrating radar theory and applications*.

Jones and Wegener Consulting Civil Engineers, 2005 *Ekhurhuleni Metropolitan Municpality: Second Report on Sinkholes and Subsidences at Bapsfontein.* (Report No.: JW190/05/9401)

Kearey, P., Brooks, M. and Hill, I., 2002. *An introduction to geophysical exploration*, 4. John Wiley & Sons.

Kleinhans, I. and Van Rooy, J.L., 2016. *Guidelines for sinkhole and subsidence rehabilitation based on generic geological models of a dolomite environment on the East Rand, South Africa. Journal of African Earth Sciences*, 117, pp.86-101.

Kleywegt, R.J. and Ensulin, J.F., 1973. *The application of the gravity method to the problem of ground settlement and sinkhole formation in the dolomite in the Far West Rand, South Africa. Proc. IAEG Symp. Sinkholes and Subsidence Engineering-Geological Problems related to soluble rocks,* Hannover, pp1-5.

Labuda, T.Z. and Baxter, A.C., 2001. *January. Mapping karst conditions using 2D and 3D resistivity imaging methods.* In *Symposium on the Application of Geophysics to Engineering and Environmental Problems 2001* (pp. GTV1-GTV1). Society of Exploration Geophysicists.

Liang, X., Hu, D., Li, Y., Zhang, Y. and Yang, X., 2022. *Application of GPR Underground Pipeline Detection Technology in Urban Complex Geological Environment*s. *Geofluids*, *2022*.

Liberty, L. and St. Clair, J., 2018. *Seismic profiling to map hydrostratigraphy in the Red Hill area, Oahu, Hawaii*. Department of Geosciences, Boise State University.

Lines, L.R. and Newrick, R.T., 2004. *Fundamentals of geophysical interpretation. Society of Exploration Geophysicists*.

Linde, N., 2005. *Characterization of Hydrogeological Media using electromagnetic geophysics* (Doctoral dissertation, Acta Universitatis Upsaliensis).

Lindgren, A., 2014. *Combined use of ground and borehole geophysical data to model spatial variations of quick clay and surrounding sediments at a Swedish landslides site. Department of Civil, Environmental and Natural Resources Engineering, Lulea University of Technology, Lulea*.

Liu, S., 2017. *Shear Wave Velocity Analysis by Surface Wave Methods in the Boston Area* (Doctoral dissertation, Boston College).

Loke, M.H. and Barker, R.D., 1995. *Least-squares deconvolution of apparent resistivity pseudosections. Geophysics*, 60(6), pp.1682-1690.

Loke, M.H., 1999*. Electrical imaging surveys for environmental and engineering studies. A practical guide to 2D and 3D Surveys*, *2*, pp.70.

Loke, M.H., 2000. *Electrical imaging surveys for environmental and engineering studies: A practical guide to 2D and 3-D surveys.* Unpublished Short Training Course Lecture Notes. Geotomo Software.

Loke, M.H., 2002. *Rapid 2D resistivity forward modeling using the finite-difference and finite-element methods.* RES2DMOD, (3), pp.1996-2002.

Loke, M. H., 2000b. *Res2dinv software user's manual, version 3.44:* Geotomo Software.

Loke, M. H., 2014. *Tutorial: 2D and 3D electrical imaging surveys*. [Online] available: https://www.geotomosoft.com/downloads.php [Accessed in February. 06, 2023]

Loke, M.H., 2015. *Tutorial: 2D and 3-D electrical imaging surveys*.

Logan, B.W., Rezak, R. and Ginsburg, R.N., 1964. *Classification and environmental significance of algal stromatolites. The Journal of Geology*, 72(1), pp.68-83

Majdi, A.M., Alashloo, S.Y.M., Hassan, N.N.A.A.N.M., Arshad, A.R. and Latiff, A.H.A., 2021*. Application of finite difference eikonal solver for traveltime computation in forward modeling and migration. Bulletin of the Geological Society of Malaysia*, 72.

Marghany, M. and Hashim, M., 2010. *Lineament mapping using multispectral remote sensing satellite data. International Journal of the Physical Sciences*, 5(10), pp.1501-1507.

Masw.com, 2023. *Data Acquisition*. [Online], Available: https://www.masw.com/DataAcquisition.html [Accessed: 24 October 2023].

Mendoza, R., Araque-Perez, C., Marinho, B., Rey, J. and Hidalgo, M.C., 2023. *Processing GPR Surveys in Civil Engineering to Locate Buried Structures in Highly Conductive Subsoils. Remote Sensing*, 15(16), pp.4019.

Meyer, R. 2014. *Hydrogeology of groundwater region 10: The Karst Belt. Water Research Commission Report No. TT 553/12. Pretoria, South Africa: Water Research Commission.* [Online], Available: https://fracking.webmaps.africa/downloads/Region_10_Karst_Belt.pdf [Accessed 26 June 2024].

Mining.com, 2021. *Old photos show South Dakota mine that caused sinkhole wasn't so hidden.* [Online] available: https://www.mining.com/old-photos-show-south-dakota-mine-that-caused-sinkhole-wasnt-so-hidden/ [accessed: 06 June 2023].

Milsom, J. and Eriksen, A., 2013. *Field geophysics.*

Miller, R., Xia, J., Park, C., Ivanov, J. and Williams, E., 1999. *Using MASW to map bedrock in Olathe, Kansas; Technical Program with biographies, SEG*. In *69th Annual Meeting, Houston, Texas*, pp. 874-877.

Mi, B., Xia, J., Shen, C., Wang, L., Hu, Y. and Cheng, F., 2017. *Horizontal resolution of multichannel analysis of surface waves. Geophysics*, 82(3), pp. 51-66.

Momubaghan, G.A., 2012. *Geotechnical Investigations for the Gautrain Mass TransitRapid Rail Link over Dolomite Bedrock in the Centurion Area, South Africa* (Doctoral dissertation, University of Pretoria).

Montgomery, J., Jackson, D., Kiernan, M. and Anderson, J.B., 2020. *Use of geophysical methods for sinkhole exploration* (No. 930-945). Auburn University. Highway Research Center.

Monty, C.L.V. and Hardie, L.A., 1976. *The geological significance of the freshwater blue-green algal calcareous mars*h. In *Developments in sedimentology*, 20, pp. 447-477. Elsevier.

Montjane, A.K., Tshibubudze, A., Woldai, T. and Heath, L., 2020. *The influence of geological fractures on karstic sinkhole development in eastern areas of Centurion, South Africa. Environmental Earth Sciences*, 79(21), pp.488.

Nanda, N.C., 2021. *Seismic data interpretation and evaluation for hydrocarbon exploration and production*. *Springer Nature Switzerland AG*.

Nex, P.A., 2005. *The structural setting of mineralisation on Tweefontein Hill, northern limb of the Bushveld Complex, South Africa. Applied Earth Science*, 114(4), pp.243-251.

NEHRP, 1997, *(National earthquake hazards reduction program*).

Ngcobo, T.A., 2006. *The risks associated with mines in dolomitic compartments. Journal of the Southern African Institute of Mining and Metallurgy*, 106(4), pp.251-264.

Niculescu, B.M. and Andrei, G., 2021*. Application of electrical resistivity tomography for imaging seawater intrusion in a coastal aquifer. Acta Geophysica*, 69(2), pp.613-630.

Novotny, O., 1999. *Seismic surface waves. Bahia, Salvador: Instituto de Geociencias*, pp 61.

Nwokebuihe, S., Torgashov, E. and Anderson, N., 2014. *A description of an effective sinkhole investigation approach: a case study of a site in Greene County, Missouri*. *Ph.D.Thesis*.

Obbes, A.M., 2000. *The structure, stratigraphy, and sedimentology of the Black Reef-Malmani-Rooihoogte succession of the Transvaal Supergroup southwest of Pretoria* 127. Pretoria: Council for Geoscience.

Olayinka, A.I. and Yaramanci, U., 2000. *Assessment of the reliability of 2D inversion of apparent resistivity data*. *Geophysical Prospecting*, 48(2), pp.293-316.

Onyebueke, E.O., Durrheim, R.J., Manzi, M.S.D., Sebothoma, S., Zhang, S.E. and Stettler, E., 2020. *High-resolution Integrated Geophysical Investigation at the Lancaster Gold Mine, Krugersdorp, South Africa*. *Pure and Applied Geophysics*, 177, pp.4845-4870.

Oosthuizen, A.C. and Richardson, S., 2011. *Sinkholes and subsidence in South Africa. Council for Geoscience,* 27, pp.1-31.

Oosthuizen, A.C., 2013. *The hazard of sinkholes formation in the Centurion CBD and surrounding areas: Pretoria, Gauteng* (Doctoral dissertation, University of Pretoria).

Osinowo, O.O., 2020. *Reprocessing of Regional 2D Marine Seismic Data of Part of Taranaki Basin, New Zealand Using Latest Processing Techniques. GeoScience Engineering*, 66(2), pp.95-116.

Parise, M. and Lollino, P., 2011. *A preliminary analysis of failure mechanisms in karst and man-made underground caves in Southern Italy. Geomorphology*, 134(1-2), pp.132-143.

Park, C.B., R.D. Miller, and J. Xia, 1999, *Multichannel Analysis of Surface Waves: Geophysics*, 64, 800-808.

Park, C.B. and Miller, R.D., 2008. *Roadside passive multichannel analysis of surface waves (MASW). Journal of environmental & engineering geophysics*, *13*(1), pp.1-11.

Park C.B., (2007). *Multichannel analysis of surface waves (MASW) — active and passive methods. The Lead Edge*, 26(1), pp 60–64.

Park, C., 2013, *MASW for geotechnical site investigation: The Leading Edge, June 2013*, 32, pp. 656-662.

Parwatiningtyas, D., 2021. *Application of the GPR (Ground Penetration Radar) method for soil investigation and building structure analysis test. In Journal of Physics: Conference Series*, 1816(1), pp. 012003. IOP Publishing.

Pokrovsky, O.S. and Schott, J., 2001. *Kinetics and mechanism of dolomite dissolution in neutral to alkaline solutions revisited. American Journal of Science*, 301, pp. 597–626.

Ponta, G.M.L., 2019. *Karst Hydrogeology. Cave and Karst Systems of Romania: Springer International Publishing AG, part of Springer Nature*.

RES2DINV ver. 3.52 for Windows 98/Me/2000/NT/XP Rapid 2D *Resistivity IP inversion using the least-squares method Wenner (α,β,γ), dipole-dipole, inline pole-pole, poledipole, equatorial dipole-dipole, Wenner-Schlumberger and non-conventional arrays On land, underwater and cross-borehole surveys*. [Online] available: file:///C:/Users/Wits_user/Downloads/Rapid_2_D_Resistivity_and_IP_inversion_u.pdf [Accessed: on 22 May 2023]

Richardson, S., 2013. *Sinkhole and subsidence record in the chuniespoort group dolomite, Gauteng, South Africa* (Doctoral dissertation, University of Pretoria).

Roth, M.J.S., Mackey, J.R., Mackey, C., and Nyquist, J.E., 2002. *A case study of the reliability of multielectrode earth resistivity testing for geotechnical investigations in karst terrains. Engineering Geology*, 65(2-3), pp.225-232.

Roux, P.J., 1991. *Geotechnical investigations for town development in areas underlain by dolomite*. *Department of Mineral and Energy Affairs*.

Rowberry, M., Dubois, C., Kaufmann, O., Baele, J.M. and Blahut, J., 2018. *Weathering by dolomite dissolution responsible for the formation of an important palaeotological locality in the Prague synform. Acta Geodynynamica et Geomaterialia*, 5(3), pp.297-309.

SANS1936 (South African National Standard): 1936-1/2/3/4, *Development of Dolomite Land*, 1st Edn, 2012.

Sandmeier, K.J., 2008. *ReflexW (version 5.0) program for processing and interpretation of reflection and transmission data*. *Karlsruhe, Germany, Sandmeier software*.

Sandmeier, 2023. *REFLEXW 32-and 64-bit Version 10.0.* [Online] available: https://www.sandmeier-geo.de/download.html [Accessed: 17 February 2022].

Scheidt, J., Lerche, I. and Paleologos, E., 2005. *Environmental and economic risks from sinkholes in west-central Florida. Environmental Geosciences*, *12*(3), pp.207-217.

Schrader, A. and Winde, F., 2015. *Unearthing a hidden treasure: 60 years of karst research in the Far West Rand, South Africa. South African Journal of Science*, 111(5-6), pp.1-7.

Shaaban, F.A., Abbas, A.M., Atya, M.A. and Hafez, M.A., 2009. *Ground-penetrating radar exploration for ancient monuments at the Valley of Mummies-Kilo 6, Bahariya Oasis, Egypt*. *Journal of Applied Geophysics*, 68(2), pp.194-202.

Slideplayer, 2015. *Seismic waves Wave propagation Hooke's law Newton's law, wave equation Wavefronts and Rays Interfaces Reflection and Transmission coefficients*. [Online] available: https://slideplayer.com/slide/5146781/ [Accessed: 20 October 2023]

Stats SA (Statistics South Africa). 2022. *60, 6 million people in South Africa*. [Online] available: https://www.statssa.gov.za/?p=15601 [Accessed: 16 January 2023].

Swart, C., Stoch, E., van Jaarsveld, C. F., and Brink, A.B.A., 2003. *The Lower Wonderfontein Spruit: an exposé.* 43, 635–653. [Online] available: https://doi.org/10.1007/s00254-002-0686-9 [Accessed: 27 June 2024]

Swart, D., 2019. *Mechanical and hydraulic properties of residual dolomite and wad found in the Malmani Subgroup in South Africa*. (Doctoral dissertation, University of Pretoria).

Telford, W.M., Geldart, L.P. and Sheriff, R.E., 1990. *Applied geophysics*. Cambridge university press.

TerraDat. (2020). *Geophysical Survey Methods*. [Online] available: https://www.terradat.co.uk/survey-methods/ [Accessed: 24March 2022].

Tesfaldet, Y.T. and Puttiwongrak, A., 2019. *Seasonal groundwater recharge characterization using time-lapse electrical resistivity tomography in the Thepkasattri Watershed on Phuket Island, Thailand. Hydrology*, *6*(2), p.36.

Tesseral Pro, 2021. [Online] available: http://www.tesseral-geo.com/products._en.php [Accessed: 20 July 2023].

Tesseral Pro, 2021.*Tesseral Geo Modeling*. http://www.tesseral-geo.com/documentation/en/general/Primer.pdf [Accessed 24 July 2023].

Trollip, N., van Rooy, L. and Eriksson, P., 2008. *Analysis of the occurrence and importance of slot development (grykes) within shallow dolomite zones in a selected type of area on the Eccles Formation. South African Journal of Geology*, 111(2-3), pp.333-344.

Ukaegbu, I.K., Gamage, K.A. and Aspinall, M.D., 2019. *Nonintrusive depth estimation of buried radioactive wastes using ground penetrating radar and a gamma ray detector. Remote Sensing,* 11(2), pp.141.

Van Eeden, E.S., De Villiers, B., Strydom, H. and Stoch, L., 2003*. Effects of dewatering and sinkholes on people and environment-an analysis of the Carletonville area in Gauteng, South Africa. Historia*, 48(1), pp.95-125.

Van Niekerk, H.J. and van der Walt I.J., 2005. *Dewatering of the far west rand dolomitic area by gold mining activities and subsequent ground instability*. [Online] available: https://onlinelibrary.wiley.com/doi/pdf/10.1002/ldr.749 [Accessed: on 15 April 2023]

Van Schoor, M. and Fourie, C.J.S., 2015*. A guide for applying geophysics to coal mining problems in South Africa*. Struik Nature, South Africa.

Van Schoor, M. and Mare, L., 2015. *The physical properties of coal*. Struik Nature South Africa.

Varnavina, A.V., Khamzin, A.K., Kidanu, S.T. and Anderson, N.L., 2019. Geophysical site assessment in karst terrain: A case study from southwestern Missouri. *Journal of Applied Geophysics*, *170*, p.103.

Wagener, F.V.M., Day, P.W, (1986). *Construction on dolomite in South Africa*. *Environ. Geol. Water Sci* 8, 83–89 (1986). https://doi.org/10.1007/BF02525561.

Xia J., Miller R.D., Park C.B., (1999) *Estimation of near-surface Shear wave velocity by inversion of Rayleigh waves*. Geophys, 64(3), pp691–700.

Zhou, H.W., 2014. *Practical seismic data analysis*. Cambridge University Press.

Appendix A

Electrical Resistivity Tomography Results

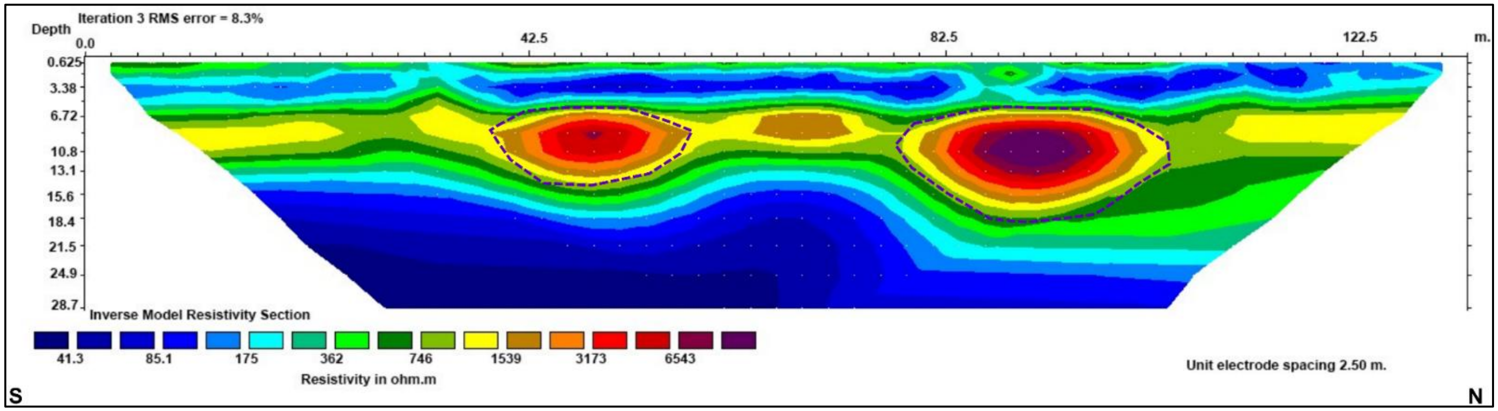

Figure A1: Line 1, trends from south to north and is the closest to the sinkhole rim of the large sinkhole that is directly above the R21 highway. The survey was conducted using the ARES system with an electrode spacing of 2.5 m.

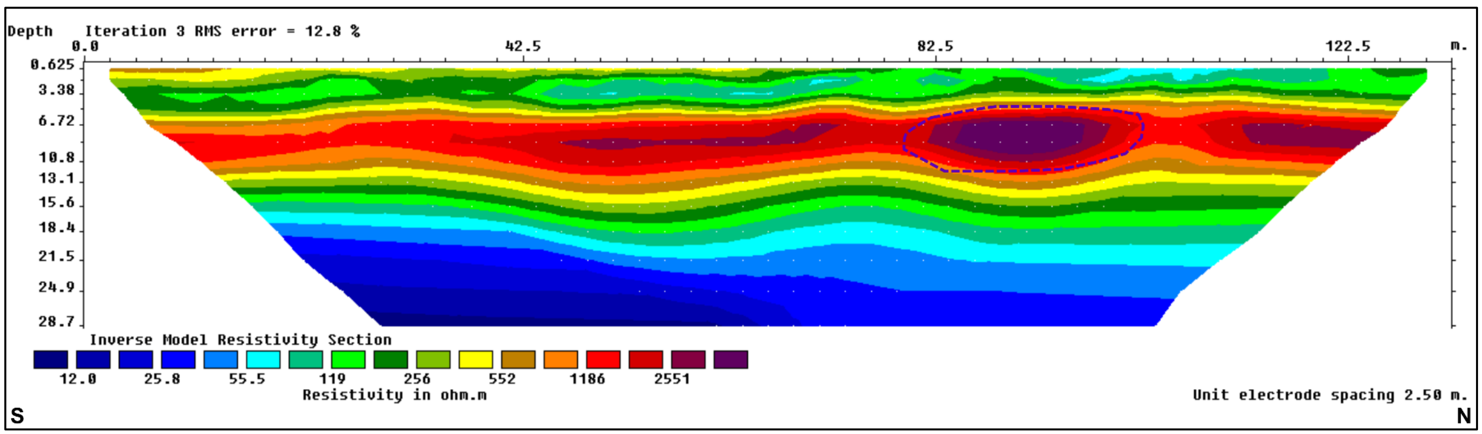

Figure A2: Line 2 follows the same south to north trend but is situated on the eastern rim of the sinkhole. It has an electrode spacing of 2.5 m.

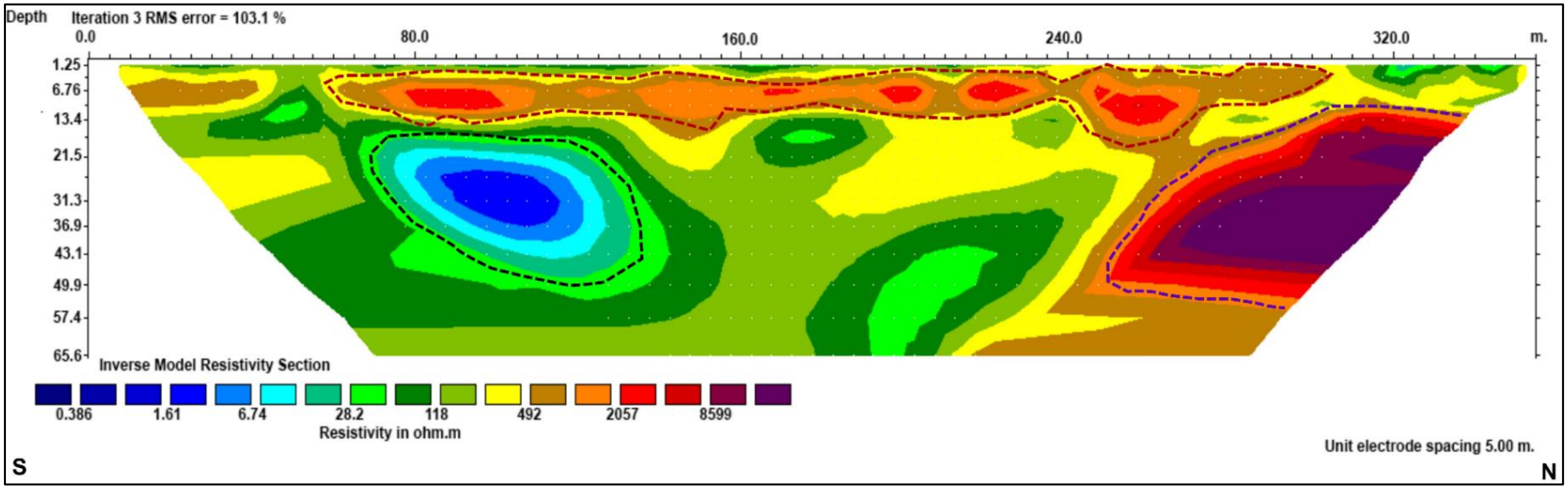

Figure A3: Line 3 trends from south to north and is also situated on the eastern side of the sinkhole. It has an electrode spacing of 2.5 m.

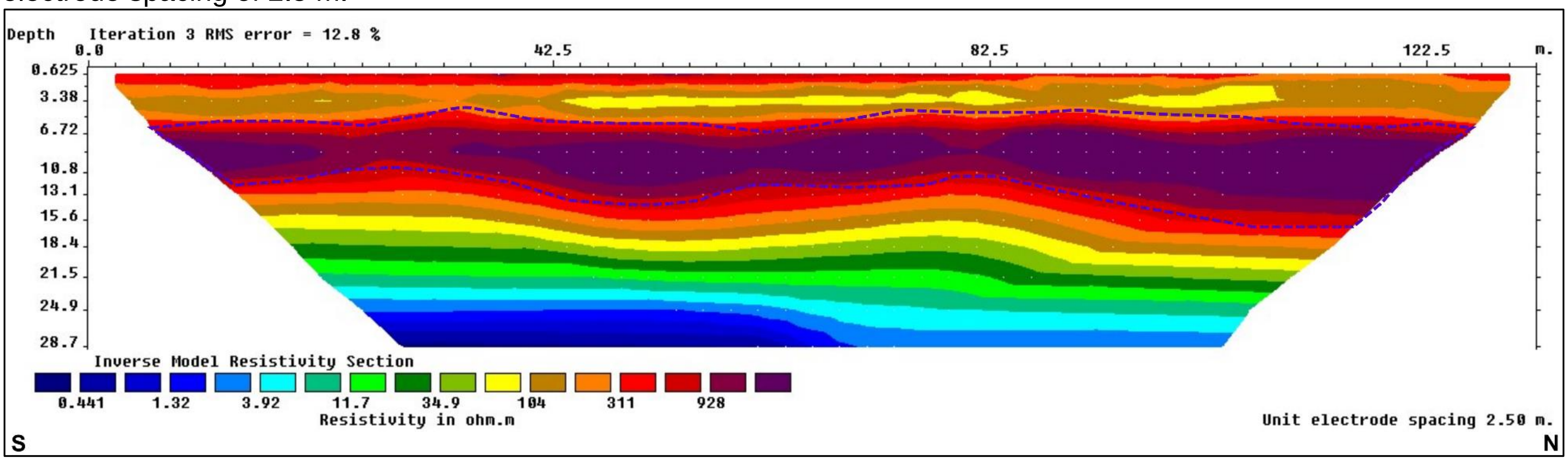

Figure A4: Line 4 is bit further from the sinkhole, in between the north bound and south bound lanes. It trends from south to north, with an electrode spacing of 5 m. This line forms part of the three lines that were designed to check if the sinkhole does extend to the other south bound lane.

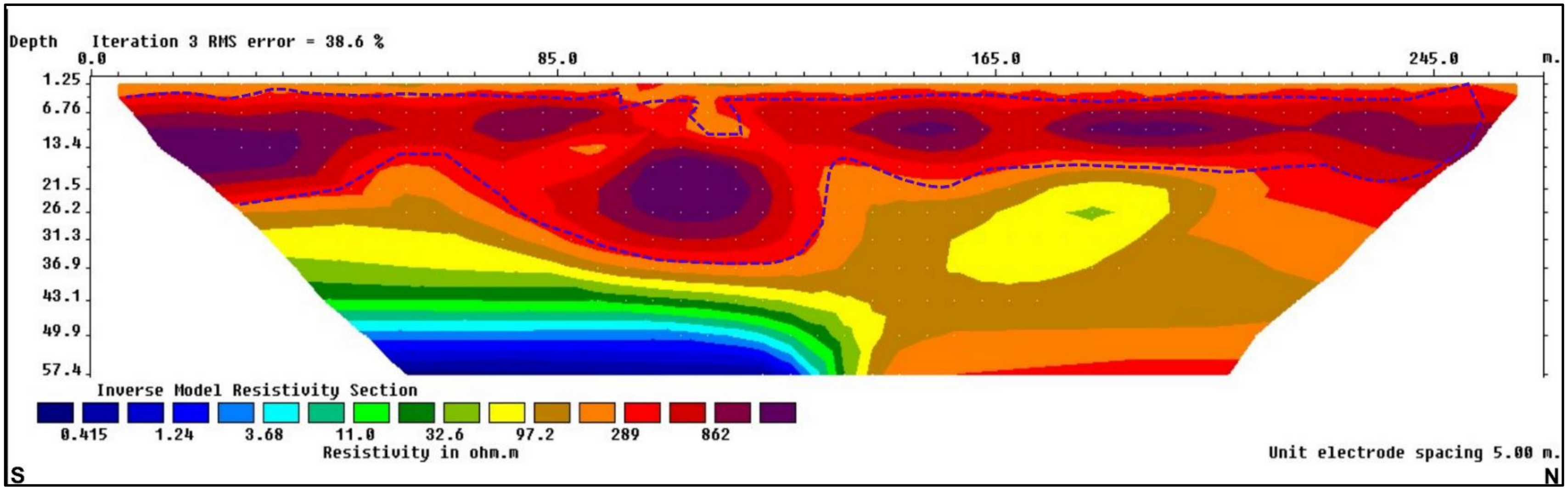

Figure A5: Line 5 is on the eastern side of the sinkhole on the sound bound lane. It has an electrode spacing of 5 m and trends south to north.

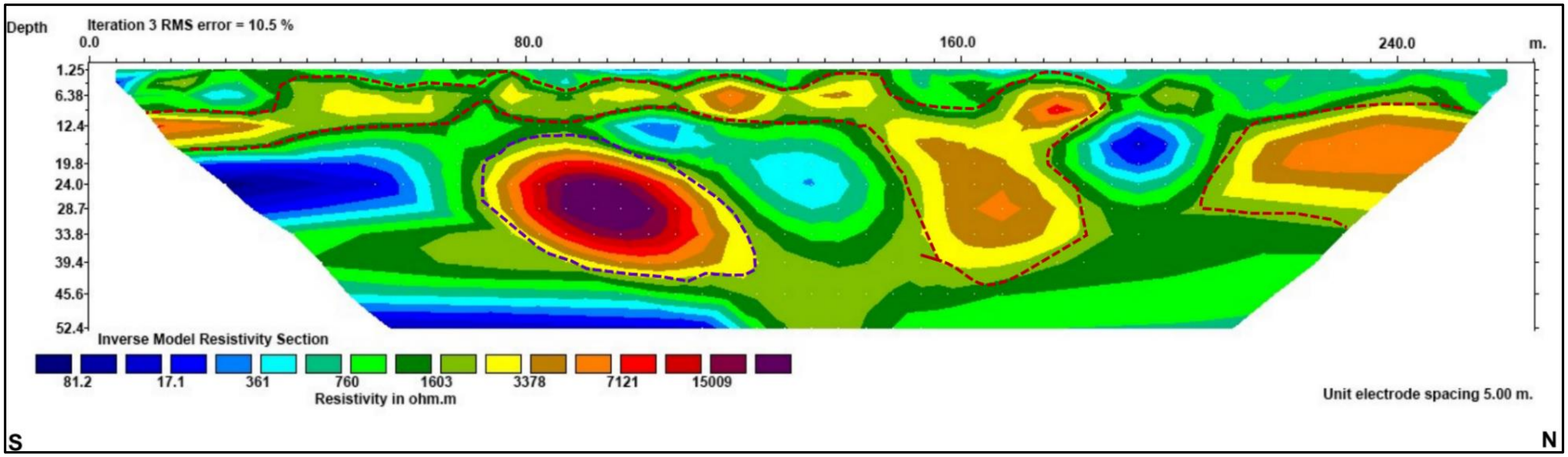

Figure A6: Line 6 is on the eastern side of the sinkhole on the sound bound lane. It has an electrode spacing of 5 m and trends south to north.

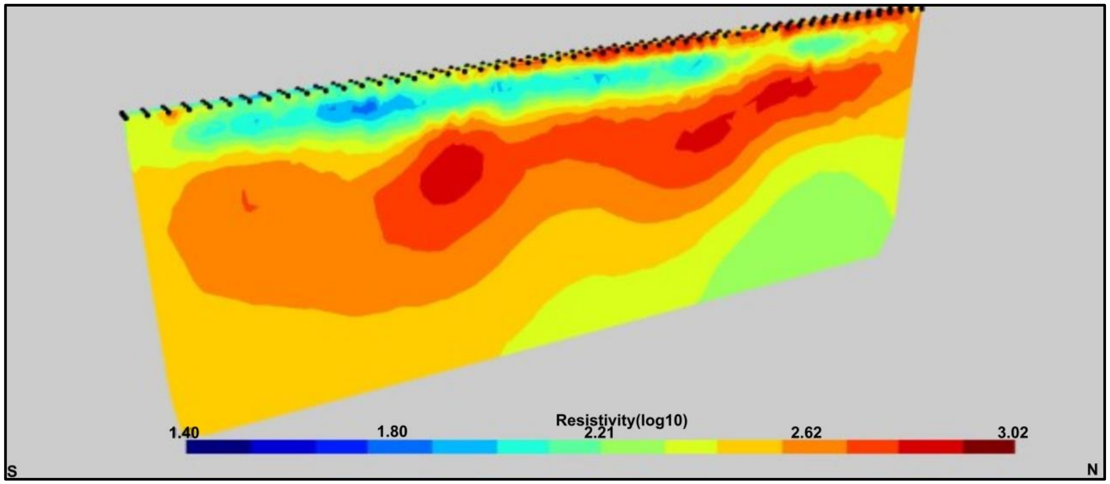

Figure A7: A combination of lines 1 to 3 shown in 3-D.

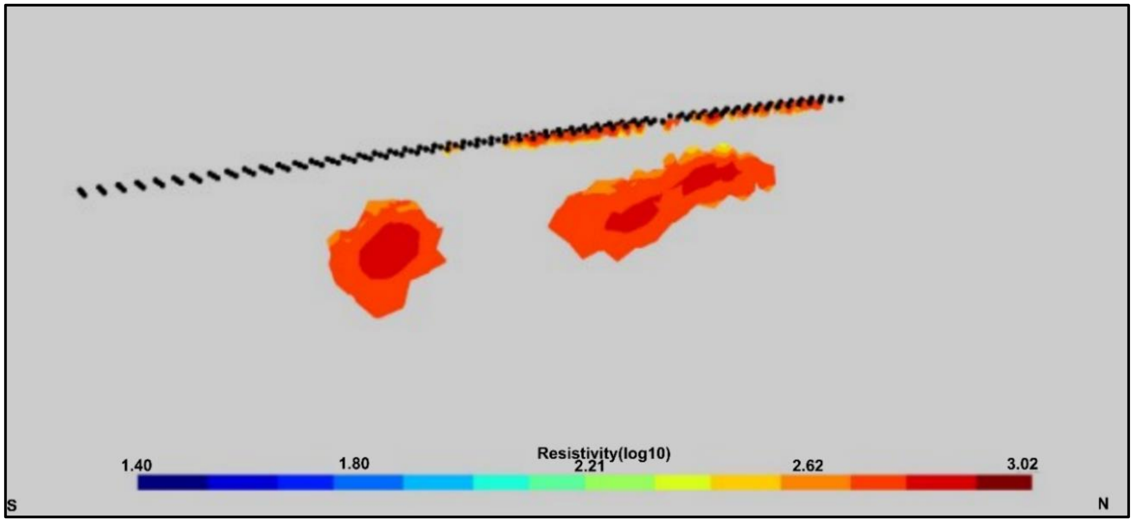

Figure A8: A trimmed out model of line 1 to 3 shown in 3-D, to clearly define the sinkholes in all three lines.

Appendix B

Ground Penetrating Radar Results

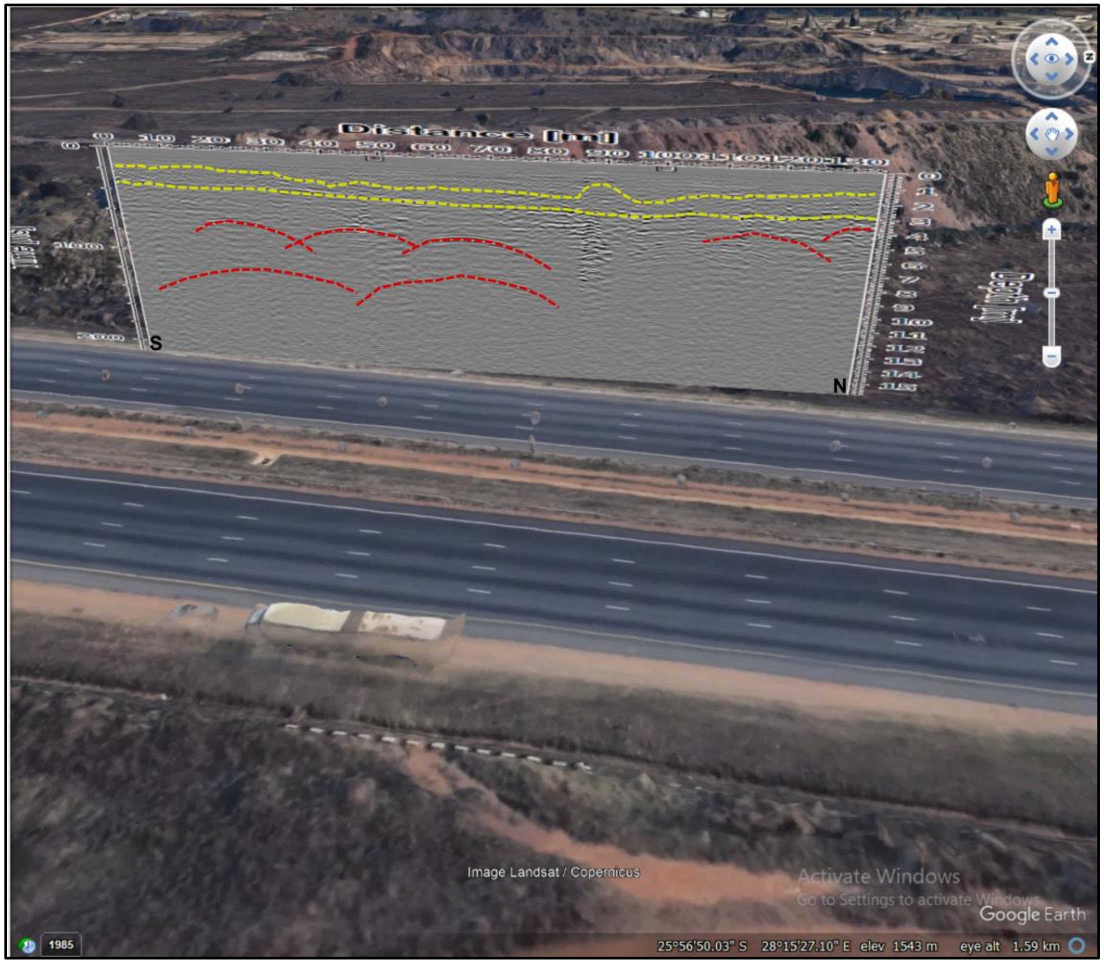

Figure B1: Google Earth image with the location of line R21SINK001_001.

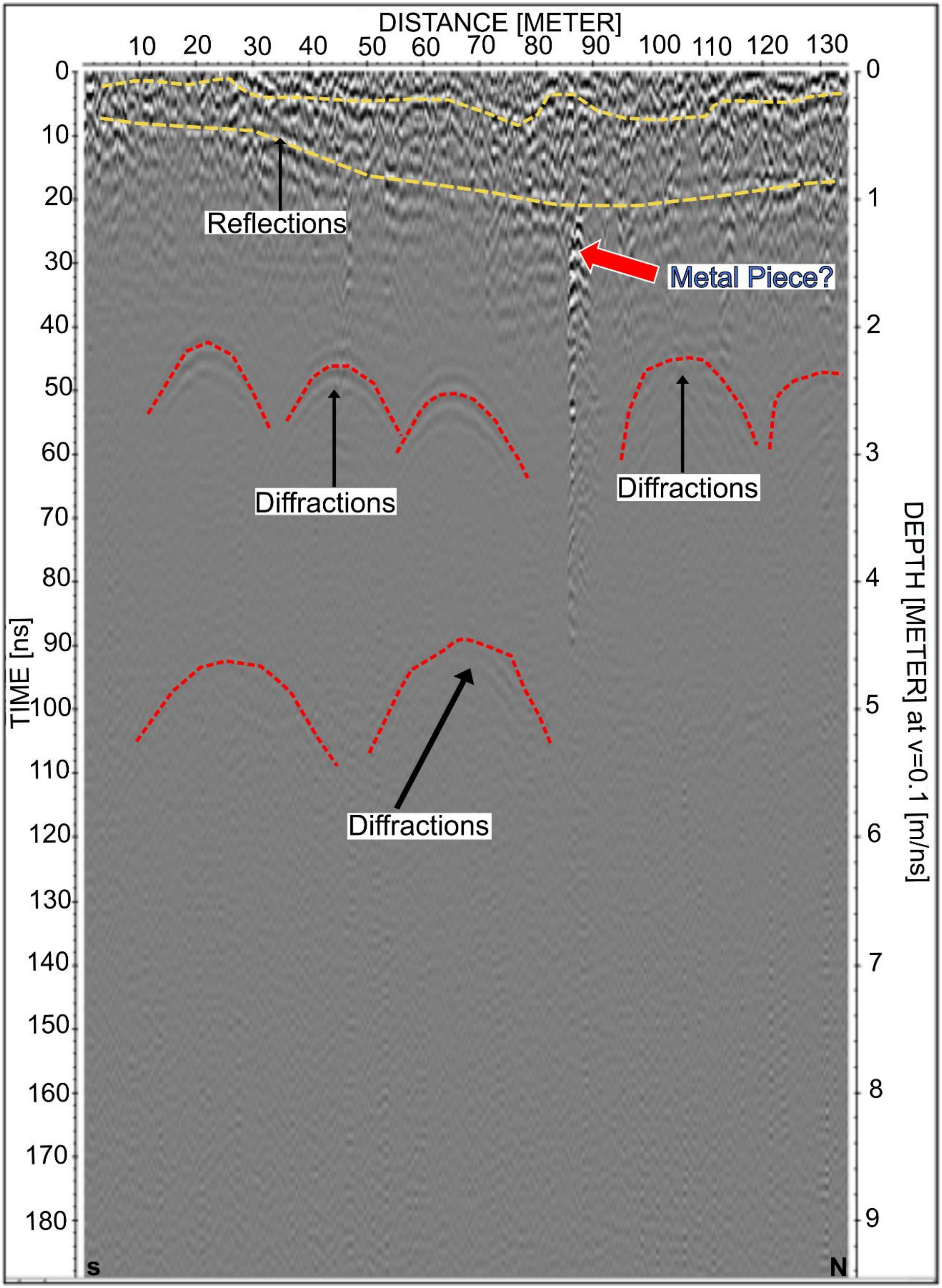

Figure B2: Processed GPR image of line R21SINK001_001, group one.

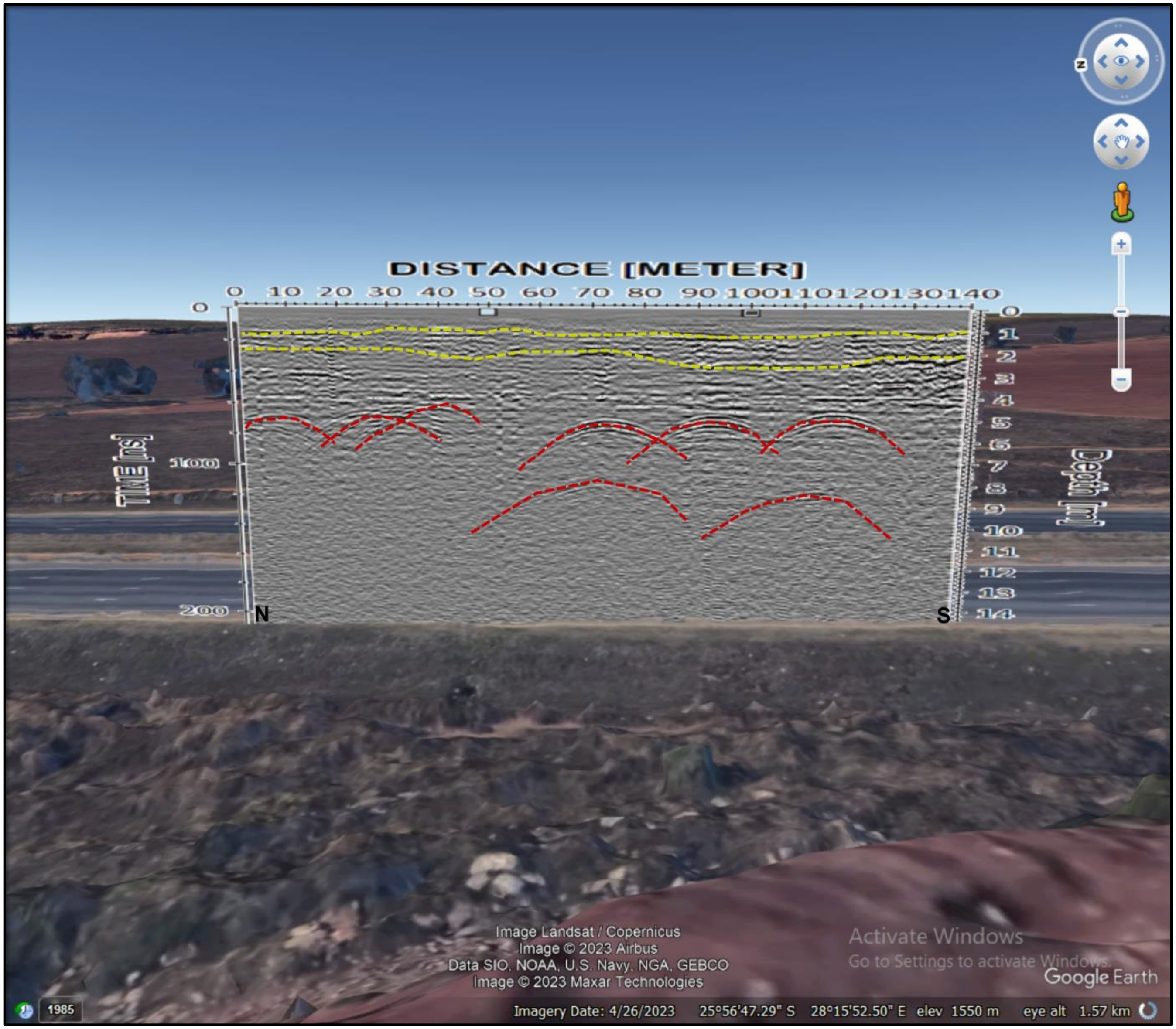

Figure B3: Google Earth image showing the location of line R21SINK001_003.

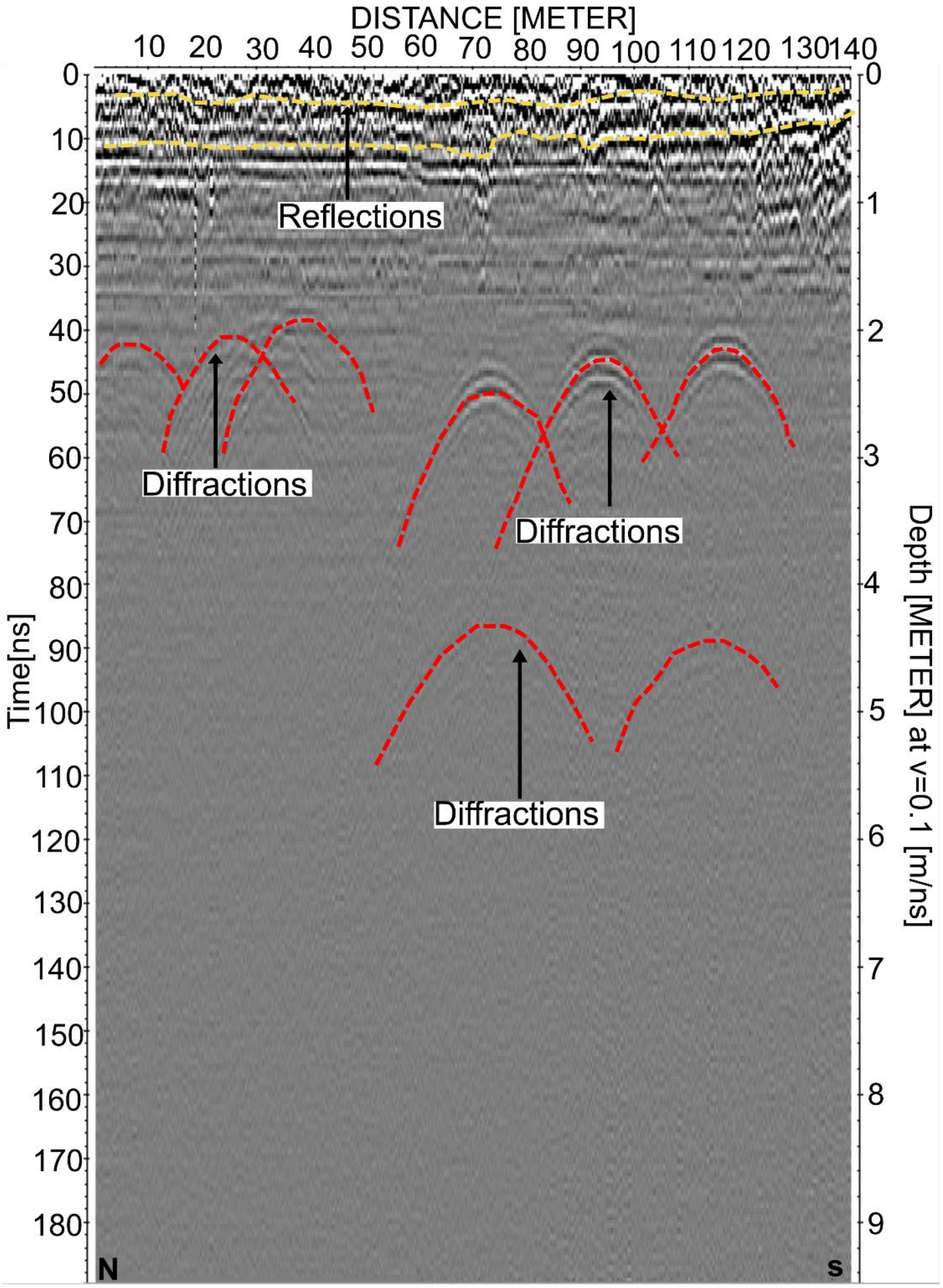

Figure B4: Processed GPR image of (R21SINK001_003) from group one.

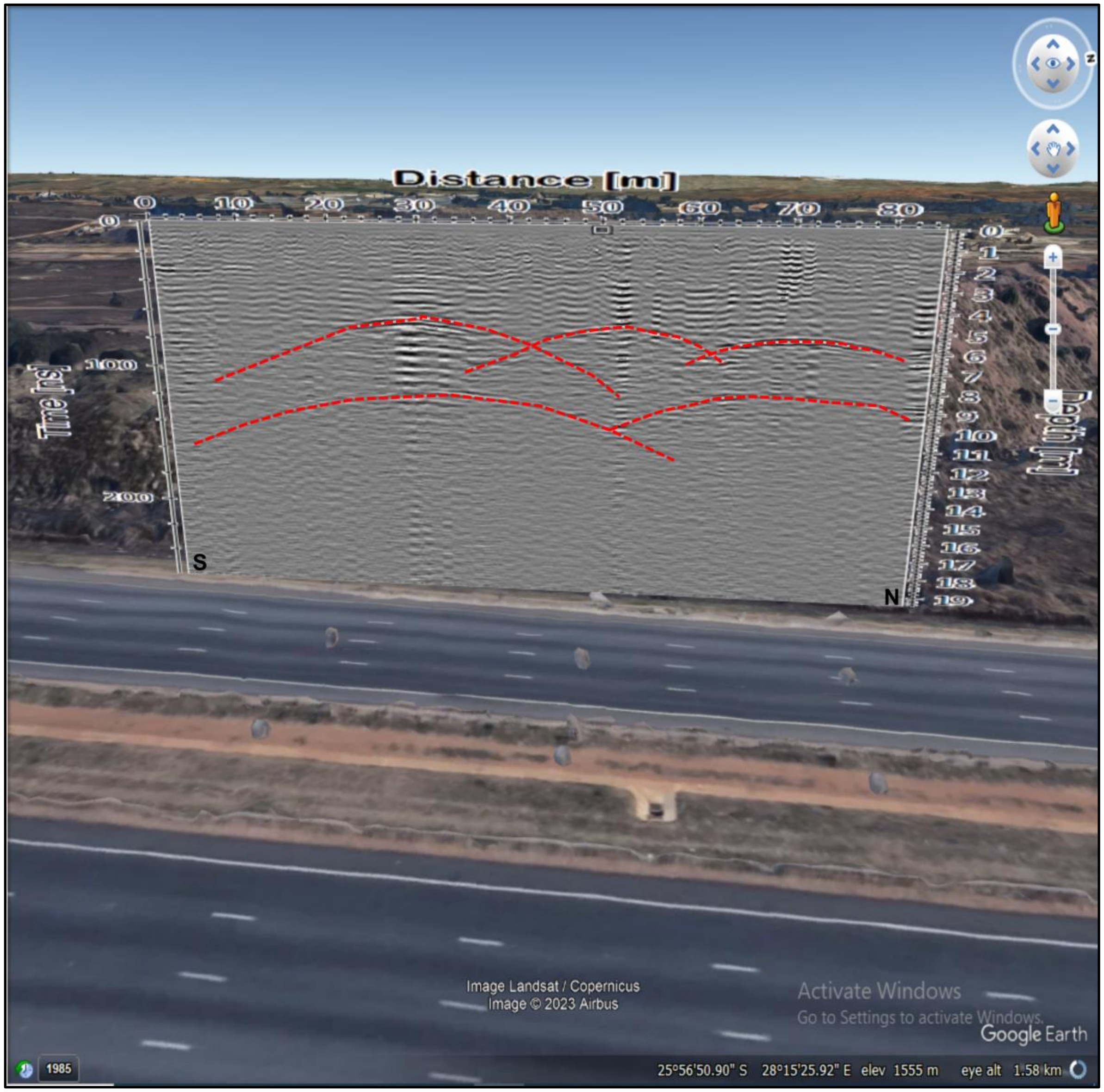

Figure B5: Google Earth image showing the location of line R21SINK002_001.

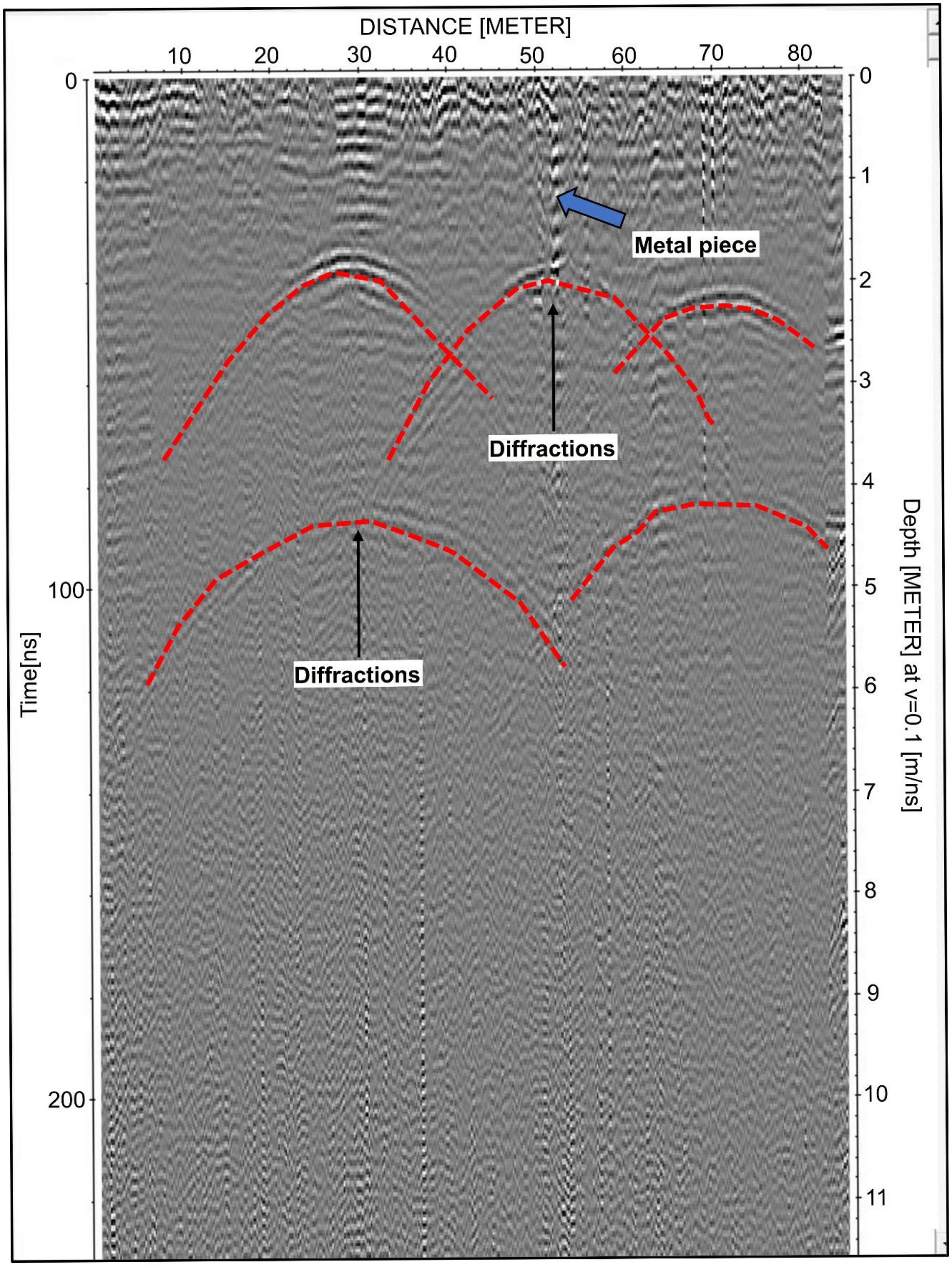

Figure B6: Processed GPR image of line R21SINK002_001 from group two.

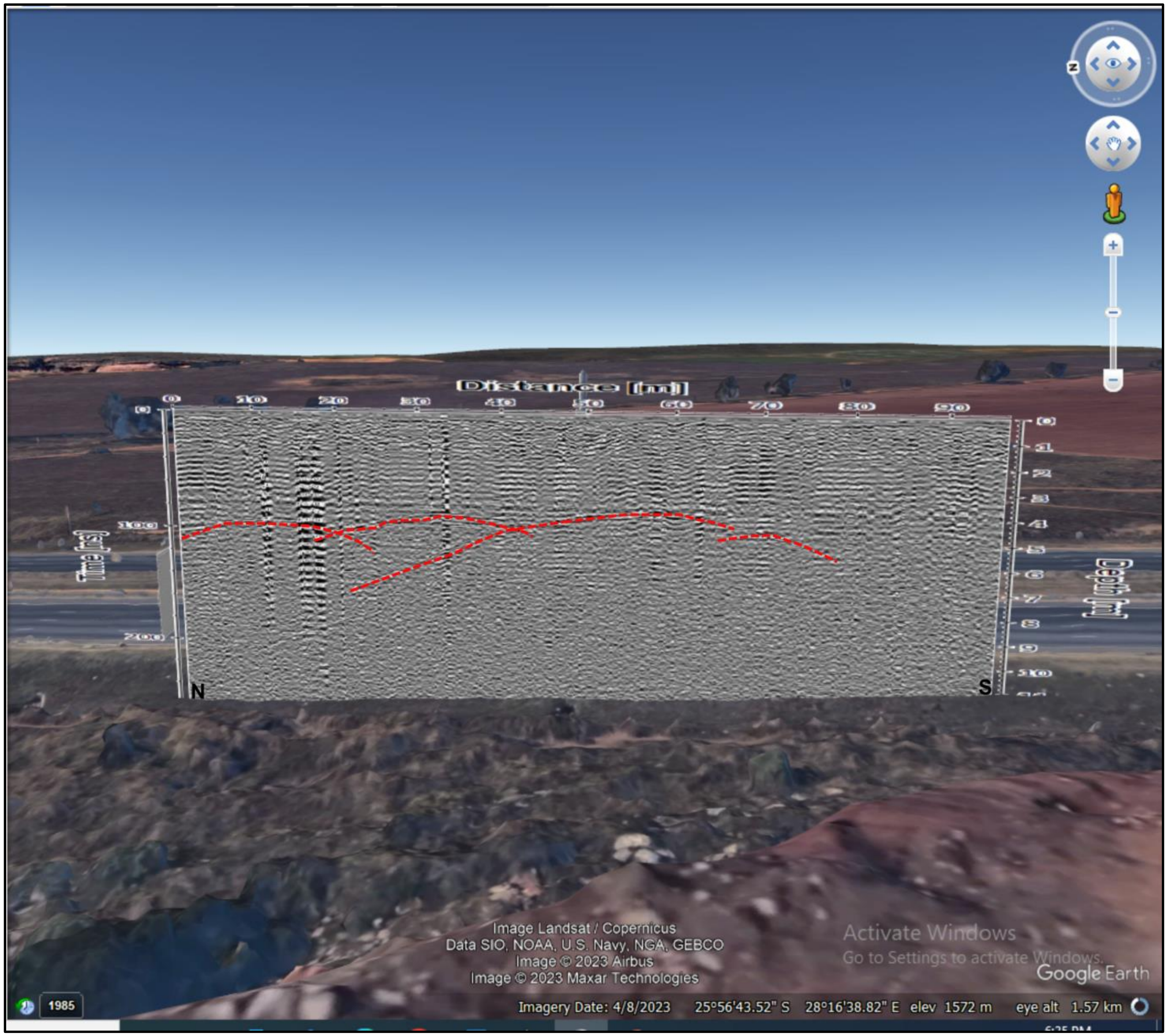

Figure B7: Google Earth Image showing the location of line R21SINK002_OO5 from group two.

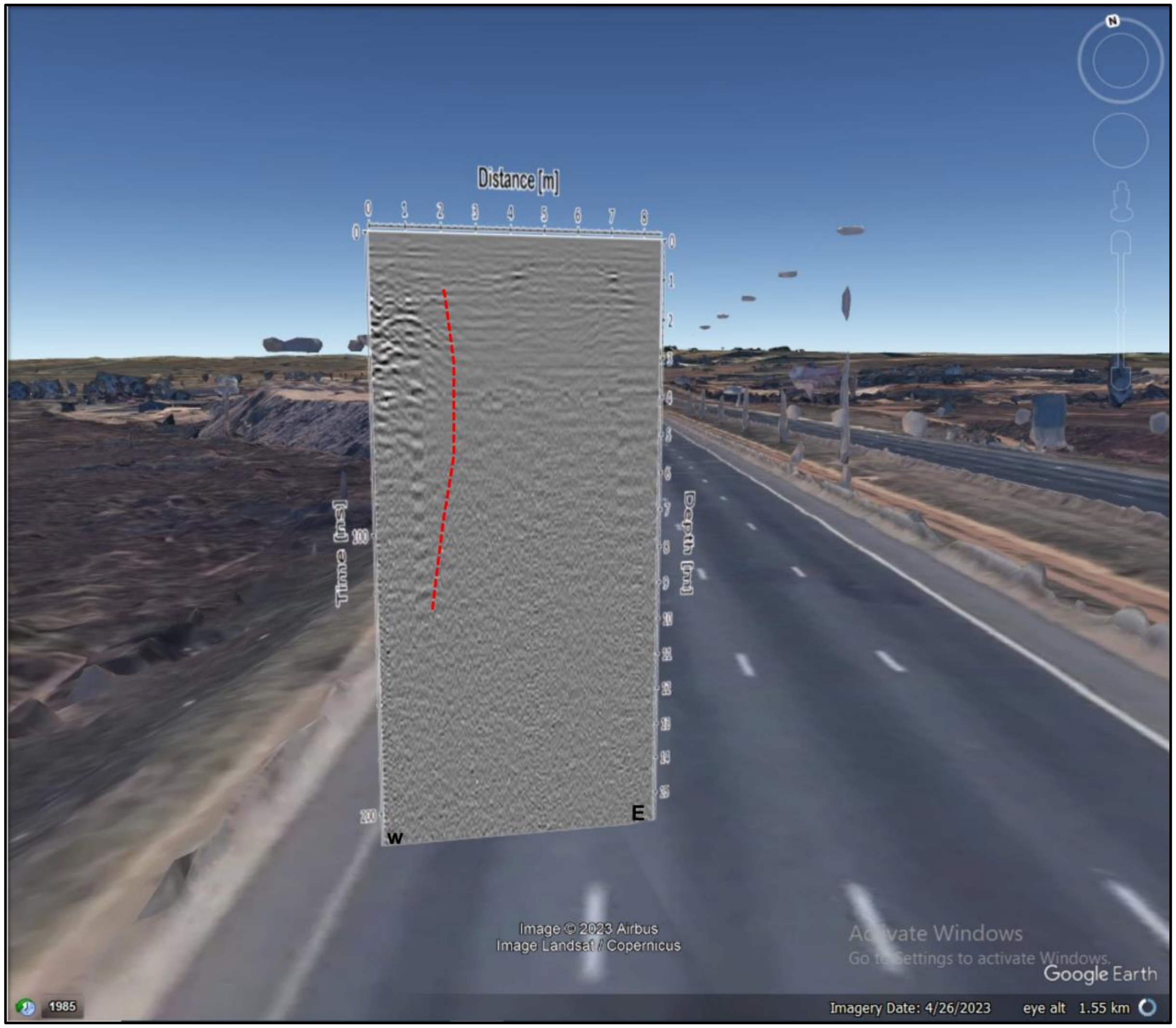

Figure B8: Google Earth Image showing the location of line R21SINK003_OO3.

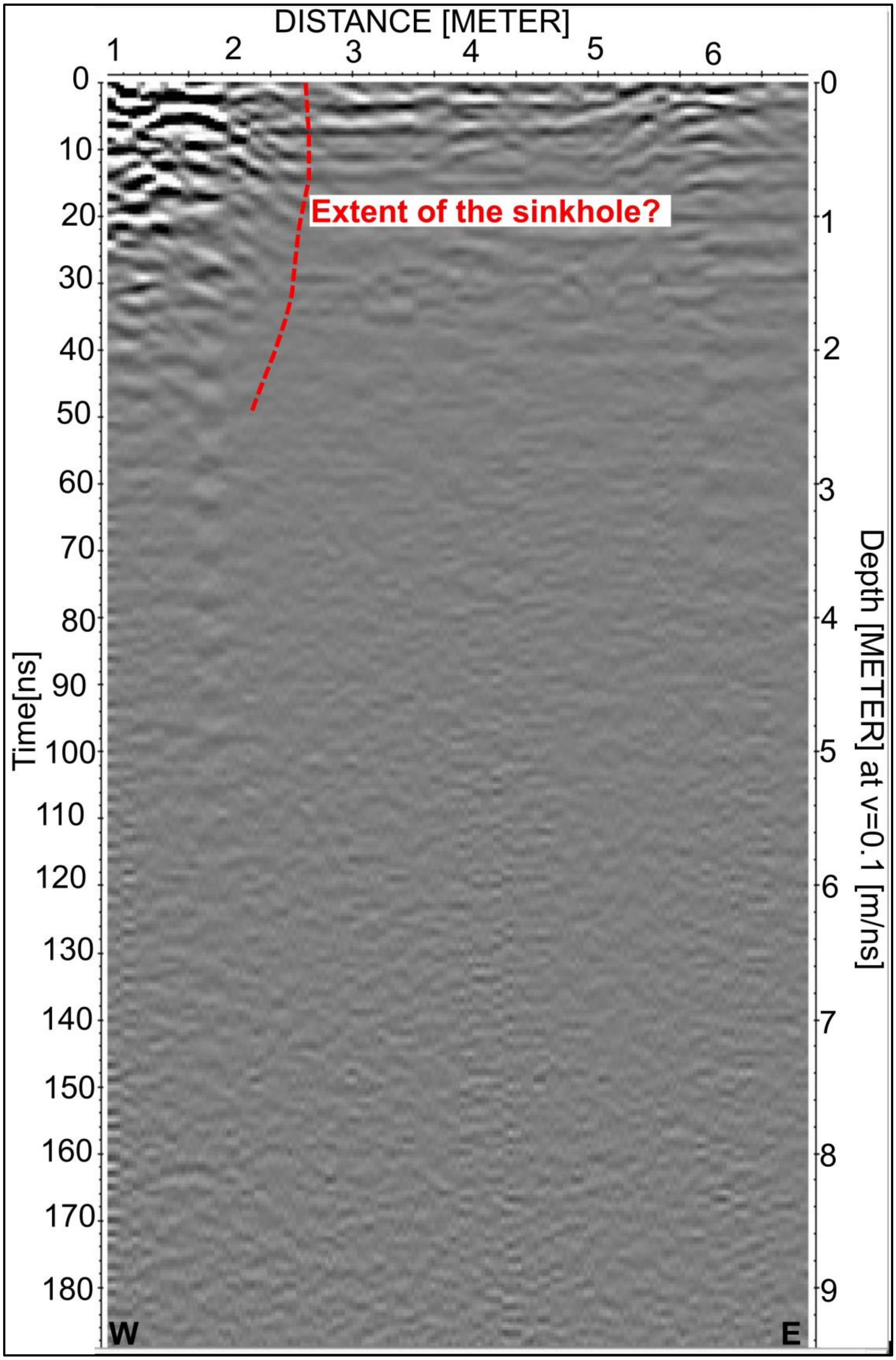

Figure B9: Processed GPR image of line R21SINK003_003 from group three.

Figure B10: Google Earth image with the location of line R21SINK003_0015 from group three.

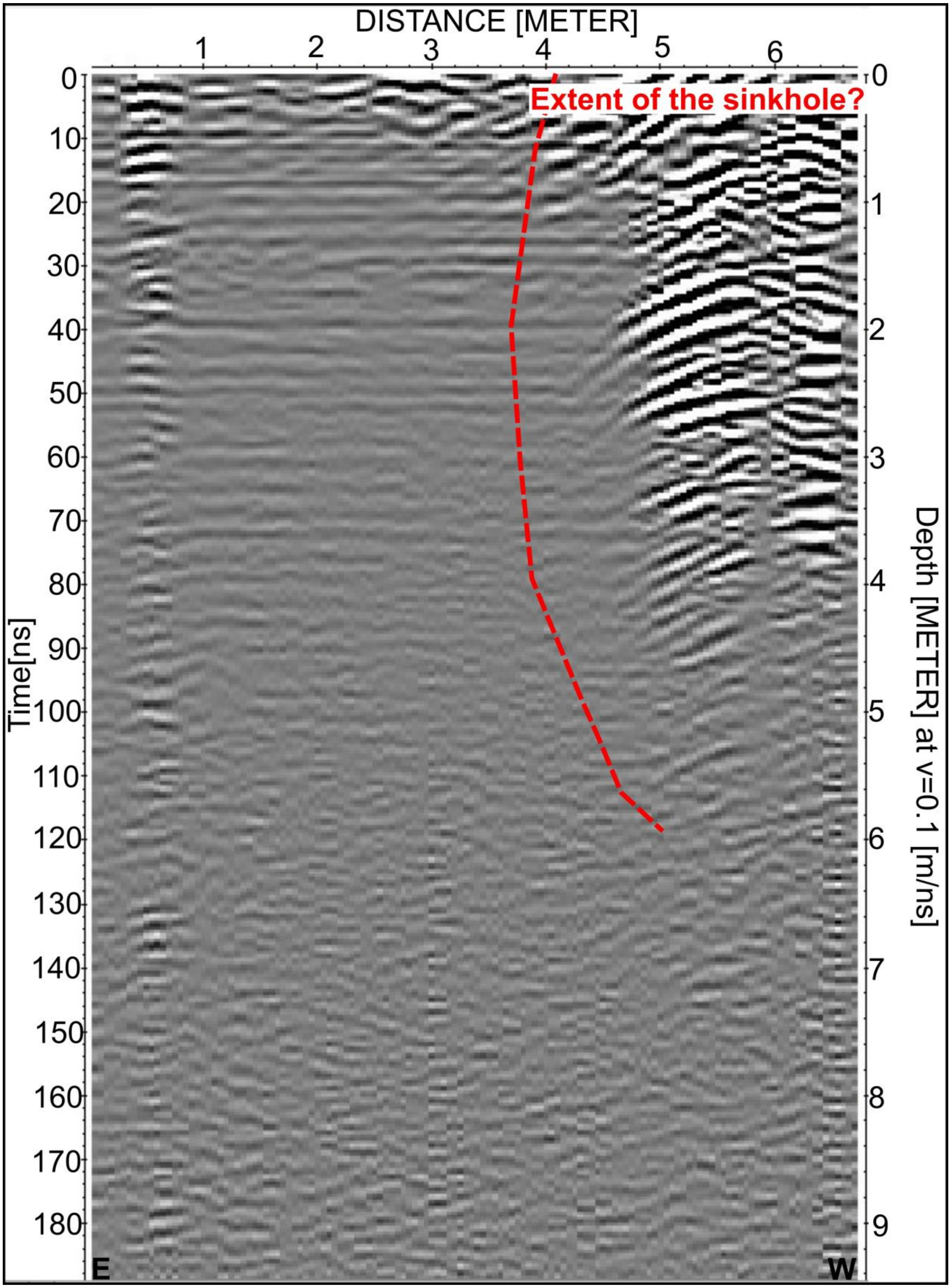

Figure B11: Processed GPR image of line R21SINK003_0015 from group three.

Figure B12: Google Earth Image showing the location of line R21SINK002_003.

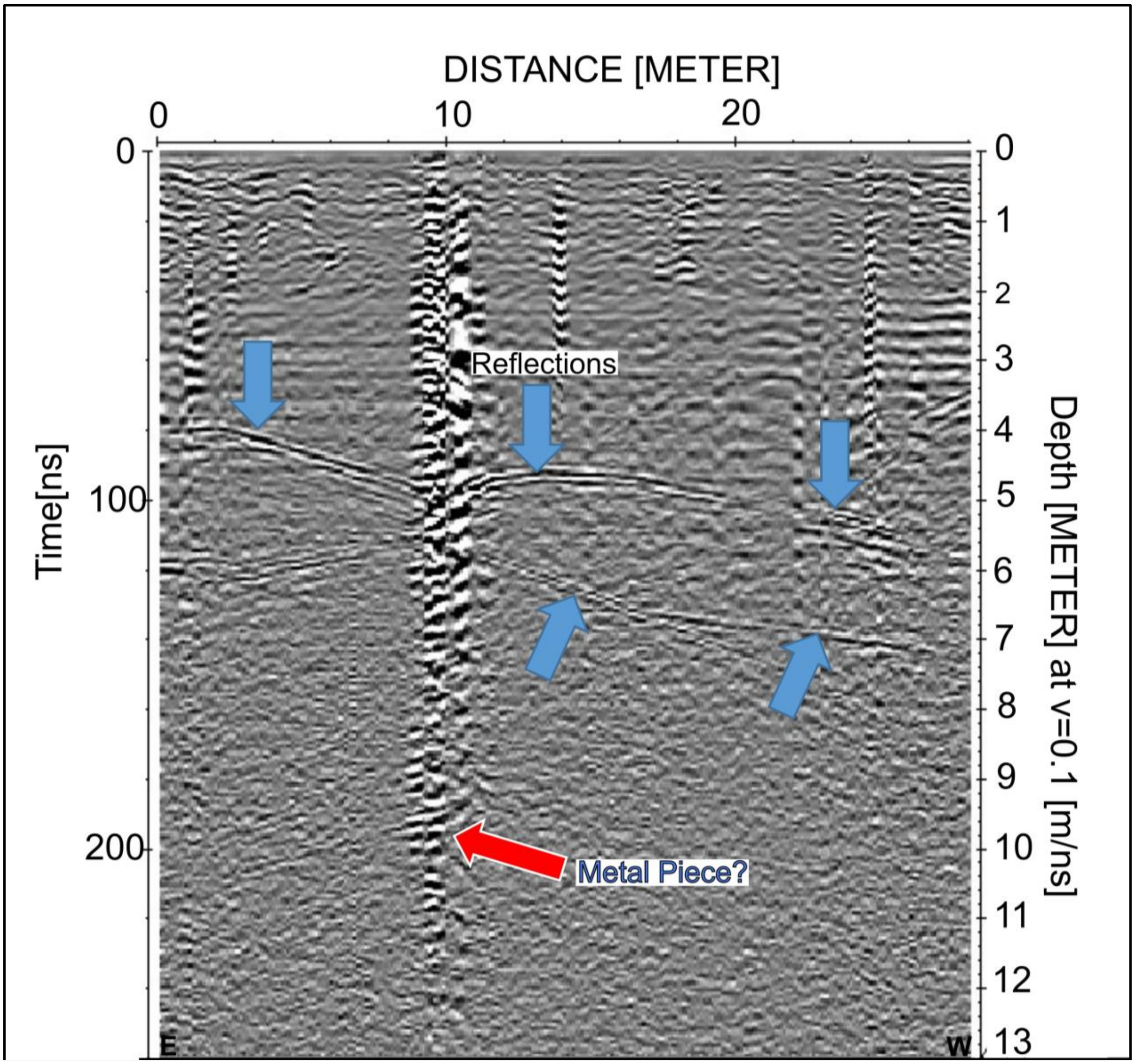

Figure B13: Processed GPR image of line R21SINK002_003 from group two.

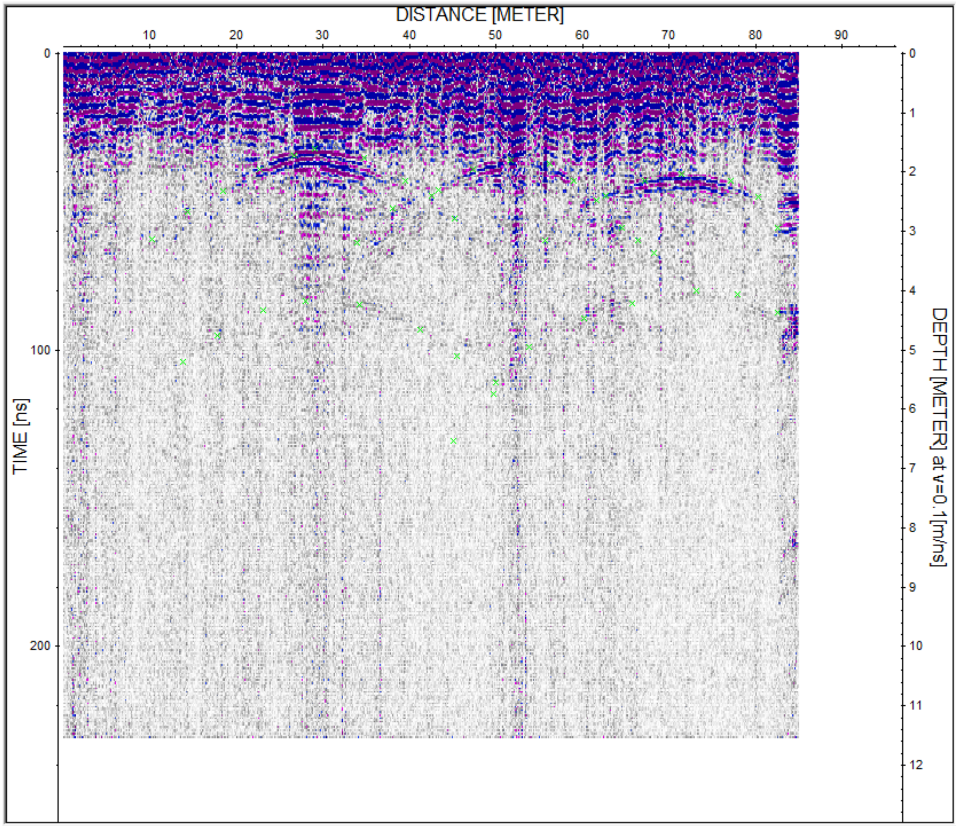

Figure B14: A time slice of line R21SINK002_005 (group R21SINK002) with all the picks, shown in green. These picks were later used to create the 3D digitised cubes.

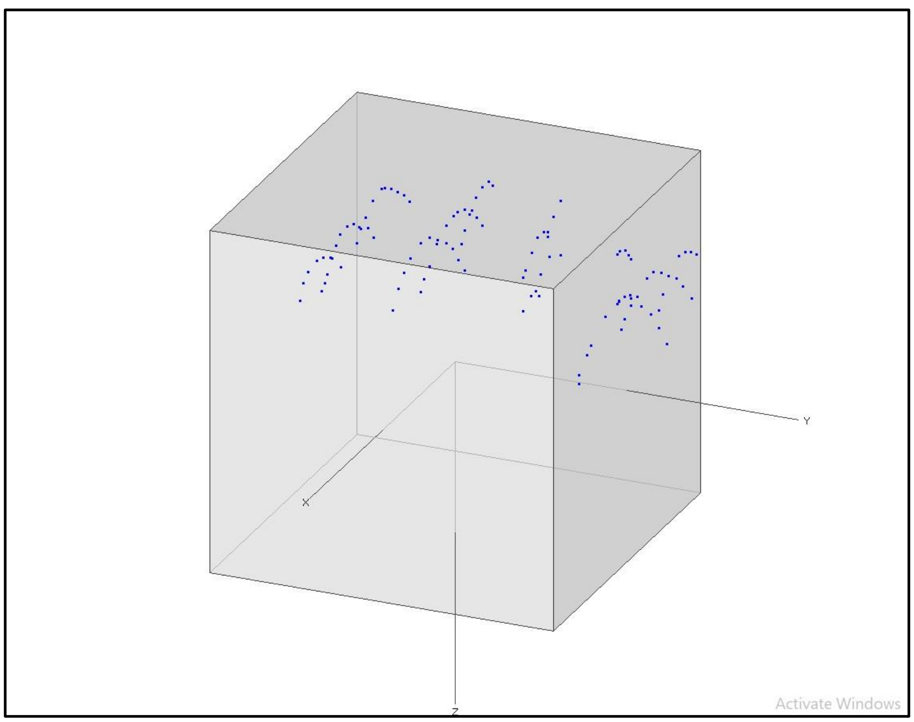

Figure B15: 3-D digitised hyperbolas showing all the points picked from group R21SINK002.

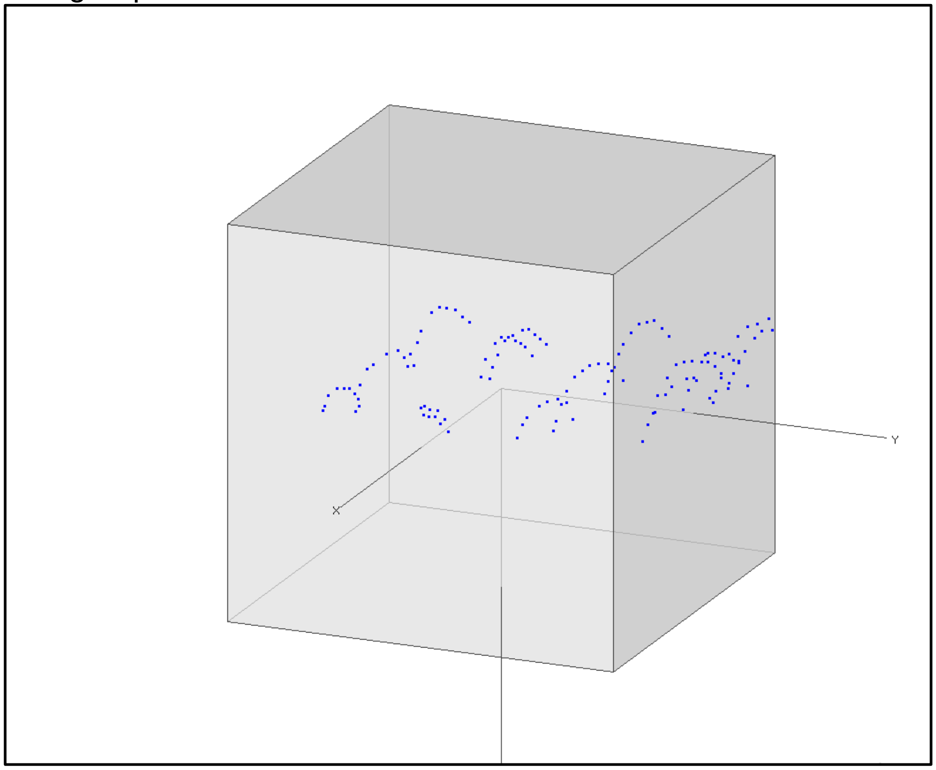

Figure B16: 3-D digitised hyperbolas showing all the points picked from group R21SINK001 (from R21SINK001_001 to R21SINK001_004).

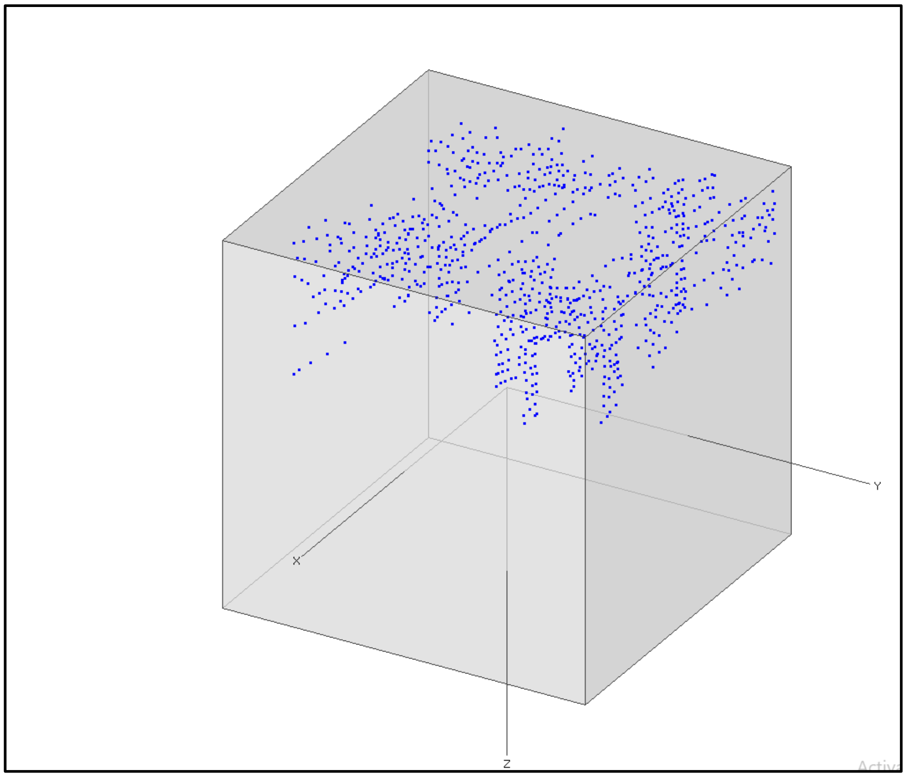

Figure B17: 3-D digitised hyperbolas showing all the points picked from group R21SINK003 (from R21SINK003_001 to R21SINK003_0025).

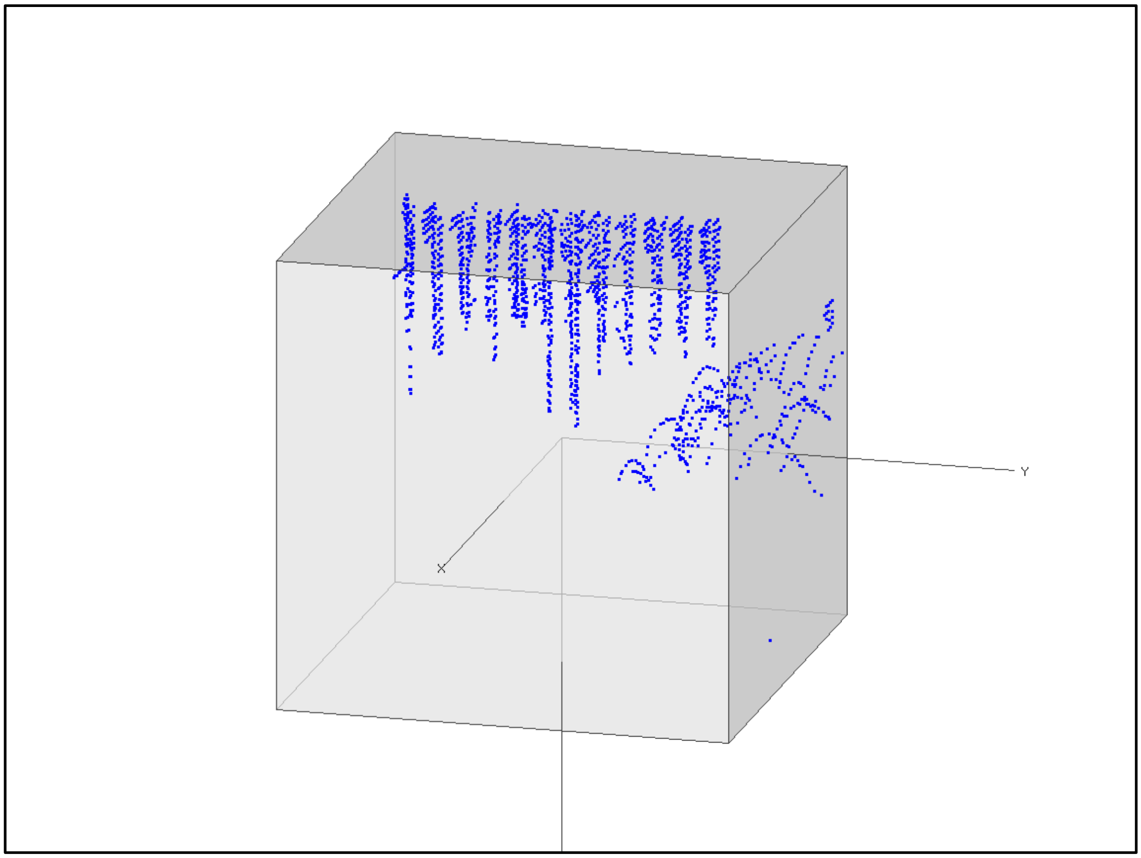

Figure B18: 3D digitised hyperbolas from All 33 Profile.

Appendix C

Seismic Results

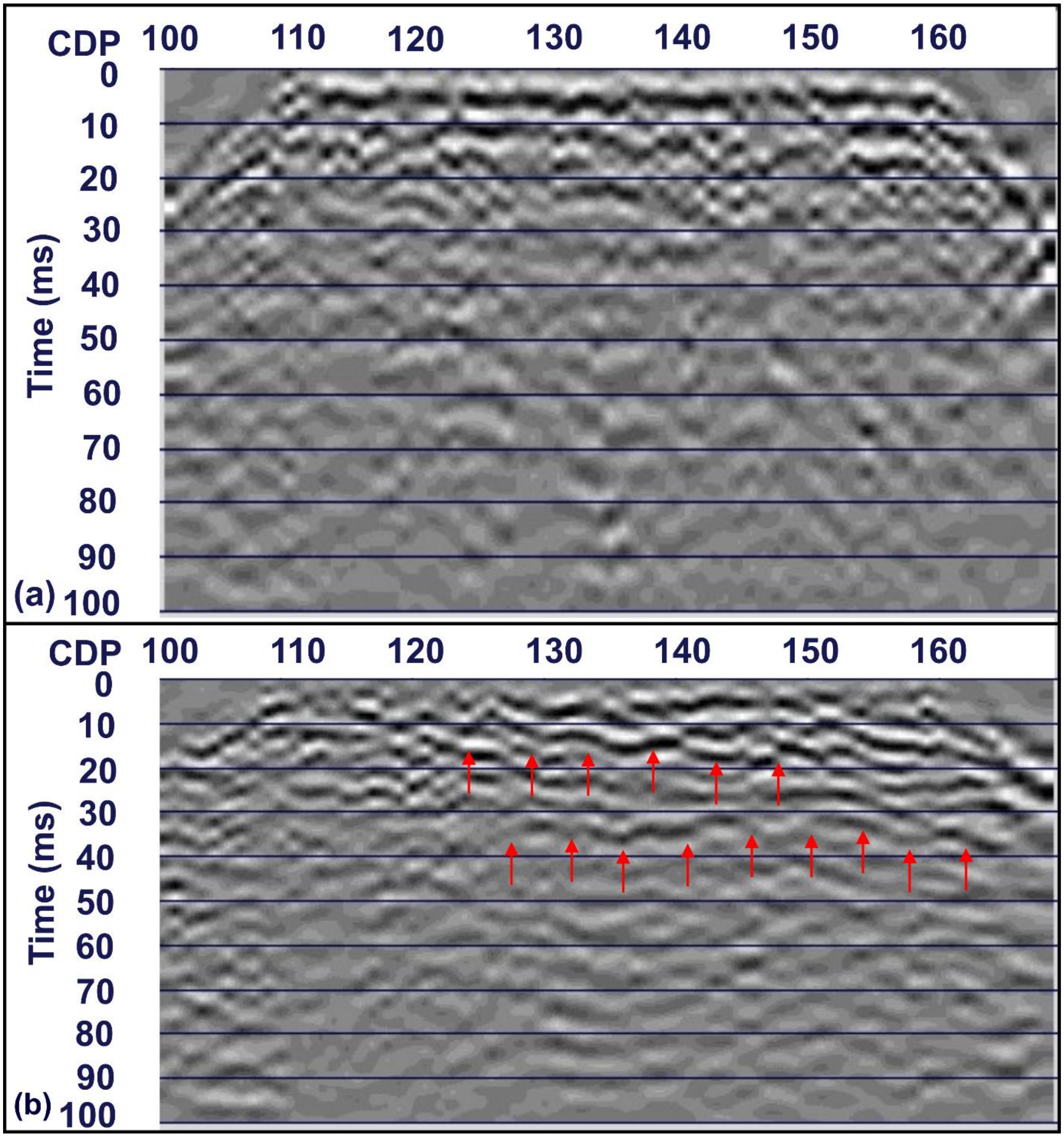

Figure C1: (a) Brute stack using 2000 m/s. (b) Processed section showing the improved reflections in red arrows from line 3.

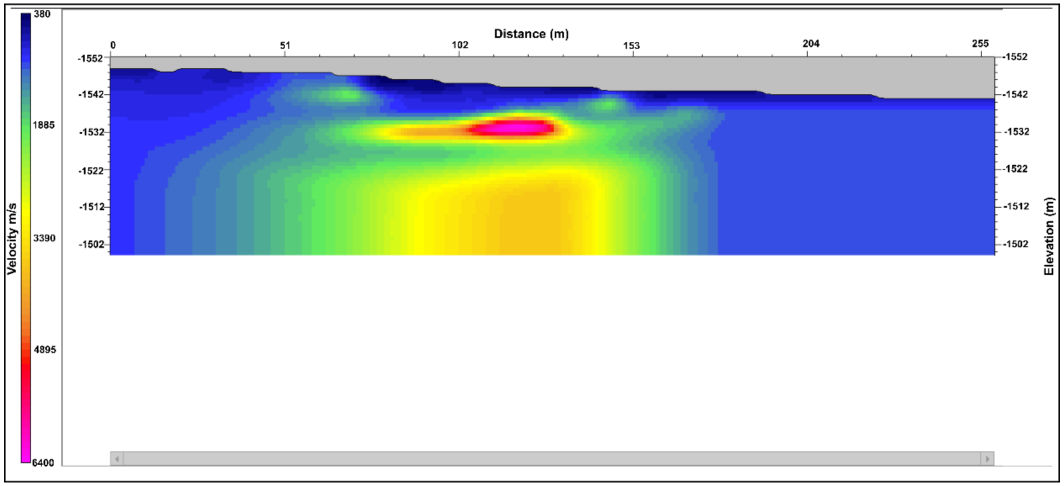

Figure C2: Refraction seismic data (tomogram) of line 1 with distance (m) on the x-axis and elevation (m) on the y-axis.

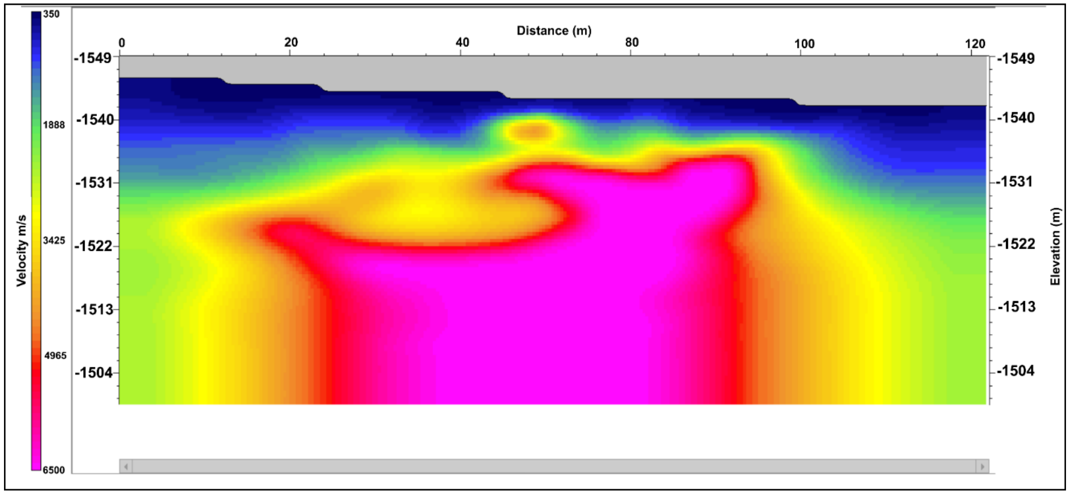

Figure C3: Refraction seismic data (tomogram) of line 2 with distance (m) on the x-axis and elevation (m) on the y-axis.

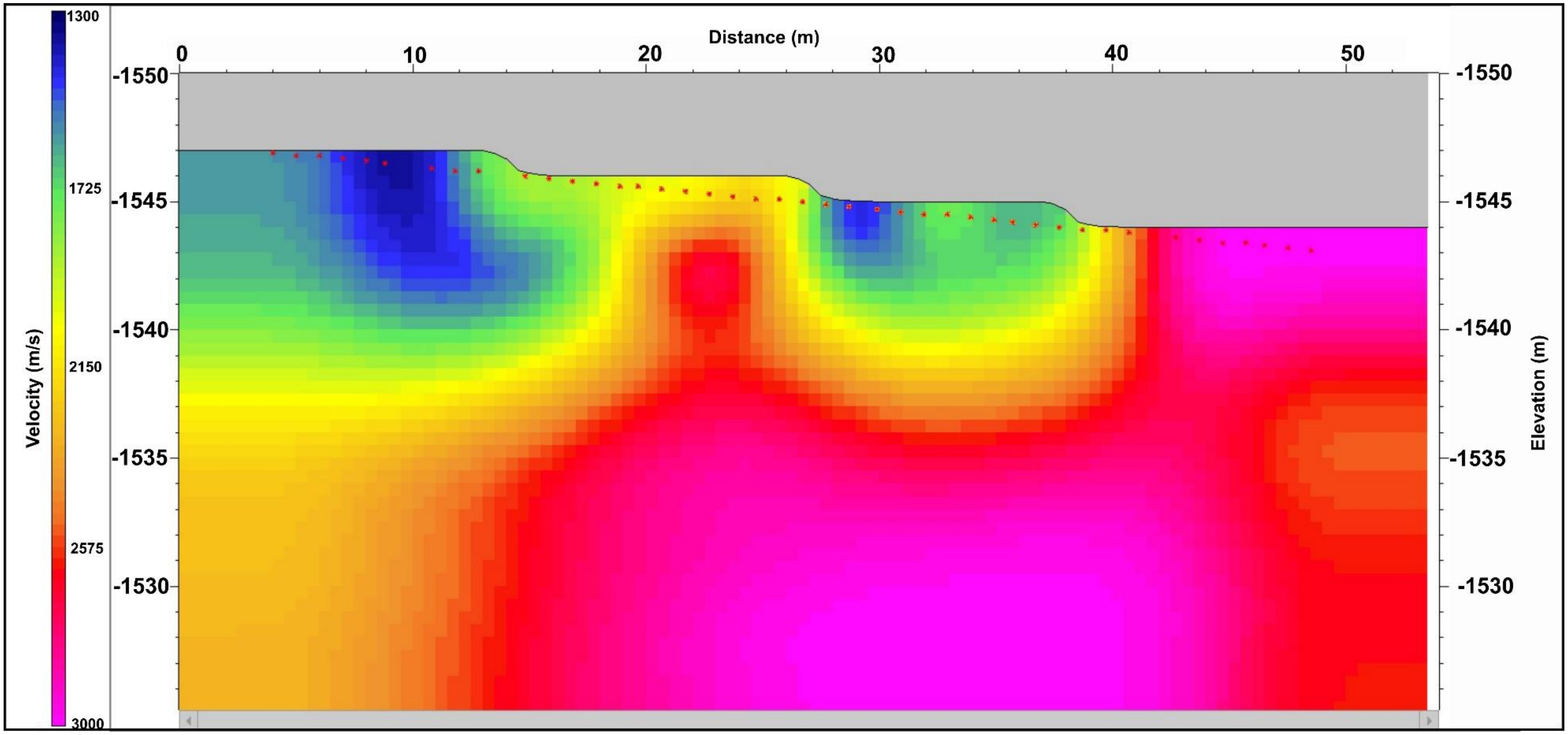

Figure C4: Refraction seismic data (tomogram) of line 3 with distance (m) on the x-axis and elevation (m) on the y-axis.

Appendix D

Multichannel Analysis of Surface Waves Results

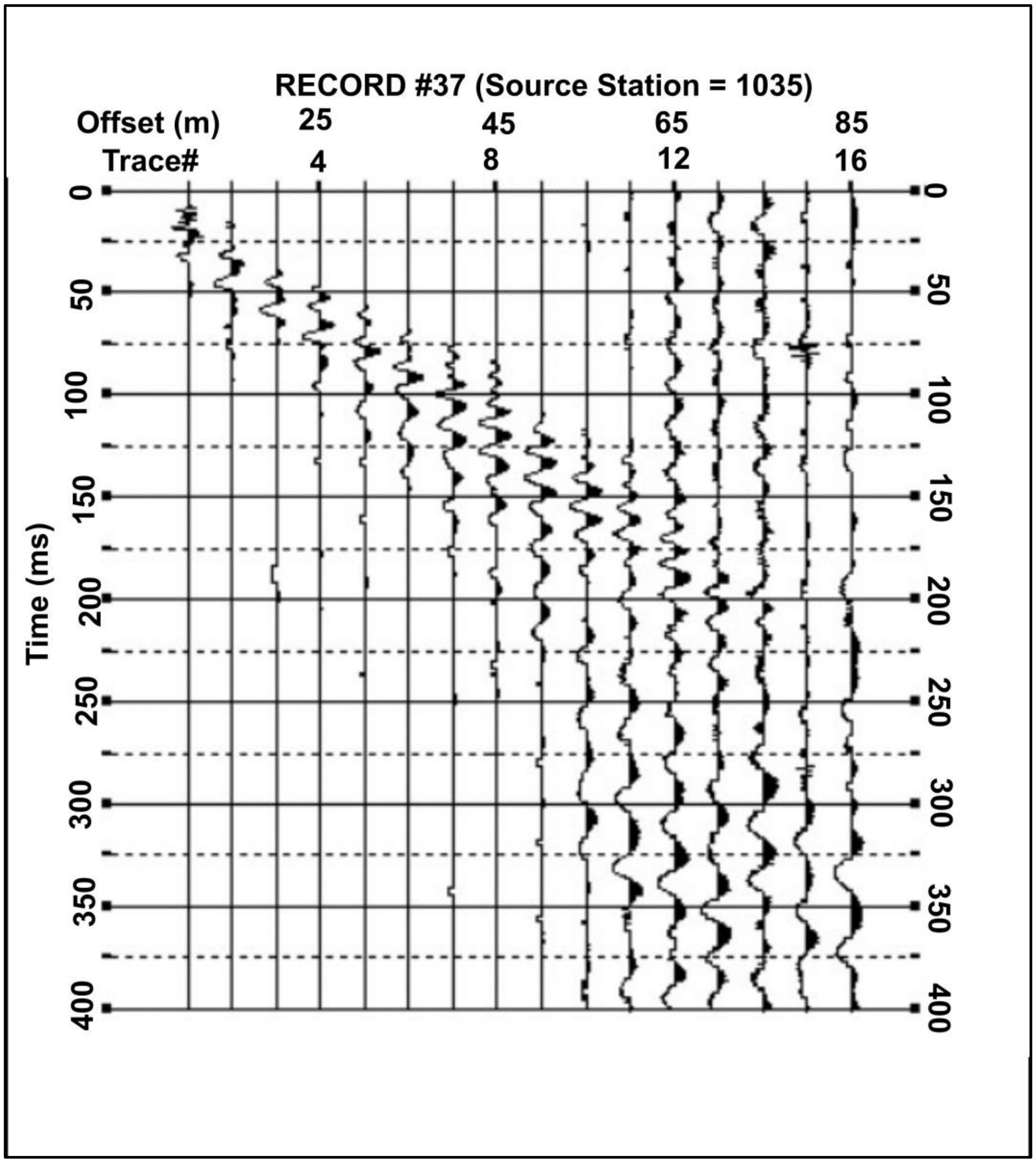

Figure D1: Raw shot gathers from line one.

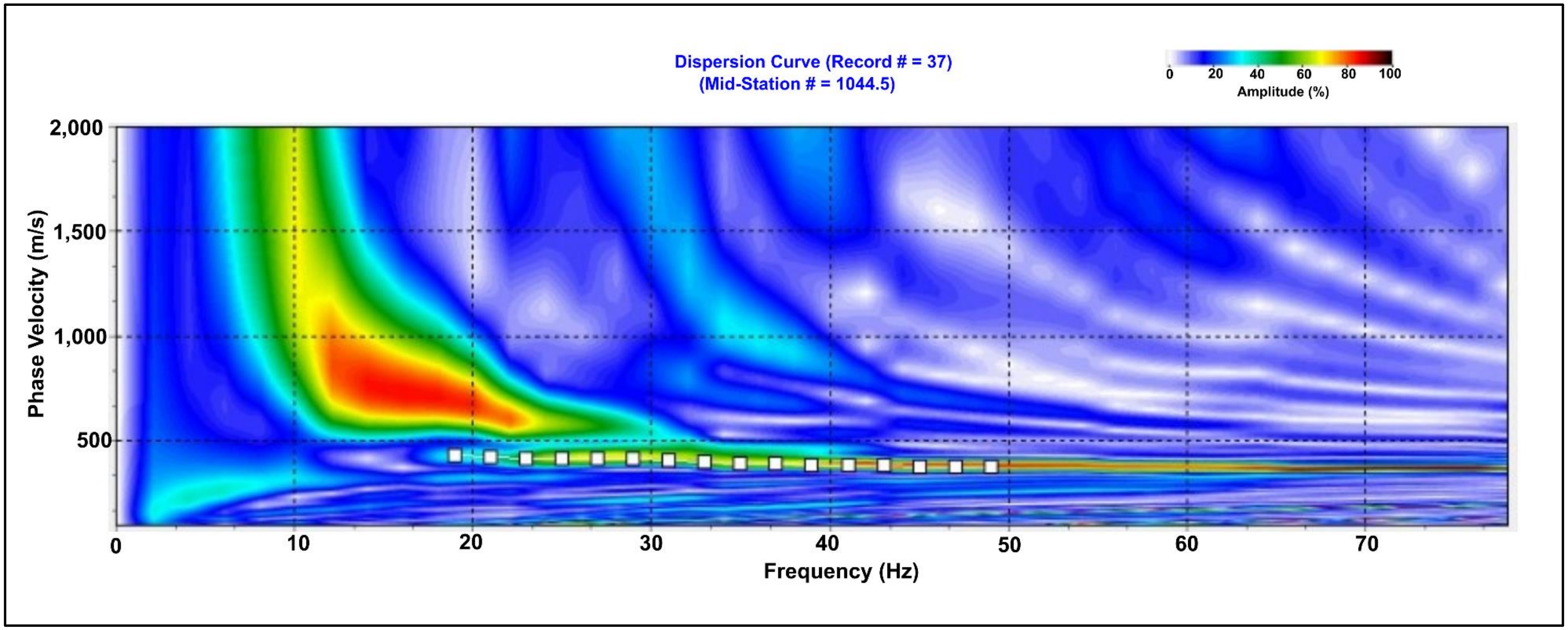

Figure D2: Corresponding dispersion curve with superimposed picks of fundamental mode or dispersion curve extraction points (white dots).

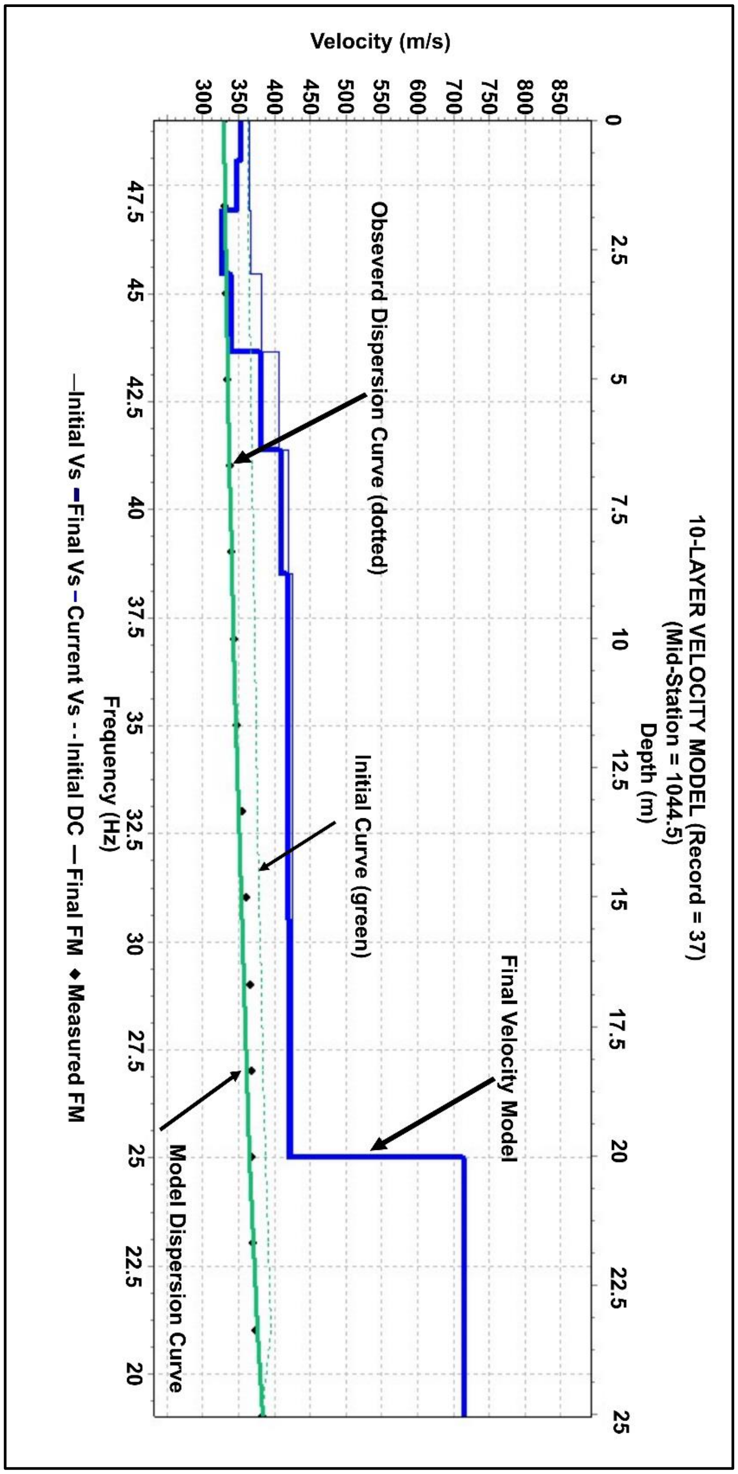

Figure D3: Dispersion curves are then extracted to be inverted for a 1D V_S profile. The dotted black line represents the observed dispersion curve as picked on the overtone image; the blue solid line represents the model dispersion curve; the green dotted line represents the initial curve, and the step-ladder-shape represents the final velocity model.

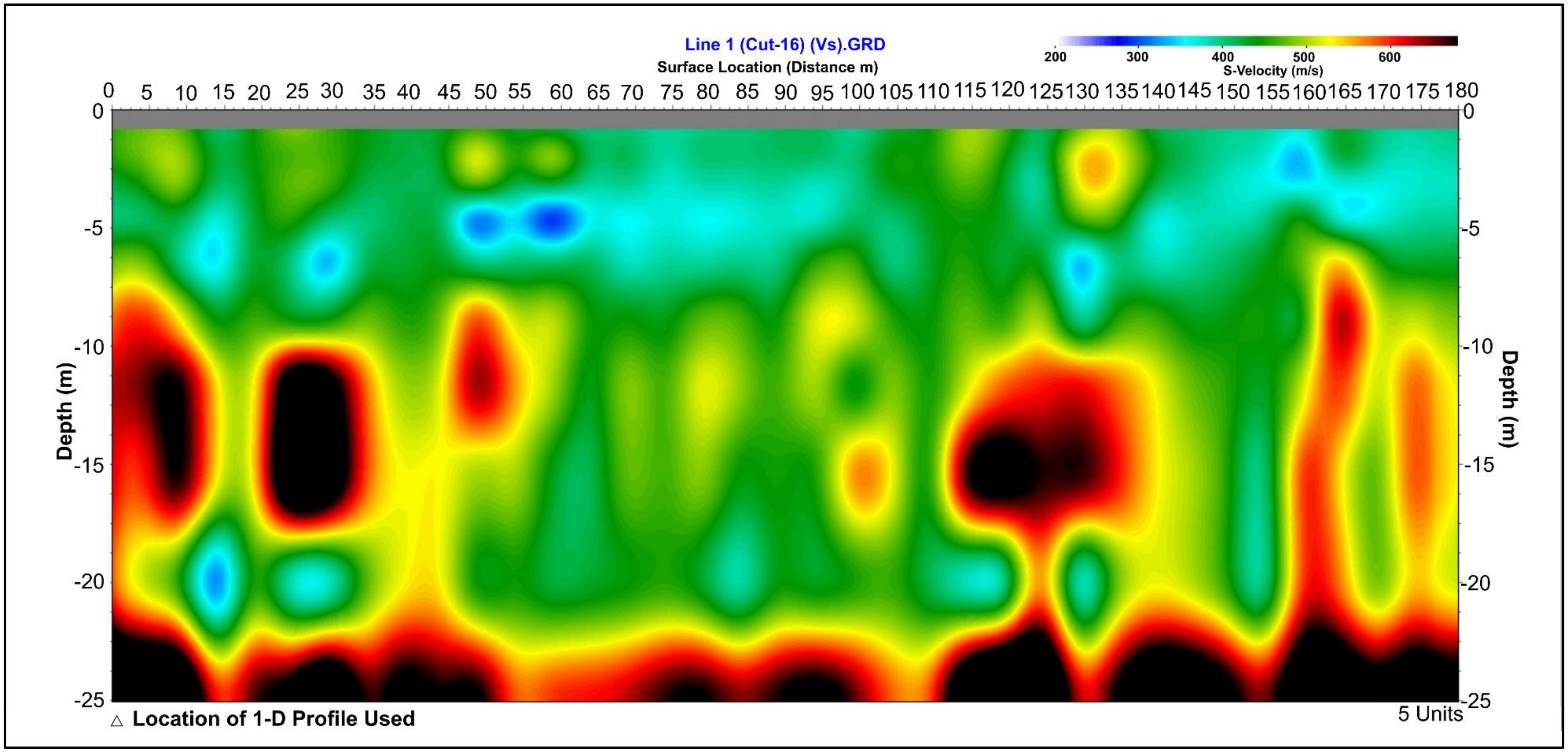

Figure D4: 2D VS map obtained from a passive R21 MASW survey using a linear 24- channel receiver array of 5-m spacing

Appendix E

Rehabilitation of the R21 Sinkhole

It is also worth mentioning that the rehabilitation and restoration process has begun almost two years since the formation of the R21 sinkhole, shown in Figure E1. The repair of this sinkhole started in December 2023. This results from a joint venture between Raubex Group Limited and Esor Construction (Pty) Ltd. The project will cost an estimated R144 245 942.80, and according the South African National Roads Agency SOC Ltd or SANRAL, it is expected to be completed by the end of August 2024.

Appendix E 1: Images from the R21 sinkhole site (adapted from Mabele, 2024).